Biological and Environmental Transformations and Applications of Two-Dimensional Nanomaterials and Hybrids

By Zhongying Wang

B.Sc., Tsinghua University, 2010

M.Sc., Brown University, 2015

A DISSERTATION SUBMITTED IN PARTIAL FULFILLMENT OF THE REQUIREMENTS FOR THE DEGREE OF DOCTOR OF PHILOSOPHY IN THE DEPARTMENT OF CHEMISTRY AT BROWN UNIVERSITY

Providence, Rhode Island

May, 2016

This dissertation by Zhongying Wang is accepted in its present form

by the Department of Chemistry as satisfying the

dissertation requirement for the degree of Doctor of Philosophy.

Date_____ _____

Professor Robert H. Hurt, Advisor

Recommended to the Graduate Council

Date_____ _____

Professor Lai-Sheng Wang, Reader

Date_____ _____

Professor Shouheng Sun, Reader

Approved by the Graduate Council

Date_____ _____

Professor Peter M. Weber,

Dean of the Graduate School

Curriculum Vita

Zhongying Wang was born on September 9th, 1987, in China. He went to Tsinghua University for undergraduate study since 2006 and graduated with a B.Sc. in Chemistry in 2010. Zhongying started doctoral study in September, 2010 in the Department of Chemistry at Brown University. His research mainly focused on chemical transformations and applications of metal and two dimensional nanomaterials in environmental and biological systems. He has published 9 peer-reviewed papers.

PUBLICATIONS

1. **Z Wang**, D Tonderys, SE Leggett, EK Williams, MT Kiani, R Spitz Steinberg, Y Qiu, IY Wong and RH Hurt. "Wrinkled, wavelength-tunable graphene-based surface topographies for directing cell alignment and morphology". *Carbon*, **2016**, 97, 14-24.
2. **Z Wang**, X Lv, Y Chen, D Liu, X Xu, GTR Palmore and RH Hurt. "Crumpled graphene nanoreactors". *Nanoscale*, **2015**, **7**, 10267-10278.
3. Y Chen, **Z Wang,** Y Qiu. "Aerosol synthesis and application of folded graphene-based materials". *International Journal of Modern Physics B.* **2015**, 29 (03), 1530003
4. Y Qiu, **Z Wang**, ACE Owens, I Kulaots, Y Chen, AB Kane, RH Hurt. "Antioxidant chemistry of graphene-based materials and its role in oxidation protection technology". *Nanoscale.* **2014**, *6* (20), 11744-11755.
5. **Z Wang**, A Von Dem Bussche, PK Kabadi, AB Kane, RH Hurt. "Biological and environmental transformations of copper-based nanomaterials". *ACS Nano*. **2013**, *7* (10), 8715-8727.
6. J Lu, Q Peng, **Z Wang**, C Nan, L Li, Y Li. "Hematite nanodiscs exposing (001) facets: synthesis, formation mechanism and application

for Li-ion batteries". *Journal of Materials Chemistry A*. **2013**, *1* (17), 5232-5237.

7. J Liu, **Z Wang**, FD Liu, AB Kane, RH Hurt. "Chemical transformations of nanosilver in biological environments". *ACS Nano*, **2012**, *6* (11), 9887-9899.
8. D Wang, **Z Wang**, P Zhao, W Zheng, Q Peng, L Liu, X Chen, Y Li. "Rare-Earth Oxide Nanostructures: Rules of Rare-Earth Nitrate Thermolysis in Octadecylamine". *Chemistry, an Asian journal*, **2010**, *5* (4), 925.
9. D Wang, X Ma, Y Wang, L Wang, **Z Wang**, W Zheng, *et al*. "Shape control of CoO and $LiCoO_2$ nanocrystals". *Nano Research*, **2010**, *3* (1), 1-7.

Acknowledgements

It would not be possible to accomplish my PhD thesis without the support from the knowledgeable professors, collaborators, friends and family, to whom I would like to express my sincere acknowledgements.

First and foremost, I would like to thank my research advisor Professor Robert Hurt for the continuous support on my PhD research and career development. His enthusiasm, encouragement, and immense knowledge inspires and guides me along my five years. His attitude and philosophy on research will influence my own work for life. Meanwhile, he always gives me great freedom to pursue my interests and encourage my own ideas. I can hardly imagine what a better advisor would be.

I would also like to thank my committee members, Professor Lai-sheng Wang, Professor Carthene R. Bazemore-Walker and Professor Shouheng Sun for their encouragement, insightful comments during my RPD, ORP and dissertation defense.

I really appreciate the instruction and assistance of the following people: Anthony McCormick for the assistance with the HRTEM, TEM, SEM; Hector Graces for assistance with the XRD, EPR, AFM and Raman spectroscopy; and Joseph Orchardo and David Murray for the assistance with the facilities in the environmental chemistry lab.

I want to thank many collaborators: Professor Agnes Kane, Dr. Annette von dem Bussche and Dr. Pranita Kabadi for their *in vitro* test in Cu transformation project; Professor G. Tayhas R. Palmore and Dan Liu for their electrochemical measurement in crumpled graphene project; and Professor Ian Wong, Susan Leggett for their cell culture works in wrinkled graphene project.

Great thanks to the members of Professor Hurt's group: Dr. Indrek Külaots, Dr. Jingyu Liu, Dr. Fei Guo, Dr. Megan Creighton, Dr. Yantao Chen, Dr. Zachary Saleeba, Yang Qiu, Ruben Spitz Steinberg, Daniel Tonderys, Xiaoshu Lv, Christy Chan and Sumaira Shah. They made my life at Brown really enjoyable.

Finally, I'd like to thank my significant other, Wen Zheng, who is always by my side through all the difficulties since we met each other in 2007. Thanks to Wen again for giving life to our little Emily, who's so adorable and cute and my best work ever. I would like to send my deep gratitude to my parents for their endless love and support throughout my life to let me chase my dreams.

Abstract of "Biological and Environmental Transformation and Applications of Two-Dimensional Nanomaterials and Hybrids" by Zhongying Wang, Ph. D., Brown University, May 2016

The widespread use of nanomaterials in established and emerging technologies will inevitably lead to human and environmental exposures that must be characterized and managed to ensure the safe development. This dissertation uses CuO nanoparticles as an example, and investigates the possible chemical transformation pathways, including particle dissolution, ion complexation, particle sulfidation, and the impacts of these transformation on nanoparticle's stability, reactive oxygen species generation and cytotoxicity. This systematic study can help predict the fate and evaluate the potential adverse impacts of CuO nanoparticles released into biological and environmental systems.

Nanoparticles are encapsulated inside crumpled graphene nanosacks, inspired by the atomically thin, conformable, and impermeable nature of graphene, which is expected to inhibit ion release and thus reduce toxicity. However, the crumpled nanosacks turn out to be open structure allowing rapid molecule exchange. In some cases, encapsulation is shown to enhance oxidation and dissolution rate of loaded nanoparticles. Though graphene nanosacks fail to detoxify nanoparticles, other fundamental behaviors are appealing including particle–particle electron transfer mediated by conductive graphene and anti-sintering property by inner walls. Another example utilizing the dimensionality of graphene-based architecture is textured graphene surface, which is fabricated by graphene oxide wet deposition onto pre-stretched elastomers followed by drying and relaxation. Multilayer graphene oxide films form periodic, delaminated buckle textures whose wavelengths and amplitudes can be systematically tuned by variation in the wet deposition

process. Human and murine fibroblasts attach to these textured films and develop pronounced alignment and elongation relative to those on planar controls.

The last part investigates the biological and environmental transformation of novel 2D nanomaterials beyond graphene. Very little is known about the potential implications of these emerging 2D nanomaterials. Because of the great chemical diversity in 2D materials, traditional toxicity testing methods will not be suitable for risk management or safe design across the entire material family. Here we evaluate simple theoretical models to screen and predict transformation and biological reactivity of 2D nanomaterials based on their fundamental chemical properties.

Table of Contents

List of Figures

List of Tables

Chapter 1 Introduction on the transformation and application of nanomaterials

1.1 Transformation of Nanomaterials in Biological and Environmental Media

1.1.1 Development of Nanomaterials

Nanomaterials are defined as those with at least one dimension less than 100 nanometer. Some nanomaterials are naturally-occurring such as ultrafine particles generated in volcanic activities and wild fires, but only after the innovations in analytical and imaging techniques nanomaterials start to be perceived, measured and manipulated. Nanomaterials possess advanced properties and have been used in a wide range of fields including devices, sensors, environment, catalysis, energy and biomedical.[1-3] According to US Environmental Protection Agency, manufactured nanomaterials have been incorporated into more than 1800 commercial products covering various aspects of daily life.[4] The excellent properties of nanomaterials are generally attributed to the confined nanoscale size, which can give rise to the following size dependent effects: surface area effect, unsatisfied coordination effect and quantum confinement effect.

Surface area effect: Considering a cube with n atoms along an edge, the total number of atoms is n^3 and the number of surface atoms is $6n^2$ if the corner and edge multi-counting is ignored when n is sufficiently large. Therefore, the faction of atoms at the surface is following the $1/n$ scaling which implies the surface atom fraction or surface area of nanomaterials grows as the diameter decreases. Such size-dependent manner of surface atom fraction is illustrated in Figure 1-1. The high surface to volume ratio has tremendous impacts on the performance of nanomaterials such as heterogeneous catalysis,[5] where more active sites are exposed in catalytic reactions, as well as environmental remediation which requires high surface area for adsorption and removal of pollutions.[6]

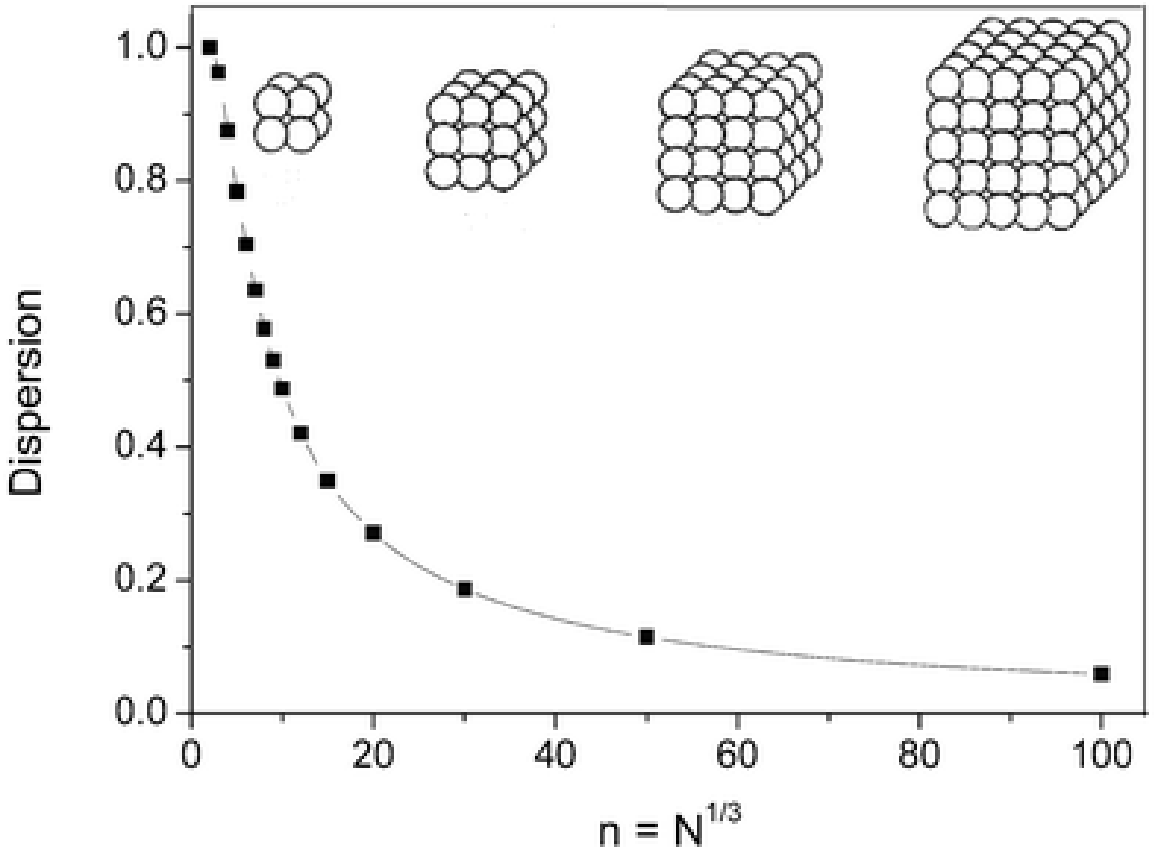

Figure 1-1. Evolution of the fraction of surface atoms as a function of *n* up to 100.The number of surface atoms is inversely related to particle size. Since the number of surface atoms may determine the material reactivity, the size is critical to define the chemical and biological properties of nanomaterials. Image reproduced from [7].

Coordination number: Generally the atoms in the interior of nanoparticles form more bonds with neighboring atoms and are more coordinated than those at the nanoparticle surface. For the model cubic nanoparticle discussed above, corner atoms are more active, followed by edge atoms and in-plane atoms since corner atoms are the most unsaturated ones. Thus decrease of nanoparticle size can give rise to reduced coordination number and increased energy level of surface atoms. Low-coordinated Au atoms have been

reported to scale with catalytic activity, which suggests that the active sites are the corner and edge Au atoms.[8]

Quantum confinement effects: In metal and semiconductor the electronic wave functions of conduction electrons are delocalized over the entire particle. But it becomes size-dependent when size is at nanometer scale. The band gap of semiconductor particles and therefore their absorption wavelength become size dependent.[7] The size-dependence of band gap in semiconductors is best seen in the luminescence properties of quantum dots (QDs). QDs' band gap increases with their size decreases, giving rise to blue shift in emission wavelengths(Figure 1-2).[9]

Figure 1-2. Solutions of QDs showing the tunability of fluorescence on varying size and compositions.Image reproduced from [9]

1.1.2 Potential Environmental and Health Impacts of Nanomaterials

The ability to design nanomaterials for specific purposes has been given rise to a range of manufactured nanomaterials that are added into industrial and consumer products. Currently the available commercial applications of nanomaterials include TiO_2 and ZnO nanoparticles for sunscreens;[10] silver nanoparticles as antimicrobial agents in food storage contains and textile fabrics;[11, 12] carbon nanotube in structural composites, coatings, polymer and microelectronics;[13] and graphene in commercial LED lightbulb; iron oxide (Fe_3O_4 or Fe_2O_3) NPs as a contrast agent for magnetic resonance imaging;[14] cerium oxide (CeO_2) NPs as a fuel-borne catalyst in diesel engines.[15]

With the widespread use of manufactured nanomaterials, these nanoparticles will inevitably enter into biological and environmental systems during the preparation, transportation, use and disposal of these nanoparticle-containing consumer products. Together with the numerous beneficial applications, on the other hand, engineered nanoparticles can also bring the potential negative environmental and health impacts.[16, 17] Even worse, because of their ultra-small size these nanoparticles may easily penetrate skins or cells, rapidly circulate in human body and even directly interact with biological targets within cells. More and more research has focused on the possible toxicity of these engineered nanomaterials, as well as the pathways how the materials come into contact with a living cell.[18-22]

The most widely used and explicitly studied nanomaterial is silver nanoparticle, which has been used as additives in textile fabrics, cosmetics, wound dressing and health supplements to utilize their antimicrobial property.[23-25] Silver has long been used as antimicrobial agent, but only recently people start to use nanosized silver to achieve better

antimicrobial properties and realize that the released silver ion from silver NPs is active species responsible for the observed antimicrobial effects.[26] Furthermore, this very released ionic species again turns out to be the origin of the toxicity of silver nanoparticle.[27, 28] Thus it's critical to study transformation behaviors of silver nanoparticle when evaluating the antibacterial or cytotoxicity in biological and environmental since these transformation reactions can significantly alter the release behavior of ionic silver species.

The transformation of silver nanoparticle has been explored extensively in the recent years, and silver NPs have been reported to undergo profound transformations in biological and environmental relevant media.[11, 26, 29, 30] For example, silver NPs can undergo oxidative dissolution to release the active ionic silver, where oxidants (*e.g.* oxygen) are needed. The role of oxidants has been demonstrated by the lack of toxicity of Ag NPs when tested under strictly anaerobic conditions.[26] The size of silver NPs is also critical to the rate of Ag oxidative dissolution because the higher surface area of smaller nanoparticles can provide more active sites for oxidation and dissolution, which explains the stronger antibacterial property of nanosized silver compared to the bulk counterpart.[31, 32] In the environment of low pH such as stomach fluid, the oxidative dissolution can be significantly enhanced since the oxidative dissolution needs proton according to the following reaction equation

$$4Ag + O_2 + 4H^+ \Leftrightarrow 4Ag^+ + 2H_2O.$$

Natural organic matters (humic acid and fulvic acids) in nature waters are reported to inhibit silver nanoparticle dissolution, which is attributed to oxidation site block by surface absorption of these organic components.[31] In the wastewater treatment plants,

silver NPs can undergo sulfidation reactions, which can significantly lower the dissolved ionic silver release and therefore reduce the cytotoxicity of silver NPs.[33] In biological culture media, the high concentration of chloride ion can reduce the availability of ionic silver by precipitation with silver ions. Thiol-containing biomolecules such as reduced glutathione (GSH) and cysteine in biological systems can complex with silver ion to form soluble complex with various stoichiometry depending on the ratio of Ag^+ and thiol groups.[34]

Guided by the transformation behaviors in biological and environmental relevant media, various approaches have been developed to actively control silver ion release in order to tune the antimicrobial property or the cytotoxicity depending on the real circumstances (Figure 1-3). For instance, surface modification techniques like ozone treatment can greatly enhance silver ion release, which can be further tuned by adjusting ozone exposure conditions.[32] Sulfidation of silver NPs has gained wide attention since sulfidation can decrease silver nanoparticle toxicity to diverse types of tested organisms.[35, 36] Silver NPs can readily react with sulfide species (S^{2-}, HS^-) to form Ag/Ag_2S core-shell structure, and this coherent sulfide layer with lower solubility can effectively protect the Ag core from oxidation dissolution even at low sulfidation extent, and thus decreases the toxicity of Ag NPs.[35, 37]

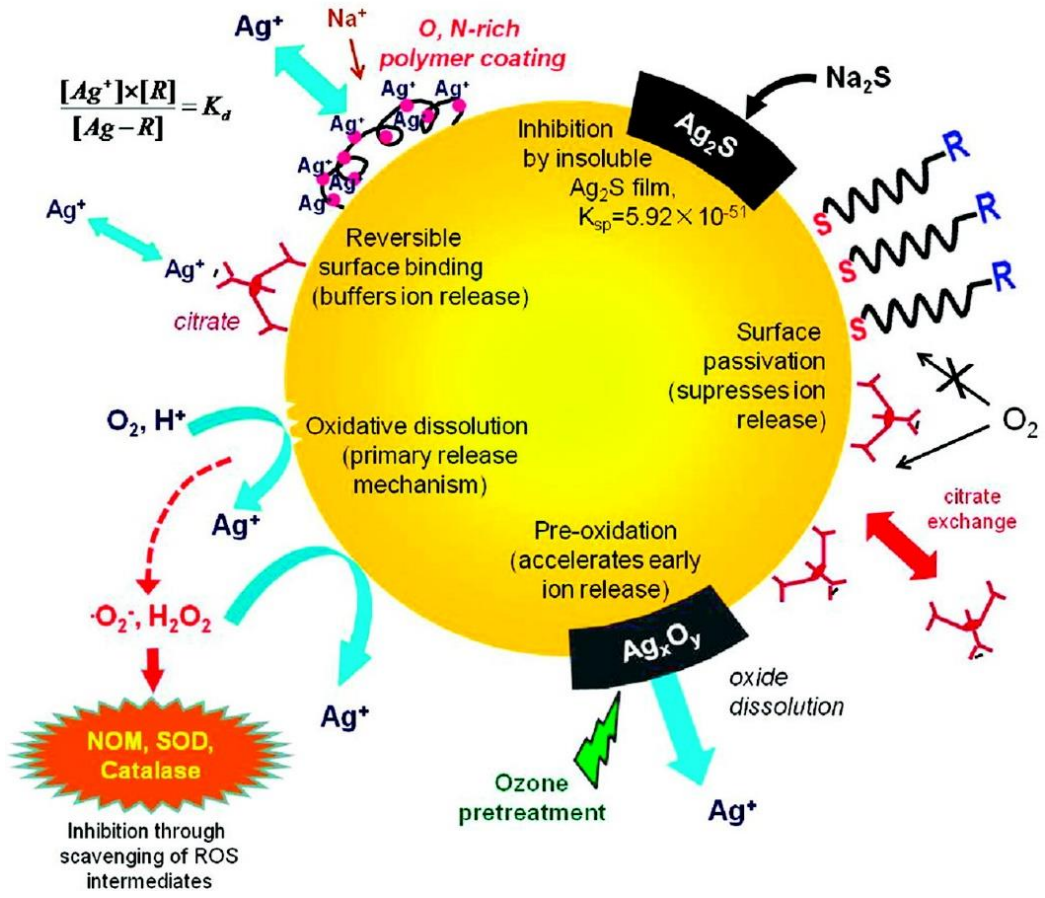

Figure 1-3. Summary of approaches to actively control silver ion release from silver nanoparticle surface. Image reproduced from [32].

Other than silver NPs, the transformation of ZnO, CeO_2 and TiO_2 NPs has been reported including dissolution, surface reduction, sulfidation, complexation, precipitation and aggregation, which has decisive effects on nanoparticle stability and reactivity, nanoparticle-cellular interactions and the potential adverse health impacts.[38-45]

Copper-based nanomaterials is one of target nanomaterials of US EPA since copper in nanoscale has been added in anti-fouling paints and coatings and in pressure treated lumber as preservatives, the market of which in North America is valued at $4.9 billion.[46] Some preliminary experimental results have indicated copper based NPs are the most

potent in terms of cytotoxicity, inducing oxidative stress induction and DNA damage.[22, 47, 48] However, the origin of these health impacts (nanoparticle surface *vs* released ions) are still under debate.[47, 49] Considering the wide use and high toxicity, it becomes very important to understand transformation behaviors of copper-based nanomaterials in relevant media when trying to elucidate the mechanism of copper toxicity, particularly address the question if the observed high toxicity of CuO NPs is associated with the "nanoscale" dimension. (Chapter 2)

1.2 The Rise of Two Dimensional Nanomaterials-Graphene

Graphene is typically defined as a monolayer of sp^2 carbon atoms packed into a honeycomb structure. Since the discovery of graphene, graphene has attracted increasing attention in the last decade.[50] The exotic properties of graphene nanomaterials have been explored and utilized such as high surface area, excellent thermal and electronic conductivity, mechanical strength and optical transparence rendering graphene promising for a wide range of applications.[51-53] Pristine graphene can be prepared by mechanical exfoliation (Scotch-tape) from natural graphite,[50] chemical vapor deposition (CVD) or epitaxial growth [54].

1.2.1 Graphene-Based Nanomaterial Family

Though the above mentioned methods can produce pristine graphene, mechanical exfoliation is laborious and finding an individual graphene sheet with good quality often needs fortune as well; CVD and epitaxial growth techniques are less productive and require specialized, expensive fabrication instruments. At the moment, the most efficient and

scalable method to prepare graphene-based nanomaterials is through the reduction of the oxide derivatives of graphene, which is synthesized from low-cost natural graphite. Although the resulting graphene-like sheets are rich of defect and re-aggregation, this highly processable method can yield bulk amounts of product that can be fabricated into various materials.[55-57]

Through Hummer's method, graphene oxide is produced by chemical oxidation of natural graphite and subsequent exfoliation in ultrasonication conditions.[58] Graphene oxide is the oxide derivative of graphene with oxygen-containing groups on the edge and basal plane. Graphene oxide is non-stoichiometry and the oxygen-containing groups can be epoxide, hydroxyl randomly distributed on basal plane and carboxylate groups primarily on the edge. The oxygen-containing groups isolate the conductive parts, introduce high density of defects, and consequently lower the electronic and mechanical properties. Because of these hydrophilic groups, however, good dispersibility in water leads to great versatility with traditional wet chemistry approaches using GO building block for advanced graphene-based architectures.[57, 59, 60]

The oxygen-containing groups of graphene oxide can be removed by chemical, thermal or UV irradiation methods.[61, 62] The resulting product is called reduced graphene oxide. Because of the defects (carbon vacancies, residual oxygen groups), reduced graphene oxide only partially restores graphene *sp2* structure, its electronic and mechanical properties as well. The structure and main properties of graphene-based nanomaterials are compared and summarized in Figure 1-4. Although reduced graphene oxide may be limited in the areas such as electronics by its poor conductivity and strength, low cost, the ease of incorporating other functional nanomaterials and flexible fabrication

into advanced architectures make graphene oxide/reduced graphene oxide as promising building blocks for preparing various composites to achieve or improve the performance as catalysis supports, bio-mimic substrate.[61, 63] (*vida infra*)

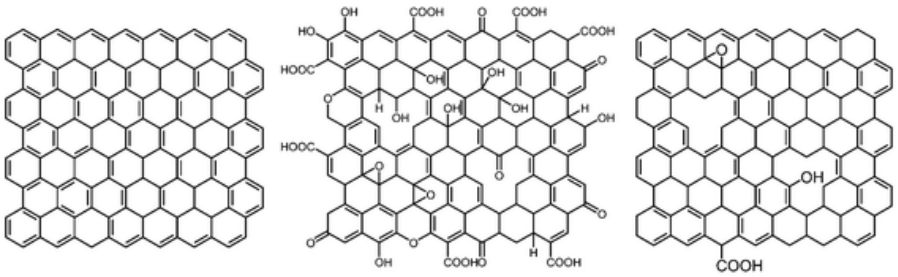

Properties	Graphene	Graphene Oxide	Reduced Graphene Oxide
Synthesis	-Chemical vapor deposition -Thermal decomposition of SiC -Graphite exfoliation	-Oxidation and exfoliation of graphite	-Reduction of graphene oxide
C:O ratio	No oxygen	2-4	8-246
Young's modulus (TPa)	1	0.2	0.25
Electron mobility ($cm^2 V^{-1} s^{-1}$)	10 000–50 000	insulator	0.05–200
Production cost	High	Low	Low

Figure 1-4. Comparisons of structure and main properties of graphene-based nanomaterials. Image reproduced from [51].

1.2.2 Novel graphene-based architectures and their environmental and biological applications

Graphene can be a fundamental building block for the rest members in the carbon nanomaterials family (Figure 1-5). For instance, graphene nanosheets can be wrapped up into zero-dimensional fullerenes, rolled into one dimensional carbon nanotubes or re-stacked into three dimensional graphite. Beyond these basic structures, graphene or

graphene oxide nanosheets have been engineered into various advanced architectures with all dimensionalities to achieve applications combining graphene intrinsic properties with other functional nanomaterials or alone.

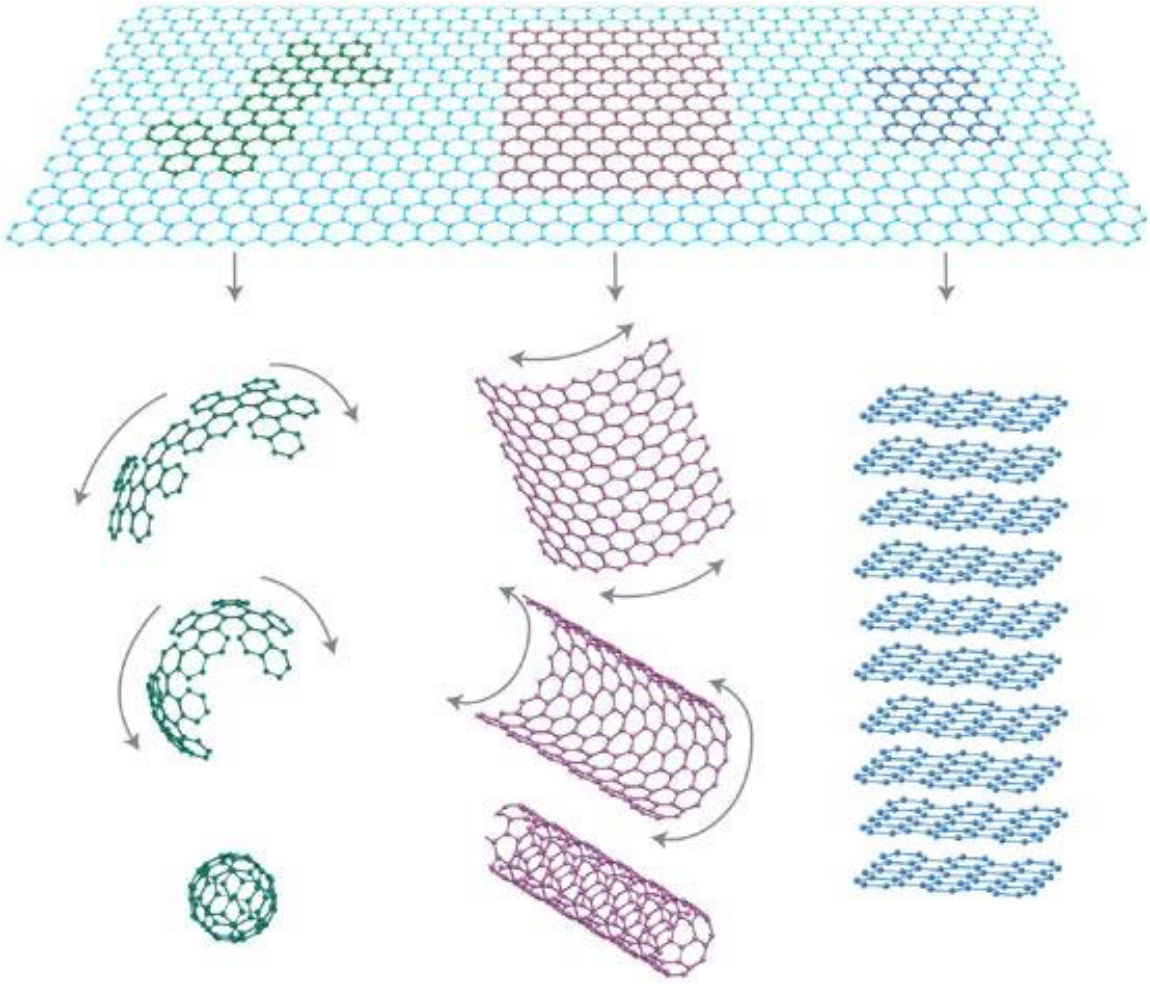

Figure 1-5. Graphene as two dimensional building blocks in carbon nanomaterials family.Image reproduced from [50].

To fully explore the novel physical and chemical properties of graphene-based nanosheets, it's of practical significance to integrate individual nanosheets into macroscopic structure by assembly of basic building blocks. For instance, 1D macroscopic fibers were prepared by wet-spinning graphene oxide suspension in the solution of CTAB,

whose positive charge can induce the assembly of the macroscopic GO fiber. [64] These graphene fibers are cost-efficient, easy to scale up, and show high performances like high mechanical strength and high electronic conductivity, which can be further improved by incorporation of conductive Ag nanowires or carbon nanotubes.[65, 66] Compared to 1D fiber that requires assembly force, it's more feasible to control the tiling of graphene-based nanosheets into 2D films and papers, which can be functionalized by incorporation of functional guest materials such as polymers, metal and semiconductor nanoparticles.[63, 67]

Three dimensional graphene-based nanomaterials has been designed to prevent 2D nanosheets re-aggregation and increase their surface area, such as graphene foam structure, which is fabricated using template-directed chemical vapor deposition for flexible and conductive platform.[68, 69] Furthermore, crumpled graphene nanosacks has attracted attention because of their high free volume, high surface area and high compressive strength.[70, 71] Crumpled graphene nanosacks can be prepared from aqueous GO nanosheets in the fast drying aerosol process, where capillary force associated with water loss can induce the transformation from 2D sheets to 3D structure. The accessible surface area is maintained even tightly packed. More importantly, the performance of crumpled graphene nanosacks can be further enhanced through loading with various functional nanoparticles, which can tremendously expand its use to a wide range of applications, such as composite electrodes, sorbents and supercapacitors.[71-74] In these applications, the crumpled graphene nanosack usually serves as a conductive support whose folded structure prevents graphene sheets from restacking and surface area loss. The fundamental behaviors of chemical reactions occurring in and on this novel 3D architecture, however, needs

further investigation including the interactions between graphene shells and loaded nanomaterial and the interactions between cargo nanoparticles mediated by graphene shells. The properties and applications of crumpled graphene with novel confined environment are explored in Chapter 3.

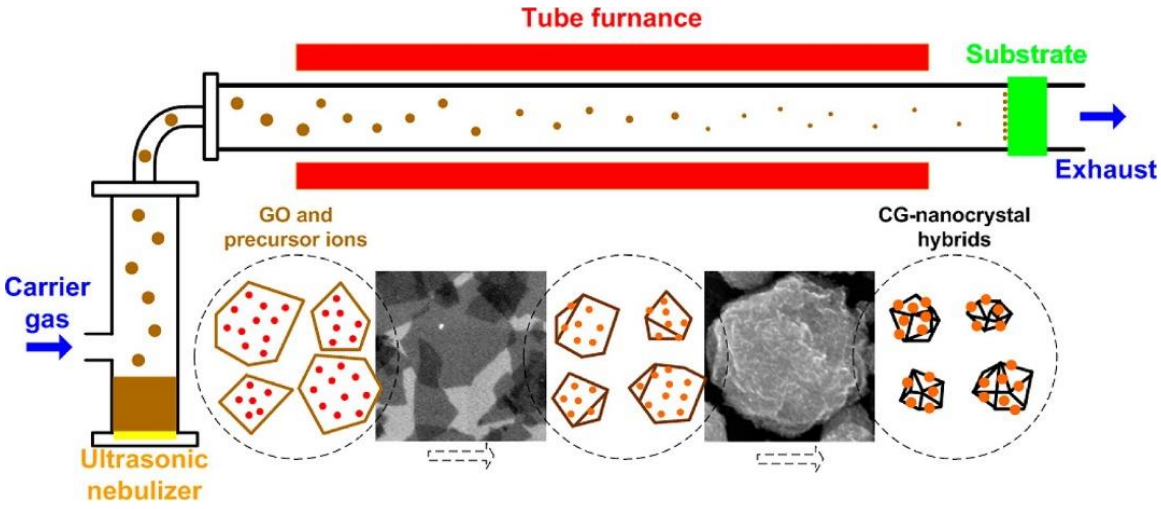

Figure 1-6. Schematic drawings illustrating the aerosol preparation of cargo-loaded crumpled graphene hybrid nanomaterials.Image reproduced from [71].

Topographical patterns (sometimes called 2.5 dimensional materials) can be created by etching or molding the surface of a single-component material, or through creation of heterostructures consisting of a substrate and a surface film with engineered texture. An emerging method for surface texturing is the creation of wrinkle patterns by controlled shrinkage of a stiffer coating on a softer, compliant substrate.[75-77] Wrinkled graphene-based surfaces have been created recently by growth or deposition of atomically thin graphene, which enables the creation of the ultrathin flexible films suitable for controlled wrinkling. Topographically patterned graphene has found numerous applications in optical and electronic devices, energy storage, and functional coatings.[61, 78-86]

Another potential application area for wrinkled graphene surfaces can be as functional substrates for cell and biological tissue, which has not been previously unexplored. Planar graphene and graphene oxide have already been explored as substrates for biological cells and tissues, and display enhanced viability.[52, 87, 88] A limitation of conventional flat, uniform 2D cell culture substrates, however, is that they lack the complexity of structural architectures found in the extracellular matrix in living tissue. On planar 2D surfaces, cells adopt strongly flattened morphologies, and the resulting cellular behavior can deviate from the natural behavior observed in a physiological 3D context.[89]

Chapter 4 will describe the fabrication process of wrinkled graphene surfaces using GO solution phase deposition on pre-stretched elastomeric substrates followed by relaxation and thermal stabilization. The topography of these stabilized graphene oxide (s-GO) surfaces is characterized and shown to be periodic which can be systematically tuned by simple variation of the GO concentration in the deposition suspension. The effect of these wrinkled graphene-based architectures on human and murine fibroblast cells is explored, and the difference of cell orientation, alignment, and morphology relative to cells on planar s-GO is also compared.

1.3 Biological and environmental interactions of the emerging 2D nanomaterials

Since the discovery of graphene, two dimensional layered nanomaterials have regained attention because of the unique properties found in the exfoliated forms, not necessarily seen in their bulk counterparts. Though strong in-plane chemical bonds, the weak out of plane bonds (van der Waals) makes it possible production of thin nanosheets

through mechanical exfoliation, which has been first demonstrated by the preparation of monolayer graphene with transparent adhesive tapes. The products are generally referred to as nanosheets with the thickness in "nano" magnitude.

1.3.1 Novel 2D nanomaterials beyond graphene

Though Graphene is fundamentally and technologically interesting for a wide range of applications, its use in electronics is considerably limited by the zero band gap property. Furthermore, graphene is chemically inert and can only be made active by functionalization for the use in the catalysis and sensor fields. The need for the novel materials, along with the methodology developed in preparing ultrathin graphene has led to the exploration of other 2D nanomaterials (Figure 1-7).[90-96]

Since then novel two dimensional layered nanomaterials beyond graphene such as metal chalcogenide, layered double hydroxides and other 2D compounds have gained renewed interest.[93] Specifically, transition metal dichalcogenides (TMD) consist of hexagonal layers of metal atoms sandwiched between two layers of chalcogen atoms. Because of the weak van der Waals force between adjacent chalcogen layers, 2D TMD nanomaterials can be relatively easily exfoliated in organic solvents or aqueous solutions assisted by polymer.[97-100] 2D nanomaterials, particularly TMD as the ideal two dimensional prototype, have received extensive attention and been reviewed in terms of preparation, [91] phase engineering, [101] hybrid composites,[102] and biomedical applications.[103]

Figure 1-7 Ball-and-stick model of crystal structures, naturally occurring forms, and exfoliated nanosheets for four example layered materials (A-C: graphite/graphene; D-F: layered silicate hydrate; G-I Molybdenite/Molybdenum disulfide; J-L: Birnessite/Manganese dioxide) Image reproduced from [98].

1.3.2 Transformation and implications of emerging 2D nanomaterials in biological and environmental systems

Exfoliation can dramatically change the fundamental properties of 2D nanomaterials. The simplest case is the tremendous increase of accessible surface area of the material when it's exfoliated into monolayer state, which is critical for the surface-based reactions. For instance, graphene has a theoretical specific surface area of ~2600 m^2/g, which is much larger than those of other carbon materials.

Another significant modification of exfoliation on materials' property is regarding the electronic band structure. Graphite is semimetal with a band overlap of about 41 meV, while monolayer graphene when exfoliated from bulk counterpart becomes the well-known zero-gap semiconductor.[104] Likewise, the bulk MoS_2 crystal is an indirect gap semiconductor with a band gap of 1.29 eV, and monolayer MoS_2 becomes direct gap semiconductor with band gap of 1.9 eV.[105] The band gap can be modified at will by tuning the thickness or the number of layers of nanosheets. This behavior is similarly expected in other layered semiconductors.

Because of the altered physicochemical properties of 2D nanomaterials, to predict their transformation and to evaluate their implications can not solely rely on the understanding on the bulk counterparts, which otherwise can underestimate the potential adverse impacts of these emerging 2D on biological and environmental systems. Currently, the study on the transformation and implications of 2D nanomaterials is limited. But some aspects are readily informed by the current literature on graphene-based 2D nanomaterials. The interactions of graphene nanomaterials with biological systems have been studied and discussed in a few review articles. [106, 107] Similar to the counterpart graphene, the unique dimensional properties of novel 2D nanomaterials (surface area, layer number, lateral dimension and surface chemistry) can lead to a variety of interactions with biological molecules including absorption and catalytic reactions, and even toxicity to cells. The large family of emerging 2D nanomaterials possess various composition, phase, which is much more complex than graphene, potentially leading to different cellular responses. The assessment process can be further complicated by various transformation occurring in

biologically relevant medium, and the specific transformation pathways may depend on the physicochemical properties of 2D in a case by case manner.

Overall, the diversity in composition and physicochemical properties of emerging 2D nanomaterials presents a challenge for scientific community to evaluate and understand potential for causing adverse health effects. Identification of the key chemical and physical feature of 2D nanomaterials plays in the behavior of 2D nanomaterials will enable the development of predictive models (*e.g.* the band-structure based framework in Chapter 5) that can be used to differentiate between the nanomaterials with higher priority and those with lower risks. Furthermore, transformation is known to affect the fate, properties and toxicities of nanomaterials in biological and environmental systems. The complexity in 2D nanomaterial composition requires a predictive models (*e.g.* redox-potential based model in Chapter 5) that can categorize the family of 2D nanomaterial into subgroups, to reduce unnecessary testing and to accelerate the evaluation process.

1.4 Reference

1. Sanchez, C.; Belleville, P.; Popall, M.; Nicole, L. Applications of advanced hybrid organic-inorganic nanomaterials: from laboratory to market. *Chem. Soc. Rev.* **2011**, 40, 696-753.
2. Frey, N. A.; Peng, S.; Cheng, K.; Sun, S. Magnetic nanoparticles: synthesis, functionalization, and applications in bioimaging and magnetic energy storage. *Chem. Soc. Rev.* **2009**, 38, 2532-2542.
3. Marambio-Jones, C.; Hoek, E. V. A review of the antibacterial effects of silver nanomaterials and potential implications for human health and the environment. *J Nanopart Res* **2010**, 12, 1531-1551.
4. Vance, M. E.; Kuiken, T.; Vejerano, E. P.; McGinnis, S. P.; Hochella, M. F., Jr.; Rejeski, D.; Hull, M. S. Nanotechnology in the real world: Redeveloping the nanomaterial consumer products inventory. *Beilstein Journal of Nanotechnology* **2015**, 6, 1769-1780.
5. Bell, A. T. The Impact of Nanoscience on Heterogeneous Catalysis. *Science* **2003**, 299, 1688-1691.
6. Yang, K.; Zhu, L.; Xing, B. Adsorption of Polycyclic Aromatic Hydrocarbons by Carbon Nanomaterials. *Environ. Sci. Technol.* **2006**, 40, 1855-1861.
7. Roduner, E. Size matters: why nanomaterials are different. *Chem. Soc. Rev.* **2006**, 35, 583-592.
8. Hvolbæk, B.; Janssens, T. V. W.; Clausen, B. S.; Falsig, H.; Christensen, C. H.; Nørskov, J. K. Catalytic activity of Au nanoparticles. *Nano Today* **2007**, 2, 14-18.
9. Shirasaki, Y.; Supran, G. J.; Bawendi, M. G.; Bulovic, V. Emergence of colloidal quantum-dot light-emitting technologies. *Nat Photon* **2013**, 7, 13-23.
10. Lewicka, Z.; Benedetto, A.; Benoit, D.; Yu, W.; Fortner, J.; Colvin, V. The structure, composition, and dimensions of TiO2 and ZnO nanomaterials in commercial sunscreens. *J Nanopart Res* **2011**, 13, 3607-3617.
11. Lorenz, C.; Windler, L.; von Goetz, N.; Lehmann, R. P.; Schuppler, M.; Hungerbühler, K.; Heuberger, M.; Nowack, B. Characterization of silver release from commercially available functional (nano)textiles. *Chemosphere* **2012**, 89, 817-824.

12. Geranio, L.; Heuberger, M.; Nowack, B. The Behavior of Silver Nanotextiles during Washing. *Environ. Sci. Technol.* **2009**, 43, 8113-8118.
13. De Volder, M. F.; Tawfick, S. H.; Baughman, R. H.; Hart, A. J. Carbon nanotubes: present and future commercial applications. *Science* **2013**, 339, 535-539.
14. Na, H. B.; Song, I. C.; Hyeon, T. Inorganic Nanoparticles for MRI Contrast Agents. *Adv. Mater. (Weinheim, Ger.)* **2009**, 21, 2133-2148.
15. Park, B.; Donaldson, K.; Duffin, R.; Tran, L.; Kelly, F.; Mudway, I.; Morin, J.-P.; Guest, R.; Jenkinson, P.; Samaras, Z. Hazard and risk assessment of a nanoparticulate cerium oxide-based diesel fuel additive—a case study. *Inhalation Toxicol.* **2008**, 20, 547-566.
16. Colvin, V. L. The potential environmental impact of engineered nanomaterials. *Nat. Biotechnol.* **2003**, 21, 1166-1170.
17. Wiesner, M. R.; Lowry, G. V.; Alvarez, P.; Dionysiou, D.; Biswas, P. Assessing the risks of manufactured nanomaterials. *Environ. Sci. Technol.* **2006**, 40, 4336-4345.
18. Ahamed, M.; Siddiqui, M. A.; Akhtar, M. J.; Ahmad, I.; Pant, A. B.; Alhadlaq, H. A. Genotoxic potential of copper oxide nanoparticles in human lung epithelial cells. *Biochem. Biophys. Res. Commun.* **2010**, 396, 578-583.
19. Jo, H. J.; Choi, J. W.; Lee, S. H.; Hong, S. W. Acute toxicity of Ag and CuO nanoparticle suspensions against Daphnia magna: The importance of their dissolved fraction varying with preparation methods. *J. Hazard. Mater.* **2012**, 227–228, 301-308.
20. Xia, T.; Zhao, Y.; Sager, T.; George, S.; Pokhrel, S.; Li, N.; Schoenfeld, D.; Meng, H.; Lin, S.; Wang, X.; Wang, M.; Ji, Z.; Zink, J. I.; Mädler, L.; Castranova, V.; Lin, S.; Nel, A. E. Decreased Dissolution of ZnO by Iron Doping Yields Nanoparticles with Reduced Toxicity in the Rodent Lung and Zebrafish Embryos. *ACS Nano* **2011**, 5, 1223-1235.
21. Kittler, S.; Greulich, C.; Diendorf, J.; Koller, M.; Epple, M. Toxicity of silver nanoparticles increases during storage because of slow dissolution under release of silver ions. *Chem. Mater.* **2010**, 22, 4548-4554.

22. Fahmy, B.; Cormier, S. A. Copper oxide nanoparticles induce oxidative stress and cytotoxicity in airway epithelial cells. *Toxicol. in Vitro* **2009**, 23, 1365-1371.
23. Madhumathi, K.; Sudheesh Kumar, P. T.; Abhilash, S.; Sreeja, V.; Tamura, H.; Manzoor, K.; Nair, S. V.; Jayakumar, R. Development of novel chitin/nanosilver composite scaffolds for wound dressing applications. *J. Mater. Sci.: Mater. Med.* **2010**, 21, 807-813.
24. Benn, T. M.; Westerhoff, P. Nanoparticle Silver Released into Water from Commercially Available Sock Fabrics. *Environ. Sci. Technol.* **2008**, 42, 4133-4139.
25. Lee, H. J.; Yeo, S. Y.; Jeong, S. H. Antibacterial effect of nanosized silver colloidal solution on textile fabrics. *J. Mater. Sci.* **2003**, 38, 2199-2204.
26. Xiu, Z.-m.; Zhang, Q.-b.; Puppala, H. L.; Colvin, V. L.; Alvarez, P. J. Negligible particle-specific antibacterial activity of silver nanoparticles. *Nano Letters* **2012**, 12, 4271-4275.
27. van der Zande, M.; Vandebriel, R. J.; Van Doren, E.; Kramer, E.; Herrera Rivera, Z.; Serrano-Rojero, C. S.; Gremmer, E. R.; Mast, J.; Peters, R. J. B.; Hollman, P. C. H.; Hendriksen, P. J. M.; Marvin, H. J. P.; Peijnenburg, A. A. C. M.; Bouwmeester, H. Distribution, Elimination, and Toxicity of Silver Nanoparticles and Silver Ions in Rats after 28-Day Oral Exposure. *ACS Nano* **2012**, 6, 7427-7442.
28. Yang, X.; Gondikas, A. P.; Marinakos, S. M.; Auffan, M.; Liu, J.; Hsu-Kim, H.; Meyer, J. N. Mechanism of silver nanoparticle toxicity is dependent on dissolved silver and surface coating in Caenorhabditis elegans. *Environmental Science and Technology* **2011**, 46, 1119-1127.
29. Reidy, B.; Haase, A.; Luch, A.; Dawson, K.; Lynch, I. Mechanisms of Silver Nanoparticle Release, Transformation and Toxicity: A Critical Review of Current Knowledge and Recommendations for Future Studies and Applications. *Materials* **2013**, 6, 2295-2350.
30. Dobias, J.; Bernier-Latmani, R. Silver Release from Silver Nanoparticles in Natural Waters. *Environ. Sci. Technol.* **2013**, 47, 4140-4146.
31. Liu, J.; Hurt, R. H. Ion Release Kinetics and Particle Persistence in Aqueous Nano-Silver Colloids. *Environmental Science and Technology* **2010**, 44, 2169-2175.

32. Liu, J.; Sonshine, D. A.; Shervani, S.; Hurt, R. H. Controlled Release of Biologically Active Silver from Nanosilver Surfaces. *ACS Nano* **2010**, 4, 6903-6913.

33. Liu, J.; Pennell, K. G.; Hurt, R. H. Kinetics and Mechanisms of Nanosilver Oxysulfidation. *Environ. Sci. Technol.* **2011**, 45, 7345-7353.

34. Liu, J.; Wang, Z.; Liu, F. D.; Kane, A. B.; Hurt, R. H. Chemical Transformations of Nanosilver in Biological Environments. *ACS Nano* **2012**, 6, 9887-9899.

35. Levard, C.; Hotze, E. M.; Colman, B. P.; Dale, A. L.; Truong, L.; Yang, X. Y.; Bone, A. J.; Brown, G. E.; Tanguay, R. L.; Di Giulio, R. T.; Bernhardt, E. S.; Meyer, J. N.; Wiesner, M. R.; Lowry, G. V. Sulfidation of Silver Nanoparticles: Natural Antidote to Their Toxicity. *Environ. Sci. Technol.* **2013**, 47, 13440-13448.

36. Reinsch, B. C.; Levard, C.; Li, Z.; Ma, R.; Wise, A.; Gregory, K. B.; Brown, G. E.; Lowry, G. V. Sulfidation of Silver Nanoparticles Decreases Escherichia coli Growth Inhibition. *Environ. Sci. Technol.* **2012**, 46, 6992-7000.

37. Levard, C.; Reinsch, B. C.; Michel, F. M.; Oumahi, C.; Lowry, G. V.; Brown, G. E. Sulfidation Processes of PVP-Coated Silver Nanoparticles in Aqueous Solution: Impact on Dissolution Rate. *Environ. Sci. Technol.* **2011**, 45, 5260-5266.

38. Pettibone, J. M.; Cwiertny, D. M.; Scherer, M.; Grassian, V. H. Adsorption of Organic Acids on TiO2 Nanoparticles: Effects of pH, Nanoparticle Size, and Nanoparticle Aggregation. *Langmuir* **2008**, 24, 6659-6667.

39. Schwabe, F.; Schulin, R.; Rupper, P.; Rotzetter, A.; Stark, W.; Nowack, B. Dissolution and transformation of cerium oxide nanoparticles in plant growth media. *J Nanopart Res* **2014**, 16, 1-11.

40. Mudunkotuwa, I. A.; Grassian, V. H. Citric Acid Adsorption on TiO2 Nanoparticles in Aqueous Suspensions at Acidic and Circumneutral pH: Surface Coverage, Surface Speciation, and Its Impact on Nanoparticle−Nanoparticle Interactions. *J. Am. Chem. Soc.* **2010**, 132, 14986-14994.

41. Xia, T.; Kovochich, M.; Liong, M.; Mädler, L.; Gilbert, B.; Shi, H.; Yeh, J. I.; Zink, J. I.; Nel, A. E. Comparison of the Mechanism of Toxicity of Zinc Oxide and Cerium Oxide Nanoparticles Based on Dissolution and Oxidative Stress Properties. *ACS Nano* **2008**, 2, 2121-2134.

42. Franklin, N. M.; Rogers, N. J.; Apte, S. C.; Batley, G. E.; Gadd, G. E.; Casey, P. S. Comparative toxicity of nanoparticulate ZnO, bulk ZnO, and ZnCl2 to a freshwater microalga (Pseudokirchneriella subcapitata): the importance of particle solubility. *Environ. Sci. Technol.* **2007**, 41, 8484-8490.
43. Bian, S.-W.; Mudunkotuwa, I. A.; Rupasinghe, T.; Grassian, V. H. Aggregation and dissolution of 4 nm ZnO nanoparticles in aqueous environments: influence of pH, ionic strength, size, and adsorption of humic acid. *Langmuir* **2011**, 27, 6059-6068.
44. Ma, R.; Levard, C.; Michel, F. M.; Brown, G. E.; Lowry, G. V. Sulfidation Mechanism for Zinc Oxide Nanoparticles and the Effect of Sulfidation on Their Solubility. *Environ. Sci. Technol.* **2013**, 47, 2527-2534.
45. Ma, R.; Levard, C.; Judy, J. D.; Unrine, J. M.; Durenkamp, M.; Martin, B.; Jefferson, B.; Lowry, G. V. Fate of Zinc Oxide and Silver Nanoparticles in a Pilot Wastewater Treatment Plant and in Processed Biosolids. *Environ. Sci. Technol.* **2014**, 48, 104-112.
46. Evans, P.; Matsunaga, H.; Kiguchi, M. Large-scale application of nanotechnology for wood protection. *Nat Nano* **2008**, 3, 577-577.
47. Karlsson, H. L.; Cronholm, P.; Gustafsson, J.; Moller, L. Copper oxide nanoparticles are highly toxic: A comparison between metal oxide nanoparticles and carbon nanotubes. *Chem. Res. Toxicol.* **2008**, 21, 1726-1732.
48. Atha, D. H.; Wang, H.; Petersen, E. J.; Cleveland, D.; Holbrook, R. D.; Jaruga, P.; Dizdaroglu, M.; Xing, B.; Nelson, B. C. Copper Oxide Nanoparticle Mediated DNA Damage in Terrestrial Plant Models. *Environ. Sci. Technol.* **2011**, 46, 1819-1827.
49. Studer, A. M.; Limbach, L. K.; Van Duc, L.; Krumeich, F.; Athanassiou, E. K.; Gerber, L. C.; Moch, H.; Stark, W. J. Nanoparticle cytotoxicity depends on intracellular solubility: Comparison of stabilized copper metal and degradable copper oxide nanoparticles. *Toxicol. Lett.* **2010**, 197, 169-174.
50. Geim, A. K.; Novoselov, K. S. The rise of graphene. *Nat. Mater.* **2007**, 6, 183-191.
51. Perreault, F.; Fonseca de Faria, A.; Elimelech, M. Environmental applications of graphene-based nanomaterials. *Chem. Soc. Rev.* **2015**.

52. Goenka, S.; Sant, V.; Sant, S. Graphene-based nanomaterials for drug delivery and tissue engineering. *J. Controlled Release* **2014**, 173, 75-88.

53. Cao, X.; Yin, Z.; Zhang, H. Three-dimensional graphene materials: preparation, structures and application in supercapacitors. *Energy Environ. Sci.* **2014**, 7, 1850-1865.

54. Yang, W.; Chen, G.; Shi, Z.; Liu, C.-C.; Zhang, L.; Xie, G.; Cheng, M.; Wang, D.; Yang, R.; Shi, D.; Watanabe, K.; Taniguchi, T.; Yao, Y.; Zhang, Y.; Zhang, G. Epitaxial growth of single-domain graphene on hexagonal boron nitride. *Nat. Mater.* **2013**, 12, 792-797.

55. Huang, X.; Qi, X.; Boey, F.; Zhang, H. Graphene-based composites. *Chem. Soc. Rev.* **2012**, 41, 666-686.

56. Eda, G.; Fanchini, G.; Chhowalla, M. Large-area ultrathin films of reduced graphene oxide as a transparent and flexible electronic material. *Nat Nano* **2008**, 3, 270-274.

57. Dikin, D. A.; Stankovich, S.; Zimney, E. J.; Piner, R. D.; Dommett, G. H. B.; Evmenenko, G.; Nguyen, S. T.; Ruoff, R. S. Preparation and characterization of graphene oxide paper. *Nature* **2007**, 448, 457-460.

58. Hummers Jr, W. S.; Offeman, R. E. Preparation of graphitic oxide. *J. Am. Chem. Soc.* **1958**, 80, 1339-1339.

59. Zangmeister, C. D.; Ma, X.; Zachariah, M. R. Restructuring of Graphene Oxide Sheets into Monodisperse Nanospheres. *Chem. Mater.* **2012**, 24, 2554-2557.

60. Park, S.; Lee, K.-S.; Bozoklu, G.; Cai, W.; Nguyen, S. T.; Ruoff, R. S. Graphene Oxide Papers Modified by Divalent Ions—Enhancing Mechanical Properties via Chemical Cross-Linking. *ACS Nano* **2008**, 2, 572-578.

61. Delle, L. E.; Lanche, R.; Law, J. K.-Y.; Weil, M.; Vu, X. T.; Wagner, P.; Ingebrandt, S. Reduced graphene oxide micropatterns as an interface for adherent cells. *physica status solidi (a)* **2013**, 210, 975-982.

62. Su, Y.; Kravets, V. G.; Wong, S. L.; Waters, J.; Geim, A. K.; Nair, R. R. Impermeable barrier films and protective coatings based on reduced graphene oxide. *Nat Commun* **2014**, 5.

63. Lightcap, I. V.; Kosel, T. H.; Kamat, P. V. Anchoring Semiconductor and Metal Nanoparticles on a Two-Dimensional Catalyst Mat. Storing and Shuttling Electrons with Reduced Graphene Oxide. *Nano Lett.* **2010**, 10, 577-583.

64. Cong, H.-P.; Ren, X.-C.; Wang, P.; Yu, S.-H. Wet-spinning assembly of continuous, neat, and macroscopic graphene fibers. *Sci. Rep.* **2012**, 2.

65. Cheng, H.; Dong, Z.; Hu, C.; Zhao, Y.; Hu, Y.; Qu, L.; Chen, N.; Dai, L. Textile electrodes woven by carbon nanotube-graphene hybrid fibers for flexible electrochemical capacitors. *Nanoscale* **2013**, 5, 3428-3434.

66. Xu, Z.; Liu, Z.; Sun, H.; Gao, C. Highly Electrically Conductive Ag-Doped Graphene Fibers as Stretchable Conductors. *Adv. Mater. (Weinheim, Ger.)* **2013**, 25, 3249-3253.

67. Kim, S.; Yoo, J.-B.; Yi, G.-R.; Lee, Y.; Choi, H. R.; Koo, J. C.; Oh, J.-S.; Nam, J.-D. An aggregation-mediated assembly of graphene oxide on amine-functionalized poly(glycidyl methacrylate) microspheres for core-shell structures with controlled electrical conductivity. *J. Mater. Chem. C* **2014**, 2, 6462-6466.

68. Chen, Z.; Ren, W.; Gao, L.; Liu, B.; Pei, S.; Cheng, H.-M. Three-dimensional flexible and conductive interconnected graphene networks grown by chemical vapour deposition. *Nat. Mater.* **2011**, 10, 424-428.

69. Dong, X.; Wang, X.; Wang, L.; Song, H.; Zhang, H.; Huang, W.; Chen, P. 3D Graphene Foam as a Monolithic and Macroporous Carbon Electrode for Electrochemical Sensing. *ACS Appl. Mater. Interfaces* **2012**, 4, 3129-3133.

70. Luo, J.; Zhao, X.; Wu, J.; Jang, H. D.; Kung, H. H.; Huang, J. Crumpled Graphene-Encapsulated Si Nanoparticles for Lithium Ion Battery Anodes. *The Journal of Physical Chemistry Letters* **2012**, 3, 1824-1829.

71. Mao, S.; Wen, Z.; Kim, H.; Lu, G.; Hurley, P.; Chen, J. A General Approach to One-Pot Fabrication of Crumpled Graphene-Based Nanohybrids for Energy Applications. *ACS Nano* **2012**, 6, 7505-7513.

72. Chen, Y.; Guo, F.; Jachak, A.; Kim, S.-P.; Datta, D.; Liu, J.; Kulaots, I.; Vaslet, C.; Jang, H. D.; Huang, J.; Kane, A.; Shenoy, V. B.; Hurt, R. H. Aerosol Synthesis of Cargo-Filled Graphene Nanosacks. *Nano Lett.* **2012**, 12, 1996-2002.

73. Chen, Y.; Guo, F.; Qiu, Y.; Hu, H.; Kulaots, I.; Walsh, E.; Hurt, R. H. Encapsulation of Particle Ensembles in Graphene Nanosacks as a New Route to Multifunctional Materials. *ACS Nano* **2013**, 7, 3744-3753.

74. Luo, J.; Zhao, X.; Wu, J.; Jang, H. D.; Kung, H. H.; Huang, J. Crumpled Graphene-Encapsulated Si Nanoparticles for Lithium Ion Battery Anodes. *J. Phys. Chem. Lett.* **2012**, 3, 1824-1829.

75. Sun, J.-Y.; Xia, S.; Moon, M.-W.; Oh, K. H.; Kim, K.-S. Folding wrinkles of a thin stiff layer on a soft substrate. *Proceedings of the Royal Society A: Mathematical, Physical and Engineering Science* **2011**.

76. Song, J.; Jiang, H.; Liu, Z. J.; Khang, D. Y.; Huang, Y.; Rogers, J. A.; Lu, C.; Koh, C. G. Buckling of a stiff thin film on a compliant substrate in large deformation. *International Journal of Solids and Structures* **2008**, 45, 3107-3121.

77. Zang, J.; Zhao, X.; Cao, Y.; Hutchinson, J. W. Localized ridge wrinkling of stiff films on compliant substrates. *Journal of the Mechanics and Physics of Solids* **2012**, 60, 1265-1279.

78. Kim, K. S.; Zhao, Y.; Jang, H.; Lee, S. Y.; Kim, J. M.; Kim, K. S.; Ahn, J.-H.; Kim, P.; Choi, J.-Y.; Hong, B. H. Large-scale pattern growth of graphene films for stretchable transparent electrodes. *Nature* **2009**, 457, 706-710.

79. Bao, W.; Miao, F.; Chen, Z.; Zhang, H.; Jang, W.; Dames, C.; Lau, C. N. Controlled ripple texturing of suspended graphene and ultrathin graphite membranes. *Nat Nano* **2009**, 4, 562-566.

80. He, Q.; Sudibya, H. G.; Yin, Z.; Wu, S.; Li, H.; Boey, F.; Huang, W.; Chen, P.; Zhang, H. Centimeter-Long and Large-Scale Micropatterns of Reduced Graphene Oxide Films: Fabrication and Sensing Applications. *ACS Nano* **2010**, 4, 3201-3208.

81. Scharfenberg, S.; Rocklin, D. Z.; Chialvo, C.; Weaver, R. L.; Goldbart, P. M.; Mason, N. Probing the mechanical properties of graphene using a corrugated elastic substrate. *Appl. Phys. Lett.* **2011**, 98, -.

82. Kunz, D. A.; Feicht, P.; Gödrich, S.; Thurn, H.; Papastavrou, G.; Fery, A.; Breu, J. Space-Resolved In-Plane Moduli of Graphene Oxide and Chemically Derived Graphene Applying a Simple Wrinkling Procedure. *Advanced Materials (Weinheim, Germany)* **2013**, 25, 1337-1341.

83. Zang, J.; Ryu, S.; Pugno, N.; Wang, Q.; Tu, Q.; Buehler, M. J.; Zhao, X. Multifunctionality and control of the crumpling and unfolding of large-area graphene. *Nature Materials* **2013**, 12, 321-325.

84. Zang, J.; Cao, C.; Feng, Y.; Liu, J.; Zhao, X. Stretchable and High-Performance Supercapacitors with Crumpled Graphene Papers. *Sci. Rep.* **2014**, 4.

85. Xu, P.; Kang, J.; Choi, J.-B.; Suhr, J.; Yu, J.; Li, F.; Byun, J.-H.; Kim, B.-S.; Chou, T.-W. Laminated Ultrathin Chemical Vapor Deposition Graphene Films Based Stretchable and Transparent High-Rate Supercapacitor. *ACS Nano* **2014**, 8, 9437-9445.

86. Faruque Ahmed, S.; Nagashima, S.; Lee, J. Y.; Lee, K.-R.; Kim, K.-S.; Moon, M.-W. Self-assembled folding of a biaxially compressed film on a compliant substrate. *Carbon* **2014**, 76, 105-112.

87. Mao, H. Y.; Laurent, S.; Chen, W.; Akhavan, O.; Imani, M.; Ashkarran, A. A.; Mahmoudi, M. Graphene: Promises, Facts, Opportunities, and Challenges in Nanomedicine. *Chem. Rev. (Washington, DC, U. S.)* **2013**, 113, 3407-3424.

88. Bitounis, D.; Ali-Boucetta, H.; Hong, B. H.; Min, D.-H.; Kostarelos, K. Prospects and Challenges of Graphene in Biomedical Applications. *Adv. Mater. (Weinheim, Ger.)* **2013**, 25, 2258-2268.

89. Baker, B. M.; Chen, C. S. Deconstructing the third dimension–how 3D culture microenvironments alter cellular cues. *J. Cell Sci.* **2012**, 125, 3015-3024.

90. Yin, W.; Yan, L.; Yu, J.; Tian, G.; Zhou, L.; Zheng, X.; Zhang, X.; Yong, Y.; Li, J.; Gu, Z. High-throughput synthesis of single-layer MoS2 nanosheets as a near-infrared photothermal-triggered drug delivery for effective cancer therapy. *ACS Nano* **2014**, 8, 6922-6933.

91. Ji, Q.; Zhang, Y.; Zhang, Y.; Liu, Z. Chemical vapour deposition of group-VIB metal dichalcogenide monolayers: engineered substrates from amorphous to single crystalline. *Chemical Society Reviews* **2015**, 44, 2587-2602.

92. Guardia, L.; Paredes, J. I.; Munuera, J. M.; Villar-Rodil, S.; Ayán-Varela, M.; Martínez-Alonso, A.; Tascón, J. M. D. Chemically Exfoliated MoS2 Nanosheets as an Efficient Catalyst for Reduction Reactions in the Aqueous Phase. *ACS Appl. Mater. Interfaces* **2014**, 6, 21702-21710.

93. Xu, M.; Liang, T.; Shi, M.; Chen, H. Graphene-Like Two-Dimensional Materials. *Chem. Rev. (Washington, DC, U. S.)* **2013**, 113, 3766-3798.

94. Chou, S. S.; Kaehr, B.; Kim, J.; Foley, B. M.; De, M.; Hopkins, P. E.; Huang, J.; Brinker, C. J.; Dravid, V. P. Chemically Exfoliated MoS2 as Near-Infrared Photothermal Agents. *Angewandte Chemie International Edition* **2013**, 52, 4160-4164.

95. Chou, S. S.; De, M.; Kim, J.; Byun, S.; Dykstra, C.; Yu, J.; Huang, J.; Dravid, V. P. Ligand Conjugation of Chemically Exfoliated MoS2. *J. Am. Chem. Soc.* **2013**, 135, 4584-4587.

96. Wang, G.; Ling, Y.; Wang, H.; Yang, X.; Wang, C.; Zhang, J. Z.; Li, Y. Hydrogen-treated WO3 nanoflakes show enhanced photostability. *Energy & Environmental Science* **2012**, 5, 6180-6187.

97. Dong, L.; Lin, S.; Yang, L.; Zhang, J.; Yang, C.; Yang, D.; Lu, H. Spontaneous exfoliation and tailoring of MoS2 in mixed solvents. *Chem. Commun. (Cambridge, U. K.)* **2014**, 50, 15936-15939.

98. Nicolosi, V.; Chhowalla, M.; Kanatzidis, M. G.; Strano, M. S.; Coleman, J. N. Liquid Exfoliation of Layered Materials. *Science* **2013**, 340.

99. Smith, R. J.; King, P. J.; Lotya, M.; Wirtz, C.; Khan, U.; De, S.; O'Neill, A.; Duesberg, G. S.; Grunlan, J. C.; Moriarty, G. Large‐Scale Exfoliation of Inorganic Layered Compounds in Aqueous Surfactant Solutions. *Adv. Mater. (Weinheim, Ger.)* **2011**, 23, 3944-3948.

100. Coleman, J. N.; Lotya, M.; O'Neill, A.; Bergin, S. D.; King, P. J.; Khan, U.; Young, K.; Gaucher, A.; De, S.; Smith, R. J. Two-dimensional nanosheets produced by liquid exfoliation of layered materials. *Science* **2011**, 331, 568-571.

101. Voiry, D.; Mohite, A.; Chhowalla, M. Phase engineering of transition metal dichalcogenides. *Chemical Society Reviews* **2015**, 44, 2702-2712.

102. Tan, C.; Zhang, H. Two-dimensional transition metal dichalcogenide nanosheet-based composites. *Chemical Society Reviews* **2015**, 44, 2713-2731.

103. Chen, Y.; Tan, C.; Zhang, H.; Wang, L. Two-dimensional graphene analogues for biomedical applications. *Chemical Society Reviews* **2015**, 44, 2681-2701.

104. Partoens, B.; Peeters, F. M. From graphene to graphite: Electronic structure around the K point. *Physical Review B* **2006**, 74, 075404.
105. Mak, K. F.; Lee, C.; Hone, J.; Shan, J.; Heinz, T. F. Atomically Thin MoS2: A New Direct-Gap Semiconductor. *Phys. Rev. Lett.* **2010**, 105, 136805.
106. Jachak, A. C.; Creighton, M.; Qiu, Y.; Kane, A. B.; Hurt, R. H. Biological interactions and safety of graphene materials. *MRS Bulletin* **2012**, 37, 1307-1313.
107. Sanchez, V. C.; Jachak, A.; Hurt, R. H.; Kane, A. B. Biological Interactions of Graphene-Family Nanomaterials: An Interdisciplinary Review. *Chemical Research in Toxicology* **2012**, 25, 15-34.

Chapter 2 Biological and environmental transformation of nanomaterial – A case study on Cu-based NPs

2.1 Introduction

Copper-based nanomaterials are used in a range of established and emerging technologies that include catalysts, printable electronics, magnetic storage, solar energy conversion, wood protection and antimicrobial products.[1-7] These uses will inevitably lead to human and environmental exposures that must be characterized and managed to ensure the safe development of copper-based nanotechnologies. In addition to engineered nanoparticles, copper also occurs as an "incidental" particle generated by chemo-mechanical polishing operations on copper-containing substrates in the semiconductor industry. [8] Copper-containing materials are widely used as antimicrobials and in agriculture as fungicides, algaecide, and herbicides. Relevant copper forms include carbonates, hydroxides, various oxide phases, and the zero-valent metal, and dissolution to bioavailable ions is a commonly assumed mode of activity. In other application fields, the most technologically important copper-based materials are zero-valent metal nanoparticles (Cu-NPs) and oxide nanoparticles, Cu_xO-NP, with x=1 or 2. The potential for widespread exposure makes copper-based nanomaterials a high priority for risk characterization.

A second factor making nano-copper a high priority for study is its significant toxicity relative to other common nanomaterials.[9-18] Karlsson et al.[15] found that CuO NPs were the most potent regarding DNA damage and cytotoxicity in a set of metal oxides and carbons studied in parallel. Fahmy et al. [17] showed greater cytotoxicity of CuO NPs in airway epithelial (HEp-2) cells relative to SiO_2 and Fe_2O_3 and demonstrated that oxidative stress was the cause of the cytotoxic effect. Studer et al. [14] attributed the cytotoxicity of CuO to its relatively high solubility in biological media and the impacts of dissolved copper ions, as also reported by Zhang et al. [9] There is a general consensus that

toxicity in Cu/Cu_xO materials is due to oxidative pathways, but there is ongoing debate about the relative importance of ions and particle surfaces in primary ROS generation. [18]

It has become clear that nanomaterials can undergo chemical transformation in the environment or human body that profoundly influences their toxicity and risk.[19-24] This is especially important for metal-based nanomaterials, where the base metals themselves are indefinitely persistent, but can occur in different compounds or phases that greatly affect metal bioavailability. Nanosilver for example, is synthesized and sold in metallic form, but over its lifetime can undergo oxidative dissolution, colloidal aggregation, sulfidation, and reaction with selenide with corresponding large changes in silver bioavailability and toxicity.[19, 22, 23, 25-29] ZnO NPs have been reported to partially dissolve in environmental and biological media and exert toxicity through the liberated zinc ions, [9, 30, 31] or to undergo sulfidation to the more stable ZnS.[32]

Several studies have examined transformations in copper-based systems.[10, 33] In comparison to silver, metallic copper NPs oxidize more readily, first forming a Cu(I) oxide shell around a zero-valent core, and eventually to Cu(II) oxide as a final product.[10] Oxidation typically begins during fabrication and storage, so at the point of exposure or environmental release, an oxide or surface oxide is the most likely phase to come into contact with biological and environmental fluid phases.[10, 34, 35] For this reason, and because the oxidation process has already been systematically studied,[10] we chose to focus our study on the interactions of pre-existing copper oxide phases with biological and environmental systems.

There is significant evidence that dissolution is an important transformation in oxidized copper NPs.[9, 10, 13, 14, 33] Though generally regarded as “insoluble”

substances, copper and copper oxides NPs appear to liberate sufficient amounts of soluble copper in relevant media to affect biological systems. Zhang et al.[9] measured the extent of dissolution of CuO in biological media and attributed cytotoxicity of CuO to the soluble fraction rather than particle surface reactions. Studer et al.[14] proposed a Trojan horse-type mechanism in which CuO NPs penetrated the cell membrane followed by intracellular dissolution into redox active copper ions. Midander et al.[33] observed size-dependent ion release and toxicity when comparing nano- and micrometer-sized copper oxide particles. Free copper ions Cu^{x+}(x=1, 2) are highly redox active species capable of producing hydroxyl radical by the Fenton-like reaction:[36, 37]

$$Cu(II) + H_2O_2 \rightleftharpoons Cu(I) + \cdot HO_2 + H^+ \quad (1)$$

$$Cu(I) + H_2O_2 \rightleftharpoons Cu(II) + \cdot OH + OH^- \quad (2)$$

so even small amounts of soluble copper can be biologically significant. Based on recent work on the dissolution in other NP systems, we hypothesize that pH, ionic strength, dissolved organic matter, and biomolecular ligands may play an important role in the toxicity of copper-based NPs by influencing the total dissolved copper concentration.[38] This concentration, together with the relative redox activity of the ion and surface, should determine the origin of ROS generation and subsequent toxicity pathways in Cu-based nanomaterials, which are factors we hope to clarify in this study.

A final relevant transformation is reaction involving the earth-abundant element sulfur, which has been shown to be important for silver, zinc, and Cd nanomaterials [39] in both environmental [32, 40-43] and biological settings [22]. Copper ions are soft (Cu^+) or borderline (Cu^{2+}) Lewis acids with high affinity for sulfide ligand, and form a highly insoluble sulfide phase, which suggests that copper oxides may undergo sulfidation to

produce a material with low copper bioavailability. The synthesis literature shows that hollow CuS nanostructures can be synthesized using Cu_2O as sacrificial template, [44, 45] but information on the natural bio-environmental sulfidation pathways are limited. Sulfidation has been suggested as a natural detoxification process for metallic nanoparticles. [40, 46, 47]

The present study investigates the transformations of CuO NPs in biological and environmental media, and their implications for copper bioavailability, redox activity, and toxicity. The results are directly relevant to CuO-based technologies, and may provide qualitative insight into technologies based on metallic Cu or Cu(I) oxide materials that are capable of environmental oxidation to CuO or CuO outer corrosion films. We show that copper oxide undergoes acid-promoted dissolution, but also ligand-assisted dissolution in the presence of amino acids at neutral pH. Copper oxide also undergoes sulfidation to produce highly insoluble CuS NPs. Surprisingly, sulfidation does not permanently suppress copper bioavailability and redox activity, because hydrogen peroxide at physiologically relevant concentrations oxidizes CuS and liberates free copper ions that partially restore redox activity in the form of ▪OH. detected here by EPR methods.[36]

2.2 Materials and Methods

CuO NPs agent were purchased from Aldrich and used as received. Phosphate buffered saline (PBS buffer, 10x) was obtained from Fisher Scientific (MA, USA) and diluted with DI (deionized) water before use.

2.2.1 CuO dissolution experiments.

CuO-NPs (200 ppm) were incubated in biological or environment relevant media that included acetate buffers (50 mM, pH 4, 5 and 6), PBS buffer (1×concentration, pH 7.4) and borate buffers (50mM, pH 8 and 9) for pH control. Acetate buffer (pH 4.9) was used as lysosome-mimic, and DMEM and RPMI cell culture media were studied supplemented with 10% FBS. The use of simulant fluids in environmental and biological studies has many limitations, but does provide well defined environments for studying the chemical transformations of materials.[48] Nanoparticles were dispersed by 15 min sonication in 5 ml of the solutions. After incubating for a pre-defined time period, the samples were centrifuged by centrifugal ultrafiltration (Amicon Ultra-4 3k) for 30 min at 4000 rpm to remove the solids, and the supernatant was separated for determination of Cu concentration by ICP-AES. All ion release experiments were conducted at room temperature (20 ℃) unless noted. The ability of centrifugal ultrafiltration to remove the nanoparticles has been proved by previous reference.[49] Therefore, solubility is defined as free metal ions and its complex, which is almost the same as all forms of metal that pass through the ultrafiltration filters in our case.

2.2.2 Electron paramagnetic resonance ROS assay.

The ability of CuO-NPs and/or associated soluble species to generate hydroxyl radical in the presence of H_2O_2 were quantified using X (9.8 GHz)-band EPR measurements at room temperature using an EMX-plus CW spectrometer (Bruker Biospin) and the spin-trap DMPO (Dojindo Molecular Technologies, Inc). In a typical experiment, 2 or 20 ppm CuO-NPs were incubated with 100 mM DMPO, 1 mM H_2O_2 in PBS buffer

(pH 7.4) for 20 min, and the reaction was initiated by addition of H_2O_2. Then the aqueous solution was drawn into 50 uL capillary (Cat No. 53432-783, VWR), and the capillary was inserted into a quartz EPR capillary tube (4 mm OD ×250 mm L × 0.5 mm wall, Wilmad LabGlass, Buena, NJ). The data acquisition parameters were set as follows: Center Field, 3508.75 G; sweep width, 100 G; sweep time, 30 s; modulation amplitude, 1G; number of scans, 10; microwave power, 2 mW; conversion time, 30 ms; time constant, 81.92 ms. Though EPR cannot quantitatively measure the radical produced due to decomposition of DMPO-OH adduct, it can give a relative ROS intensity by comparing the peak height if the incubation time and instrument parameters are constant.

2.2.3 Sulfide and dissolved oxygen (DO) depletion measurements.

The sulfidation of CuO NPs were studied by tracking sulfide depletion using the method of Liu et al. [41] Soluble sulfide concentration was measured with a sulfide-ion-selective electrode following removal of solids by centrifugal ultrafiltration (Amicon Ultra-4 3k). In a typical experiment, 1 mg CuO-NP powder was added to 4.5 mL DI water, followed with sonication for 15 min to disperse the aggregates, and then 0.5 mL of 125 mM Na_2S solution was added to initiate the reaction at a starting sulfide concentration of 12.5 mM. The pH of 12.5 mM Na_2S solution is around 9.3, where the main soluble sulfide species is bisulfide (HS^-). After rotating the mixture for a pre-determined time, the bisulfide solution was separated by centrifugal ultrafiltration and the sulfide antioxidant buffer (ASOB, Orion 941609 Thermo Scientific) was added to prevent bisulfide oxidation and volatilization before analysis. Bisulfide concentration in the filtrate was measured with sulfide-ISE (Orion 9616BNWP Silver/Sulfide combination electrode, Thermo Scientific)

at room temperature. DO levels were monitored in situ during incubation of either copper ions or CuO NPs in bisulfide solutions in a closed amber glass bottle under magnetic stirring using a DO probe (Orion 083010MD, Thermo Scientific) at 3 s sampling frequency.

2.2.4 Cell toxicity studies.

An immortalized murine macrophage cell line, J774.A1 (ATCC number TIB-67) was used as a target cell for assessment of uptake, H_2O_2 generation, and toxicity of CuO and CuS NPs. Carbon black (M120, Cabot) with a primary particle diameter ~ 75 nm was used as a nontoxic reference particle. Test particles were dispersed in RPMI 1640 medium containing 1% FBS at a concentration of 250 ppm and sonicated at 100W in a Branson 2510 sonicating water bath for 60 min prior to dilution at final concentrations of 5-20 ppm in cell culture medium. Murine macrophages were cultured in RPMI 1640 medium (Invitrogen 11875) containing 10% FBS, 2 mM glutamine, 1 mM sodium pyruvate, and 500 ul penicillin-streptomycin in ultralow attachment culture dishes (Corning 3262) at 37 ℃ in air with 5% CO_2. For microscopy, cells were plated on glass coverslips in 12 well plates (Coster, 22 mm in diameter) at 70% confluence and allowed to attach for 3 hours, then exposed to test particles for 3-24 hours. To visualize uptake of test particles, cells were rinsed and stained with 4’6-diamidino-2-phenylindole (DAPI) and visualized under brightfield and fluorescence illumination using a spinning disk Olympus confocal inverted microscope (Model 1X81). To assess viability, cells were visualized using brightfield imaging to assess morphology and cell detachment, and confirmed by staining with 1:1000 Syto 10/ethidium homodimer (Invitrogen) for 5 min. Viable (green fluorescence) and dead cells (red fluorescence) were imaged using a spinning disk Olympus confocal inverted

microscope equipment with fluorescence filters. Cell viability using DNA content as a surrogate for cell number was quantitated using a fluorescence assay (Pico Green, Invitrogen) that quantitatively binds to DNA according to the manufacturer's instructions. For quantitation of H_2O_2 generation, murine macrophages were seeded in RPMI growth medium at 75,000 cells per well in a black clear bottom 96-well plate (Costar 3603). Cells were allowed to equilibrate overnight at 37 ℃, after which growth medium was aspirated and subsequently replaced with 200 ul of medium per well containing 50 uM Amplex Red reagent (Invitrogen A1222), 2ul of 10 U/ml horse radish peroxidase (Invitrogen 012001), and 2.5, 5, and 10 ppm of test particles.[50] Continuous fluorescence measurements were obtained using a spectrophotometer with an excitation of 566 nm and an emission of 587 nm. Data were acquired every 5 minutes and reported after 20 min of exposure to test particles. Statistical significance was determined using an unpaired t-test to compare differences between the means (± SD) of untreated and treated cultures in triplicate. A p value of <0.05 was considered to be statistically significant.

2.2.5 Visual MINTEQ 3.0 calculation

The equilibrium dissolved metal ion concentration was estimated using Visual MINTEQ 3.0. (results in Figure 2-1) [51] The phases considered were TiO_2, ZnO, NiO, CuO and Ag_2O and the sulfides ZnS, NiS, CuS and Ag_2S. The parameters for metal oxide calculation were set as follows: pH is fixed at 7; temperature is 25℃; ionic strength is to be calculated depending on components added; 1 mM Na^+ and 1 mM NO_3^- is added as components; the metal oxide of interest is specified as infinite solid phase. The parameters for metal sulfide calculation were set as follows: pH is fixed at 7; temperature is 25℃;

ionic strength is to be calculated depending on components added; 1 mM S^{2-} is added as components; the metal sulfide of interest is specified as infinite solid phase.

The equilibrium dissolved copper ion concentration was estimated using Visual MINTEQ 3.0. (results in Figure 2-3) The parameters were set as follows: pH is fixed at 4, 5, 6, 7.4, 8, 9, respectively; temperature is 25℃; ionic strength is to be calculated depending on components added; 2.5 mM CuO (tenorite) is specified as finite solid phase. The calculated equilibrium concentration of dissolved Cu is 2.5 mM, 2.5 mM, 4.7E-02 mM, 1.3E-04 mM, 2.1E-05 mM and 4.1E-06 mM, respectively. In the case of pH 7.4, the effect of phosphate was investigated through calculation by Visual MINTEQ 3.0. The parameters were set as follows: pH is fixed at 7.4; temperature is 25℃; ionic strength is to be calculated depending on components added; 11.9 mM phosphate (concentration in PBS buffer) is added as components; 2.5 mM CuO (tenorite) is specified as finite solid phase; specify $Cu_3(PO_4)_2(s)$ as possible solid phase. The calculated equilibrium concentration of dissolved Cu is 2.4E-03 mM, which is predicted to be slightly higher than the one at same pH but without consideration of buffer effect (1.3E-04 mM) because of the formation of soluble $CuHPO_4$ complex. These calculations show that the effect of phosphate complexation is limited and the extra low equilibrium concentration of dissolved Cu is predicted with or without consideration of phosphate buffer effect.

2.2.6 Product characterization.

UV-vis spectra of sulfidated CuO NP samples were recorded on a V-630 spectrophotometer (Jasco, MD) over the range 400 to 800 nm. The sizes of secondary CuS particles (formed by dissolution and precipitation) were monitored using dynamic light

scattering (DLS) with a Zetasizer Nano ZS system (Malvern Instruments). The morphologies of the sulfidated CuO NPs were observed in high-resolution transmission electron microscopy (HRTEM) on a JEOL JEM-2010. The samples were prepared by placing one drop of purified sample solution on carbon-coated copper grids, followed by drying at room temperature overnight. The compositions and phases of sulfidated CuO samples were identified by X-ray diffraction spectrometry (XRD) on a Bruker AXS D8 Advance instrument with Cu Kα radiation (λ=1.5418Å). The XRD samples were prepared by adding purified and concentrated sulfidated CuO NPs suspension onto a glass slide, followed by overnight drying.

2.3 Results

2.3.1 Comparative solubilities of oxide and sulfide phases

Ion-particle partitioning is a major determinant of the fate, transport, and toxicity of nanoparticles, and understanding dissolution behavior has become an important theme in environmental nanotechnology and nanotoxicology research. [9, 19, 21, 30, 46, 49, 52, 53] Figure 2-1 shows the equilibrium solubilities of oxide and sulfide phases for several metals found in the most common commercial nanomaterial types. Although based on bulk thermodynamic properties, this plot shows several trends that provide insight into reported nanomaterial behavior. First, the most soluble oxides are those of Ag, Ni, and Zn, and all three have been reported to be toxic through dissolution mechanisms.[31, 54, 55] ZnO toxicity has been related to dissolution in several recent studies [9, 30, 31] and NiO toxicity *in vitro* has been reported to correlate with the concentration of dissolved Ni^{2+} ion. [54] Silver oxidizes slowly and is typically synthesized and sold as the zero-valent metal,

but does dissolve upon use and disposal[46, 49] through a mechanism that may pass through a Ag_2O surface intermediate. [56] Because the oxide has a relatively high solubility, the rate limiting step is typically the initial oxidation step. [57, 58] Lower solubility oxides are titania, whose biological responses have not typically been related to dissolution, and copper, the subject of the present study.

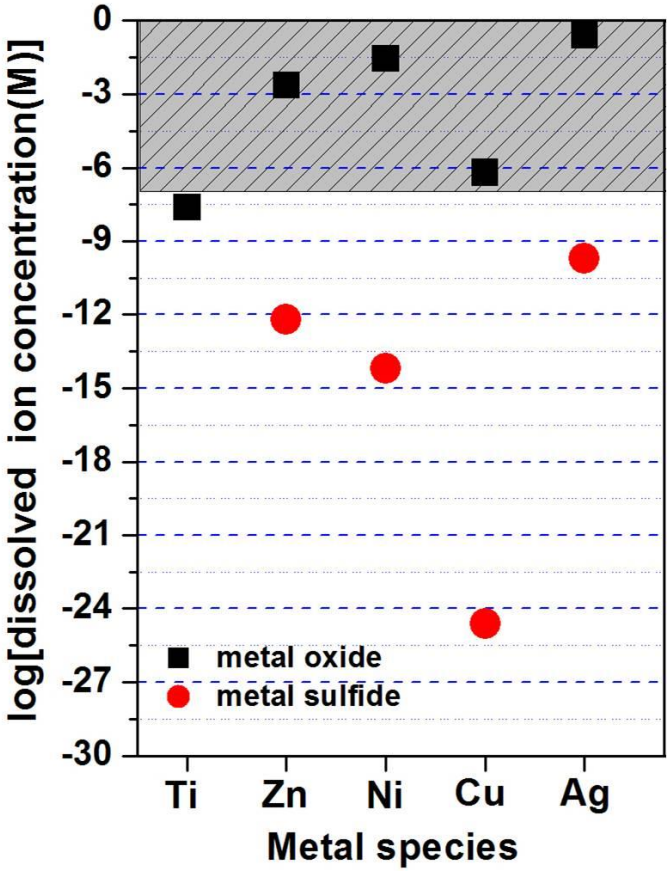

Figure 2-1. Equilibrium solubility of the oxide and sulfide forms of common metal-based nanoparticles. The equilibrium dissolved metal ion concentration was estimated using Visual MINTEQ 3.0 using bulk thermodynamic parameters. The phases considered were TiO_2, ZnO, NiO, CuO and Ag_2O and the sulfides ZnS, NiS, CuS and Ag_2S. The incubation conditions for the metal oxide calculations were aqueous solution (pH 7) and 1 mM $NaNO_3$ as electrolyte, and for metal sulfide ligand-free aqueous solution (pH 7) containing an environmentally relevant total sulfide concentration (1 mM). Please note the calculations ignore any oxidative dissolution. Toxicity studies on free ions typically show adverse biological effects at micromolar doses (> 0.1 uM), [62-65] which defines the shaded region above. Data points that fall in the shaded region all correspond to cases where nanoparticle toxicity has been attributed to dissolution mechanisms (oxides of Zn, Ni, Cu, Ag), which is possible due to the finite solubility of the oxide phase. TiO_2 solubility in contrast is too low to yield ions above the micromolar range, where ion-induced toxicity is often seen in other systems.

Sulfide phases are typically much less soluble, and have been reported to form when nanosilver is exposed to the natural environment [23, 24, 40-43, 47] or biological fluid phases,[22] and to reduce the toxicity relative to the original zero-valent form. [23, 40, 47, 59] Sulfidation has been proposed as a natural detoxification mechanism for nanosilver [40, 41, 47] and potentially other chalcophile metals.[60, 61] This is based on the fact that the equilibrium free metal in each of these sulfide systems is in the nanomolar range or below (Figure 2-1), which is well below typical threshold concentrations for biological effects. Copper (I) sulfide, CuS, is unique in its extremely low solubility (Figure 2-1), which led us to hypothesize that sulfidation would effectively detoxify nano-Cu or nano-CuO. We found here, however, that copper sulfides do form, but the redox activity of the product is not fully suppressed (*vida infra*).

2.3.2 Copper oxide characterization and dissolution behaviors

The CuO NPs were synthesized using the molten salt synthesis method according to manufacturer and some organic matter was observed on the surface according to FT-IR (Figure 2-2).The particles were characterized for size (mean 50 nm determined by TEM), surface charge in PBS buffer (zeta potential -25 mV), size distribution in PBS buffer and crystalline phase (tenorite). (Figure 2-2) The increased size of particles in PBS buffer indicated the aggregation of CuO NPs.

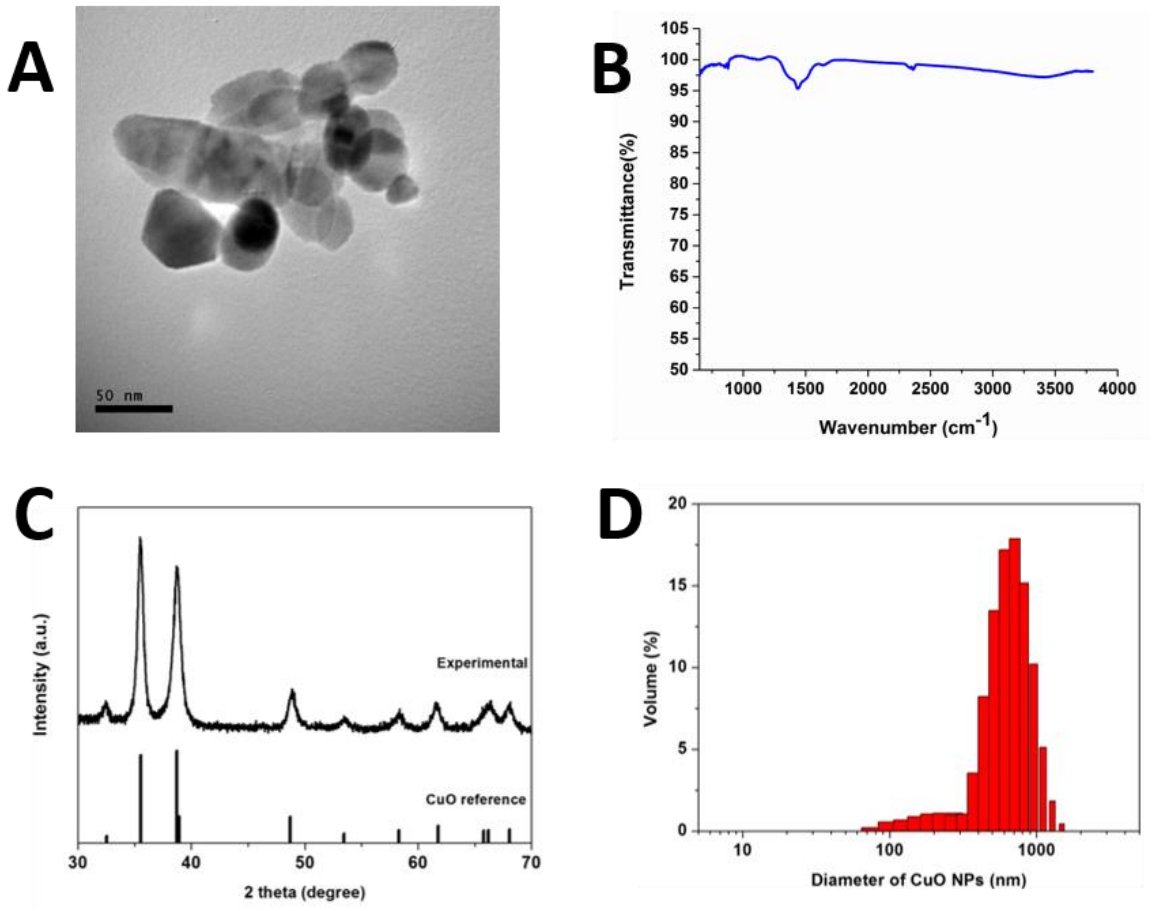

Figure 2-2. Characterization of commercial CuO nanoparticles. (A) TEM image of CuO after dispersion in DI water and drying overnight. (B) FT-IR spectrum showing the limited number and intensity of peaks, which may be residue of organic ligands during synthesis process. (C) XRD spectra indicating the CuO (tenorite) crystalline. (D) Size distribution of CuO dispersed in PBS buffer which indicated strong aggregation (determined by DLS).

Copper (II) oxide is described as insoluble in basic chemistry references, but at the ppm levels of interest in nanotoxicology and the environment it is sufficiently soluble for the released ions to be key determinants of toxicity.[9, 13, 14] Based on Equation 3, we expect CuO ion release to be pH dependent, and this is confirmed in Figure 2-3A.

$$CuO_{(s)} + 2H^{+}_{(aq)} \rightleftharpoons Cu^{2+}_{(aq)} + H_2O_{(l)} \qquad (3)$$

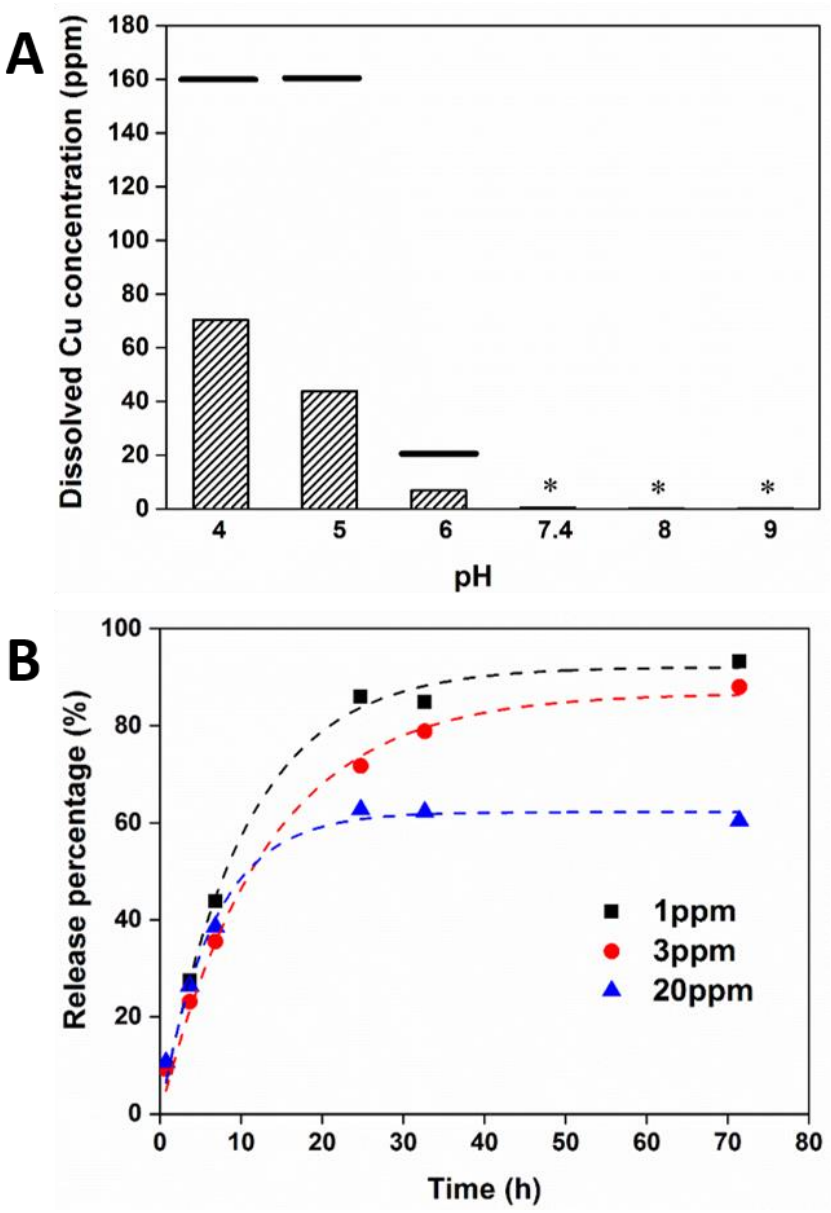

Figure 2-3. Dissolution behavior of CuO in various buffer solution. (A) Soluble copper produced by 24 hr incubation of CuO NPs (initial concentration 200 ppm) as a function of pH (50 mM acetate buffers at pH 4, 5 and 6, PBS buffer at pH 7.4 and 50 mM borate buffers at pH 8 and 9). The black bars indicated the equilibrium concentration in the corresponding pH conditions calculated by Visual MINTEQ 3.0, the stars indicated that both the calculated equilibrium concentration and real dissolved Cu concentration is close to the ICP-AES detection limit. (B) Effect of initial CuO NP loading on dissolution kinetics (acetate buffer at pH 4.9) for 3 days expressed as percent of total copper. Over 80% of CuO was dissolved after 30 hours for 1 ppm initial loading of CuO NPs and then dissolved Cu concentration slowly increased.

Solubility at lysosomal pH (4-5) is significant, and can be close to complete at low particle loadings (Figure 2-3 B), but at extracellular pH (7.4 in PBS buffer) is very low. The very low ion release at pH 7.4 was initially surprising since copper ions have been reported to be the primary source of toxicity in several *in vitro* studies.[9, 13, 14] Calculations with Visual MINTEQ 3.0 at this pH confirm low values of dissolved copper ion (154 ppb) at equilibrium. These low values were further confirmed in time-resolved measurements (labeled with PBS in Figure 2-4A), which gave copper concentrations about 20 ppb, which approached the detection limit of our inductively coupled plasma atomic emission spectroscopy (ICP-AES) technique.

To understand how Cu-ions exist in biological studies, we studied dissolution directly in two types of cell culture media (Figure 2-4A). We measure significant release in both media despite the high pH (7.4), suggesting dissolution is assisted by ligands, either thermodynamically by reducing the concentration of the free ion in equilibrium with the solid, and/or through kinetic effects at the particle surface. We tested a variety of single components found in cell culture media in an attempt to identify the primary types of ligands involved. Glucose and the buffering agent, HEPES, did not promote copper ion release, but fetal bovine serum (FBS) and glutamine did (Figure 2-4B). Glutamine and other amino acids have been reported to form a high-affinity complex with copper, and the overall stability constant is very high ($\log\beta_2$ of 11.6).[66] The removal of free ion shifts the ion-particle equilibrium and favors dissolution. The complex formation (stability) equilibrium constant, $K = \{L - Cu^{2+}\}/\{Cu^{2+}\}\{L\}$, can be rearranged to give a dissolution enhancement factor:

$$\frac{\{total\ copper\}}{\{free\ ion\}} = \frac{(\{L-Cu^{2+}\}+\{Cu^{2+}\})}{\{Cu^{2+}\}} = 1 + K\{L\} \qquad (4)$$

which is 108 - 109 when the concentration of ligands (e.g. glutamine) in cell culture media is in the mM range. We further investigated the effects of a larger series of amino acids (Figure 2-4C), which all promoted dissolution, but to differing degrees. We thought this may be due to involvement of the side chain in complex formation, but previous studies have reported that only the amino and carboxylate terminal groups were involved.[67] Indeed the Cu^{2+} complexes with glutamine and histidine do not have higher stability constants than other amino acids, which also suggests their higher activity is not thermodynamic in origin. In the search for an alternative explanation, ligands have been reported to promote the dissolution of iron oxide through formation of surface complexes that kinetically enhance the detachment.[68] The surface binding constant for CuO-histidine is reported to be higher than that for other amino acids, [69] and the ion concentrations in Figure 2-3A are well below estimated equilibrium values (see horizontal bars). Both of these facts suggest the different activities among the amino acids are kinetics differences associated with ligand-specific surface binding ability.

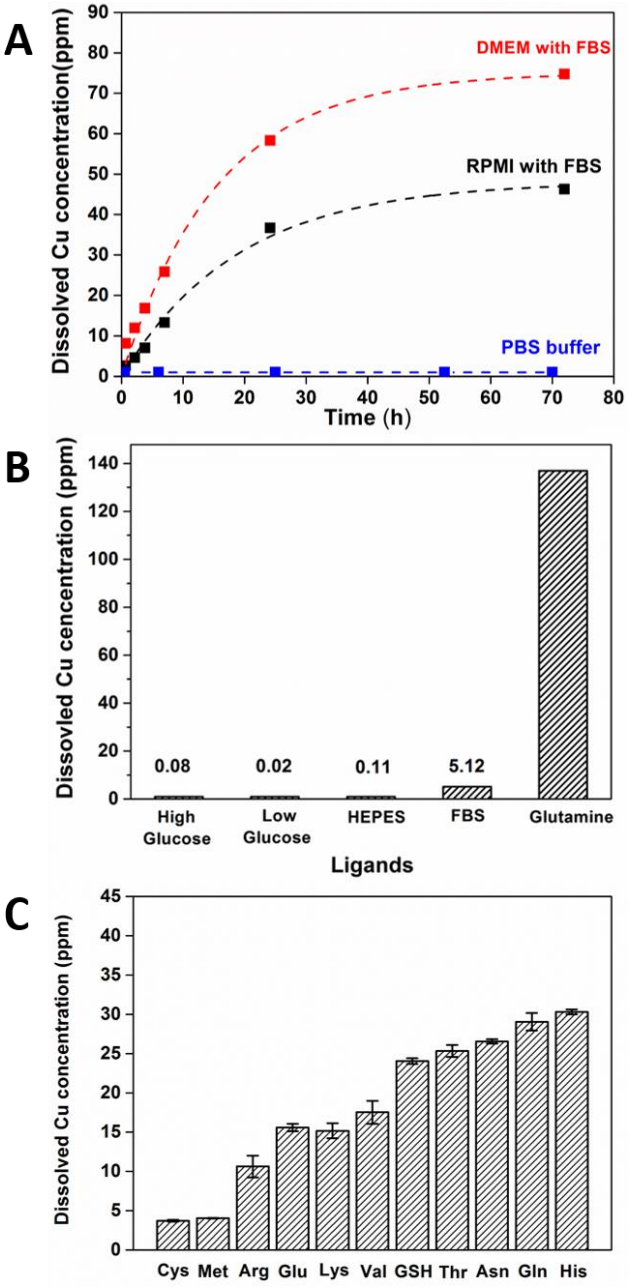

Figure 2-4. Dissolution behavior of CuO in various biologically-relevant media. (A) Soluble copper produced by 3-day incubation of CuO NPs (initial concentration 200ppm) in PBS buffer, DMEM and RPMI cell culture media supplemented with 10% FBS at pH 7.4. Note the much elevated Cu ion release relative to PBS buffer at pH 7.4. (B) The effects of various components in cell culture media on the dissolution of CuO (initial concentration 200 ppm) in PBS buffer in one day. High glucose: 4500 mg/L. Low glucose: 1000 mg/L; HEPES: 5958 mg/L; FBS: 10%; Glutamine: 20 mM. (C) Ligand effects on CuO (initial concentration 200 ppm) dissolution using a series of amino acids and the tripeptide glutathione at 2 mM in PBS buffer. Please be noted that the dissolved copper measured is those that pass through the ultrafilters. Therefore, about cysteine, the dissolved copper concentration may be underestimated due to the formation of insoluble precipitate through copper-thiol bond.

2.3.3 ROS production in Cu-NP systems

Several studies of nano-Cu or nano-CuO toxicity report ROS generation and oxidative stress as a mechanism.[12, 16, 17] In copper-containing systems, ROS may be produced by heterogeneous reactions at the particle surfaces, or by dissolved copper, which can exhibit Fenton-like chemistry through the Cu(II)/Cu(I) redox couple.[12, 70, 71] Resolving the relative particle-ion contributions is key to understanding the mechanism of nano-Cu toxicity and interpreting nanotoxicology data. Studies showing correlation between dissolved Cu and toxicity suggest the primary redox species are in solution,[13] not on the surface, but direct evidence is needed. Here, we use EPR spin-trap techniques to quantify ROS production from particles, ions, and sulfidated products. We focus on the hydroxyl radical by using the spin trap DMPO, which is known to react with ▪OH to form an ▪OH-DMPO adduct that exhibits a characteristic EPR peak quartet (see Figure 2-5). Incubation of CuO NPs or copper ions with DMPO and peroxide in PBS buffer gives this characteristic EPR spectra, but with varying peak intensities as shown in Figure 2-5. Each of the copper-containing solutions triggers Fenton chemistry and produces the ▪OH-DMPO adduct. Comparing the data on particles and their clear filtrates (Figure 2-5A) indicates that most of the activity in the CuO NP cases is associated with the soluble fraction. Figure 2-3 predicts that this soluble fraction should be quite low under these conditions (< 100 ppb), and indeed the "ion-only" experiments in Figure 2-5B show similar peak heights for 6-100 ppb free copper. Even at this limited degree of dissolution (neutral pH with no added ligands), the main source of ROS is the trace concentration of free copper ion.

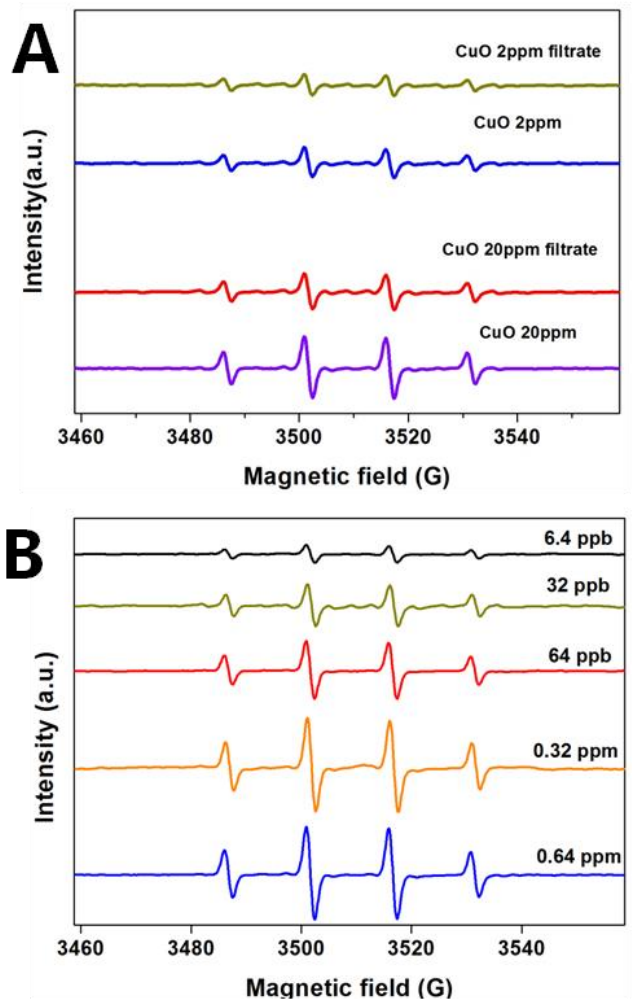

Figure 2-5. ROS production catalyzed by copper-based species. Hydroxyl radical EPR signal (DMPO spin trap) induced by (A) 2 or 20 ppm CuO NPs suspension or its filtrate containing only the soluble forms, (B) free copper ions ($CuCl_2$) at various concentrations (ppb ng-Cu/g-solution). These experiments used 1 mM hydrogen peroxide and 100 mM DMPO in PBS buffer for 20 min. To isolate the effect of the ion associated with the particles, CuO NPs were incubated for 20 min in PBS buffer then subjected to ultrafiltration, and the filtrate added to 100 mM DMPO and 1 mM hydrogen peroxide in PBS for 20 min before the spectra were obtained ("filtrate" cases in A).

We were interested in whether the ligands that promote Cu dissolution also affect redox activity in solution. Previous studies have shown that complex formation can reduce the catalytic ability of Cu ions in peroxide reduction to ▪OH.[72] Figure 2-6 shows a strong attenuation of the ▪OH signal when simple PBS buffer (Figure 2-5) is replaced by cell culture medium (Figure 2-6A). Some redox activity remains in media (the ▪OH-DMPO

quartet is clearly visible), and is primarily associated with the soluble fraction, since the particles and their clear filtrates give similar peak heights (Figure 2-6A). The redox behavior is quite low in the presence of 1 mM glutamine (Figure 2-6B), which is a high affinity ligand ($\log\beta_2$ of 11.6) and strong promoter of dissolution. The catalytic ROS production by Cu is significantly reduced in the media containing glutamine, but the complexed Cu can still catalyze the reaction though in a much slower manner.

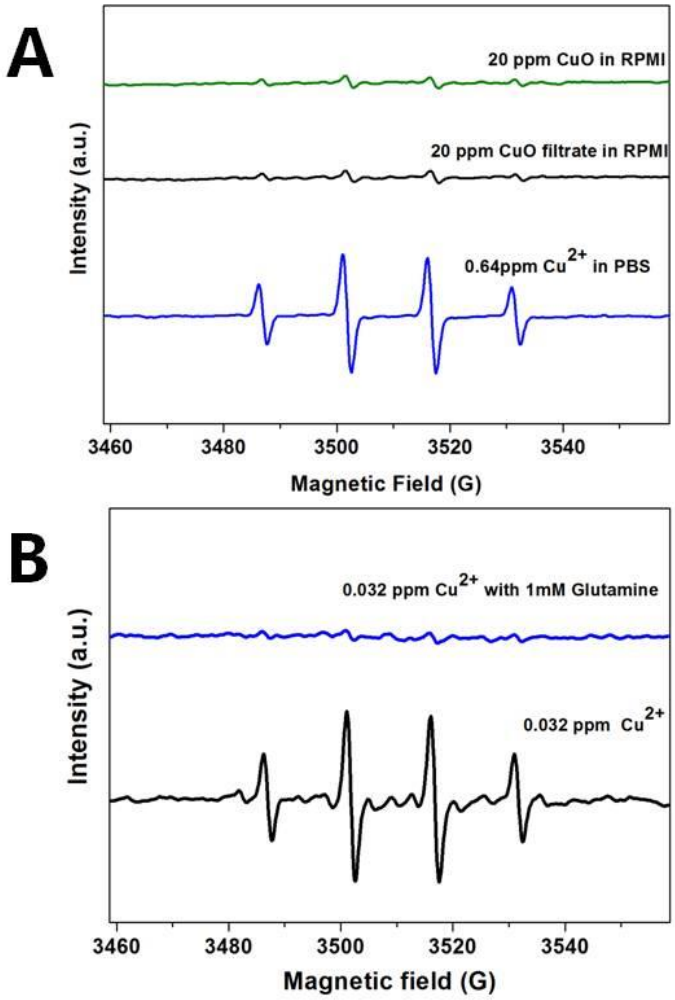

Figure 2-6. Ligand effects in the ROS activity of CuO-NPs and soluble salts. (A) Comparison of ROS activity of 20 ppm CuO NPs or its filtrate in cell culture media with 0.64 ppm copper ions in PBS buffer. Note that the ion released from 20 ppm CuO-NPs in medium is much greater than the 0.64 ppm free ion concentration (Figure 2-4), but is still less redox active due to ligand binding in medium. (B) ROS activity of 0.032 ppm Cu^{2+} with or without the presence of 1 mM glutamine in PBS buffer. Please be noted that the induced EPR peaks with glutamine were reduced but not eliminated.

Overall, the data in Figures (2-4, 2-6) suggest that complex biological media will promote copper dissolution but then partially suppress the redox activity of the resulting soluble species. It is doubtful that simple assays for dissolution and redox activity in water or simple buffers will have predictive value for the toxicity of copper-containing NPs.

2.3.4 Copper oxide sulfidation

Recent research has shown that nanoparticles based on silver, zinc and cadmium undergo reactions with reduced sulfur species (and in some cases selenium species) [22] in the environment and the human body to produce low-solubility metal sulfide (or selenide) phases. These transformations are expected to have profound effects on transport, bioavailability, toxicity and risk. [22-24, 32, 40, 47, 60, 73] Here we studied the reaction of CuO-NPs with soluble sulfide (main species is HS^-) as a function of time and CuO:sulfide stoichiometric ratios. Figure 2-7 shows conversion of CuO NPs to sulfide phases within one day with the extent of conversion depending on the starting CuO:bisulfide molar ratio. At high sulfide (CuO:bisulfide = 1:5) the conversion is essentially complete as the XRD spectra lose all characteristic peaks for crystalline CuO and match quite well with Cu(I)S (covellite) reference spectra (Figure 2-7A). Though the formation of any Cu_2S phase was not observed, absence of a crystalline Cu_2S phase under these conditions may indicate a slow phase transition that prevents the crystalline phase from being observed over our time scales.[74] The morphologies of the sulfidated samples show a number of particles substantially smaller than the original CuO particles, and at least some of them in a crystalline state, indicated by HRTEM fringes (Figure 2-7B). The theoretical amount of bisulfide needed to stoichiometrically convert CuO to CuS is only at

the ratio 1:1, but the data in Figure 2-7 only achieve complete sulfidation at the ratio 5:1, so sulfidation is either limited by kinetics, or there are competing reactions for bisulfide (*vida infra*).

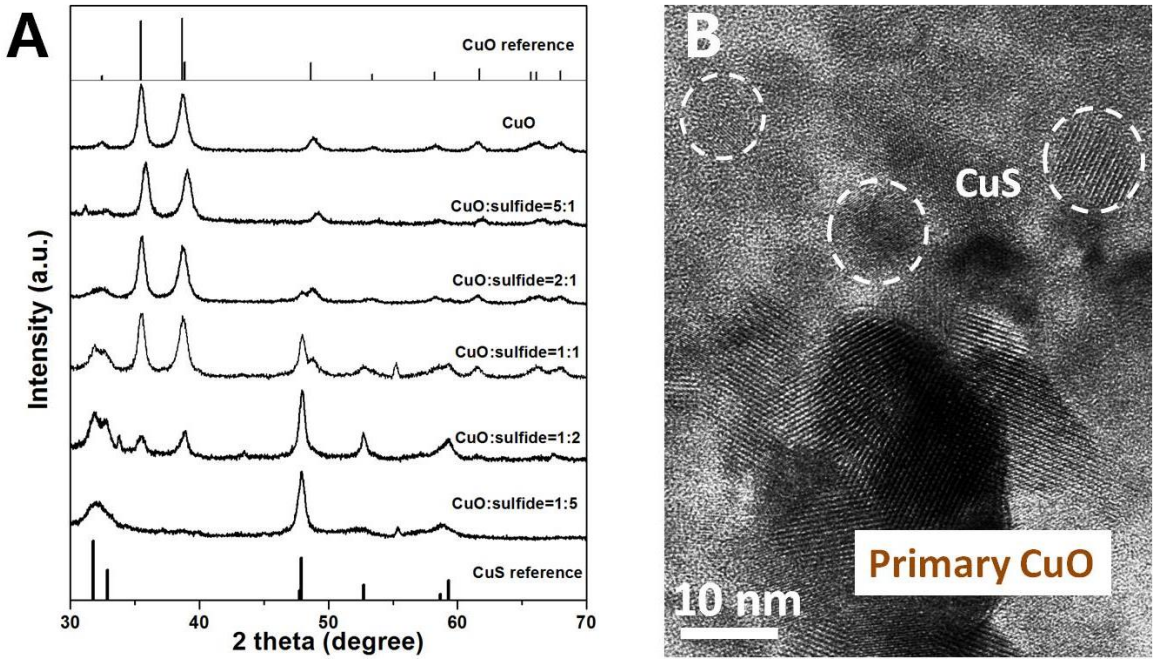

Figure 2-7. Phases and morphologies of the solid products from reaction of CuO NPs with soluble HS^-. (A) XRD patterns of sulfidated CuO NPs generated from initial Cu/S ratios that vary from 0.2 to 5. CuO (tenorite) and CuS (covellite) reference is presented for comparison. Please note the CuO/CuS peak intensity ratio can't be used to calculate the percentage of CuS produced, but it can show a general trend that CuS produced increase with decreasing CuO to bisulfide ratio. (B) HRTEM image of sulfidated CuO NPs (generated from 2.5 mM of CuO NPs incubated in 5mM Na_2S solution for one day), corresponding to a CuO/bisulfide molar ratio of 1:2. The images show the formation of small secondary particles with size 5 to 10 nm, and showing lattice fringes indicating the presence of at least some crystalline products.

We carried out additional experiments to understand the sulfidation mechanism and reaction stoichiometry. The presence of small particles surrounding a central core suggests a dissolution-precipitation mechanism rather than a direct solid-state exchange reaction. Recent research has reported dissolution-precipitation mechanism for the sulfidation of ZnO NPs [32] with similar morphologies in the sulfidation products.

To better understand sulfidation pathways, we interrupted the sulfidation process and examined the soluble products or clusters (after half hour incubation) that passed through a 200 nm syringe filter.[75] Figure 2-8 shows UV-vis spectra of this filtrate after aging for up to 3 hours, which shows an absorption feature that starts to appear around 600 nm that likely belongs to CuS.[76] The aged filtrate was washed three times with water and then concentrated for DLS analysis (Figure 2-8C), which shows 10 nm mean particle size. These are much smaller than the starting CuO NPs (50 nm) suggesting they are secondary particles/clusters formed by dissolution-precipitation. XRD analysis identifies them as CuS (Figure 2-8D). We also investigated the filtrate of the solution after 3 hour incubation and did not observe the characteristic CuS peak, which suggests these ultrafine CuS clusters have grown or else attached to larger particles. [40] As a control we incubated CuO NPs in NaOH at the same pH (9.3) as the sulfide solutions (but without sulfide) and performed the ultrafiltration, but did not see particles/clusters in the filtrate. The filtrate from this control was treated with sulfide and the product investigated with UV-vis, but no characteristic CuS peak was observed. In another separate experiment, the filtrate was digested with nitric acid and prepared for ICP-AES analysis to determine the copper concentration. No detectable copper was found in the filtrate by ICP-AES. Together these data indicate that CuO NPs undergo rapid sulfidation and the mechanism involves dissolution-precipitation. However, the detection of secondary CuS NPs does not exclude the possibility of some direct solid-phase conversion. It is interesting that this can even occur at high pH (9.3) where CuO dissolution is extremely limited. Bisulfide is a high-affinity ligand for ionic copper, and the data indicate that it promotes copper dissolution from CuO NPs at the same time it forms the insoluble CuS phases as secondary particles

in the immediate vicinity of the mobilization sites. The dual role of bisulfide as dissolution promoter and precipitating agent explain the essential behavior in Figure 2-8.

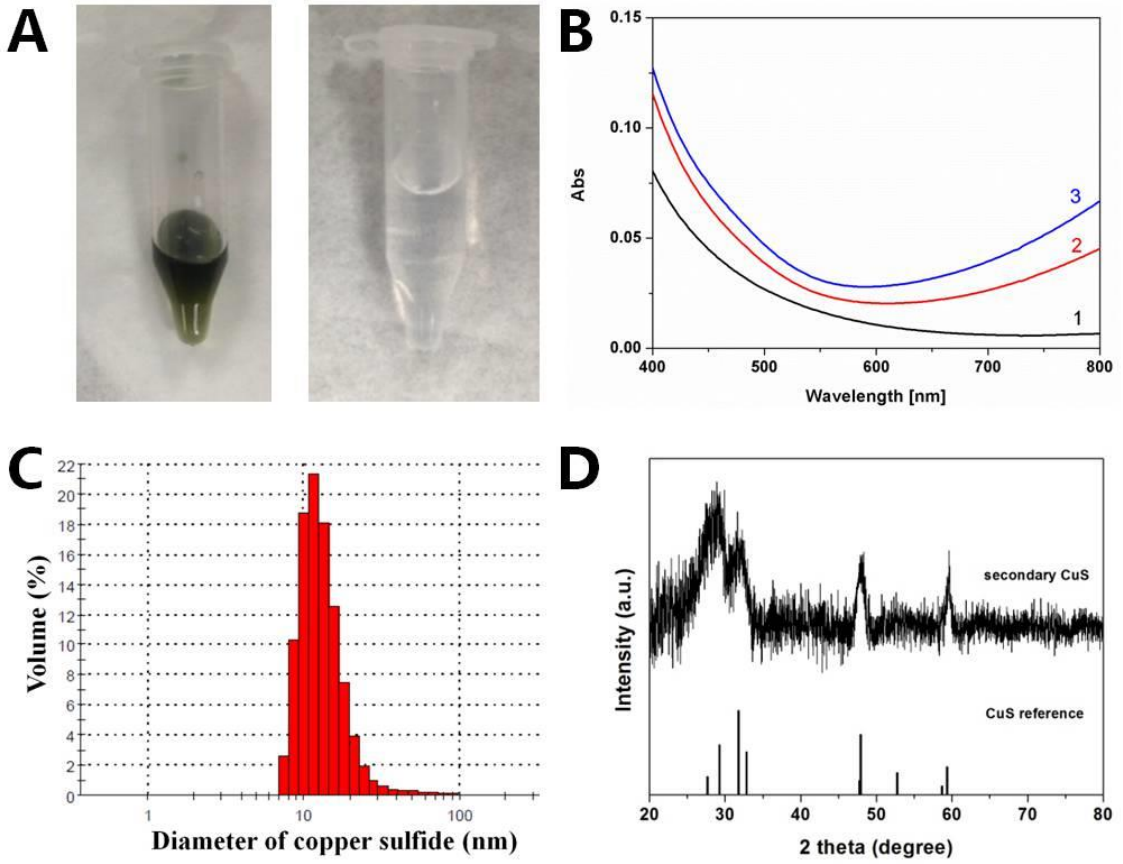

Figure 2-8. Characterization of secondary CuS NPs generated by sulfidation of CuO. (A) Optical images of concentrated secondary CuS particles through 200 nm filter (left) and the filtrate after CuO NPs suspension in NaOH solution through 200 nm filter (right). (B) UV-vis spectra shows formation of CuS NPs. Curves 1,2,3 correspond to aging for 0, 1, 3 hours, respectively (C) The size distribution of secondary CuS determined by DLS. The original mean size of CuO NPs is 50 nm. (D)XRD pattern confirms the formation of CuS. In these experiments, Na_2S and CuO NPs were incubated at a molar ratio of 2:1.

2.3.5 Properties of CuS - catalysis of sulfide oxidation

The data in Figure 2-7 show that a great excess of bisulfide is needed to fully convert CuO NPs to CuS. While this could indicate kinetic limitations for this reaction, we instead have evidence that it is due to bisulfide consumption by oxygen that is catalyzed

by the same CuS that is produced as the sulfidation product. In time-resolved studies we observed a rapid depletion of bisulfide upon addition of copper oxide NPs (Figure 2-9A), even if the bisulfide concentration was 5 times greater than the Cu on a molar basis. This cannot be explained by CuS precipitation stoichiometry, and instead must indicate either superstoichiometric sulfide phases or catalytic loss of bisulfide by oxidation. The XRD results show CuS as a main product, so bisulfide oxidation seemed more likely. To test this hypothesis, we added copper chloride (the concentration is 0.1, 1 or 2 mM, respectively) to existing excess bisulfide solutions and saw rapid drops in dissolved oxygen concentration (Figure 2-9B). The O_2 depletion rate increased with increasing Cu^{2+} addition. Copper ion has been shown to catalyze the oxidation of bisulfide in the presence of oxygen,[77] and the reduction of Cu (II) to Cu(I) has been observed on the surface of CuO when incubated in bisulfide solutions.[78] However, in our experiments it was still not clear whether dissolved copper ions or CuO NPs were the active catalyst. To investigate this, the catalytic ability of CuO NPs was compared with that of equimolar Cu ion in excess bisulfide solution and the depletion of bisulfide was also monitored at the same time. Figure 2-9C shows the depletion of bisulfide is much faster in the presence of free Cu ion than the presence of CuO NPs. Therefore, catalytic ability of CuO NPs in bisulfide oxidation is not significant. Further, the oxygen concentrations were unchanged if copper ion was added in equimolar amounts to HS^- to make stoichiometric CuS, which indicated copper ions readily reacted with bisulfide before catalyzing the oxidation of bisulfide. Overall it is clear that CuS is the catalytic phase for bisulfide oxidation.[79] Comparison experiments indicated both the soluble CuS clusters and CuS particles contribute to the catalytic oxidation of bisulfide in the presence of oxygen. (Figure 2-9D) The curve of consumption of oxygen in

the presence of precipitate is almost identical to that induced by the total, which indicated that the precipitate CuS played a significant role in catalytic oxidation of sulfide. The catalytic activity of CuS intermediate cluster may be very strong considering its ultralow concentration.

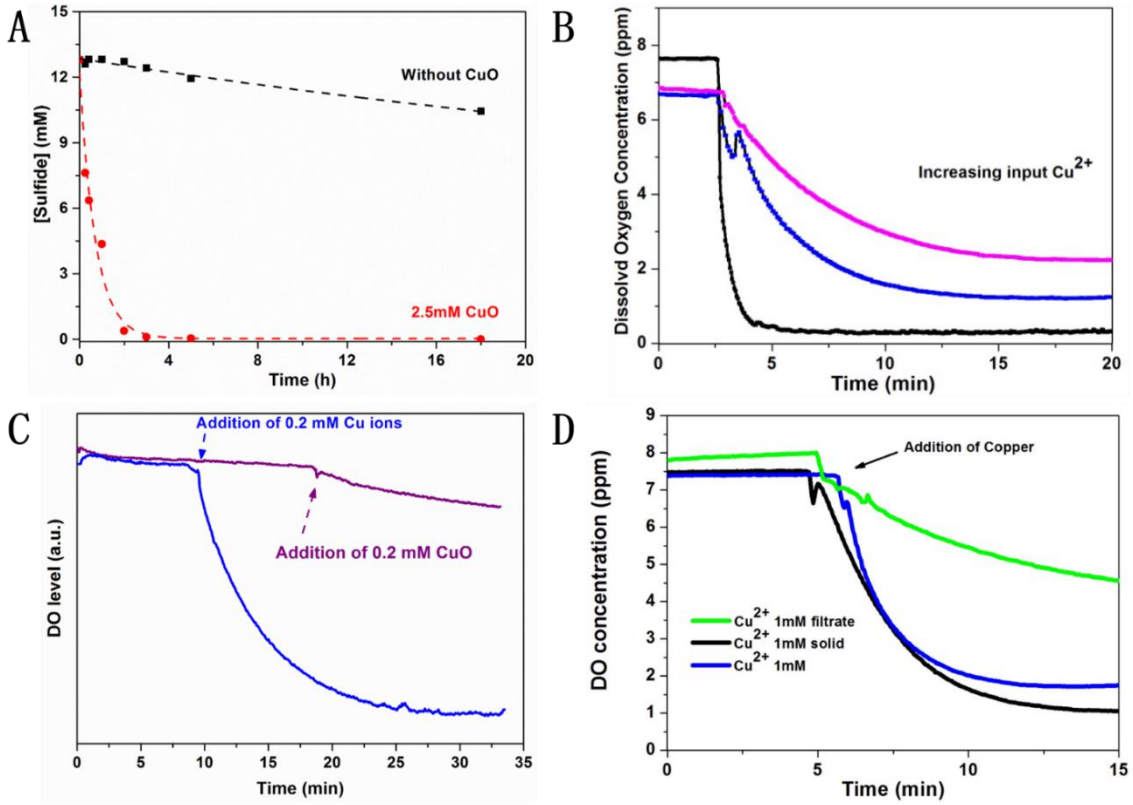

Figure 2-9. Sulfidation of CuO NPs and the catalytic ability of CuS. (A) Depletion of 12.5 mM of sulfide in the presence of 2.5 mM CuO nanoparticles. (B) CuS clusters and NPs serve as catalysts for bisulfide oxidation. Reaction tracked through depletion of dissolved oxygen upon addition of copper ions to excess Na_2S solution. Pink, blue and black curves correspond to addition of 0.1, 1 or 2 mM copper ion. (C) Comparison of catalytic activity of copper ions and CuO nanoparticles at equimolar concentration in sulfide oxidation reactions. (D) Comparison of catalytic ability of CuS precipitate and filtrate after separation by Amicon 3k ultrafilter. The catalytic ability of the clusters and precipitate was compared by monitoring the oxygen consumption in the presence of 2 mM sulfide solution.

2.3.6 Implications for Cu-NP Toxicity

The environmental transformation of a nanomaterial immediately raises questions about the behavior and toxicity of the transformed product(s), which may represent a greater or less risk than the original material. Metal sulfidation is often regarded as a passivation or detoxification process [60, 61] due to the very low equilibrium solubilities and thus metal bioavailabilities of the sulfide phases (Figure 2-1).

We were also surprised, however to observe that CuS NPs and sulfidated CuO-NPs continued to show redox activity in our EPR Fenton assay (Figure 2-10A). These CuS NPs were made by Cu^{2+}/S^{2-} precipitation processes and the excess ions were removed by water washing prior to the ROS assay. Here again soluble species were the source of the redox activity, as evidenced by comparing the particle-induced ROS to that of filtrate, which were similar (Figure 2-10A). Although CuS is highly insoluble, the ROS assay uses H_2O_2 as a reactant, and we hypothesized that the soluble, redox-active species were copper ions produced by peroxide oxidation of CuS. Sulfide can be oxidized, and the conversion to oxidized sulfur species may destabilize copper in the CuS lattice and lead to ion release and solution-based Fenton activity.

To pursue this hypothesis, we studied copper mobilization from CuS NPs and a series of partially sulfidated CuO NPs (Figure 2-10B). Partial sulfidation has almost no effect on the rate of copper release from the CuO NPs undergoing transformation (bisulfide:CuO ratios from 1:5 up to 1:1). It is clear that partial sulfidation does not passivate CuO surfaces, which is consistent with the dissolution-precipitation mechanism that produces distinct secondary particles rather than protective coatings. Only at bisulfide:CuO ratios above 2:1 do we begin to see reductions in soluble copper release.

The model CuS NPs formed from Cu^{2+} and S^{2-} showed very low copper ion release, as expected, but addition of H_2O_2 at the 60 hr time point caused significant release (Figure 2-10B, green circles). In fact, EPR results suggest much more copper ions released from CuS than CuO when both were exposed to H_2O_2 at the same pH. These data provide support for CuS oxidation by H_2O_2 as the source of the redox activity seen in the EPR spectra of Figure 2-10A. The combined results suggest that sulfidation of Cu NPs or CuO NPs can reduce copper metal bioavailability, but only if the sulfidation is extensive and progresses to near stoichiometric completion, and oxidation with re-release of soluble copper may prevent CuS from being a fully nontoxic end state for copper-containing nanomaterials in the environment. Others have reported that nanoscale Cu and Zn sulfides are not fully stable and can transform into other species under aerobic conditions.[80, 81]

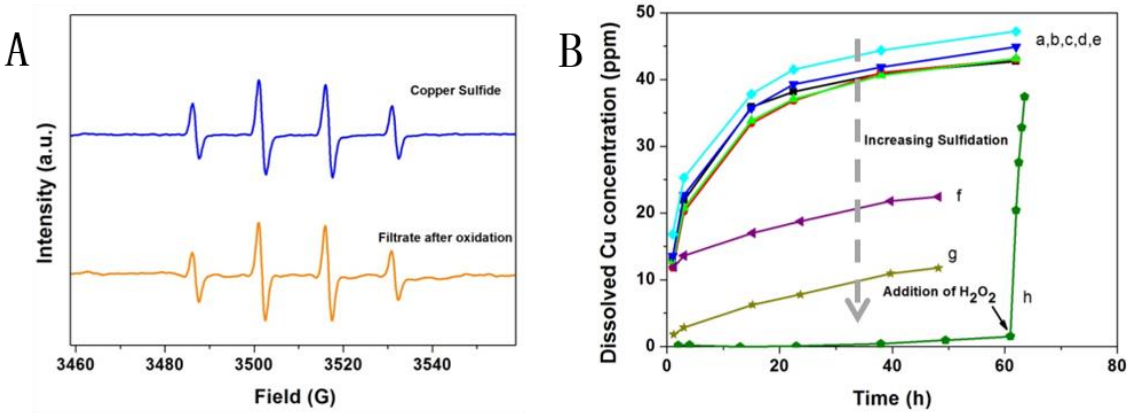

Figure 2-10. Properties of sulfidated CuO NPs and implications for toxicity. (A) Hydroxyl radical EPR signal induced by a 0.1 mM CuS suspension and its particle-free filtrate after hydrogen peroxide treatment. Despite low solubility, CuS shows redox activity associated with soluble species. (B) Dissolution behavior of CuS and a series of partially sulfidated CuO NPs at pH 4 acetate buffer. The sulfidation was carried out using 2.5mM CuO at the initial S/Cu ratios from 0.2 to 5. (a, b, c, d, e represents the dissolution of CuO, sulfidated CuO with S/Cu at 0.1, 0.2,0.5,1, which has little effect on CuO dissolution; f, g represents the dissolution behavior of sulfidated CuO with S/Cu at 2,5 respectively, which can slow the dissolution rate.) The pure CuS solid was prepared through precipitation of Cu^{2+} and bisulfide in stoichiometric mixture followed by washing and resuspension. To understand the redox behavior in (A) the oxidative-dissolution of CuS was investigated by adding H_2O_2 solution in equimolar proportion to CuS.

Finally, we were interested in the biological implications of copper material transformations, and the effects of sulfidation on toxicity in particular. Previous studies showed that copper NPs are internalized by target cells and release soluble ions more rapidly than micron-sized particles at the acidic pH in lysosomes as predicted by the "Trojan-horse mechanism" for metallic nanoparticle toxicity. [33, 82] Here, uptake and toxicity of CuO and CuS NPs were assessed using a murine macrophage cell line in cell culture in comparison with carbon black NPs as a nontoxic particle control. Following exposure to test and control particles for 3 hours, well-dispersed particles were visualized in the cytoplasm of target cells (Figure 2-11A). Cell viability was assessed after 24 hours using a combination of brightfield (Figure 2-11B) and fluorescence (Figure 2-11C) microscopy. Only CuO NPs induced cell death and detachment after 24 hours. Intracellular mobilization of Cu ions induces redox cycling resulting in generation of ROS, induction of oxidative stress, and cell death.[83] Delivery of CuO or CuS NPs, triggered generation of higher levels of H_2O_2 in murine macrophages after 20 min compared to untreated cells or cells exposed to carbon black NPs. (Figure 2-12A). Over the same range of doses, CuO NPs induced significantly higher toxicity than CuS NPs after 48 hours (Figure 2-12B), consistent with the lower Cu bioavailability in CuS.

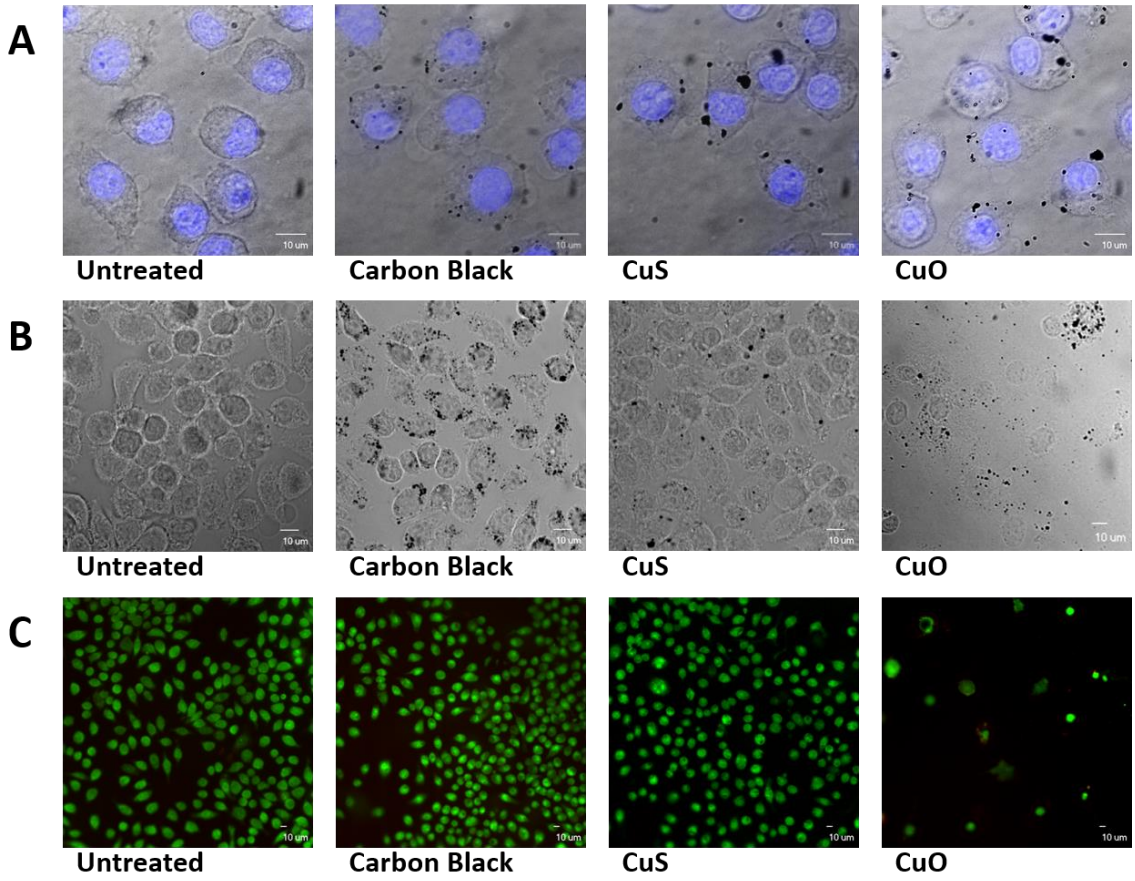

Figure 2-11. Target cell uptake and toxicity of carbon black, CuS, and CuO NPs. (A) Confocal images of murine macrophages after exposure to 5 ppm of test particles for 3 hours; nuclei were visualized (blue fluorescence) using 4'6-diamidino-2-phenylindole (DAPI). (B) Brightfield microscopic images of murine macrophages 24 hours after exposure to 5 ppm of test nanoparticles. (C) Viability of target cells 24 hours after exposure to 5 ppm of test nanoparticles. Viable cells show green cytoplasmic fluorescence (Syto 10/ethidium homodimer assay).

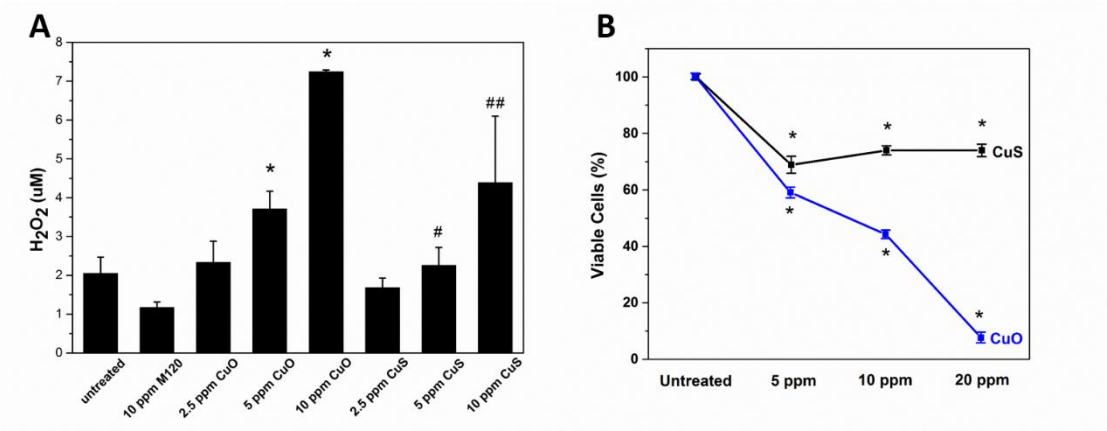

Figure 2-12. ROS generation and viability of cells when exposed to copper based nanomaterials. (A) Generation of H_2O_2 by murine macrophages exposed to carbon black, CuO and CuS NPs. Detection of H_2O_2 production in macrophages exposed to 2.5 ppm, 5 ppm, or 10 ppm of CuO, CuS or M120 (carbon black) as determined using the Amplex Red assay 20 minutes after exposure. Cells exposed to higher concentrations of CuO demonstrate significantly increased generation of H_2O_2 compared to untreated controls or CuS-exposed cells. *p <0.05 compared to control; #p <0.05 compared to 5 ppm CuO; ##p <0.05 compared to 10 ppm CuO. (B) Viability of murine macrophages after exposure to CuS NPs or CuO NPs for 48 hours. DNA content relative to untreated control cells was determined using Pico Green fluorescence as a surrogate for cell number. Differences in viability of cells exposed to each dose of CuS or CuO NPs relative to untreated controls was statistically significant after 48 hours. *p <0.05 compared to control.

2.4 Conclusions

Copper-containing nanomaterials are a particularly complex case for EHS studies, since they undergo oxidation, dissolution, sulfidation, and further oxidation of the sulfide phases over the time scales relevant for human health and environmental impacts. Figure 2-13 summarizes the main transformation and redox pathways observed for CuO NPs in this study. CuO NPs or oxide films on metallic Cu-NPs dissolve at low pH, or at neutral pH in the presence of ligands in biological environments, including those containing amine functional groups. The redox activity in copper NP systems appears to be associated with the soluble fraction and is mitigated but not eliminated by ligand binding in solution. CuO NPs undergo sulfidation through a dissolution/precipitation mechanism to produce

complex secondary aggregates of CuS NPs. These CuS NPs are active catalysts for bisulfide oxidation. Sulfidation reduces Cu solubility, redox activity, and cytotoxicity but may not necessarily fully and permanently detoxify copper, since CuS can be oxidized in environments containing H_2O_2 to produce free copper that continues to cycle in solution producing hydroxyl radicals through Fenton-like chemistry. The results are directly relevant for CuO NPs, and may also be qualitatively relevant for elemental nano-copper whose surfaces consist of oxide phases following environmental exposure.

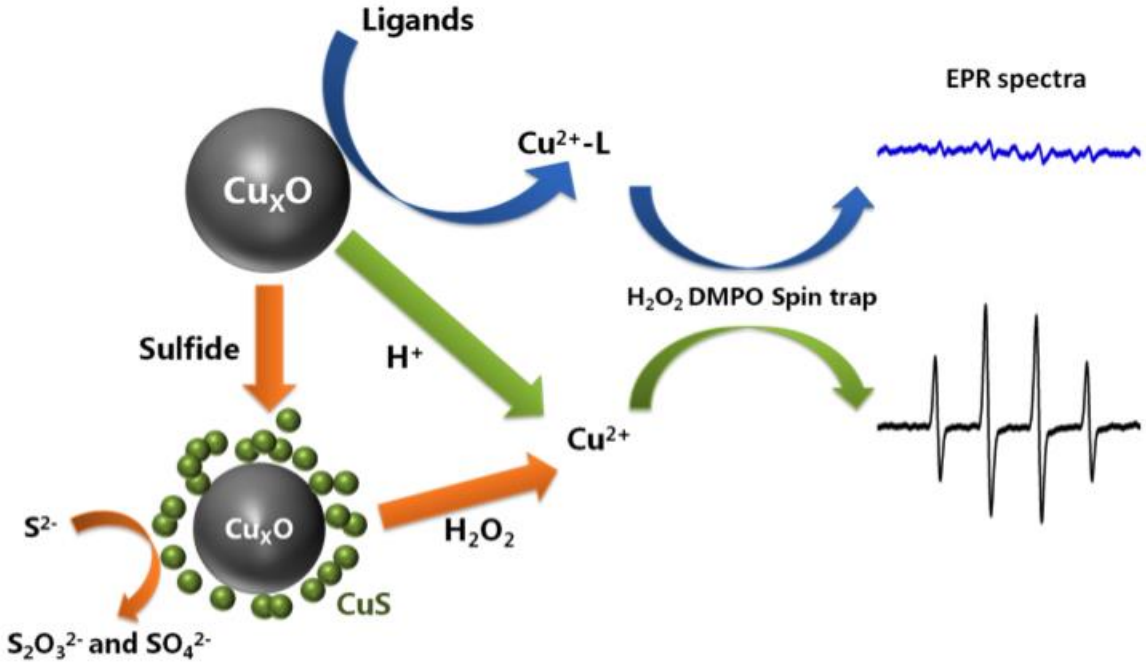

Figure 2-13. Summary of chemical transformations and redox behaviors of Cu-based NPs in biological and environmental media.

2.5 Reference

1. Evans, P.; Matsunaga, H.; Kiguchi, M. Large-scale application of nanotechnology for wood protection. *Nat Nano* **2008**, 3, 577-577.
2. Wu, Y.; Wadia, C.; Ma, W.; Sadtler, B.; Alivisatos, A. P. Synthesis and Photovoltaic Application of Copper(I) Sulfide Nanocrystals. *Nano Lett.* **2008**, 8, 2551-2555.
3. Youngil, L.; Jun-rak, C.; Kwi Jong, L.; Nathan, E. S.; Donghoon, K. Large-scale synthesis of copper nanoparticles by chemically controlled reduction for applications of inkjet-printed electronics. *Nanotechnology* **2008**, 19, 415604.
4. Ren, G.; Hu, D.; Cheng, E. W. C.; Vargas-Reus, M. A.; Reip, P.; Allaker, R. P. Characterisation of copper oxide nanoparticles for antimicrobial applications. *International Journal of Antimicrobial Agents* **2009**, 33, 587-590.
5. PandeyA; BrovelliS; ViswanathaR; LiL; Pietryga, J. M.; Klimov, V. I.; Crooker, S. A. Long-lived photoinduced magnetization in copper-doped ZnSe-CdSe core-shell nanocrystals. *Nat Nano* **2012**, 7, 792-797.
6. Maithreepala, R. A.; Doong, R.-a. Reductive Dechlorination of Carbon Tetrachloride in Aqueous Solutions Containing Ferrous and Copper Ions. *Environ. Sci. Technol.* **2004**, 38, 6676-6684.
7. Doong, R.-a.; Chang, S.-m.; Tsai, C.-w. Enhanced photoactivity of Cu-deposited titanate nanotubes for removal of bisphenol A. *Applied Catalysis B: Environmental* **2013**, 129, 48-55.
8. Huang, H.-L.; Wang, H. P.; Wei, G.-T.; Sun, I. W.; Huang, J.-F.; Yang, Y. W. Extraction of Nanosize Copper Pollutants with an Ionic Liquid. *Environ. Sci. Technol.* **2006**, 40, 4761-4764.
9. Zhang, H.; Ji, Z.; Xia, T.; Meng, H.; Low-Kam, C.; Liu, R.; Pokhrel, S.; Lin, S.; Wang, X.; Liao, Y.-P.; Wang, M.; Li, L.; Rallo, R.; Damoiseaux, R.; Telesca, D.; Mädler, L.; Cohen, Y.; Zink, J. I.; Nel, A. E. Use of Metal Oxide Nanoparticle Band Gap To Develop a Predictive Paradigm for Oxidative Stress and Acute Pulmonary Inflammation. *ACS Nano* **2012**, 6, 4349-4368.

10. Mudunkotuwa, I. A.; Pettibone, J. M.; Grassian, V. H. Environmental Implications of Nanoparticle Aging in the Processing and Fate of Copper-Based Nanomaterials. *Environ. Sci. Technol.* **2012**, 46, 7001-7010.
11. Li, Y.; Zhang, W.; Niu, J.; Chen, Y. Mechanism of Photogenerated Reactive Oxygen Species and Correlation with the Antibacterial Properties of Engineered Metal-Oxide Nanoparticles. *ACS Nano* **2012**, 6, 5164-5173.
12. Applerot, G.; Lellouche, J.; Lipovsky, A.; Nitzan, Y.; Lubart, R.; Gedanken, A.; Banin, E. Understanding the Antibacterial Mechanism of CuO Nanoparticles: Revealing the Route of Induced Oxidative Stress. *Small* **2012**, 8, 3326-3337.
13. Gunawan, C.; Teoh, W. Y.; Marquis, C. P.; Amal, R. Cytotoxic Origin of Copper(II) Oxide Nanoparticles: Comparative Studies with Micron-Sized Particles, Leachate, and Metal Salts. *ACS Nano* **2011**, 5, 7214-7225.
14. Studer, A. M.; Limbach, L. K.; Van Duc, L.; Krumeich, F.; Athanassiou, E. K.; Gerber, L. C.; Moch, H.; Stark, W. J. Nanoparticle cytotoxicity depends on intracellular solubility: comparison of stabilized copper metal and degradable copper oxide nanoparticles. *Toxicology letters* **2010**, 197, 169-174.
15. Karlsson, H. L.; Cronholm, P.; Gustafsson, J.; Moller, L. Copper oxide nanoparticles are highly toxic: A comparison between metal oxide nanoparticles and carbon nanotubes. *Chem. Res. Toxicol.* **2008**, 21, 1726-1732.
16. Ahamed, M.; Siddiqui, M. A.; Akhtar, M. J.; Ahmad, I.; Pant, A. B.; Alhadlaq, H. A. Genotoxic potential of copper oxide nanoparticles in human lung epithelial cells. *Biochem. Biophys. Res. Commun.* **2010**, 396, 578-583.
17. Fahmy, B.; Cormier, S. A. Copper oxide nanoparticles induce oxidative stress and cytotoxicity in airway epithelial cells. *Toxicology In Vitro* **2009**, 23, 1365-1371.
18. Jo, H. J.; Choi, J. W.; Lee, S. H.; Hong, S. W. Acute toxicity of Ag and CuO nanoparticle suspensions against Daphnia magna: The importance of their dissolved fraction varying with preparation methods. *J. Hazard. Mater.* **2012**, 227–228, 301-308.
19. Lowry, G. V.; Gregory, K. B.; Apte, S. C.; Lead, J. R. Transformations of Nanomaterials in the Environment. *Environ. Sci. Technol.* **2012**, 46, 6893-6899.

20. Borm, P.; Klaessig, F. C.; Landry, T. D.; Moudgil, B.; Pauluhn, J.; Thomas, K.; Trottier, R.; Wood, S. Research Strategies for Safety Evaluation of Nanomaterials, Part V: Role of Dissolution in Biological Fate and Effects of Nanoscale Particles. *Toxicol. Sci.* **2006**, 90, 23-32.

21. Reidy, B.; Haase, A.; Luch, A.; Dawson, K.; Lynch, I. Mechanisms of Silver Nanoparticle Release, Transformation and Toxicity: A Critical Review of Current Knowledge and Recommendations for Future Studies and Applications. *Materials* **2013**, 6, 2295-2350.

22. Liu, J.; Wang, Z.; Liu, F. D.; Kane, A. B.; Hurt, R. H. Chemical Transformations of Nanosilver in Biological Environments. *ACS Nano* **2012**, 6, 9887-9899.

23. Levard, C.; Hotze, E. M.; Lowry, G. V.; Brown, G. E. Environmental Transformations of Silver Nanoparticles: Impact on Stability and Toxicity. *Environ. Sci. Technol.* **2012**, 46, 6900-6914.

24. Lowry, G. V.; Espinasse, B. P.; Badireddy, A. R.; Richardson, C. J.; Reinsch, B. C.; Bryant, L. D.; Bone, A. J.; Deonarine, A.; Chae, S.; Therezien, M.; Colman, B. P.; Hsu-Kim, H.; Bernhardt, E. S.; Matson, C. W.; Wiesner, M. R. Long-Term Transformation and Fate of Manufactured Ag Nanoparticles in a Simulated Large Scale Freshwater Emergent Wetland. *Environmental Science & Technology* **2012**, 46, 7027-7036.

25. Kent, R. D.; Vikesland, P. J. Controlled Evaluation of Silver Nanoparticle Dissolution Using Atomic Force Microscopy. *Environ. Sci. Technol.* **2011**, 46, 6977-6984.

26. Kennedy, A. J.; Hull, M. S.; Bednar, A. J.; Goss, J. D.; Gunter, J. C.; Bouldin, J. L.; Vikesland, P. J.; Steevens, J. A. Fractionating Nanosilver: Importance for Determining Toxicity to Aquatic Test Organisms. *Environ. Sci. Technol.* **2010**, 44, 9571-9577.

27. Stebounova, L.; Guio, E.; Grassian, V. Silver nanoparticles in simulated biological media: a study of aggregation, sedimentation, and dissolution. *J Nanopart Res* **2011**, 13, 233-244.

28. Sotiriou, G. A.; Pratsinis, S. E. Antibacterial Activity of Nanosilver Ions and Particles. *Environ. Sci. Technol.* **2010**, 44, 5649-5654.

29. Lorenz, C.; Windler, L.; von Goetz, N.; Lehmann, R. P.; Schuppler, M.; Hungerbühler, K.; Heuberger, M.; Nowack, B. Characterization of silver release from commercially available functional (nano)textiles. *Chemosphere* **2012**, 89, 817-824.

30. Xia, T.; Zhao, Y.; Sager, T.; George, S.; Pokhrel, S.; Li, N.; Schoenfeld, D.; Meng, H.; Lin, S.; Wang, X.; Wang, M.; Ji, Z.; Zink, J. I.; Mädler, L.; Castranova, V.; Lin, S.; Nel, A. E. Decreased Dissolution of ZnO by Iron Doping Yields Nanoparticles with Reduced Toxicity in the Rodent Lung and Zebrafish Embryos. *ACS Nano* **2011**, 5, 1223-1235.

31. Franklin, N. M.; Rogers, N. J.; Apte, S. C.; Batley, G. E.; Gadd, G. E.; Casey, P. S. Comparative Toxicity of Nanoparticulate ZnO, Bulk ZnO, and ZnCl2 to a Freshwater Microalga (Pseudokirchneriella subcapitata): The Importance of Particle Solubility. *Environ. Sci. Technol.* **2007**, 41, 8484-8490.

32. Ma, R.; Levard, C.; Michel, F. M.; Brown, G. E.; Lowry, G. V. Sulfidation Mechanism for Zinc Oxide Nanoparticles and the Effect of Sulfidation on Their Solubility. *Environ. Sci. Technol.* **2013**, 47, 2527-2534.

33. Midander, K.; Cronholm, P.; Karlsson, H. L.; Elihn, K.; Möller, L.; Leygraf, C.; Wallinder, I. O. Surface Characteristics, Copper Release, and Toxicity of Nano- and Micrometer-Sized Copper and Copper(II) Oxide Particles: A Cross-Disciplinary Study. *Small* **2009**, 5, 389-399.

34. Pettibone, J. M.; Adamcakova-Dodd, A.; Thorne, P. S.; O'Shaughnessy, P. T.; Weydert, J. A.; Grassian, V. H. Inflammatory response of mice following inhalation exposure to iron and copper nanoparticles. *Nanotoxicology* **2008**, 2, 189-204.

35. Sotiriou, G. A.; Meyer, A.; Knijnenburg, J. T. N.; Panke, S.; Pratsinis, S. E. Quantifying the Origin of Released Ag+ Ions from Nanosilver. *Langmuir* **2012**, 28, 15929-15936.

36. Yamamoto, K.; Kawanishi, S. Hydroxyl free radical is not the main active species in site-specific DNA damage induced by copper (II) ion and hydrogen peroxide. *Journal of Biological Chemistry* **1989**, 264, 15435-40.

37. Drouin, R.; Rodriguez, H.; Gao, S.-W.; Gebreyes, Z.; O'Connor, T. R.; Holmquist, G. P.; Akman, S. A. Cupric ion/ascorbate/hydrogen peroxide-induced DNA

damage: DNA-bound copper ion primarily induces base modifications. *Free Radical Biol. Med.* **1996**, 21, 261-273.

38. Erickson, R. J.; Benoit, D. A.; Mattson, V. R.; Leonard, E. N.; Nelson, H. P. The effects of water chemistry on the toxicity of copper to fathead minnows. *Environ. Toxicol. Chem.* **1996**, 15, 181-193.
39. Cabot, A.; Smith, R. K.; Yin, Y.; Zheng, H.; Reinhard, B. r. M.; Liu, H.; Alivisatos, A. P. Sulfidation of Cadmium at the Nanoscale. *ACS Nano* **2008**, 2, 1452-1458.
40. Levard, C.; Reinsch, B. C.; Michel, F. M.; Oumahi, C.; Lowry, G. V.; Brown, G. E. Sulfidation Processes of PVP-Coated Silver Nanoparticles in Aqueous Solution: Impact on Dissolution Rate. *Environmental Science & Technology* **2011**, 45, 5260-5266.
41. Liu, J.; Pennell, K. G.; Hurt, R. H. Kinetics and Mechanisms of Nanosilver Oxysulfidation. *Environmental Science & Technology* **2011**, 45, 7345-7353.
42. Kim, B.; Park, C.-S.; Murayama, M.; Hochella, M. F. Discovery and Characterization of Silver Sulfide Nanoparticles in Final Sewage Sludge Products. *Environ. Sci. Technol.* **2010**, 44, 7509-7514.
43. Wiesner, M. R.; Lowry, G. V.; Casman, E.; Bertsch, P. M.; Matson, C. W.; Di Giulio, R. T.; Liu, J.; Hochella, M. F. Meditations on the Ubiquity and Mutability of Nano-Sized Materials in the Environment. *ACS Nano* **2011**, 5, 8466-8470.
44. Zhu, H.; Wang, J.; Wu, D. Fast Synthesis, Formation Mechanism, and Control of Shell Thickness of CuS Hollow Spheres. *Inorg. Chem.* **2009**, 48, 7099-7104.
45. Jiao, S.; Xu, L.; Jiang, K.; Xu, D. Well-Defined Non-spherical Copper Sulfide Mesocages with Single-Crystalline Shells by Shape-Controlled Cu2O Crystal Templating. *Adv. Mater. (Weinheim, Ger.)* **2006**, 18, 1174-1177.
46. Liu, J.; Sonshine, D. A.; Shervani, S.; Hurt, R. H. Controlled Release of Biologically Active Silver from Nanosilver Surfaces. *ACS Nano* **2010**, 4, 6903-6913.
47. Reinsch, B. C.; Levard, C.; Li, Z.; Ma, R.; Wise, A.; Gregory, K. B.; Brown, G. E.; Lowry, G. V. Sulfidation of Silver Nanoparticles Decreases Escherichia coli Growth Inhibition. *Environ. Sci. Technol.* **2012**, 46, 6992-7000.

48. Li, M.; Zhu, L.; Lin, D. Toxicity of ZnO Nanoparticles to Escherichia coli: Mechanism and the Influence of Medium Components. *Environ. Sci. Technol.* **2011**, 45, 1977-1983.

49. Liu, J.; Hurt, R. H. Ion Release Kinetics and Particle Persistence in Aqueous Nano-Silver Colloids. *Environmental Science and Technology* **2010**, 44, 2169-2175.

50. VanWinkle, B. A.; de Mesy Bentley, K. L.; Malecki, J. M.; Gunter, K. K.; Evans, I. M.; Elder, A.; Finkelstein, J. N.; Oberdörster, G.; Gunter, T. E. Nanoparticle (NP) uptake by type I alveolar epithelial cells and their oxidant stress response. *Nanotoxicology* **2009**, 3, 307-318.

51. Gustafsson, J. P. Visual MINTEQ version 3.0 http://vminteq.lwr.kth.se/ Stockholm, Sweden. **2013**.

52. MacCuspie, R. Colloidal stability of silver nanoparticles in biologically relevant conditions. *J Nanopart Res* **2011**, 13, 2893-2908.

53. Akaighe, N.; MacCuspie, R. I.; Navarro, D. A.; Aga, D. S.; Banerjee, S.; Sohn, M.; Sharma, V. K. Humic Acid-Induced Silver Nanoparticle Formation Under Environmentally Relevant Conditions. *Environ. Sci. Technol.* **2011**, 45, 3895-3901.

54. Pietruska, J. R.; Liu, X.; Smith, A.; McNeil, K.; Weston, P.; Zhitkovich, A.; Hurt, R.; Kane, A. B. Bioavailability, Intracellular Mobilization of Nickel, and HIF-1α Activation in Human Lung Epithelial Cells Exposed to Metallic Nickel and Nickel Oxide Nanoparticles. *Toxicol. Sci.* **2011**, 124, 138-148.

55. Yang, X.; Gondikas, A. P.; Marinakos, S. M.; Auffan, M.; Liu, J.; Hsu-Kim, H.; Meyer, J. N. Mechanism of Silver Nanoparticle Toxicity Is Dependent on Dissolved Silver and Surface Coating in Caenorhabditis elegans. *Environ. Sci. Technol.* **2011**, 46, 1119-1127.

56. Li, X.; Lenhart, J. J.; Walker, H. W. Dissolution-Accompanied Aggregation Kinetics of Silver Nanoparticles. *Langmuir* **2010**, 26, 16690-16698.

57. Ho, C.-M.; Wong, C.-K.; Yau, S. K.-W.; Lok, C.-N.; Che, C.-M. Oxidative Dissolution of Silver Nanoparticles by Dioxygen: A Kinetic and Mechanistic Study. *Chemistry – An Asian Journal* **2011**, 6, 2506-2511.

58. Ho, C.-M.; Yau, S. K.-W.; Lok, C.-N.; So, M.-H.; Che, C.-M. Oxidative Dissolution of Silver Nanoparticles by Biologically Relevant Oxidants: A Kinetic and Mechanistic Study. *Chemistry – An Asian Journal* **2010**, 5, 285-293.

59. Hirsch, M. P. Toxicity of silver sulfide-spiked sediments to the freshwater amphipod (Hyalella azteca). *Environmental Toxicology and Chemistry* **1998**, 17, 601-604.

60. Besser, J. M.; Ingersoll, C. G.; Giesty, J. P. Effects of spatial and temporal variation of acid-volatile sulfide on the bioavailability of copper and zinc in freshwater sediments. *Environ. Toxicol. Chem.* **1996**, 15, 286-293.

61. Di Toro, D. M.; Mahony, J. D.; Hansen, D. J.; Scott, K. J.; Hicks, M. B.; Mayr, S. M.; Redmond, M. S. Toxicity of cadmium in sediments: The role of acid volatile sulfide. *Environ. Toxicol. Chem.* **1990**, 9, 1487-1502.

62. Bozym, R. A.; Chimienti, F.; Giblin, L. J.; Gross, G. W.; Korichneva, I.; Li, Y.; Libert, S.; Maret, W.; Parviz, M.; Frederickson, C. J.; Thompson, R. B. Free zinc ions outside a narrow concentration range are toxic to a variety of cells in vitro. *Experimental Biology and Medicine* **2010**, 235, 741-750.

63. Zhang, L.; Yu, J. C.; Yip, H. Y.; Li, Q.; Kwong, K. W.; Xu, A.-W.; Wong, P. K. Ambient Light Reduction Strategy to Synthesize Silver Nanoparticles and Silver-Coated TiO2 with Enhanced Photocatalytic and Bactericidal Activities. *Langmuir* **2003**, 19, 10372-10380.

64. Macomber, L.; Imlay, J. A. The iron-sulfur clusters of dehydratases are primary intracellular targets of copper toxicity. *Proceedings of the National Academy of Sciences* **2009**.

65. Chaturvedi, K. S.; Hung, C. S.; Crowley, J. R.; Stapleton, A. E.; Henderson, J. P. The siderophore yersiniabactin binds copper to protect pathogens during infection. *Nat. Chem. Biol.* **2012**, 8, 731-736.

66. Doğan, A.; Köseoğlu, F.; Kılıç, E. The Stability Constants of Copper(II) Complexes with Some α-Amino Acids in Dioxan–Water Mixtures. *Anal. Biochem.* **2001**, 295, 237-239.

67. Deschamps, P.; Zerrouk, N.; Nicolis, I.; Martens, T.; Curis, E.; Charlot, M. F.; Girerd, J. J.; Prangé, T.; Bénazeth, S.; Chaumeil, J. C.; Tomas, A. Copper(II)–l-

glutamine complexation study in solid state and in aqueous solution. *Inorg. Chim. Acta* **2003**, 353, 22-34.

68. Szecsody, J. E.; Zachara, J. M.; Bruckhart, P. L. Adsorption-Dissolution Reactions Affecting the Distribution and Stability of CoIIEDTA in Iron Oxide-Coated Sand. *Environ. Sci. Technol.* **1994**, 28, 1706-1716.
69. Joshi, S.; Ghosh, I.; Pokhrel, S.; Mädler, L.; Nau, W. M. Interactions of Amino Acids and Polypeptides with Metal Oxide Nanoparticles Probed by Fluorescent Indicator Adsorption and Displacement. *ACS Nano* **2012**, 6, 5668-5679.
70. Oikawa, S.; Kawanishi, S. Site-Specific DNA Damage Induced by NADH in the Presence of Copper(II): Role of Active Oxygen Species†. *Biochemistry* **1996**, 35, 4584-4590.
71. Folk, D. S.; Franz, K. J. A Prochelator Activated by β-Secretase Inhibits Aβ Aggregation and Suppresses Copper-Induced Reactive Oxygen Species Formation. *J. Am. Chem. Soc.* **2010**, 132, 4994-4995.
72. Mira, L.; Tereza Fernandez, M.; Santos, M.; Rocha, R.; Helena Florêncio, M.; Jennings, K. R. Interactions of Flavonoids with Iron and Copper Ions: A Mechanism for their Antioxidant Activity. *Free Radical Res.* **2002**, 36, 1199-1208.
73. Besser, J. M.; Brumbaugh, W. G.; Ingersoll, C. G.; Ivey, C. D.; Kunz, J. L.; Kemble, N. E.; Schlekat, C. E.; Garman, E. R. Chronic toxicity of nickel-spiked freshwater sediments: Variation in toxicity among eight invertebrate taxa and eight sediments. *Environ. Toxicol. Chem.* **2013**, n/a-n/a.
74. Chakrabarti, D.; Laughlin, D. The Cu-S (copper-sulfur) system. *Bulletin of Alloy Phase Diagrams* **1983**, 4, 254-271.
75. Luther, G. W.; Theberge, S. M.; Rozan, T. F.; Rickard, D.; Rowlands, C. C.; Oldroyd, A. Aqueous Copper Sulfide Clusters as Intermediates during Copper Sulfide Formation. *Environ. Sci. Technol.* **2002**, 36, 394-402.
76. Gautam, U.; Mukherjee, B. A simple synthesis and characterization of CuS nanocrystals. *Bull. Mater. Sci.* **2006**, 29, 1-5.
77. Hoffmann, M. R.; Lim, B. C. Kinetics and mechanism of the oxidation of sulfide by oxygen: catalysis by homogeneous metal-phthalocyanine complexes. *Environ. Sci. Technol.* **1979**, 13, 1406-1414.

78. Hollmark, H. M.; Vegelius, J. R.; Kristiansen, P.; Werme, L.; Duda, L.-C. Exposure of Oxidized Copper Surfaces to Aqueous Na2S Solution Studied with Soft X-Ray Spectroscopy. *J. Electrochem. Soc.* **2011**, 158, C1-C5.

79. Raevskaya, A. E.; Stroyuk, A. L.; Kuchmii, S. Y.; Kryukov, A. I. Catalytic activity of CuS nanoparticles in hydrosulfide ions air oxidation. *Journal of Molecular Catalysis A: Chemical* **2004**, 212, 259-265.

80. Donner, E.; Howard, D. L.; Jonge, M. D. d.; Paterson, D.; Cheah, M. H.; Naidu, R.; Lombi, E. X-ray absorption and micro X-ray fluorescence spectroscopy investigation of copper and zinc speciation in biosolids. *Environ. Sci. Technol.* **2011**, 45, 7249-7257.

81. Lombi, E.; Donner, E.; Tavakkoli, E.; Turney, T. W.; Naidu, R.; Miller, B. W.; Scheckel, K. G. Fate of Zinc Oxide Nanoparticles during Anaerobic Digestion of Wastewater and Post-Treatment Processing of Sewage Sludge. *Environ. Sci. Technol.* **2012**, 46, 9089-9096.

82. Limbach, L. K.; Wick, P.; Manser, P.; Grass, R. N.; Bruinink, A.; Stark, W. J. Exposure of Engineered Nanoparticles to Human Lung Epithelial Cells: Influence of Chemical Composition and Catalytic Activity on Oxidative Stress. *Environ. Sci. Technol.* **2007**, 41, 4158-4163.

83. Jomova, K.; Valko, M. Advances in metal-induced oxidative stress and human disease. *Toxicology* **2011**, 283, 65-87.

Chapter 3 Aerosol synthesis and applications of 3D Nanoparticle-loaded crumpled graphene nanoreactor

3.1 Introduction

The atomically thin, conformable, and impermeable nature of graphene suggests its use as an outer shell in nano- or micro-encapsulation technologies. Graphene coatings have been explored as protective barriers or selectively permeable films on 2D substrates,[1-4] and they have also been proposed as 3D encapsulants for the immobilization or environmental protection of microscale or nanoscale materials or devices.[5-14] Recently, aerosol microdroplet drying has been demonstrated as an effective method for encapsulating nanoparticle cargos in conductive,[15] electron-transparent, crumpled multilayer graphene shells.[5-8, 10, 16] This process uses graphene oxide sheets of microscale lateral dimension, which assemble through tiling and stacking into quasi-continuous multilayer shells that crumple during the drying process[8].

These crumpled graphene nanosacks have been reported to be open porous structures, rather than perfectly sealed structures,[2] and this may make them poor barriers for protection of the encapsulated material from surrounding fluid environments. The open porosity of crumpled graphene, however, may enable other applications that do not require such barrier protection. For example, if chemically reactive nanoparticles are encapsulated, the crumpled graphene shell can be regarded as a type of "nanoreactor" that creates an engineered confined nanospace for chemical reactions to occur, and the diffusive transport of small molecules between their interior and exterior should allow the influx of reactants and the out flux of products necessary for reactor function.

In general, a nanoreactor can be defined as a complex material system that has been engineered to host, catalyze, or steer a chemical reaction process occurring in an internal nanoscale cavity. Nanoreactors may host and immobilize chemically active particles, and

may alter chemical reaction pathways through confinement effects on transition states or products, by perturbing molecular transport to and/or from the active surfaces, or through electron transfer or other types of interactions between the active particles and the outer shell structure that builds the nano-cavity. The nanoreactor concept has been explored in other material systems, including silica,[17, 18] reverse micelles[19] and proteins with cage-like structures.[20]

The nanoreactor concept has not been systematically developed for graphene-based structures, but the development can be informed by a significant recent literature on crumpled graphene hybrids. Since the first report of crumpled graphene particles in 2011,[10] there has been intense interest in their hybridization with active nanoparticles to create composite electrodes, sorbents, and catalysts.[6, 21-27] In these applications, the crumpled graphene serves as a conductive additive and/or support whose folded structure prevents graphene sheet restacking and surface area loss. To support further development, it is important to systematically address the fundamental behaviors of chemical reactions occurring in and on these new material architectures, including the effects of graphene on reactant and product transport, active site accessibility through conformal covering and passivation of internal particle surfaces, as well as particle mobility, stability, sintering, and electron transfer interactions.

Here we synthesize graphene nanosacks filled with nanoparticles of ZnO, Ag, Cu, Ni, Fe, Pt, Pd, and TiO_2 either alone or in combination, as models to explore the fundamental behaviors of crumpled graphene nanoreactors. The filled nanoreactor geometry will be seen to give rise to particle-graphene and particle-graphene-particle interactions that lead to novel reaction behaviors, including enhanced particle oxidation

rates, inhibited particle sintering rates, galvanic interactions that affect oxidation and dissolution, and the photochemical control of dissolution and ion release rates. We then use these novel behaviors to demonstrate several example applications of graphene nanoreactors in heterogeneous catalysis, controlled release on antibacterial silver ions, and Fe-mediated reduction of environmental hexavalent chromium.

3.2 Materials and Methods

3.2.1 Synthesis of silver stock solution

Citrate-stabilized Ag nanoparticles with average size of 20 nm were prepared according to a published method[28] with modification. A 190 mL solution containing 2 mM silver nitrate (Fisher) and 6 mM trisodium citrate (Fisher) was prepared with deionized (DI) water and stirred vigorously at room temperature for 15 min, followed by dropwise addition of 10 ml of 0.12 M $NaBH_4$. After 4 hour stirring at room temperature, the silver nanoparticle stock solution was washed with water and concentrated by centrifugal ultrafiltration (Amicon Ultra-15 3k) and stored at 4 ℃ until further use.

3.2.2 Synthesis of GO and nanoparticle-filled graphene nanosacks

Graphene oxide was synthesized by a modified Hummers method and purified to remove the byproducts, following a previously published procedure.[2, 29] The GO sheets with a nominal size of 1-2 um are primarily in monolayer form, with more complete characterization data can be found in previous publications.[5, 8] Various particle-filled graphene nanosacks were prepared by an aerosol method.[8] Briefly, an ultrasonic nebulizer was used to create a suspended mist from an aqueous suspension of GO (0.5mg/ml) and the target nanoparticle cargo, and carried by nitrogen gas flow through a

heated horizontal furnace. The resulting hybrid materials were captured on a PTFE membrane filter (PTU024750, Sterlitech Co.). Most feed suspensions contained nanoparticles (ZnO 1mg/ml commercial NPs from Fisher; Ag: 1mg/ml citrate-stabilized nanoparticles; Ag/TiO_2: 1mg/ml Ag and 0.125mg/ml Evonik P25 grade TiO_2). Cu nanosacks were prepared from Cu(II)-EDTA solution containing 0.5 mg/ml of GO. During the heating process, Cu(II) is reduced to form copper NPs *in situ*. Ag/Cu nanosacks were prepared from a colloid mixture of Ag NPs and Cu(II)-EDTA complex (Ag/Cu mass ratio 2:1) in the presence of 0.5 mg/ml GO. Ag/Ni nanosacks were prepared from a colloid mixture of Ag NPs and Ni NPs from Alfa Aesar (Ag/Ni mass ratio 2:1) in the presence of 0.5 mg/ml GO. In evaluating the effect of Ag/GO ratio on preventing sintering, Ag-rGO nanosacks were prepared from various Ag/GO ratios in the feed suspension. The concentration of Ag and GO is 0.5 mg/ml and 0.5 mg/ml (1:1), 2 mg/ml and 0.5 mg/ml (4:1), 5 mg/ml and 0.5 mg/ml (10:1), 2 mg/ml and 0.05 mg/ml (40:1), respectively.

3.2.3 Electrochemical testing

Electrochemical tests were performed in a CO_2 saturated 0.1M $KHCO_3$ aqueous solution using a conventional H-type two compartment cell separated by a Nafion membrane. The counter electrode was a platinum gauze, and the reference electrode was Ag/AgCl. To prepare the working electrode, Cu/Graphene composite was dispersed in ethanol and drop casted on a carbon paper electrode with a mass density of $2mg/cm^2$.

3.2.4 Preparation of Fe (0) nanosacks and Cr (VI) removal

Fe_3O_4-GO nanosacks were synthesized according to the previous work: 10 mg Fe_3O_4 NPs were mixed with 2mL GO suspension, and then this mixture was diluted to 10 mL. After stirring, ultrasonic were placed to facilitate well dispersion of Fe_3O_4 NPs. Finally, the mixture transferred to the reactor and ultrasonically nebulized into aerosol micro-droplets (feed rate 5 mL/h). Nitrogen gas (0.7 L/min) was purged into the reactor carrying the droplets to pass through a 600 ^oC bench-top electric tube furnace. Synthesized Fe_3O_4-GO nanosacks were collected on the end of the tube by PTFE membrane filter, and these black powders were rinsed by pure alcohol for several times before dried in the oven under 40 ^oC overnight. Empty GO nanosacks were synthesized in the same way from GO suspension. Reduced Fe_3O_4-GO nanosacks (Fe^0-rGO nanosacks) and empty rGO nanosacks were made by reduction of Fe_3O_4-GO nanosacks at 700 ^oC under forming gas (H_2/N_2) for 2 hrs. Bare Fe_3O_4 NPs without GO wrapping were reduced under the same condition to obtain Fe^0 particles for comparison.

Chromium (VI) was chosen as the target pollutant to investigate reactivity of Fe^0-rGO nanosacks and Fe^0 particles made from hydrogen reduction. 2 mg of each synthesized powder (0.2 mg empty GO nanosacks) was added in centrifuge tube, which containing 10 mL potassium dichromate solution (initial concentration of 20 mg/L, pH at 5.0), and the tube was placed on a rotator (60 rpm). Aliquots of the samples were taken at certain time intervals within 2 hrs, and analyzed after being filtered through a 0.22 μm membrane filter. Cr(VI) concentration was determined at 540 nm using a UV-Vis spectrophotometer by the diphenylcarbazine method.

3.2.5 Dissolution Experiments

ZnO nanosacks or agglomerates were incubated in 10 mM $NaNO_3$ solution. After incubating for a predefined time period, the filtrates were separated from the solids using centrifugal ultrafiltration (Amicon ultra-4 3k) for 30 min at 4000 rpm, and were diluted for measurements of zinc by inductively coupled plasma atomic emission spectroscopy (ICP-AES). Silver-based nanosack oxidative dissolution was measured similarly but UV irradiation was involved in fraction of the Ag/TiO_2 samples, and Ag or Cu (in Ag/Cu samples) was measured by graphite furnace atomic absorption spectrometry (Perkin Elmer 4100ZL, GFAAs). All ion release experiments were conducted at room temperature (20℃).

3.2.6 Product Characterization

The morphology and size of nanoparticles or NP-filled nanosacks were determined by transmission electron microscopy (TEM) on a Philips CM20 at 200 kV and scanning electron microscope (SEM) using a LEO 1530 field-emission SEM. The samples were prepared by placing one drop of purified sample solution on carbon-coated copper grids or silicon wafer, followed by drying at room temperature overnight. UV–Vis spectra of 4-nitrophenol sample was recorded on a Jasco V-630 spectrophotometer over the range 300 to 500 nm. The compositions and phases of samples were identified by X-ray diffraction spectrometry (XRD) on a Bruker AXS D8 Advance instrument with Cu Kα radiation (λ = 1.5418 Å). The XRD samples were prepared by adding purified and concentrated suspension onto a glass slide, followed by overnight drying.

3.3 Results

3.3.1 Nanoreactor synthesis and morphology

Figure 3-1 shows example morphologies of particle-filled graphene nanosacks synthesized by the in-flight drying of suspended microdroplets. The aerosol process can be carried out with pre-fabricated nanoparticles in the feed suspension (Fig. 3-1A,B) as reported previously,[7, 8, 25, 30] or using dissolved salt or molecular precursors that form nanoparticles during the encapsulation process or subsequent annealing.[6] High quality encapsulation requires that the second component be dissolved or stably co-suspended with GO to form a homogeneous two-component feed suspension that segregates into the cargo-sack (core-shell) structure during drying.[5] In the case of particle cargos this homogeneous feed suspension often can be created by tuning the pH so it lies either above or below the isoelectric point of both the GO and particles, giving rise to a repulsive regime where both colloidal materials (particles and GO) have the same surface charge sign and experience electrostatic repulsion in co-suspension.[5] When using salt precursors, the challenge is different - to prevent GO aggregation caused by cation screening of the negative charge on GO, or by GO-cation-GO bridging. Cation-GO binding can cause colloidal instability, but also lead to heterogeneous nucleation of particles on random positions on both sides of the GO sheets, which grow into particles located on both the inside and outside surfaces of the sacks, rather than perfect encapsulation.[6] For this study we developed a technique to avoid these problems with salt precursors using a chelating agent to avoid cation-GO binding. Figure 1C, D shows Cu-filled graphene nanosacks synthesized using $CuCl_2$/EDTA solutions with suspended GO. The addition of EDTA converts the Cu^{2+} to a complex anion with a large stability constant (K_s for Cu-EDTA of

$6.3*10^{18}$)[31] that prevents Cu^{2+}-GO association and also introduces a reducing agent for formation of copper nanoparticles[32, 33]. Figure 3-1C and D show the morphology of nanosacks containing zero-valent copper NPs confirmed by XRD (see below), which are successfully encapsulated in graphene with no particles visible on the external surfaces or outside the sack. It is interesting that the Cu-filled nanoreactor structures (Fig. 3-1C, D) have smoother and more regular surfaces than those made from pre-fabricated Ag particles (Fig. 3-1A, B). We believe this difference is due to an internal framework from the high Cu particle loadings that limits collapse and crumpling of the graphene, and to gas evolution associated with pyrolytic decomposition of EDTA, which can expand the sack and partially reverse the capillary crumpling that occurs during drying. This chelation method can likely be applied to other salt precursors to allow a range of divalent or trivalent metals at higher concentrations to be used for *in situ* encapsulation. The nanoreactor studies in this paper use filled nanosacks prepared by both methods: particle wrapping, and *in situ* reduction of chelated metal cations, as appropriate.

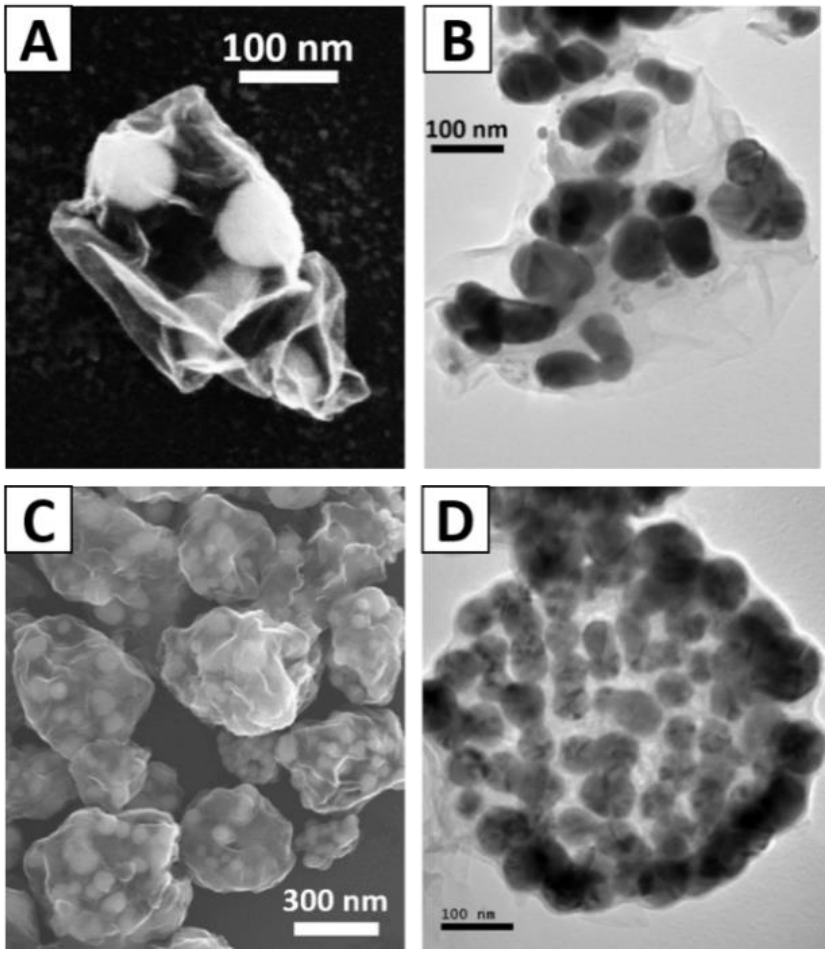

Figure 3-1. Example morphologies of graphene nanoreactors filled with metallic nanoparticles. (A, B) Ag-filled rGO nanoreactors with a crumpled shell structure fabricated by encapsulation of pre-synthesized Ag-nanoparticles; (C,D) Cu-filled rGO nanoreactors with balloon-like morphology fabricated using a Cu/EDTA complex as a precursor for in situ formation of Cu-nanoparticles during the aerosol wrapping process. (A, C are SEM images; B, D TEM images). It is interesting that the Cu-filled nanoreactor structures (C,D) have smoother and more regular surfaces than those made from pre-fabricated Ag particles (A,B). We believe this difference is due to an internal framework from the high Cu particle loadings that limits collapse and crumpling of the graphene, and to gas evolution associated with pyrolytic decomposition of EDTA, which can expand the sack and partially reverse the capillary crumpling that occurs during drying.

3.3.2 Particle stability and dissolution

The nanoparticles have been shown in this study and reported to be completely encapsulated inside,[7] but it's not known if the crumpled graphene is open structure and encapsulated nanoparticles can be accessible to the surrounding solution media. We began

the study of nanoreactor behavior by investigating whether graphene encapsulation could stabilize particles to dissolution in aqueous media to test accessibility of encapsulated nanoparticles. The model cargo we chose is zinc oxide nanoparticles, which has been applied extensively in catalysis and sensor applications and widely used in consumer products including sunscreens and cosmetics. The studies on dissolution of zinc oxide nanoparticle is of significance not only to nanoparticles' water stability and usage durability,[34, 35] but also to the evaluation of cytotoxicity and environmental implications of ZnO nanoparticles, of which the released ions are highly toxic to a range of aquatic organisms.[36-39] The present study compares the dissolution behavior of free and encapsulated ZnO NPs of similar primary particle size in 10 mM $NaNO_3$ solution (pH 5.8). To control for any changes in the particle phase or surface during the aerosol encapsulation process, and to control for aggregation effects, we prepared controlled agglomerates of ZnO NPs by repeating the aerosol droplet drying process but in the absence of graphene oxide. The result is a set of equi-axed ZnO agglomerates (Fig. 3-2B) of similar size and shape to the graphene-ZnO nanosacks (Fig. 3-2A). XRD spectra (Fig. 3-2C) indicate the aerosol encapsulation process did not alter the composition or phase of ZnO.

Figure 3-2D shows the rapid dissolution of free ZnO agglomerates within 20 hours in agreement with Ma et al.[40] The ZnO particles inside crumpled graphene sacks show a similar time scale for dissolution, but with an offset in the total amount dissolved that may be caused by adsorption of Zn^{2+} on polar functional groups on rGO,[41] or by some small fraction of deeply imbedded ZnO. For both samples, the concentration of dissolved Zn reaches an apparent equilibrium after 20 hours. Based on calculations performed using the aqueous-phase thermodynamics package *Visual Minteq*[42] the equilibration is not due

to formation of $Zn(OH)_2$, but instead is caused by an increase in pH from 5.8 to 6.7, which we measured over the course of the dissolution process. Overall, these results show that encapsulation in graphene nanosacks does not protect ZnO NPs from dissolution. Neither transport limitations on exiting Zn-ions nor the coverage of particle surfaces by graphene sheets have a major effect on the rate of dissolution of ZnO.

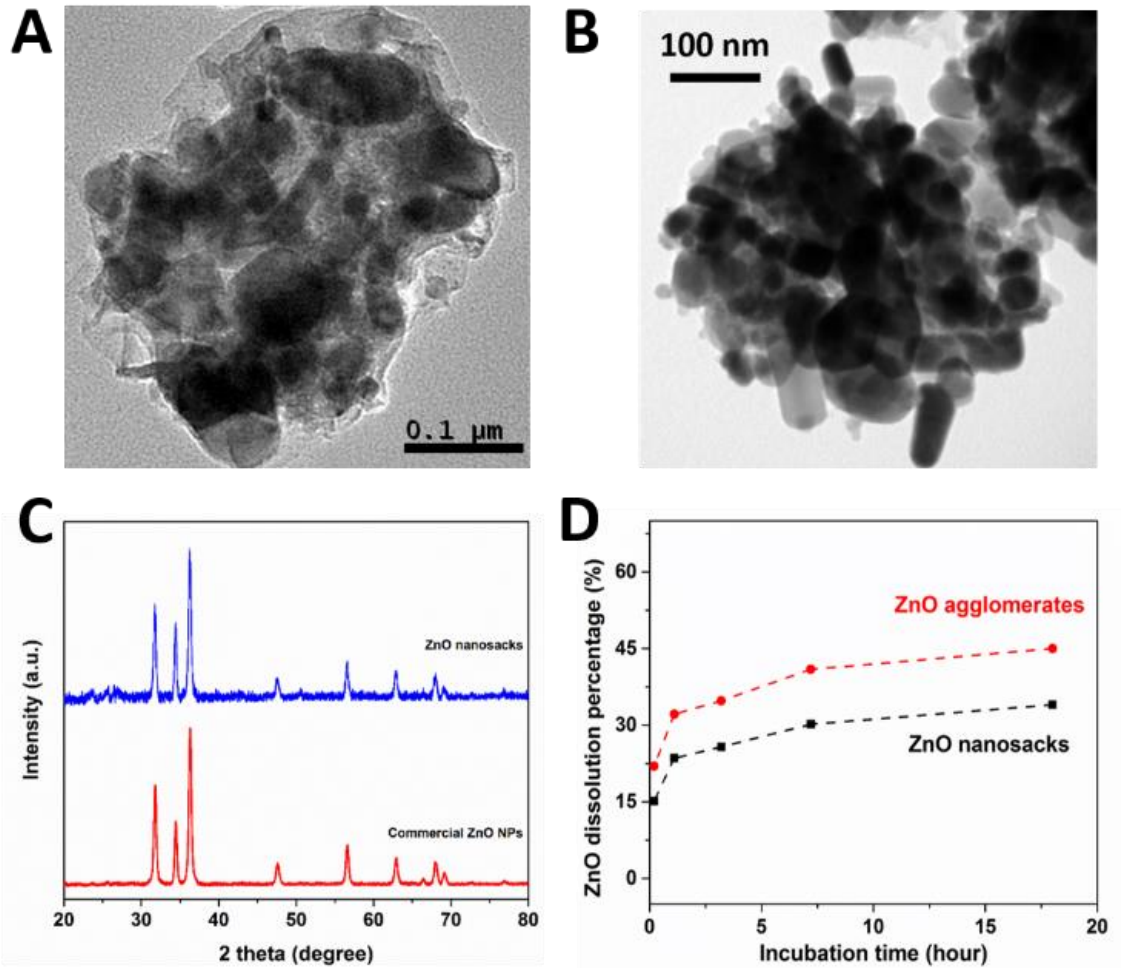

Figure 3-2. Characterization and dissolution behavior of ZnO agglomerates and nanosacks. TEM images of (A) ZnO-filled graphene nanosacks and (B) controlled agglomerates of free ZnO NPs, both made by the aerosol drying process; (C) XRD spectra of the free and encapsulated ZnO NPs, showing encapsulation does not alter the phase of ZnO; (D) ZnO dissolution behavior in 10mM $NaNO_3$.

3.3.3 Anomalous enhancement of particle oxidation

Many nanomaterials are stable to dissolution in their current oxidation states, but in the presence of O_2 undergo oxidation with release of soluble ions or complexes.[28, 43, 44] This oxidative dissolution has been shown to be important in the biological and environmental behavior of nanoscale Ag, [28, 44, 45] Cu,[43, 46] Ni[47] and Fe,[48, 49] where it determines the concentration of the soluble ionic species that can be the primary toxic species in particle-containing suspensions.[43, 45, 48] Here we report the surprising finding that encapsulation in graphene sacks *increases* the rate of oxidation of nanoscale Cu and Ag despite the introduction of an apparent physical barrier to oxygen access.

We tracked the appearance of soluble copper and silver ions during the incubation of the crumpled rGO hybrids and free metal nanoparticles. Figure 3 shows their dissolution rates in acetate buffer (pH 5.7). The Cu dissolution rate is extraordinarily fast within the crumpled graphene nanoreactors, a result that can be directly observed in the form of Cu-depleted reactor structures after incubation for only one hour (Fig. 3-3C). The encapsulated and free particles have a similar size and crystal phase (Fig. 3-3A), so the effect must be related to the hybridization of the particles with carbon. Recent studies on graphene-coated planar substrates suggest that electron transfer from the metal to graphene can promote metal oxidation by providing a conductive pathway from the unoxidized metal core to the external oxidant that bypasses an insulating oxide shell.[50, 51] For nano-Cu, it is known that a solid oxide film forms during the oxidative dissolution process,[46] and electron transfer through an insulating Cu_2O film has been proposed as the rate-limiting step in Cu corrosion.[51] Within the nanoreactor, the metallic particles are in direct contact with internal carbon structures that include multilayer rGO sheets and near-spherical carbon

shells formed by EDTA pyrolytic decomposition, which are easily seen in Fig. 3-3C. Copper is known to transfer electrons to graphene to equilibrate the Fermi levels,[52, 53] and we propose that Cu transfers electrons to these internal carbon structures and spreads them to the high-area outer surface where they participate in oxygen reduction.[54, 55]

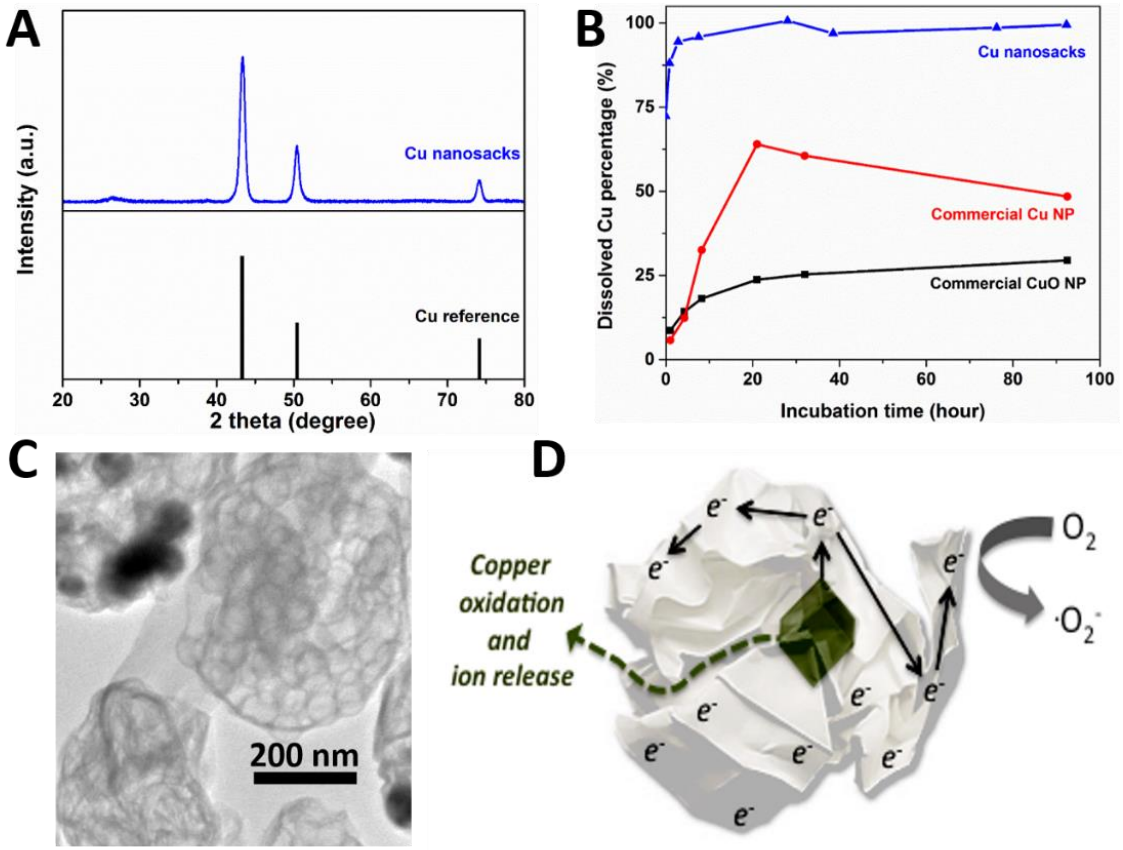

Figure 3-3. Copper-nanoparticle oxidation is accelerated inside graphene nanoreactors.XRD spectra of copper NPs within graphene nanosacks. (B) Time-dependent dissolution behavior of copper in rGO-Cu nanosacks and commercial Cu NPs in acetate buffer. Note that the decrease of dissolved Cu seen in the Cu NP sample after 20 hours is due to the comproportionation of Cu NPs and dissolved Cu^{2+} to form the insoluble Cu_2O shell.[56] (C) TEM image of rGO-Cu nanosacks after one-hour incubation in acetate buffer showing the depletion of Cu-NPs with intact sack structure. Note the internal spherical structures, which are EDTA-derived carbon shells at the locations of the original Cu-NP surfaces. (D) Mechanism of electron transfer to rGO and Cu-ion release by diffusion through the irregular pore structure of the folded structure.

Facile electron transport through conductive rGO replaces slower electron transport through Cu_2O and thus accelerates the reaction. In addition, reduced oxygen species

formed through electron transfer to dissolved O_2 are generated primarily at the surface of the graphene sack and not the surface of Cu, and as such, are not readily available to facilitate formation of Cu-oxide. This physical separation of newly formed oxide species from copper may limit the formation of surface oxide and instead favor direct Cu-cation release. When electron transfer through graphene is coupled with diffusion of soluble Cu ions through the porous, water-filled sack structure (see above), the result is a complete redox process with the net effect of accelerating nanoparticle oxidation (Fig. 3-3D).

Figure 3-4 shows that this enhancement also can be observed in the silver-graphene system in some cases. Oxidative dissolution of silver NPs have been extensively studied [28, 57-59], and is seen here to be accelerated when Ag particles are formed within crumpled rGO using EDTA as an additive (see "Ag-C-rGO hybrid" curve). Interestingly, if pre-fabricated Ag particles are encapsulated without the use of EDTA, the rGO sack alone has little effect on dissolution (see "Ag-rGO hybrid" curve). This suggests that the EDTA-derived carbon shells ("C" in "Ag-C-rGO hybrids") are the primary feature that enhances corrosion by promoting electron transport through or around the surface metal oxide layers due to their intimate contact with the particle surfaces and connection to the outer graphene shell (Fig. 3-3C and D).

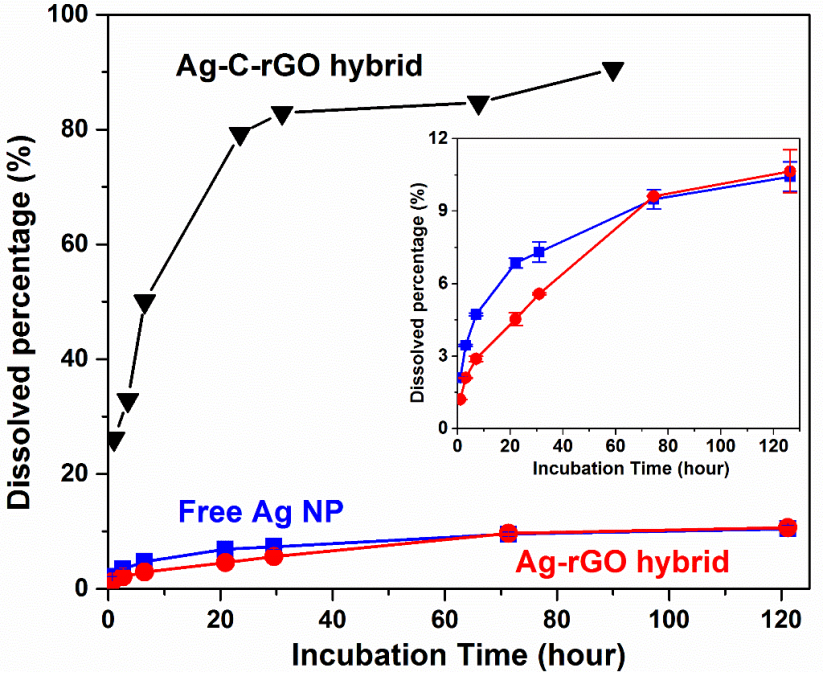

Figure 3-4. Ag-nanoparticle oxidation is accelerated inside graphene nanoreactors. Similar effect seen in the Ag-graphene system when EDTA is used as an additive to create carbon shells around the particles (Ag-C-rGO hybrid), but not in the presence of the rGO sack alone as the only carbon component (Ag-rGO hybrid).

Finally we also used these same methods to create Pt- and Pd-filled nanosacks (structures in Fig. 3-5), but oxidative dissolution of these metals was too slow to be used as a diagnostic for the effect of graphene encapsulation. Combined with ZnO dissolution data, graphene nanosacks show incapability of suppression of particle dissolution due to its open structure and non-conformal wrapping. The carbon shells from EDTA pyrolysis provide conformal wrapping on particles, and promote electron transport and eventually enhance these metal dissolution observed in Fig. 3-3 and 3-4.

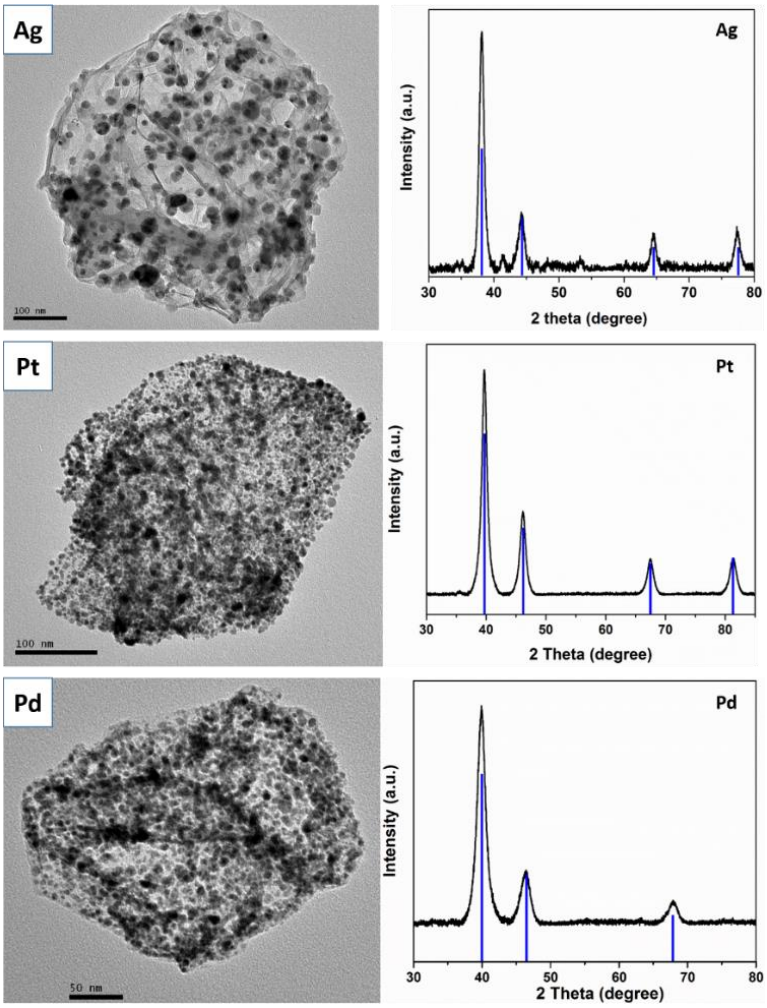

Figure 3-5. SEM images and XRD spectra of Ag, Pt, and Pd -filled rGO sacks synthesized by adding EDTA at equi-molar concentrations to the metal precursor salt ($AgNO_3$, Na_2PtCl_4, and Na_2PdCl_4) in the GO suspension. In all cases, metal ions are reduced to zero-valent metal nanoparticles.

3.3.4 Inner-space catalysis

There is great interest in graphene-particle hybrids as advanced architectures for heterogeneous catalysis and electrocatalysis.[60-64] It is clear that the internal spaces in graphene sack nanoreactors are accessible to small molecule solutes (Fig. 3-2 and 3-3), but the ability of nanoreactors to serve as functioning catalytic systems is unknown. Here we investigated the catalytic activities of Cu-NPs and Ag-NPs in nanoreactor environments

for electrochemical reduction of CO_2 and 4-nitrophenol reduction, respectively. Copper is known to be one of the most effective metallic catalysts for carbon dioxide electroreduction.[65-67] Fig. 3-6A shows cyclic voltammograms of rGO-Cu sacks in 0.1 M aqueous $KHCO_3$ sparged with 1 bar CO_2 gas.

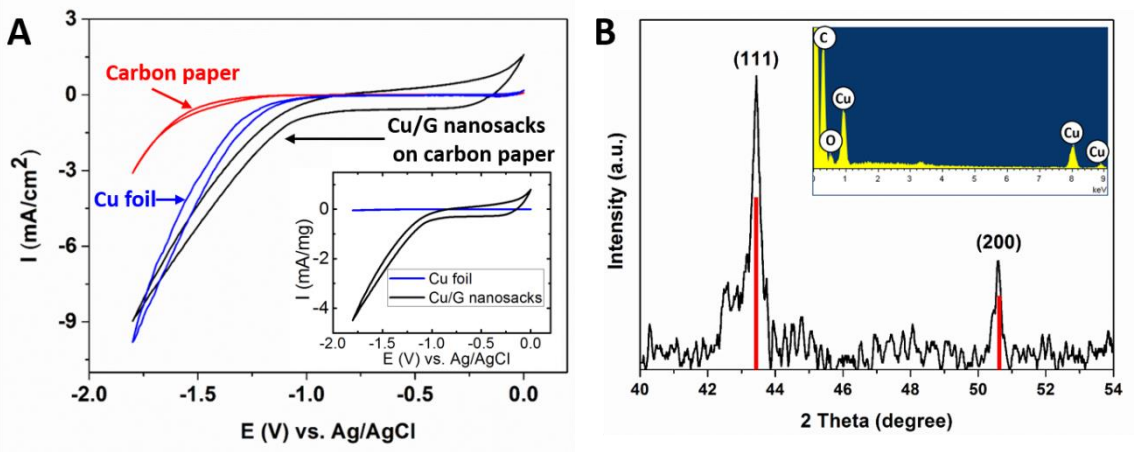

Figure 3-6. Catalytic activity of Cu NPs when encapsulated in graphene nanosacks. (A) Cyclic voltammogram showing activity of rGO-Cu nanoreactors for the electrochemical reduction of CO_2 in 0.1 M aqueous $KHCO_3$. The inset plot shows current density normalized by copper mass. (B) GI-XRD and EDX spectra of Cu/rGO-nanoreactors after electrochemical testing, showing stability of Cu metal phase.

The lower onset potential and higher current density of this graphene-particle hybrid relative to the carbon paper control demonstrates the catalytic activity of the rGO-Cu nanosacks. It is noteworthy that the nanosacks give a lower onset potential for CO_2 electroreduction than pure Cu foil (Fig. 3-6A). The current density per superficial electrode area is similar for the nanoreactors and the Cu-foil, but the Cu mass density in the nanoreactor electrode (2 mg/cm^2) must be lower than that of the foil (224 mg/cm^2), so the current density per unit Cu mass is much higher for the nanoreactor sample (Fig. 3-6A inset). Energy dispersive X-ray spectroscopy (EDX) and Grazing Incidence X-ray

Diffraction (GI-XRD) results in Fig. 3-6B show that the Cu phase is stable during cycling, and overall the data suggest that graphene nanoreactors can function as a support architecture for electrocatalysis.

For a non-electrochemical reaction, we used Ag-catalyzed reduction of 4-nitrophenol (Nip) to aminophenol as a model reaction (inset of Fig. 3-7). The reduction of Nip by borohydride is catalyzed on Ag and Au surfaces, and this catalytic reaction has often been used as a model to benchmark the activity of nanoparticle catalyst formulations.[68-70] Here, the characteristic UV-vis adsorption peak of Nip at 400 nm is used to monitor this reaction in the presence of rGO-Ag nanosacks. Ag nanosacks (1mg/mL, 2μL) were added to a 1 mL solution containing Nip (1.4×10^{-4} M) and $NaBH_4$ (4.2×10^{-2} M), and Fig. 3-7 shows the Nip depletion dynamics in the presence of the rGO-Ag nanoreactors, which demonstrates rGO-Ag nanosacks are catalytically active. For comparison, Ag catalyst prepared by the same aerosol process without graphene wrapping was also used in the nitrophenol reduction reaction at the same mass of Ag-rGO nanosacks, but showed no activity. The Nip reduction rate is expected to be proportional to the amount of Ag surface available for surface hydride formation (by BH_4^-) Nip adsorption, surface reaction, and desorption, according to the accepted mechanism for catalytic Nip reduction.[71] Without graphene wrapping, the loss of Ag activity is due to thermal sintering at 600℃ (*vida infra*). The role of graphene nanoreactors in sintering inhibition is explored in more detail in the following section.

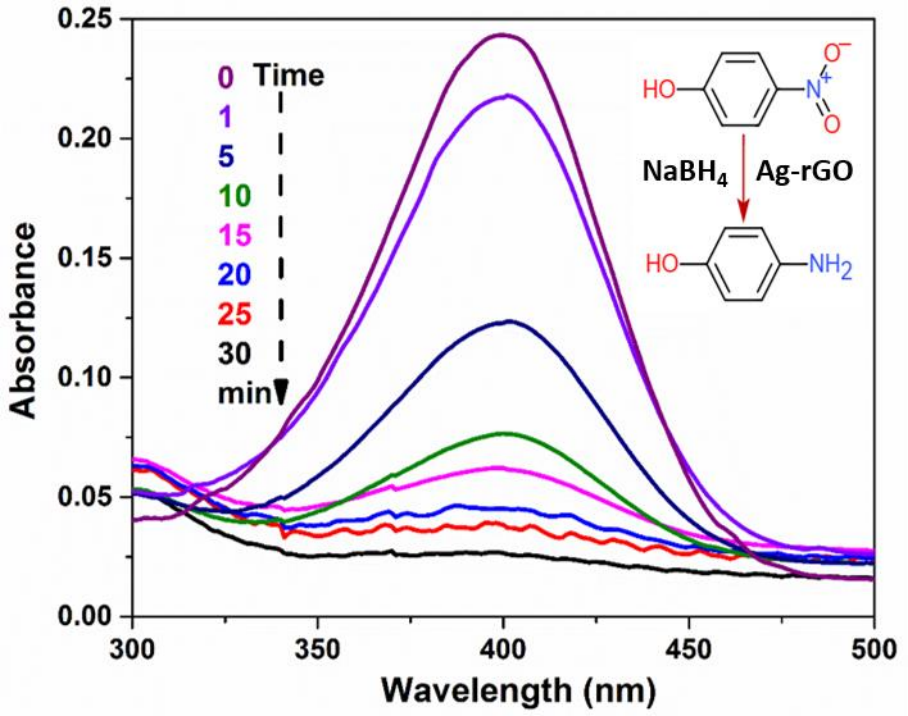

Figure 3-7. Catalytic activity of Ag NPs when encapsulated in graphene nanosacks. Time dependent adsorption spectra of 4-nitrophenol showing its depletion by borohydride reduction catalyzed by rGO-Ag nanoreactors.

3.3.5 Sintering inhibition

Among the desired functions of a catalyst support is to enhance and maintain particle dispersion and active surface area. Both particle mobility and atomic mobility at particle surfaces can cause a loss in surface area and catalytic activity under reaction conditions at elevated temperatures. We found the crumpled graphene nanoreactor architecture to be effective at suppressing particle-particle interactions and thermal sintering. Figure 3-8 compares the behavior of free and encapsulated Ag NPs heated at 400 ℃ (A, B) and 600 ℃ (C, D) in inert gas. Controlled Ag-NP agglomerates were made by nebulization of Ag-NP suspensions and *in situ* drying, and in the absence of graphene, these agglomerates undergo rapid partial fusion at temperatures as low as 400 ℃ (Fig. 3-

8A). At 600 ℃ one large rounded Ag particle forms from the complete fusion of the initial agglomerate (Fig. 3-8C). The addition of graphene, however, maintains the initial particle structure at both temperatures during the aerosol process (Fig. 3-8 B, D), which we believe is due to physical restriction of particle motion by internal graphene structures. Sintering suppression is characteristic of crumpled graphene nanoreactors, whose folded structures create internal nanoscale pockets for the particles that serve as physical barriers to particle mobility or release (Fig. 3-8E), but whose characteristic pore sizes around 4 nm[5, 8] allows small molecule reactants (< 4 nm) access to catalyst active sites.

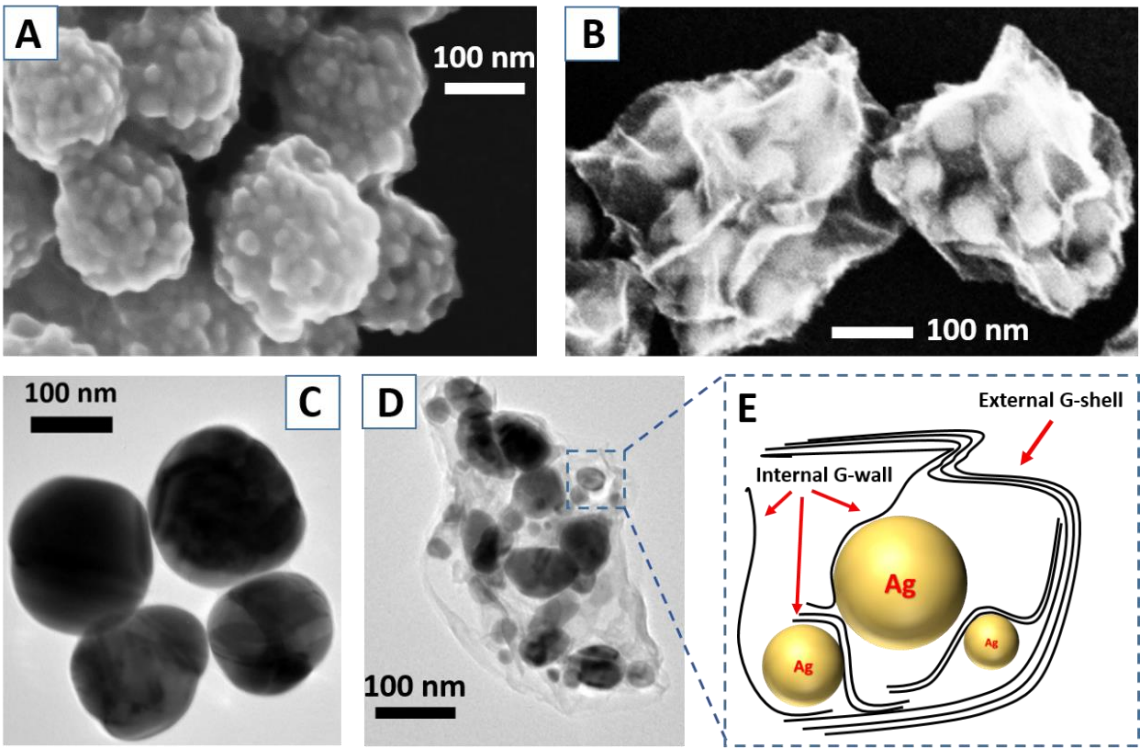

Figure 3-8. Sintering inhibition of nanoparticles within crumpled graphene nanoreactors. (A, B) Final Ag particle structures after rapid thermal treatment in flight at 400 ℃ in N_2 gas during the aerosol process: (A) controlled Ag agglomerates with no graphene, (B) Ag-NPs inside crumpled graphene nanoreactors. (C, D) Final Ag particle structures after rapid thermal treatment in flight at 600 ℃ in N_2 gas during the aerosol process: (C) controlled Ag agglomerates with no graphene, (D) Ag-NPs inside crumpled graphene nanoreactors. (E) Sketch of internal graphene structures that are proposed to prevent particle-particle interactions and release, while allowing small molecule solutes access to active surfaces.

Figure 3-9 shows that the sintering inhibition depends on the relative amounts of Ag and graphene in the filled reactor structures. As the initial Ag/GO mass ratio increases from 1 to 40, the ability of internal graphene structures to inhibit sintering declines. We believe that high graphene content produces more internal compartments and fewer Ag-NPs per compartment, leading to smaller final particles after thermal treatment.

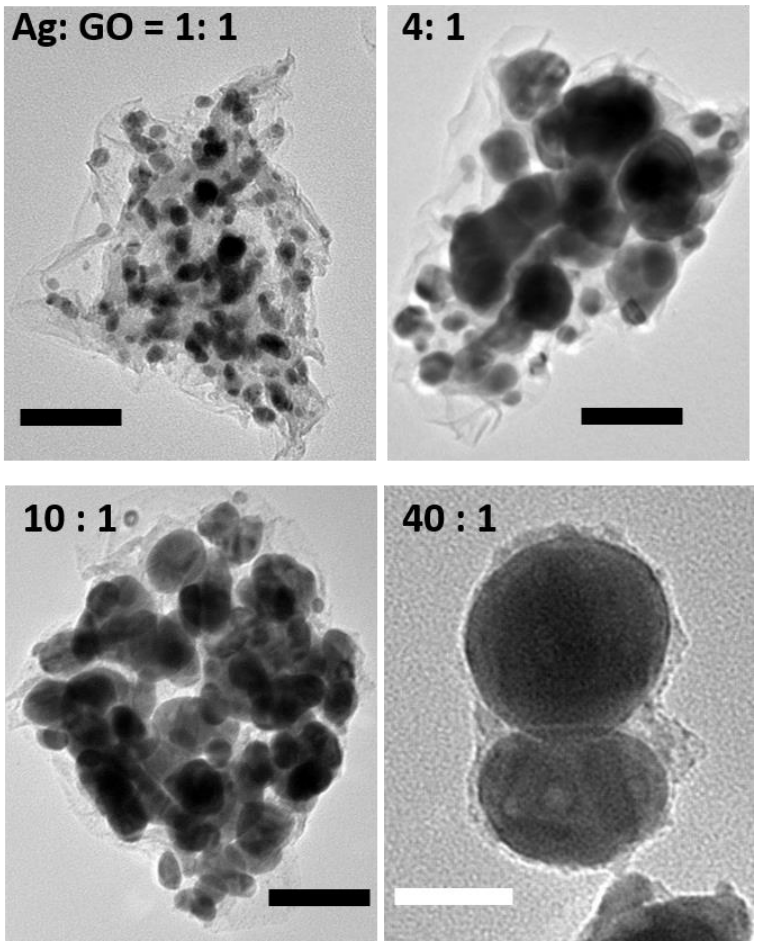

Figure 3-9. The effect of GO/Ag ratio in sintering inhibition. Sintering inhibition is more effective at high GO:Ag ratio. TEM images of sintered Ag in graphene nanoreactors treated at 600 ℃ at different Ag:GO ratios (left to right): 1, 4, 10, 40. The black scale bar represents 100 nm, while the white scale bar represents 50 nm.

To test sintering inhibition at longer times, we treated pre-fabricated Ag-filled nanoreactors to temperatures ranging from 500-700 ℃ for one hour in a horizontal tube

furnace. The Ag nanoparticles were stable inside graphene nanoreactors for one hour at 500 ℃ in N_2 and at 700 ℃ in 5/95% H_2/N_2 (Fig. 3-10 B, D). Interestingly, the graphene nanoreactors were destroyed and the Ag-NPs fully sintered at 700 ℃ in the absence of H_2 (Fig. 3-10C), which is likely due to trace oxygen in the N_2 annealing gas environment. The crumpled graphene shells here are composed of only about 10 atomic layers,[8] and it is not surprising that they are easily gasified by exposure to trace oxygen at 700℃, which is above the typical initiation temperature for rGO oxidation by air.

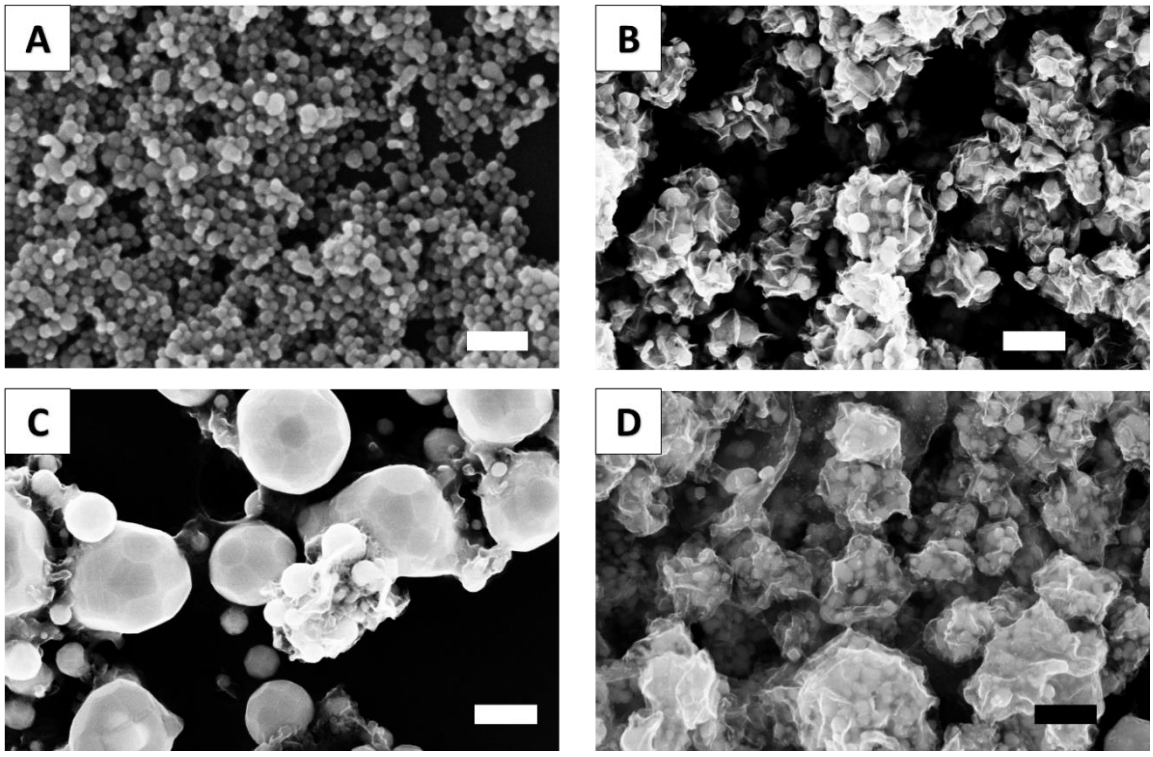

Figure 3-10. Morphology of Ag nanoparticles under various thermal treatment conditions. SEM images of as-prepared Ag NPs (A), Ag-rGO nanosacks incubated at 500 ℃ in 99.99% nitrogen for one hour (B), Ag-rGO nanosacks incubated at 700 ℃ in 99.99% nitrogen for one hour (C), and Ag-rGO nanosacks incubated at 700 ℃ in 5/95% H_2/N_2 for one hour (D). All scale bars represent 100 nm.

3.3.6 Case study: Fe0-NPs for environmental reduction of Cr(VI)

The graphene nanoreactor architecture also can be used to increase the reactivity of nano-zero-valent iron (nZVI) for the environmental remediation of Cr (VI) through chemical reduction. One route to nZVI is reduction of Fe_3O_4 nanoparticles with low Cr (VI) removal efficiency, but sintering or aggregation at the high-temperatures employed reduces the activity of the nZVI. [72, 73] Surface coatings based on silica[74] or carbon[75] have been explored to maintain the iron oxide nanostructure during reduction. Here we compare the reductive activity of derived nZVI prepared from Fe_3O_4 particles in the free state and imbedded in graphene nanoreactors. Figure 3-11 shows that free particles undergo significant sintering and area loss during the 700 ℃ hydrogen reduction step (A→D), while the encapsulated particles show better size and area retention (B→C). Though Fe as free particles and within nanoreactors have the same composition and phase (Fig. 3-11E), the nZVI particles within the nanoreactors are more effective at Cr (VI) reduction (Fig. 3-11F). The initial kinetics are fast in both cases, but the free iron particles lose activity at just over 50% conversion while Fe^0-filled graphene nanoreactors retain activity through the complete elimination of Cr (VI). Note that rGO nanosacks alone at the same mass loading showed very limited adsorption/reduction of Cr (VI), so the effects observed relate to differences in the activity of the iron phases. We believe the improved performance of the nanoreactor sample is the result of two effects: (i) encapsulation inhibits sintering during synthesis and yields smaller particles with higher external area, and (ii) electron transfer between Fe^0 and graphene allows indirect reduction of Cr (VI) by Fe^0 at the sack surface and prevents the formation of a passivating oxide film at local points of particle-graphene contact. This enhanced reductive activity toward Cr (VI) is analogous

to the enhanced reductive activity toward O_2 observed for Cu-rGO nanosacks that leads to fast Cu dissolution (above).

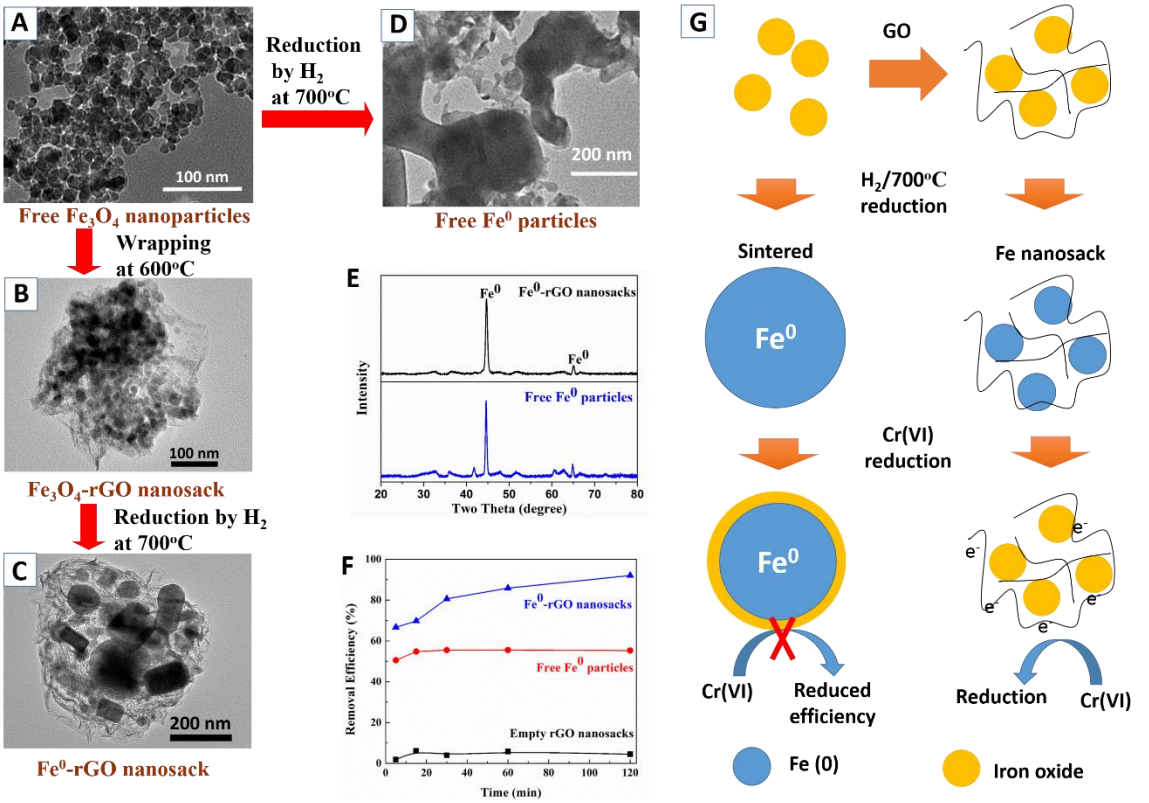

Figure 3-11. Use of graphene nanoreactors to increase the activity of Fe^0-NPs for environmental reduction of Cr (VI). TEM images of (A) free Fe_3O_4 NPs; (B) Fe_3O_4-filled nanoreactors; (C) Fe^0-filled nanoreactors; (D) free Fe^0 particles. (E) XRD spectra of Fe^0-filled nanoreactors and free Fe^0 particles. (F) Comparison of Cr (VI) removal efficiency within 2 hrs. Note: the graphene-only control shows the main activity for Cr (VI) removal is associated with the iron phases. (G) Proposed mechanism.

3.3.7 Complex nanoreactors: photochemical control of Ag-ion release

The data above have shown novel behaviors that arise from particle-graphene interactions in the nanoreactor architecture. Even more complex behaviors emerge when multiple particle types are introduced into the graphene nanoreactor interior. Figure 3-12 for example shows the controlled dissolution behavior of ternary Ag/TiO_2-rGO nanosacks in aqueous suspension in the presence and absence of UV illumination. Ag control release

is of scientific significance and has wide potential applications since the dissolved Ag determines the cytotoxicity and antibacterial properties of silver-based nanomaterials.[76-79] As a measure of the rate of oxidation of nano-Ag, the time evolution of dissolved silver concentration was monitored by graphite furnace atomic absorption spectroscopy after nanosack removal by ultrafiltration.[28] The rate of oxidative dissolution of nano-Ag in the dark is similar to that reported previously, [28, 80, 81] but the release is completely suppressed during UV illumination (Fig. 3-12B). Oxidative dissolution restarts immediately when the UV lamp is switched off, and when the lamp is turned back on the accumulated Ag^+ undergoes active reduction lowering silver ion concentration (Fig. 3-12B). This demonstrates active control of Ag-ion release and re-reduction using three-component graphene nanosacks.

Some aspects of this behavior are readily understood from the existing literature. Titania is an active photocatalyst, but when present as isolated particles, electron-hole recombination can limit its efficiency.[60, 82] Hybridizing TiO_2 with graphene has been reported to increase photoefficiency by electron transport and spreading onto the 2D carbon sheet, which promotes electron-hole separation and inhibits recombination.[82, 83] Furthermore, high efficiencies in Ag-TiO_2-graphene systems have been reported through graphene (rGO) transport of excited electrons for Ag reduction, though the effect on Ag transformations was not studied. Silver ion reduction also has been reported on illuminated TiO_2 surfaces.[84] The data shown in Fig. 3-12C reveals a behavior unique to Ag/TiO_2-rGO nanoreactors. Here Ag ion release is suppressed by trace amounts of TiO_2 (1% of the Ag loading). This amount of TiO_2 is <u>not</u> effective when present as free particles in suspension with nano-Ag (Fig. 3-12C). We propose that the highly sensitive control of

Ag-ion release in Ag/TiO_2-rGO nanoreactors is due to the enhancement of TiO_2 photoreactivity by direct electron transfer through graphene to silver[82] combined with the elevated concentration of the Ag and TiO_2 components that are concentrated in the reactor interior. Any silver ion produced through nano-Ag oxidation must encounter electron-doped graphene structures before diffusion through the porous sack, and the internal reduction process is too fast to allow measurable release (Fig. 3-12D). Photo-controlled release and capture of silver ions shown by Ag/TiO_2-rGO nanosacks is unique and may have potential in controlled release antibacterial or other delivery applications

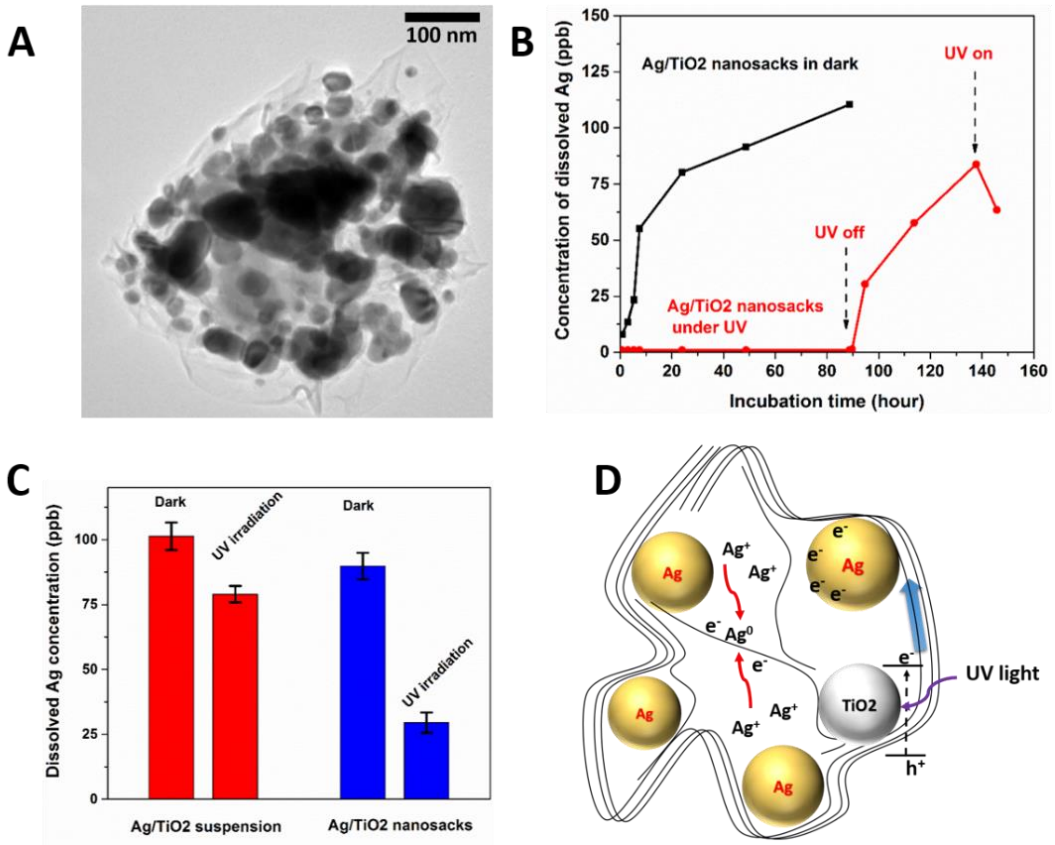

Figure 3-12. Complex nanoreactors: photochemical control of Ag-ion release. (A) TEM image of Ag/TiO_2-rGO nanosacks; (B) Time-resolved measurement of Ag ion release from Ag/TiO_2-rGO nanosacks in dark or under UV irradiation; (C) Ag ion release from Ag/TiO_2-rGO nanosacks with small amounts of TiO_2 in dark or UV irradiation incubated for one day. Here the oxidation protection provided by TiO_2 is much more effective in the nanoreactor configuration than from free Ag and TiO_2 in suspension under the same conditions; (D) Proposed mechanism for suppression of Ag oxidation by electron transfer and active Ag^+ reduction on graphene surfaces.

3.3.8 Complex nanoreactors: galvanic control of Ag-ion release

Another emergent behavior of three-component nanoreactors involves galvanic interactions between dissimilar imbedded metals. We explored the addition of a less noble metal to Ag-rGO nanoreactors as a non-photochemical method to control Ag-ion release. Figure 3-13 shows the behavior for Cu (A-C) and Ni (D-F) introduced as the less noble metal. The Ag/Cu-rGO reactors (A-C) were prepared by the aerosolization of GO with the dissolved Cu-EDTA complex described in Fig. 3-1. For a better comparison, the Ag-rGO nanoreactors were made from pre-synthesized particles as in Fig. 3-1, but also with the addition of EDTA that may affect the ion release rates.

Figure 3-13C shows the time-dependent dissolution behavior for both elements. The dissolution of Cu is fast, as observed previously for the simple Cu-rGO system (see Fig. 3-3), and the Ag oxidative dissolution is unaffected by addition of copper. The inability of Cu to influence Ag-ion release is easily understood – Cu oxidation and dissolution is rapid enough that the Cu-NPs are not present for most of the time period of Ag oxidation. The mismatch between Ag and Cu oxidation kinetics prevents Cu from being effective as a method for galvanic control of Ag-ion release. A different behavior is seen in the case with nickel. Figure 3-13 D-F show the behavior of Ag/Ni-rGO nanoreactors. The similar rates of oxidative dissolution for free silver and encapsulated Ni allow Ni to strongly suppress Ag-ion release. This suppression can be the result of a galvanic replacement reaction (e.g. $2Ag^{+} + Ni \rightarrow 2Ag + Ni^{2+}$) or by electron transfer from Ni through rGO to Ag, providing cathodic protection that prevents Ag oxidation. . The use of various amounts of the sacrificial metal can alter the induction period before Ag ion

release starts, and this has potential applications where extended release is needed such as antibacterial bandages.

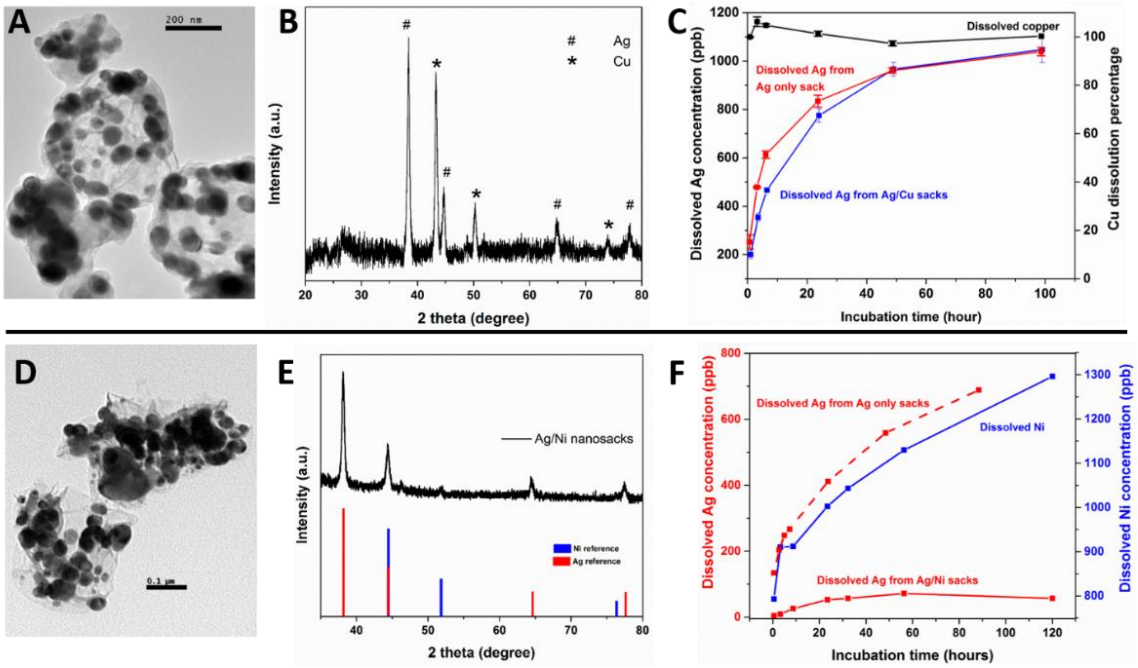

Figure 3-13. Complex nanoreactors: galvanic control of Ag-ion release. (A-C) Ag/Cu-rGO nanosacks, (A) morphology by TEM, (B) phases by XRD, and (C) oxidative dissolution behavior for both Ag (total Ag concentration is 3 ppm) and Cu components in acetate buffer. Cu oxidation and dissolution is rapid, and does not alter the oxidative dissolution profile of nano-Ag observed when present alone in Ag-rGO nanosacks. (D-F) Ag/Ni-rGO nanosacks, (D) Morphology by TEM, (E) phases by XRD, (F) oxidative dissolution behavior of both Ag and Ni components in acetate buffer.

3.4 Conclusions

Crumpling graphene around chemically reactive or catalytic particles can lead to "nanoreactor" systems with active internal cavities that can be exploited for the engineering of chemical reactions. The crumpled structure can be designed to immobilize and retain the active nanoparticles, while providing diffusional pathways through < 4 nm pores for small molecule reactants and products to enter and exit the internal nanocavity during

reaction. This paper explores nanoreactor behaviors using ZnO, Cu, Ag, Ni, Fe, and TiO_2 NPs as model fillers. We show that the complex 3D crumpled structure and electrical conductivity of the graphene shell gives rise to novel behavior that includes (i) inhibition of particle sintering (Ag, Fe), (ii) enhancement of particle oxidation (Cu, Ag) through improved electron transfer, (iii) cathodic protection against oxidation (Ag) using a co-imbedded sacrificial particle (Ni), (iv) TiO_2-mediated photochemical control of silver ion release, (v) and enhanced performance in the Fe-based reduction of environmental Cr(VI). These novel behaviors coupled with the continuous fabrication method and the flexible ability to fill the graphene shells with one or multiple types of chemically reactive or catalytic particles, make crumpled graphene nanoreactors attractive for a variety of applications in catalysis, electrocatalysis, controlled release, and environmental nanotechnology.[85]

3.5 Reference

1. Geim, A. K.; Grigorieva, I. V. Van der Waals heterostructures. *Nature* **2013**, 499, 419-425.
2. Guo, F.; Silverberg, G.; Bowers, S.; Kim, S.-P.; Datta, D.; Shenoy, V.; Hurt, R. H. Graphene-Based Environmental Barriers. *Environ. Sci. Technol.* **2012**, 46, 7717-7724.
3. Su, Y.; Kravets, V. G.; Wong, S. L.; Waters, J.; Geim, A. K.; Nair, R. R. Impermeable barrier films and protective coatings based on reduced graphene oxide. *Nat Commun* **2014**, 5.
4. Berry, V. Impermeability of graphene and its applications. *Carbon* **2013**, 62, 1-10.
5. Chen, Y.; Guo, F.; Qiu, Y.; Hu, H.; Kulaots, I.; Walsh, E.; Hurt, R. H. Encapsulation of Particle Ensembles in Graphene Nanosacks as a New Route to Multifunctional Materials. *ACS Nano* **2013**, 7, 3744-3753.
6. Mao, S.; Wen, Z.; Kim, H.; Lu, G.; Hurley, P.; Chen, J. A General Approach to One-Pot Fabrication of Crumpled Graphene-Based Nanohybrids for Energy Applications. *ACS Nano* **2012**, 6, 7505-7513.
7. Luo, J.; Zhao, X.; Wu, J.; Jang, H. D.; Kung, H. H.; Huang, J. Crumpled Graphene-Encapsulated Si Nanoparticles for Lithium Ion Battery Anodes. *J. Phys. Chem. Lett.* **2012**, 3, 1824-1829.
8. Chen, Y.; Guo, F.; Jachak, A.; Kim, S.-P.; Datta, D.; Liu, J.; Kulaots, I.; Vaslet, C.; Jang, H. D.; Huang, J.; Kane, A.; Shenoy, V. B.; Hurt, R. H. Aerosol Synthesis of Cargo-Filled Graphene Nanosacks. *Nano Lett.* **2012**, 12, 1996-2002.
9. Ma, X.; Zachariah, M. R.; Zangmeister, C. D. Crumpled Nanopaper from Graphene Oxide. *Nano Lett.* **2011**, 12, 486-489.
10. Luo, J.; Jang, H. D.; Sun, T.; Xiao, L.; He, Z.; Katsoulidis, A. P.; Kanatzidis, M. G.; Gibson, J. M.; Huang, J. Compression and Aggregation-Resistant Particles of Crumpled Soft Sheets. *ACS Nano* **2011**, 5, 8943-8949.
11. Cassagneau, T.; Fendler, J. H. Preparation and Layer-by-Layer Self-Assembly of Silver Nanoparticles Capped by Graphite Oxide Nanosheets. *J. Phys. Chem. B* **1999**, 103, 1789-1793.

12. Zhou, W.; Zhu, J.; Cheng, C.; Liu, J.; Yang, H.; Cong, C.; Guan, C.; Jia, X.; Fan, H. J.; Yan, Q.; Li, C. M.; Yu, T. A general strategy toward graphene@metal oxide core-shell nanostructures for high-performance lithium storage. *Energy Environ. Sci.* **2011**, 4, 4954-4961.
13. Zhu, M.; Chen, P.; Liu, M. Graphene Oxide Enwrapped Ag/AgX (X = Br, Cl) Nanocomposite as a Highly Efficient Visible-Light Plasmonic Photocatalyst. *ACS Nano* **2011**, 5, 4529-4536.
14. Yang, S.; Feng, X.; Ivanovici, S.; Müllen, K. Fabrication of Graphene-Encapsulated Oxide Nanoparticles: Towards High-Performance Anode Materials for Lithium Storage. *Angew. Chem., Int. Ed.* **2010**, 49, 8408-8411.
15. Tan, S. M.; Ambrosi, A.; Chua, C. K.; Pumera, M. Electron transfer properties of chemically reduced graphene materials with different oxygen contents. *J. Mater. Chem. A* **2014**, 2, 10668-10675.
16. Luo, J.; Jang, H. D.; Huang, J. Effect of Sheet Morphology on the Scalability of Graphene-Based Ultracapacitors. *ACS Nano* **2013**, 7, 1464-1471.
17. Zong, J.; Zhu, Y.; Yang, X.; Shen, J.; Li, C. Synthesis of photoluminescent carbogenic dots using mesoporous silica spheres as nanoreactors. *Chem. Commun. (Cambridge, U. K.)* **2011**, 47, 764-766.
18. Liu, J.; Qiao, S. Z.; Budi Hartono, S.; Lu, G. Q. Monodisperse Yolk–Shell Nanoparticles with a Hierarchical Porous Structure for Delivery Vehicles and Nanoreactors. *Angew. Chem., Int. Ed.* **2010**, 49, 4981-4985.
19. Lee, Y.; Lee, J.; Bae, C. J.; Park, J. G.; Noh, H. J.; Park, J. H.; Hyeon, T. Large-Scale Synthesis of Uniform and Crystalline Magnetite Nanoparticles Using Reverse Micelles as Nanoreactors under Reflux Conditions. *Adv. Funct. Mater.* **2005**, 15, 503-509.
20. Sun, C.; Yang, H.; Yuan, Y.; Tian, X.; Wang, L.; Guo, Y.; Xu, L.; Lei, J.; Gao, N.; Anderson, G. J.; Liang, X.-J.; Chen, C.; Zhao, Y.; Nie, G. Controlling Assembly of Paired Gold Clusters within Apoferritin Nanoreactor for in Vivo Kidney Targeting and Biomedical Imaging. *J. Am. Chem. Soc.* **2011**, 133, 8617-8624.

21. Wang, W.-N.; Jiang, Y.; Fortner, J. D.; Biswas, P. Nanostructured Graphene-Titanium Dioxide Composites Synthesized by a Single-Step Aerosol Process for Photoreduction of Carbon Dioxide. *Environ. Eng. Sci.* **2014**, 31, 428-434.
22. Smith, A. J.; Chang, Y.-H.; Raidongia, K.; Chen, T.-Y.; Li, L.-J.; Huang, J. Molybdenum Sulfide Supported on Crumpled Graphene Balls for Electrocatalytic Hydrogen Production. *Advanced Energy Materials* **2014**, 4, n/a-n/a.
23. Mao, S.; Wen, Z.; Huang, T.; Hou, Y.; Chen, J. High-performance bi-functional electrocatalysts of 3D crumpled graphene-cobalt oxide nanohybrids for oxygen reduction and evolution reactions. *Energy & Environmental Science* **2014**, 7, 609-616.
24. Mao, S.; Wen, Z.; Bo, Z.; Chang, J.; Huang, X.; Chen, J. Hierarchical Nanohybrids with Porous CNT-networks Decorated Crumpled Graphene Balls for Supercapacitors. *ACS Appl. Mater. Interfaces* **2014**.
25. Jiang, Y.; Wang, W.-N.; Biswas, P.; Fortner, J. D. Facile Aerosol Synthesis and Characterization of Ternary Crumpled Graphene–TiO2–Magnetite Nanocomposites for Advanced Water Treatment. *ACS Appl. Mater. Interfaces* **2014**, 6, 11766-11774.
26. Chen, X.; Wu, G.; Lan, T.; Chen, W. Autonomous micromotor based on catalytically pneumatic behavior of balloon-like MnOx-graphene crumples. *Chem. Commun. (Cambridge, U. K.)* **2014**, 50, 7157-7159.
27. Jang, H. D.; Kim, S. K.; Chang, H.; Choi, J.-W.; Luo, J.; Huang, J. One-step synthesis of Pt-nanoparticles-laden graphene crumples by aerosol spray pyrolysis and evaluation of their electrocatalytic activity. *Aerosol Sci. Technol.* **2013**, 47, 93-98.
28. Liu, J.; Hurt, R. H. Ion Release Kinetics and Particle Persistence in Aqueous Nano-Silver Colloids. *Environmental Science and Technology* **2010**, 44, 2169-2175.
29. Kim, F.; Luo, J.; Cruz-Silva, R.; Cote, L. J.; Sohn, K.; Huang, J. Self-Propagating Domino-like Reactions in Oxidized Graphite. *Adv. Funct. Mater.* **2010**, 20, 2867-2873.

30. Jia, X.; Cheng, Y.; Lu, Y.; Wei, F. Building Robust Carbon Nanotube-Interweaved-Nanocrystal Architecture for High-Performance Anode Materials. *ACS Nano* **2014**, 8, 9265-9273.

31. Choi, D. W.; Zea, C. J.; Do, Y. S.; Semrau, J. D.; Antholine, W. E.; Hargrove, M. S.; Pohl, N. L.; Boyd, E. S.; Geesey, G. G.; Hartsel, S. C.; Shafe, P. H.; McEllistrem, M. T.; Kisting, C. J.; Campbell, D.; Rao, V.; de la Mora, A. M.; DiSpirito, A. A. Spectral, Kinetic, and Thermodynamic Properties of Cu(I) and Cu(II) Binding by Methanobactin from Methylosinus trichosporium OB3b†. *Biochemistry* **2006**, 45, 1442-1453.

32. Escriv á, E.; Fuertes, A.; Folgado, J. V.; Mart ínez-Tamayo, E.; Beltr án-Porter, A.; Beltr án-Porter, D. Study of the thermal behaviour of ordered bimetallic EDTA complexes. *Thermochim. Acta* **1986**, 104, 223-245.

33. Bhat, T. R.; Krishna Iyer, R. Studies on EDTA complexes—VIII: Thermal behaviour in air and in nitrogen atmosphere of some metal-EDTA complexes. *J. Inorg. Nucl. Chem.* **1967**, 29, 179-185.

34. Hariharan, C. Photocatalytic degradation of organic contaminants in water by ZnO nanoparticles: Revisited. *Applied Catalysis A: General* **2006**, 304, 55-61.

35. Tang, X.; Choo, E. S. G.; Li, L.; Ding, J.; Xue, J. One-pot synthesis of water-stable ZnO nanoparticles via a polyol hydrolysis route and their cell labeling applications. *Langmuir* **2009**, 25, 5271-5275.

36. Bian, S.-W.; Mudunkotuwa, I. A.; Rupasinghe, T.; Grassian, V. H. Aggregation and dissolution of 4 nm ZnO nanoparticles in aqueous environments: influence of pH, ionic strength, size, and adsorption of humic acid. *Langmuir* **2011**, 27, 6059-6068.

37. Xia, T.; Kovochich, M.; Liong, M.; Mädler, L.; Gilbert, B.; Shi, H.; Yeh, J. I.; Zink, J. I.; Nel, A. E. Comparison of the mechanism of toxicity of zinc oxide and cerium oxide nanoparticles based on dissolution and oxidative stress properties. *ACS Nano* **2008**, 2, 2121-2134.

38. Zhang, H.; Ji, Z.; Xia, T.; Meng, H.; Low-Kam, C.; Liu, R.; Pokhrel, S.; Lin, S.; Wang, X.; Liao, Y.-P.; Wang, M.; Li, L.; Rallo, R.; Damoiseaux, R.; Telesca, D.; M ädler, L.; Cohen, Y.; Zink, J. I.; Nel, A. E. Use of Metal Oxide Nanoparticle Band

Gap To Develop a Predictive Paradigm for Oxidative Stress and Acute Pulmonary Inflammation. *ACS Nano* **2012**, 6, 4349-4368.

39. Franklin, N. M.; Rogers, N. J.; Apte, S. C.; Batley, G. E.; Gadd, G. E.; Casey, P. S. Comparative toxicity of nanoparticulate ZnO, bulk ZnO, and ZnCl2 to a freshwater microalga (Pseudokirchneriella subcapitata): the importance of particle solubility. *Environ. Sci. Technol.* **2007**, 41, 8484-8490.
40. Ma, R.; Levard, C.; Michel, F. M.; Brown, G. E.; Lowry, G. V. Sulfidation Mechanism for Zinc Oxide Nanoparticles and the Effect of Sulfidation on Their Solubility. *Environ. Sci. Technol.* **2013**, 47, 2527-2534.
41. Sitko, R.; Turek, E.; Zawisza, B.; Malicka, E.; Talik, E.; Heimann, J.; Gagor, A.; Feist, B.; Wrzalik, R. Adsorption of divalent metal ions from aqueous solutions using graphene oxide. *Dalton Trans.* **2013**, 42, 5682-5689.
42. Gustafsson, J. P. Visual MINTEQ version 3.0 http://vminteq.lwr.kth.se/ Stockholm, Sweden. **2013**.
43. Wang, Z.; von dem Bussche, A.; Kabadi, P. K.; Kane, A. B.; Hurt, R. H. Biological and Environmental Transformations of Copper-Based Nanomaterials. *ACS Nano* **2013**, 7, 8715-8727.
44. Levard, C.; Hotze, E. M.; Lowry, G. V.; Brown, G. E. Environmental Transformations of Silver Nanoparticles: Impact on Stability and Toxicity. *Environ. Sci. Technol.* **2012**, 46, 6900-6914.
45. Liu, J.; Sonshine, D. A.; Shervani, S.; Hurt, R. H. Controlled Release of Biologically Active Silver from Nanosilver Surfaces. *ACS Nano* **2010**, 4, 6903-6913.
46. Mudunkotuwa, I. A.; Pettibone, J. M.; Grassian, V. H. Environmental Implications of Nanoparticle Aging in the Processing and Fate of Copper-Based Nanomaterials. *Environ. Sci. Technol.* **2012**, 46, 7001-7010.
47. Pietruska, J. R.; Liu, X.; Smith, A.; McNeil, K.; Weston, P.; Zhitkovich, A.; Hurt, R.; Kane, A. B. Bioavailability, Intracellular Mobilization of Nickel, and HIF-1α Activation in Human Lung Epithelial Cells Exposed to Metallic Nickel and Nickel Oxide Nanoparticles. *Toxicol. Sci.* **2011**, 124, 138-148.

48. Phenrat, T.; Long, T. C.; Lowry, G. V.; Veronesi, B. Partial Oxidation ("Aging") and Surface Modification Decrease the Toxicity of Nanosized Zerovalent Iron. *Environ. Sci. Technol.* **2008**, 43, 195-200.

49. Lee, C.; Kim, J. Y.; Lee, W. I.; Nelson, K. L.; Yoon, J.; Sedlak, D. L. Bactericidal Effect of Zero-Valent Iron Nanoparticles on Escherichia coli. *Environ. Sci. Technol.* **2008**, 42, 4927-4933.

50. Schriver, M.; Regan, W.; Gannett, W. J.; Zaniewski, A. M.; Crommie, M. F.; Zettl, A. Graphene as a Long-Term Metal Oxidation Barrier: Worse Than Nothing. *ACS Nano* **2013**, 7, 5763-5768.

51. Zhou, F.; Li, Z.; Shenoy, G. J.; Li, L.; Liu, H. Enhanced Room-Temperature Corrosion of Copper in the Presence of Graphene. *ACS Nano* **2013**, 7, 6939-6947.

52. Giovannetti, G.; Khomyakov, P.; Brocks, G.; Karpan, V.; Van den Brink, J.; Kelly, P. Doping graphene with metal contacts. *Phys. Rev. Lett.* **2008**, 101, 026803.

53. Frank, O.; Vejpravova, J.; Holy, V.; Kavan, L.; Kalbac, M. Interaction between graphene and copper substrate: The role of lattice orientation. *Carbon* **2014**, 68, 440-451.

54. Wang, L.; Sofer, Z.; Ambrosi, A.; Šimek, P.; Pumera, M. 3D-graphene for electrocatalysis of oxygen reduction reaction: Increasing number of layers increases the catalytic effect. *Electrochem. Commun.* **2014**, 46, 148-151.

55. Pumera, M. Electrochemistry of graphene, graphene oxide and other graphenoids: Review. *Electrochem. Commun.* **2013**, 36, 14-18.

56. Wen, F.; Xie, C.; Xia, X.; Le, G. Electrochemical study of the corrosion behaviour of copper/low-density polyethylene microcomposite in the simulated uterine solution. *J. Electroanal. Chem.* **2007**, 603, 219-226.

57. Liu, J.; Wang, Z.; Liu, F. D.; Kane, A. B.; Hurt, R. H. Chemical Transformations of Nanosilver in Biological Environments. *ACS Nano* **2012**, 6, 9887-9899.

58. Ho, C.-M.; Wong, C.-K.; Yau, S. K.-W.; Lok, C.-N.; Che, C.-M. Oxidative Dissolution of Silver Nanoparticles by Dioxygen: A Kinetic and Mechanistic Study. *Chemistry – An Asian Journal* **2011**, 6, 2506-2511.

59. Kent, R. D.; Vikesland, P. J. Controlled Evaluation of Silver Nanoparticle Dissolution Using Atomic Force Microscopy. *Environ. Sci. Technol.* **2011**, 46, 6977-6984.

60. Zhang, H.; Lv, X.; Li, Y.; Wang, Y.; Li, J. P25-Graphene Composite as a High Performance Photocatalyst. *ACS Nano* **2009**, 4, 380-386.

61. Luo, Q.-P.; Yu, X.-Y.; Lei, B.-X.; Chen, H.-Y.; Kuang, D.-B.; Su, C.-Y. Reduced Graphene Oxide-Hierarchical ZnO Hollow Sphere Composites with Enhanced Photocurrent and Photocatalytic Activity. *J. Phys. Chem. C* **2012**, 116, 8111-8117.

62. Liang, Y.; Wang, H.; Zhou, J.; Li, Y.; Wang, J.; Regier, T.; Dai, H. Covalent Hybrid of Spinel Manganese–Cobalt Oxide and Graphene as Advanced Oxygen Reduction Electrocatalysts. *J. Am. Chem. Soc.* **2012**, 134, 3517-3523.

63. Guo, S.; Wen, D.; Zhai, Y.; Dong, S.; Wang, E. Platinum Nanoparticle Ensemble-on-Graphene Hybrid Nanosheet: One-Pot, Rapid Synthesis, and Used as New Electrode Material for Electrochemical Sensing. *ACS Nano* **2010**, 4, 3959-3968.

64. Guo, S.; Dong, S.; Wang, E. Three-dimensional Pt-on-Pd bimetallic nanodendrites supported on graphene nanosheet: facile synthesis and used as an advanced nanoelectrocatalyst for methanol oxidation. *ACS Nano* **2009**, 4, 547-555.

65. Reske, R.; Mistry, H.; Behafarid, F.; Roldan Cuenya, B.; Strasser, P. Particle Size Effects in the Catalytic Electroreduction of CO2 on Cu Nanoparticles. *J. Am. Chem. Soc.* **2014**, 136, 6978-6986.

66. Gattrell, M.; Gupta, N.; Co, A. A review of the aqueous electrochemical reduction of CO2 to hydrocarbons at copper. *J. Electroanal. Chem.* **2006**, 594, 1-19.

67. Sen, S.; Liu, D.; Palmore, G. T. R. Electrochemical Reduction of CO2 at Copper Nanofoams. *ACS Catal.* **2014**, 4, 3091-3095.

68. Saha, S.; Pal, A.; Kundu, S.; Basu, S.; Pal, T. Photochemical Green Synthesis of Calcium-Alginate-Stabilized Ag and Au Nanoparticles and Their Catalytic Application to 4-Nitrophenol Reduction. *Langmuir* **2009**, 26, 2885-2893.

69. Esumi, K.; Isono, R.; Yoshimura, T. Preparation of PAMAM− and PPI−Metal (Silver, Platinum, and Palladium) Nanocomposites and Their Catalytic Activities for Reduction of 4-Nitrophenol. *Langmuir* **2003**, 20, 237-243.

70. Wunder, S.; Polzer, F.; Lu, Y.; Mei, Y.; Ballauff, M. Kinetic Analysis of Catalytic Reduction of 4-Nitrophenol by Metallic Nanoparticles Immobilized in Spherical Polyelectrolyte Brushes. *J. Phys. Chem. C* **2010**, 114, 8814-8820.

71. Ciganda, R.; Li, N.; Deraedt, C.; Gatard, S.; Zhao, P.; Salmon, L.; Hernandez, R.; Ruiz, J.; Astruc, D. Gold nanoparticles as electron reservoir redox catalysts for 4-nitrophenol reduction: a strong stereoelectronic ligand influence. *Chem. Commun. (Cambridge, U. K.)* **2014**, 50, 10126-10129.

72. Costa, R. C. C.; Moura, F. C. C.; Ardisson, J. D.; Fabris, J. D.; Lago, R. M. Highly active heterogeneous Fenton-like systems based on Fe0/Fe3O4 composites prepared by controlled reduction of iron oxides. *Appl. Catal., B* **2008**, 83, 131-139.

73. Costa, R. C. C.; Moura, F. C. C.; Oliveira, P. E. F.; Magalh ães, F.; Ardisson, J. D.; Lago, R. M. Controlled reduction of red mud waste to produce active systems for environmental applications: Heterogeneous Fenton reaction and reduction of Cr(VI). *Chemosphere* **2010**, 78, 1116-1120.

74. Piao, Y.; Kim, J.; Na, H. B.; Kim, D.; Baek, J. S.; Ko, M. K.; Lee, J. H.; Shokouhimehr, M.; Hyeon, T. Wrap-bake-peel process for nanostructural transformation from [beta]-FeOOH nanorods to biocompatible iron oxide nanocapsules. *Nat. Mater.* **2008**, 7, 242-247.

75. Wu, P.; Du, N.; Zhang, H.; Yu, J.; Yang, D. Carbon Nanocapsules as Nanoreactors for Controllable Synthesis of Encapsulated Iron and Iron Oxides: Magnetic Properties and Reversible Lithium Storage. *J. Phys. Chem. C* **2011**, 115, 3612-3620.

76. Kittler, S.; Greulich, C.; Diendorf, J.; Koller, M.; Epple, M. Toxicity of silver nanoparticles increases during storage because of slow dissolution under release of silver ions. *Chem. Mater.* **2010**, 22, 4548-4554.

77. Kumar, A.; Vemula, P. K.; Ajayan, P. M.; John, G. Silver-nanoparticle-embedded antimicrobial paints based on vegetable oil. *Nat. Mater.* **2008**, 7, 236-241.

78. Xiu, Z.-m.; Zhang, Q.-b.; Puppala, H. L.; Colvin, V. L.; Alvarez, P. J. Negligible particle-specific antibacterial activity of silver nanoparticles. *Nano Letters* **2012**, 12, 4271-4275.

79. Yang, X.; Gondikas, A. P.; Marinakos, S. M.; Auffan, M.; Liu, J.; Hsu-Kim, H.; Meyer, J. N. Mechanism of silver nanoparticle toxicity is dependent on dissolved

silver and surface coating in Caenorhabditis elegans. *Environmental Science and Technology* **2011**, 46, 1119-1127.

80. Geranio, L.; Heuberger, M.; Nowack, B. The Behavior of Silver Nanotextiles during Washing. *Environ. Sci. Technol.* **2009**, 43, 8113-8118.
81. Dobias, J.; Bernier-Latmani, R. Silver Release from Silver Nanoparticles in Natural Waters. *Environ. Sci. Technol.* **2013**, 47, 4140-4146.
82. Lightcap, I. V.; Kosel, T. H.; Kamat, P. V. Anchoring Semiconductor and Metal Nanoparticles on a Two-Dimensional Catalyst Mat. Storing and Shuttling Electrons with Reduced Graphene Oxide. *Nano Lett.* **2010**, 10, 577-583.
83. Liang, Y. T.; Vijayan, B. K.; Lyandres, O.; Gray, K. A.; Hersam, M. C. Effect of Dimensionality on the Photocatalytic Behavior of Carbon–Titania Nanosheet Composites: Charge Transfer at Nanomaterial Interfaces. *J. Phys. Chem. Lett.* **2012**, 3, 1760-1765.
84. Xiang, Q.; Yu, J.; Cheng, B.; Ong, H. C. Microwave-Hydrothermal Preparation and Visible-Light Photoactivity of Plasmonic Photocatalyst Ag-TiO2 Nanocomposite Hollow Spheres. *Chem. - Asian J.* **2010**, 5, 1466-1474.
85. Cao, X.; Yin, Z.; Zhang, H. Three-dimensional graphene materials: preparation, structures and application in supercapacitors. *Energy Environ. Sci.* **2014**, 7, 1850-1865.

Chapter 4 Prestrain-induced 2.5D wrinkled graphene surface for directing cell alignment

4.1 Introduction

Patterning of surface topography is a powerful technique for controlling interfacial interactions between a material and its environment. [1] Topographical patterns can be created by etching or molding the surface of a single-component material, or through creation of heterostructures consisting of a substrate and a surface film with engineered texture. An emerging method for surface texturing is the creation of wrinkle patterns by controlled shrinkage of a stiff coating on a softer, compliant substrate. [2-5] This approach has been experimentally implemented in a variety of polymeric and inorganic material systems[6], and the wrinkle morphologies have been the subject of theoretical treatments of buckling instability. [7-9] An exciting new approach to the creation of these textured surface films is the growth or deposition of two-dimensional, sheet-like nanomaterials, such as graphene, whose atomically thin nature enables the creation of the ultrathin flexible films suitable for controlled wrinkling. Topographically patterned graphene has found numerous applications in optical and electronic devices, energy storage, and functional coatings. [10-19]

Here we demonstrate another application area for graphene surfaces with engineered wrinkle structures: as functional substrates for cell and tissue engineering. Planar graphene and graphene oxide (GO) have already been explored as substrates for biological cells and tissues[20-22], and remarkably, mesenchymal stem cells, myoblasts and fibroblasts appear to display enhanced viability compared to conventional tissue culture substrates[23-27]. A limitation of conventional flat, uniform 2D cell culture substrates, however, is that they lack the complexity of structural architectures found in the extracellular matrix in living tissue. On planar 2D surfaces, cells adopt strongly flattened

morphologies, and the resulting cellular behavior can deviate from the natural behavior observed in a physiological 3D context.

Modern nanopatterning approaches strive to create biomimetic features that are comparable in size and geometry with molecular elements of the natural microenvironment. [28-31] In particular, interstitial collagen in the extracellular matrix are bundled together with diameters from tens to hundreds of nanometers, as well as pore sizes or gaps on the order of 5-20 μm. [32] These anisotropic topographies can affect cell morphology and orientation, a phenomenon known as contact guidance [33]. Cell-substrate interactions that mimic this anisotropy using aligned grooves have been previously investigated on polymeric materials using controlled buckling [34-36] and micropatterning [37-41], revealing altered migration dynamics, proliferation, gene expression and differentiation. In this context, graphene substrates incorporating microscale topography are intriguing as functional substrates for cell and tissue engineering, but have not, to our knowledge, been previously examined. Overall, the design of biomaterial interfaces based on graphene represents an exciting approach for understanding fundamental cell biology, nanostructured scaffolds for tissue engineering and regenerative medicine as well as to promote biocompatibility and biointegration of functional medical implants in neuronal, cardiovascular or epidermal tissues.

In this chapter, we demonstrate the formation of wrinkled multilayer graphene surfaces using GO solution phase deposition on pre-stretched elastomeric substrates followed by relaxation and thermal stabilization. We find that the topography of these stabilized graphene oxide (s-GO) surfaces is maintained during thermal treatment, and displays exceptionally sharp features, whose spatial periodicity can be systematically tuned

by simple variation of the GO concentration in the deposition suspension. We examine the effect of these wrinkled s-GO architectures on human and murine fibroblast cells, which attach and remain viable, and cause important changes in cell orientation, alignment, and morphology relative to cells on planar s-GO. This work establishes the feasibility of graphene wrinkle engineering for the fabrication of textured substrates for cell and tissue engineering and potential applications in biomedical implants.

4.2 Materials and Methods

4.2.1. Fabrication of textured surfaces

GO suspensions were prepared by a modified Hummer's method and purified and characterized as described previously. These GO sheets are primarily in monolayer form in aqueous suspension and are 1-5 μm in lateral dimension with a C/O atomic ratio of approximately 1.8 [42]. The elastomeric substrates were silicone rubber sheets (McMaster-Carr) of 1/16" thickness and either 50A or 20A hardness. The elastic modulus of the substrates was measured using an Instron 5882. The elastomer films were cut into 4x2 cm pieces, washed with deionized water, and fixed at one end to glass slides. The films were stretched uniaxially to a desired pre-strain (1.5%-50%) and secured with a fastener. A specific volume of GO aqueous suspension (typically 150 uL of 0.2 g/L GO) was pipetted onto the substrate, dried overnight, and relaxed to form the wrinkle patterns (Fig. 4-1). For cell studies the films were rendered stable to re-dissolution in cell culture medium by mild thermal treatment through annealing overnight at 120 ℃ in air.

4.2.2. Morphology characterization

Morphologies of the textured surfaces were characterized by optical microscopy, atomic force microscopy (Asylum MFP-3D Origin AFM) in pulse mode, and field emission SEM (LEO 1530 VP) in the variable operating pressure mode without coating the samples, in top view (for wavelength determination) or high tilt (for transverse profiles). The characteristic wavelength of the wrinkle features were quantified by sampling grey-scale line profiles from the micrographs using Gatan DigitalMicrograph, followed by Fast Fourier Transformation in MATLAB (Mathworks).

4.2.3. Cell culture

NIH-3T3 mouse fibroblasts were a gift from Dr. Agnes Kane (Brown University), while normal human fibroblasts (NHF cells) derived from neonatal foreskin were a gift from Dr. Jeffrey Morgan (Brown University). Cells were cultured in high glucose, pyruvate Dulbecco's Modified Eagle's Medium (DMEM, Life Technologies # 11995) supplemented with 10% Fetal Bovine Serum (FBS), 100 units/mL penicillin, and 100 ug/mL streptomycin. Both cell lines were carried out under standard culture conditions: incubation at 37˚C in a 5% CO_2 gaseous environment, which pairs with the DMEM's sodium bicarbonate buffer system to maintain physiological pH, cells were cultured in T-25 flasks, and passaged at 70-80% confluence. Only low passage numbers were used in experiments (P5-P12 for NIH-3T3s and P4-P10 for NHFs).

4.2.4. Preparation of s-GO-coated substrates for cell culture experiments

Paired wrinkled and flat s-GO substrates were prepared as described previously. For cell culture, substrates were further processed by immersion and rinsing in DI water (Milli-Q, 18.2 MΩ) for at least 12 hours to remove debris and any contaminants. Substrates were then sterilized by UV exposure with a 30W lamp for 1 hour before transferring to a 24 well plate.

Once the s-GO materials were prepared and sterilized, cells cultured in T25 flasks were incubated with HyClone 0.05% Trypsin for detachment. Once cells were lifted off the flask, the suspension was transferred to a conical tube containing growth medium and centrifuged at 1000RPM for 5 minutes. The cell pellet was then re-suspended in culture medium, and cells were subsequently counted using an automated cell viability counter (Nexcelom Cellometer Auto 1000). Next, a 100uL droplet with a concentration of 40,000 cells/mL was deposited on the materials, allowed to settle for ~1 hour, and then the well was filled with 1 mL of culture media. After 48 h, the cell culture media was replenished.

4.2.5. Cell viability

After culturing cells on polystyrene, flat s-GO, and wrinkled s-GO substrates for 96 hours, culture medium was aspirated and replenished with media containing Hoechst (bis-Benzimide), diluted 1:2000. Cells were incubated for 30 minutes at 37˚C in 5% CO_2 to label cell nuclei, the Hoechst-media was aspirated, and cells were rinsed with 1X phosphate buffered saline (PBS). To label dead cells, DRAQ7 (BioStatus), diluted 1:100 in culture medium, was added to each well. Cells were incubated for an additional 10 minutes, and then imaged using an inverted epifluorescence microscope (Nikon TiE).

Images were acquired using a 10X Plan Fluor objective (NA 0.3, long working distance) with fluorescence illumination, provided by using a light-guide coupled Lumen Dynamics X-Cite 120 LED system. All images were acquired with 14-bit resolution using a sCMOS camera (Andor Neo). Care was taken to ensure that all images were recorded with identical acquisition parameters (exposure time, camera gain/gamma control and microscope aperture settings). To determine the percentage of viable cells in each condition, the total cell nuclei (Hoechst label) and dead cells (DRAQ7 label) were counted using CellProfiler (version 2.1, Broad Institute). Cell viability was defined by the ratio of live cells (Total nuclei count – Dead cell count) to the total number of cells (Total nuclei count); the results were plotted as bar graphs, with the use of MATLAB (Mathworks).

4.2.6. Immunostaining and fluorescence imaging

After 96 h of culture on wrinkled and flat s-GO substrates, cells were fixed using 4% paraformaldehyde in 1X PBS. Cells were then permeabilized with 0.1% Triton-X 100 in 1X PBS. For F-actin microfilament detection, cells were immunostained with a conjugated antibody, Alexa Fluor 647 Phalloidin (Invitrogen), diluted 1:80 in 1% nonfat dry milk in 1X PBS. Cell nuclei were also labeled by counterstaining with Hoechst (bis-Benzimide), diluted 1:5000 in 1X PBS. 1X PBS was added to the wells, and immunostained samples were placed upside down in a new 24 well plate for imaging using an inverted epifluorescence microscope (Nikon TiE). Images were acquired using a 10X Plan Fluor objective (NA 0.3, long working distance) or a 20X Super Plan Fluor objective (NA 0.45, extra long working distance). Fluorescence illumination was provided using a light-guide coupled Lumencore Sola white light excitation system. All images were

acquired with 14-bit resolution using a sCMOS camera (Andor Neo). Care was taken to ensure that all images were recorded with identical acquisition parameters (exposure time, camera gain/gamma control and microscope aperture settings).

4.2.7. Image processing for quantification of cell morphology

CellProfiler (version 2.1, Broad Institute) was utilized for cell segmentation and analysis [43], with manual verification afterwards. First, fluorescently labeled nuclei were segmented as primary objects using maximum correlation thresholding (MCT) and clumped objects were resolved using shape and intensity. Next, based on the location of the nuclei, fluorescently labeled F-actin in the cell body was segmented as a secondary object. For wrinkled surfaces, secondary objects were best segmented by a robust background threshold and adaptive threshold strategy. Instead, for flat controls, secondary objects were best segmented using the Ostu thresholding method and global thresholding strategy. Finally, the "MeasureObjectSizeShape" module was employed to extract the following shape descriptors for the detected objects:

Area: The actual number of pixels in the region.

Eccentricity: The eccentricity of the ellipse that has the same second-moments as the region. The eccentricity is the ratio of the distance between the foci of the ellipse and its major axis length. The value is between 0 and 1. (0 and 1 are degenerate cases; an ellipse whose eccentricity is 0 is actually a circle, while an ellipse whose eccentricity is 1 is a line segment.)

Solidity: The proportion of the pixels in the convex hull that are also in the object, i.e. ObjectArea/ConvexHullArea. Equals 1 for a solid object (i.e., one with no holes or has

a concave boundary), or <1 for an object with holes or possessing a convex/irregular boundary.

Orientation: The angle (in degrees ranging from -90 to 90 degrees) between the x-axis and the major axis of the ellipse that has the same second-moments as the region.

Compactness: The variance of the radial distance of the object's pixels from the centroid divided by the area.

MinorAxisLength: The length (in pixels) of the minor axis of the ellipse that has the same normalized second central moments as the region.

MaxFeretDiameter: The Feret diameter is the distance between two parallel lines tangent on either side of the object (imagine taking a caliper and measuring the object at various angles). The maximum Feret diameter is the largest possible diameter, rotating the calipers along all possible angles.

We found that width of a cell was poorly approximated by the minor axis of an ellipse with equivalent second central moments, resulting in an overestimation of cell width. Instead, we defined an alternate metric:

Average Cell Width = Area/MaxFeretDiameter, which is based on the actual area of the cell.

4.2.8. Cell orientation and statistical analysis

A variety of circular statistical tests were applied using Oriana (Kovach Computing Services) to test whether cellular orientations were uniformly distributed (one-sample tests) or to compare the similarity of two distributions (multiple sample tests) [44]. Rao's Spacing

Test was used to evaluate the null hypothesis that a given circular dataset is uniformly distributed by checking if the differences between successive measurements are comparable to 180 °/N, where N is the number of measurements. In addition, the Mardia-Watson-Wheeler test was used to evaluate the null hypothesis that two samples have identical distributions as a circular analogue of the two sample t-test. It should be noted that, for simplicity, the coordinate system for wrinkled materials was defined along the length of the wrinkles. Circular statistics were plotted in MATLAB (Mathworks) using ROSE.

For all other metrics of cell morphology, the statistical distributions were compared using the two-sample Kolmonogorov-Smirnov test in MATLAB (Mathworks). Statistical significance was determined by rejecting the null hypothesis at $p \leqslant 0.05$ (5% significance level). Plots were also generated in MATLAB, as a combination of BOXPLOT, where the dividing line corresponds to the median, 25th and 75th percentiles are indicated by the box edges and whiskers correspond to 99.3% coverage, as well as PLOTSPREAD (MATLAB File Exchange), which displays data points representing individual cell measurements.

4.3 Results and discussion

4.3.1 Film fabrication and structure

The main objective of this research was to explore wrinkled GO surfaces as anisotropic cell attachment substrates for control of cell alignment and morphology in tissue engineering applications. We chose a fabrication route based on GO wet deposition and mild thermal treatment, which is a potentially practical and scalable method that is an attractive alternative to large-area coverage by pristine CVD graphene. Figure 4-2 shows

the basic morphology of the wrinkled GO surfaces prior to thermal treatment created by relaxation of substrates with 50% uniaxial pre-strain and covered by 200 nm thick GO multilayer films. Relaxation produces a series of nearly parallel ridges with high-curvature crests separated by broader valleys (Fig. 4-1).

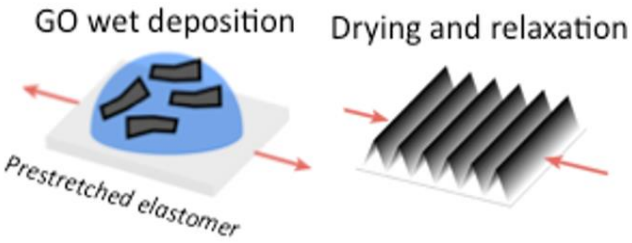

Figure 4-1. Illustration of the fabrication process for wrinkled GO multilayer films.

The wrinkle patterns can be removed by re-stretching to the initial state (Fig. 4-2A), and the process is reversible over multiple cycles. These features are similar to those observed previously for pristine few-layer graphene coatings undergoing similar uniaxial compression [16, 18]. The present films show longitudinal cracking (Fig. 4-2B) during relaxation, which we suspected was due to Poisson expansion in the transverse direction. The cracks here did not appear to affect the periodic wrinkle textures, but do reveal the underlying substrate, which would be an undesirable feature in some applications. We therefore sought a solution, and found that the cracks could be suppressed by fixing the sides of the film during the pre-stretch to mechanically constrain its Poisson contraction, which then also suppresses its subsequent Poisson expansion during the relaxation and wrinkling process (Fig. 4-2C).

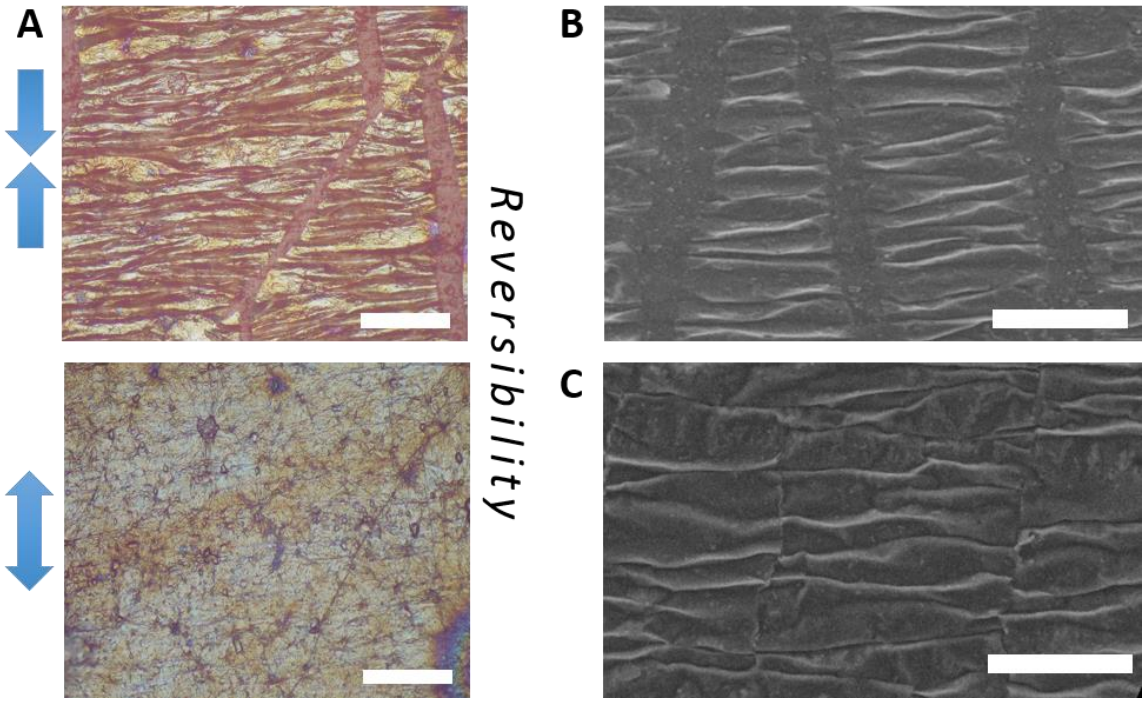

Figure 4-2. Reversibility of wrinkled graphene and suppression of microcracks by transverse constraint. (A) Demonstration of reversibility by re-stretching under an optical microscope, scale bar is 100 μm. (B) AFM image showing the basic morphology of parallel ridges with sharp crests (light) and broader valleys (dark). Film thickness is 20 nm and scale bar is 20 μm. (C) SEM showing longitudinal microcracks that form when simple uniaxial relaxation occurs (left image). These cracks can be suppressed (right image) if the substrate is constrained in the transverse direction during relaxation to prevent the expansion associated with the Poisson effect, scale bar 100 μm.

The longitudinal cracks in the films fabricated in our early attempts without transverse pinning were undesired, but did make it possible to directly view the cross-section wrinkle profiles in detail (Fig. 4-3). The wrinkles are delaminated buckled structures with nearly straight slopes and with curvatures concentrated at the ridge tops. The ridge tops have characteristic curvatures on the order of the film thickness, and are similar to the sharp ridges seen in crumpled graphene particles formed during isotropic compression [45, 46], which are 3D structures having both ridges and vertices. The films remain on the substrate through adhesion at the valley floor regions, and the local delamination produces cavities with triangular cross-sections between the substrate and

film. This delamination buckling in multilayer GO has also been observed in pristine few-layer or multi-layer graphene films [16, 18], while amorphous carbon films fabricated by ion beam deposition from hydrocarbons do not show such local delamination when they undergo spontaneous buckling associated with growth-induced film compression [19]. The difference may reflect very different film-substrate bonding in the graphene-based films and the ion-beam deposited films.

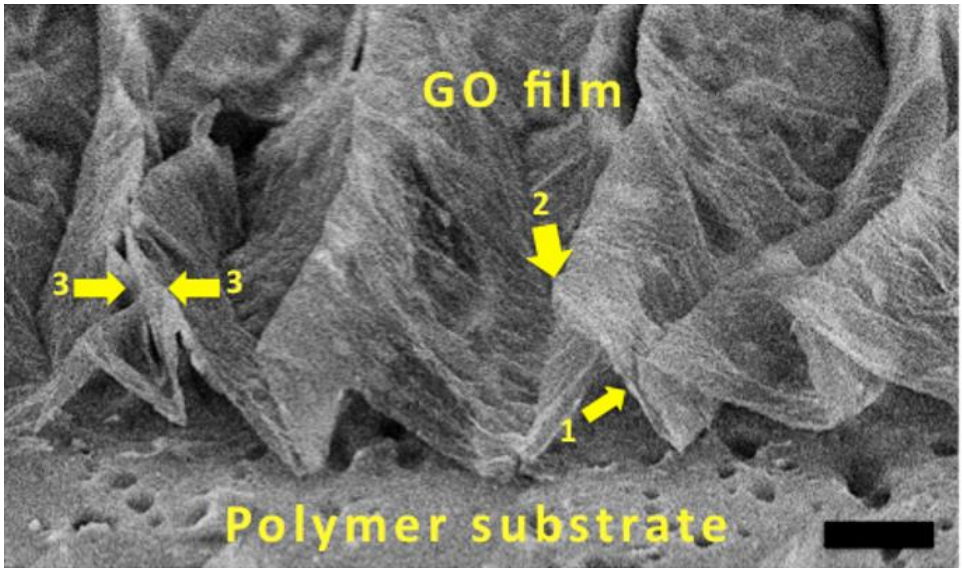

Figure 4-3. High-tilt SEM image of transverse profiles , which shows a delaminated buckle structure with nearly straight slopes (arrow 1) and curvature concentrated at the ridge tops (arrow 2). These wrinkles are high-amplitude buckled ridges in which some primary peaks have collapsed on neighbors to create double-ridges (arrow 3). Scale bar 20 μm. The samples unless noted use 50% pre-stretch and 200 ug/ml GO suspension that gives a nominal GO film thickness of 200 nm.

4.3.2 Wavelength and amplitude tuning

For manipulation of cell alignment and morphology, it is desirable to control the amplitude and wavelength of the wrinkle patterns in our multilayer graphene films. Approaches to this control are readily suggested by the significant literature on the theoretical and experimental mechanics of stiff thin films on pre-stretched compliant

substrates [15, 47, 48]. The critical buckling strain is reported to be $\varepsilon_c = 1/4\left[\frac{3E_s(1-\nu_f^2)}{E_f(1-\nu_s^2)}\right]^{2/3}$, where E_f and E_s are the Young's modulus of film and substrate, respectively, and ν_s and ν_f are the Poisson's ratio of elastomer substrate and stiff film, respectively. When this strain is exceeded, wrinkles develop with a wavelength:

$$\lambda_0 = 2\pi h_f \left[\frac{E_f(1-\nu_s^2)}{3E_s(1-\nu_f^2)}\right]^{1/3} \quad (1)$$

where, h_f is the film thickness. This theory is valid in the limit of small deformation. When the deformation is large, wavelength becomes strain-dependent [49], and consequently the corresponding wavelength is [50]

$$\lambda = \frac{\lambda_0}{(1+\varepsilon_{pre})(1+\xi)^{1/3}} \quad (2)$$

where λ_0 is the wavelength based on small deformation theory, ε_{pre} is the pre-strain and a pre-stretch factor $(1+\varepsilon_{pre})(1+\xi)^{1/3}$ is included with $\xi = 5\varepsilon_{pre}(1+\varepsilon_{pre})/32$. When ε_{pre} is constant, the superficial wavelength λ only depends on the thickness of the film.

Equation (1) suggests the use of film thickness or substrate stiffness to tune wavelength. The former is an attractive option for multilayer GO films, whose thickness can be easily and systematically altered by changing the concentration in the deposition fluid. The results of both methods for wavelength tuning are illustrated in Fig. 4-4. For a given substrate, wavelengths can be changed by an order of magnitude (e.g. 3 to 30 μm for the softer substrate) by varying GO film thickness from 20-200 nm through increasing GO suspension concentration from 0.02-0.2 mg/ml. Based on the work of Kunz et al [15], we anticipate the ability to extend to nanoscale features by using monolayer or few-layer s-

GO, though it becomes increasingly difficult to fully cover the substrate with such ultrathin films made by tiling microscale GO sheets.

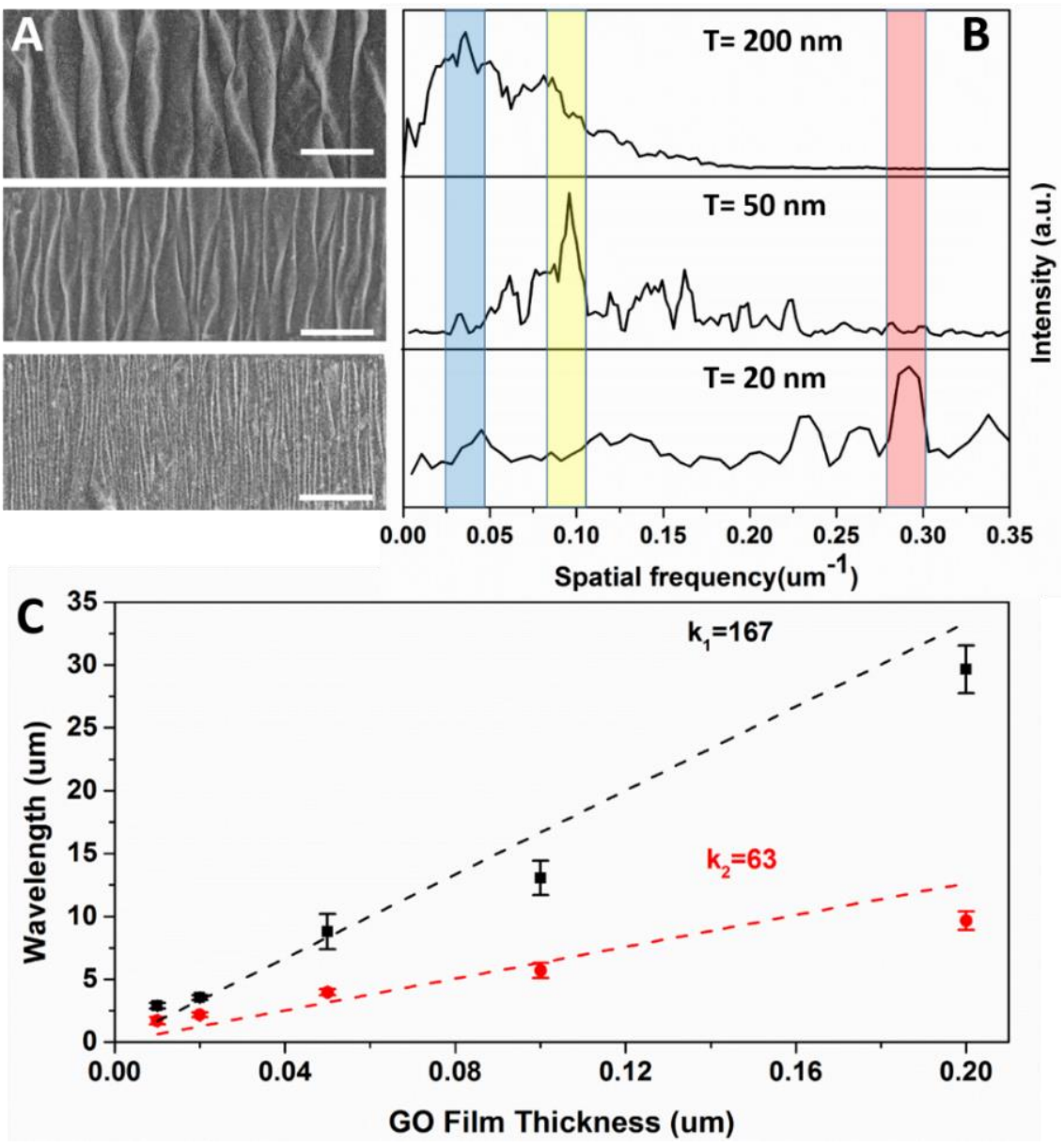

Figure 4-4. Wavelength tunability through control of multilayer GO film and through substrate selection. (A) SEM images of wrinkled GO films of thickness from 10 nm to 200 nm on the softer elastomer (modulus $5{\cdot}10^4$ Pa) and (B) their Fourier transform spectra with the dominant spatial frequency shaded. (C) Thickness-dependent wavelengths on softer (black squares) and stiffer elastomer (modulus $6{\cdot}10^5$ Pa; red circles) with linear regression slopes $\frac{\lambda}{h_f}$ shown. The scale bars in (A) represent 50 nm.

The linear relationship between the wavelength and film thickness is consistent with Eq. 1, and can be used to estimate the Young's modulus of the multilayer GO film. Taking $\varepsilon_{pre} = 50\%$, $\nu_f = 0.197$, [51] $\nu_s = 0.48$, we can obtain from equation (1) and (2),

$$E_f = 0.057 E_s \left(\frac{\lambda}{h_f}\right)^3 \tag{3}$$

giving an estimate of the film modulus of 8.6-13.3 GPa, which is similar to published experimental results obtained by other methods [52, 53]. The wavelength of our wrinkle features decreases with increasing pre-stretch in agreement with Eq. 2 as shown in Figure 4-5.

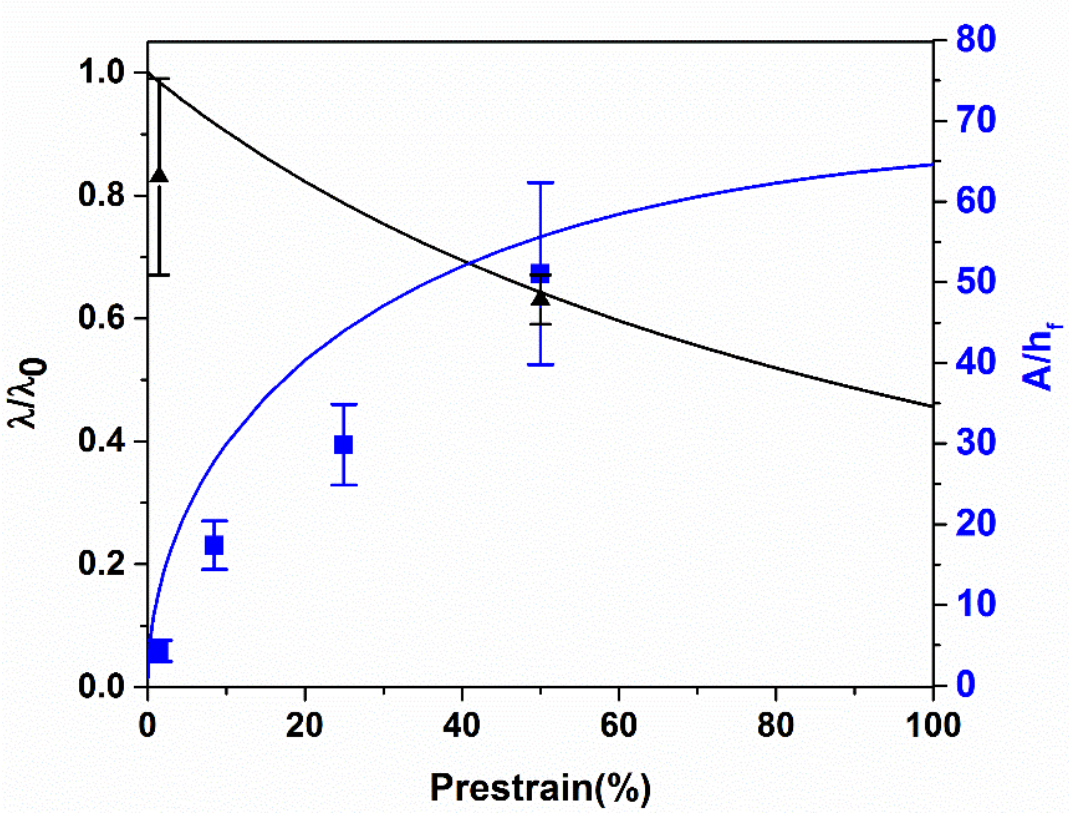

Figure 4-5. Dependence of wavelength λ normalized by small-strain wavelength λ_0 and amplitude A normalized by film thickness h_f as a function of pre-strain. Lines give behavior predicted by Eq. (2) and (4), which is compared to measurements from this study. Squares: amplitude; triangles: wavelength.

In dynamic experiments under the optical microscope, we observe that the ridges do not all appear at once during relaxation, but rather in pairs separated by a distance corresponding to the characteristic wavelength. Upon further relaxation the ridge pairs migrate closer together in response to the substrate shrinkage and the characteristic periodic wrinkle structure becomes uniform over large areas. The amplitude of the sinusoidal wrinkles that appear at small deformation is predicted by theory to be $A_0 = h_f\sqrt{\frac{\varepsilon_{pre}}{\varepsilon_c} - 1}$, while for large deformation, Song et al. proposed [50]

$$A = \frac{A_0}{\sqrt{1+\varepsilon_{pre}}(1+\xi)^{1/3}} \qquad (4)$$

This suggests that both film thickness and pre-stretch can be used to control feature height. Though these relations are for adherent and elastically deformed films, they can be used as an estimate for the delaminated buckle structures observed here.

The height and periodicity of these buckled structures was quantified through the use of atomic force microscopy (AFM). A representative scan of a buckled structure formed after a small pre-strain (1.5%) is shown in Fig. 4-6. The corresponding height profile for these structures shows a characteristic ridge height of ~2 μm (Fig. 4-6B). At moderate pre-strains (8.5 % or 25 %), increased ridge heights of approximately 7 and 12 μm were observed, respectively (Fig. 4-7). Finally, for large pre-strains (50%), the ridge heights became large enough that characterization with high-tilt SEM was more appropriate than AFM. These ridge heights were ~24 μm (Fig. 4-6C), with no correction for foreshortening needed to estimate these values at the high tilt angle used. Overall, pre-strain affects ridge amplitude much more than it affects wavelength (Fig. 4-5), so it is an effective and facile means to control feature height.

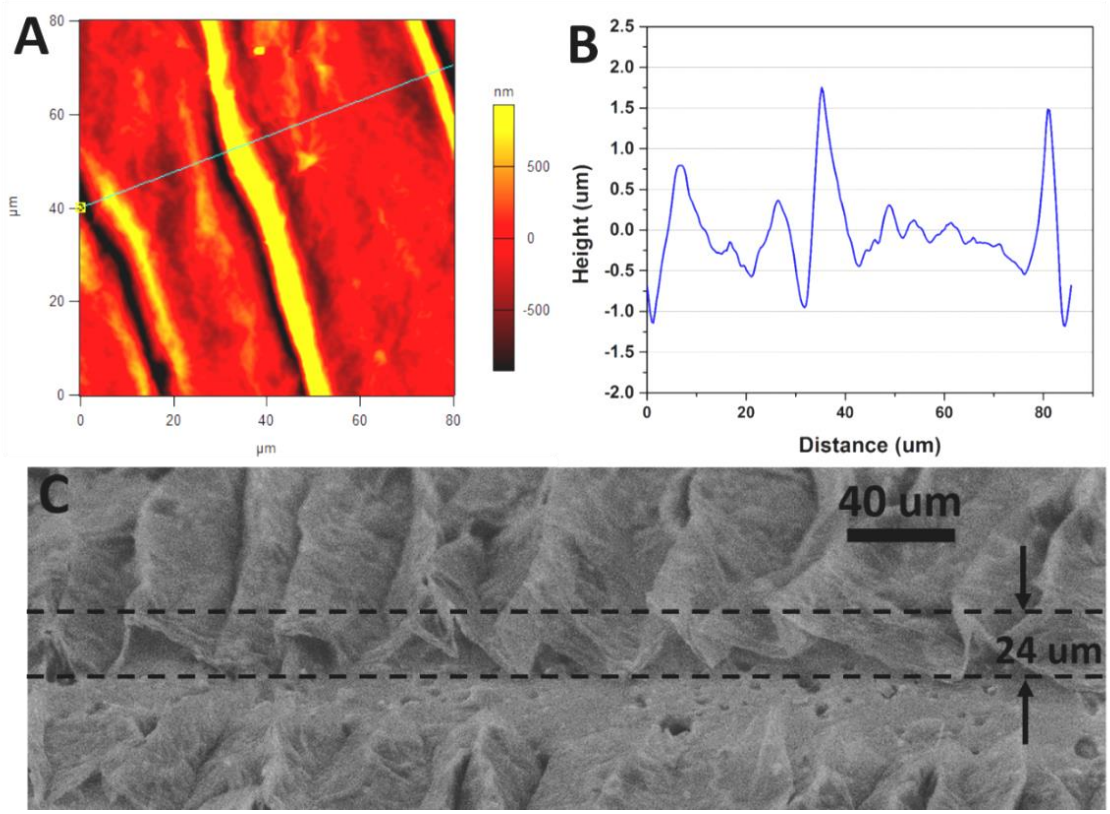

Figure 4-6. Pre-strain provides effective control over wrinkle feature height. (A) AFM image of multilayer graphene oxide film after release of 1.5% pre-strain on the softer elastomer substrate. (B) Height profile along line marked in (A). (C) High-tilt SEM image of wrinkled graphene on the soft elastomer substrate with 50% pre-strain.

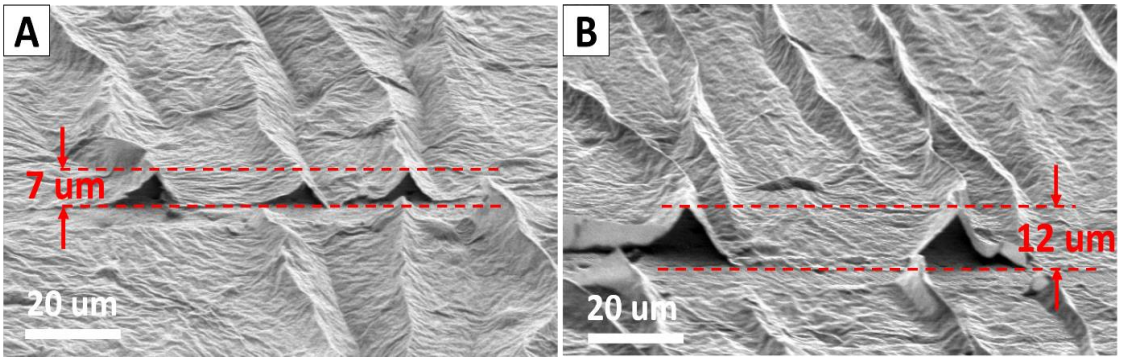

Figure 4-7. Tilt-view SEM images showing the average height of the GO wrinkles induced by 8.5% pre-strain (left) and 25 % pre-strain (right). GO film thickness: 200 nm.

4.3.3 Mild thermal treatment for liquid phase stability

The data above are for multilayer GO films in their as-produced, fully-oxidized state. We observed that these films were poorly suited for biological applications due to gradual re-dissolution of GO sheets in cell culture medium as well as instability in the feature heights in response to wetting and drying cycles. Infiltration of aqueous solutions into the delamination cavities between the film and substrate leads to peak collapse by capillary forces when the solution is driven out during the drying process (Figure 4-8). We hypothesize this effect is due to the hydrophilicity of GO, and could be managed by partial deoxygenation. We could not fully reduce GO due to the limited thermal stability of the elastomer substrate, and therefore explored long-time, mild heating as a possible route to stabilization.

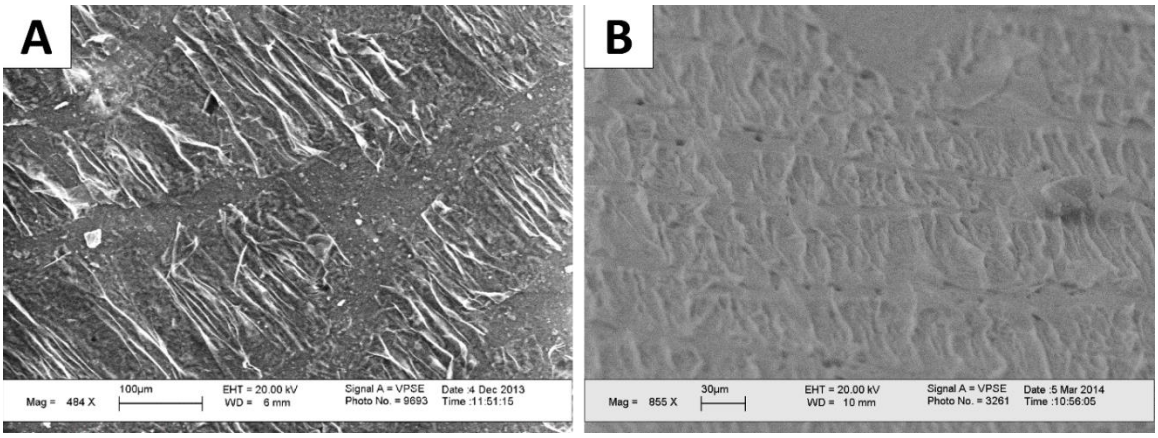

Figure 4-8. Top-down and tilt-view SEM images of wrinkled GO films after deposition and drying of one water droplet , showing capillary collapse and reduced feature height compared to 20 um height in Fig. 4-6C under the same conditions.

After overnight heating at 120 ℃ in air, we found the GO samples lost absorption peaks at ~850 and ~1200 cm^{-1} measured by Fourier transform infrared spectroscopy (Figure 4-9), which are typically assigned to C-O vibrations and may be due to the removal

or alteration of epoxides.[54] The reduced intensity of broad peak (O-H stretch) at ~3300 cm^{-1} indicates the removal of interstitial water, which may also contribute to the stabilization of GO. Most importantly, the stabilized graphene oxide (s-GO) films showed good retention of the wrinkle features in GO and also good stability following water immersion and drying (Figure 4-10).

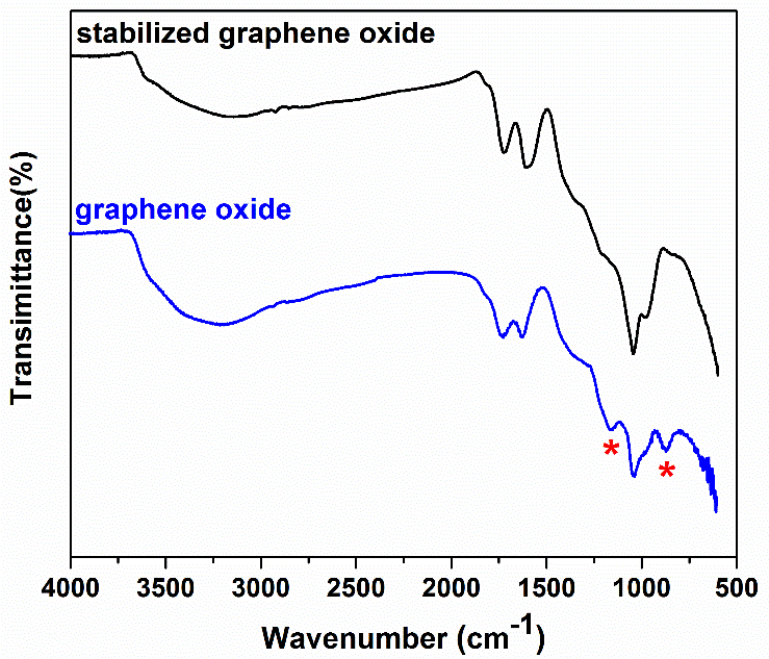

Figure 4-9. FT-IR of GO film and stabilized GO films prepared by thermal treatment at 120℃ overnight.

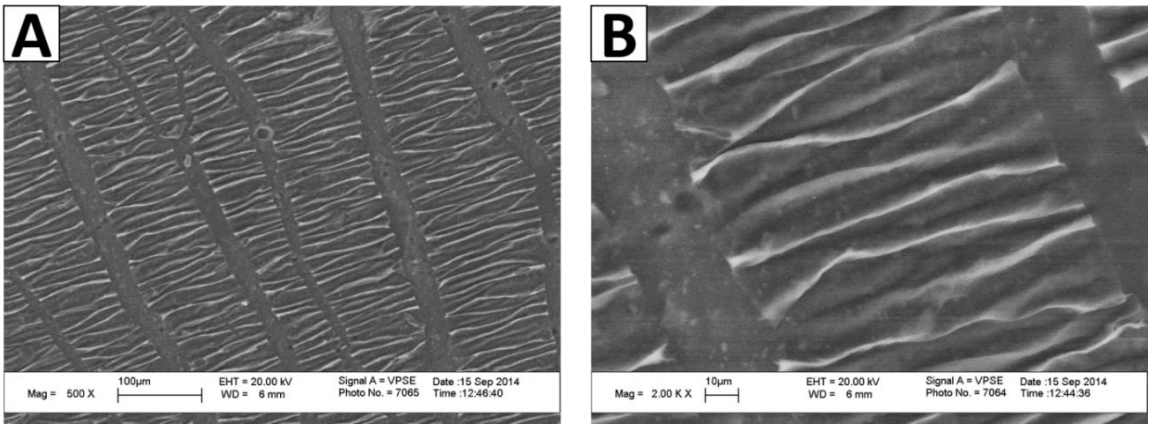

Figure 4-10. SEM images of winkled s-GO after deposition and drying of one water droplet , showing good stability against capillary forces during water evaporation.

These s-GO films were therefore used exclusively in the cell studies below. We were also interested in whether the wrinkled s-GO films could be made if the thermal treatment was carried out prior to the relaxation step. We found that relaxing pre-thermally-treated films led to a less regular wrinkle pattern and a larger number of small cracks (Figure 4-11). This may reflect stronger adhesion of s-GO to the substrate, but was not further investigated, and the higher quality films made by post-wrinkling thermal treatment were used in all of the cell studies.

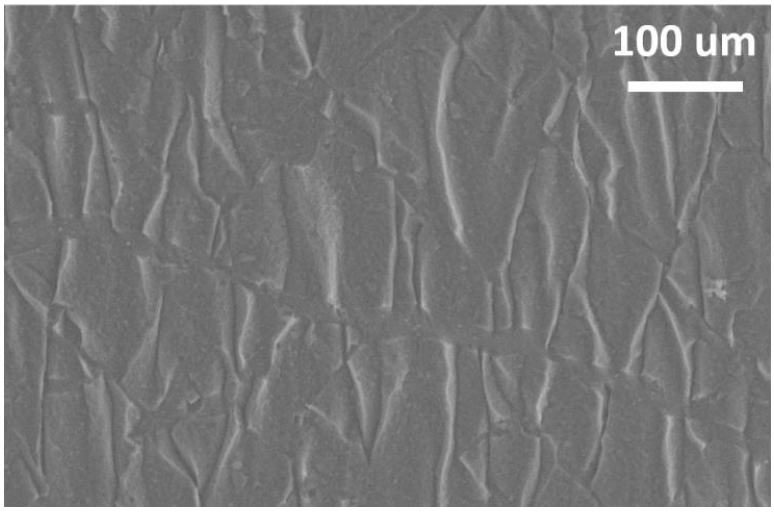

Figure 4-11. SEM image of less regular wrinkled s-GO that results from carrying out the thermal reduction stop prior to relaxation and wrinkling.

4.3.4 Cell alignment on flat and wrinkled s-GO substrates

Based on previous studies of cellular interactions with anisotropic grooved substrates, we hypothesized that wrinkled s-GO substrates with wavelength $\lambda \sim 25$ μm would be sufficient for cell confinement and alignment through contact guidance mechanisms [28-31]. As a model system, we chose to study murine and human fibroblasts on matched samples of 25 μm wavelength and flat s-GO substrates. Cell viability was measured on wrinkled and flat s-GO substrates compared with conventional tissue culture

plastic (polystyrene) using DRAQ7 (Biostatus), a far-red fluorescent DNA dye that only stains dead and membrane compromised cells [55]. These measurements showed that cell viability was consistently over 95% on wrinkled and flat s-GO substrates (Figures 4-12 and 4-13), indicating excellent biocompatibility.

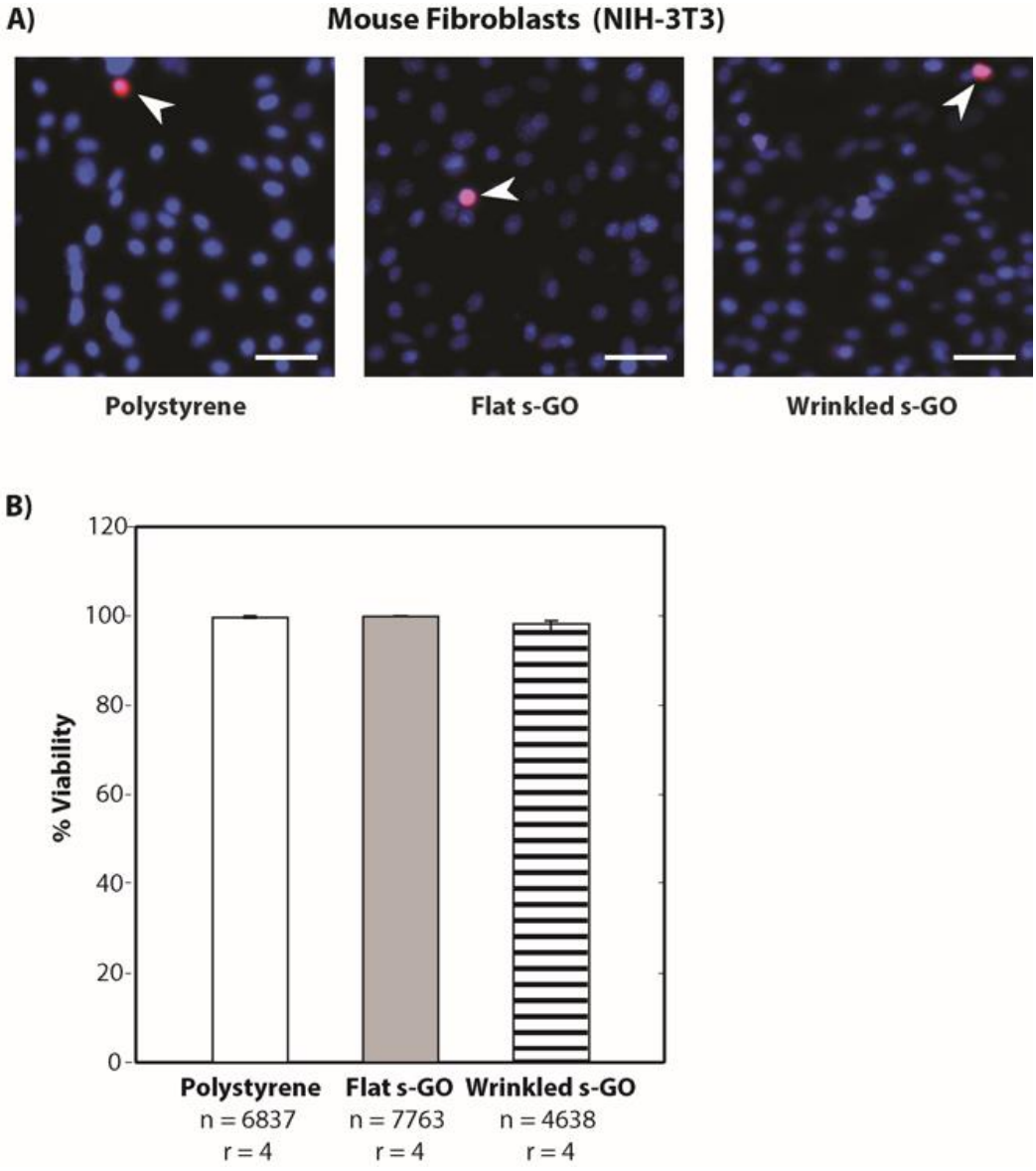

Figure 4-12. The viability of NIH-3T3 cells cultured on s-GO materials. (A) Fluorescence images of nuclei (blue, Hoechst) and dead cells (red, DRAQ7) for NIH-3T3 cells cultured on polystyrene, flat graphene, or wrinkled graphene substrates (~25 μm period) for 96 hours. White arrows point to representative dead cells. (B) Bar graph of the percentage of viable NIH-3T3 cells on the indicated substrates. The total number of cells counted per condition is indicated by (n); the number of replicates per condition is indicated by (r). Scale bar = 50 μm.

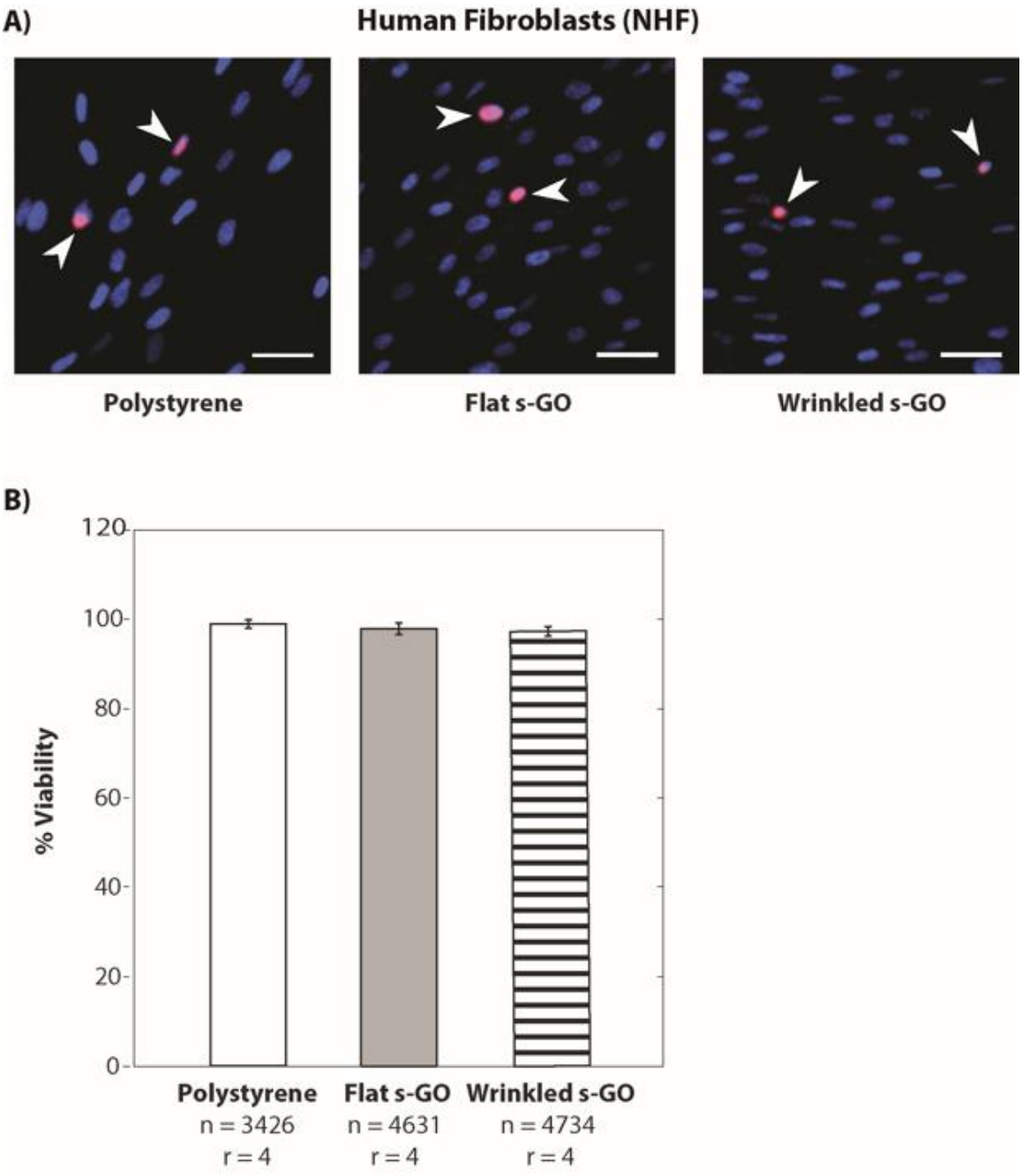

Figure 4-13. Viability of NHF cells cultured on s-GO materials. (A) Fluorescence images of nuclei (blue, Hoechst) and dead cells (red, DRAQ7) for NHF cells cultured on polystyrene, flat graphene, or wrinkled graphene substrates (~25 μm period) for 96 hours. White arrows point to representative dead cells. (B) Bar graph of the percentage of viable NHF cells on the indicated substrates. The total number of cells counted per condition is indicated by (n); the number of replicates per condition is indicated by (r). Scale bar = 50 μm.

The angular orientation of NIH-3T3 mouse fibroblasts was then compared on wrinkled (~25 μm wavelength) and flat s-GO substrates after culture for 96 h. To better visualize the cell morphology, both the nuclei and F-actin cytoskeleton were immunostained with fluorescent markers (Fig. 4-14). Qualitatively, NIH-3T3 fibroblasts appeared highly aligned on the wrinkled substrates (Fig. 4-14A) and randomly oriented on the flat substrates (Fig. 4-14B). To quantify this alignment, the cell morphology was automatically extracted using CellProfiler (Broad Institute) based on F-actin immunostaining. This software then determined an orientation based on the major axis of a best-fit ellipse to the cell morphology, which was manually verified. A circular histogram of these results are plotted as a rose plot for wrinkled (n = 164) and flat substrates (n = 137). The coordinate system for the wrinkled s-GO was defined so that 0 ° points along the wrinkle patterns (perpendicular to the axis of uniaxial stretch). NIH-3T3 fibroblasts on wrinkled substrates displayed a mean orientation angle of 0 ° with a standard deviation of 15 °. In contrast, NIH-3T3 fibroblasts on flat substrates displayed a mean orientation angle of 13 ° and a standard deviation of 57 °, which approximates a random orientation (with 0 ° mean, 52 ° standard deviation). To corroborate these results, primary human fibroblasts derived from neonatal foreskin (Normal Human Fibroblasts, NHF cells) were also cultured on these substrates. NHF cells also displayed qualitatively similar alignment on wrinkled substrates relative to flat substrates (Fig. 4-14C and D). Quantitatively, NHF cells on wrinkled substrates displayed a mean orientation angle of 0 ° with a standard deviation of 18 °. In comparison, NHF cells on flat s-GO substrates displayed a mean orientation angle of 16 ° with a standard deviation of 53 °, also approximating a random orientation distribution.

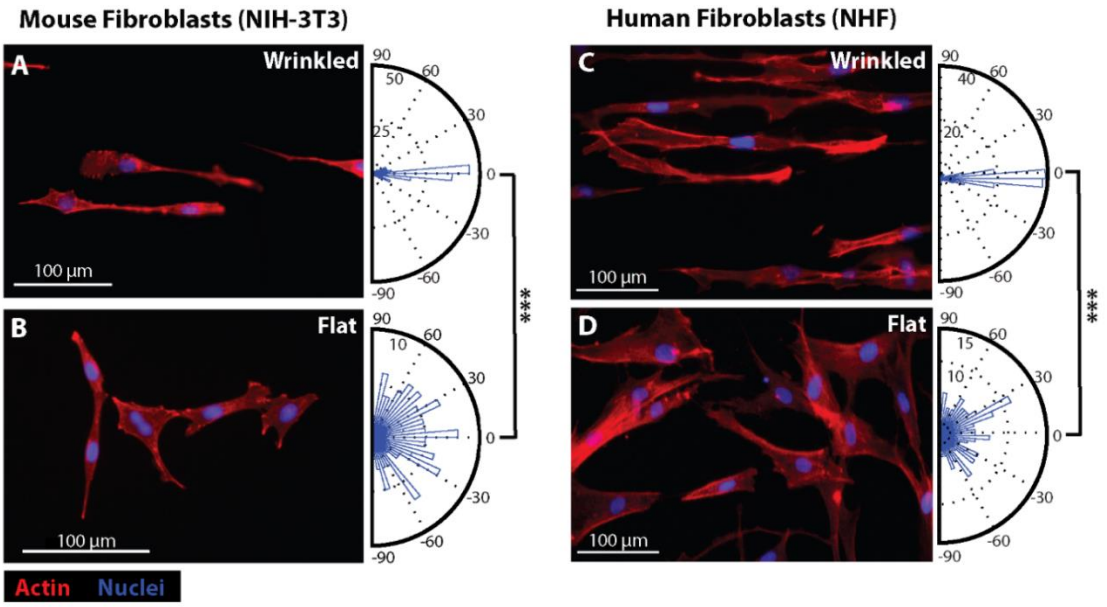

E

	NIH-3T3 Cells		NHF Cells	
Variable	Flat (n=137)	Wrinkled (n=164)	Flat (n=156)	Wrinkled (n=163)
Circular Standard Deviation	57°	15°	53°	18°
Rao's Spacing Test (p)	0.50 < p < 0.90	< 0.01	0.10 < p < 0.50	< 0.01
Mardia-Watson-Wheeler (p)	< 1E-12		< 1E-12	

Figure 4-14. Fibroblast culture on wrinkled graphene materials results in highly aligned cells. (A-D) Fluorescence images of Actin-phalloidin (red) and nuclei (blue) for NIH-3T3 and NHF cells cultured on 200 nm wrinkled s-GO substrates (~25 µm period) for 96 hours (A, C) and on paired flat graphene controls (B,D). Circular histograms of fibroblast orientation, ranging from -90 ° to 90 °, for cells on wrinkled and flat materials are displayed as orientation rose plots to the right of each corresponding fluorescence image (A-D). (E**)** Table of statistics summarizing circular standard deviation, and statistical significance for uniformity (one-sample test) and distribution (two-sample test) using Rao's spacing test and Mardia-Watson-Wheeler test, respectively.

The statistical significance of these results was assessed using two metrics. First, Rao's Spacing Test was used to evaluate the null hypothesis that a given circular dataset is uniformly distributed (Fig. 4-14E). For both NIH-3T3 and NHF cells, the angular orientation on wrinkled substrates was non-uniform ($p < 0.01$), while the angular orientation on flat substrates was uniform ($p > 0.10$). Next, the Mardia-Watson-Wheeler test was used to evaluate the null hypothesis that two circular datasets have identical

distributions. For both NIH-3T3 and NHF cells, the distribution of angular orientations of wrinkled and flat substrates were significantly different ($p < 10\text{-}12$).

4.3.5 Cell morphology on flat and wrinkled s-GO substrates.

The morphology of NIH-3T3 and NHF cells was analyzed by extracting cell shape based on F-actin immunostaining. Briefly, CellProfiler was used to segment fluorescent nuclei in the blue fluorescent channel, which served as a starting point to segment the surrounding cell body in the red fluorescent channel (Fig. 4-15A). The morphology was then quantified using a number of geometric parameters.

First, an average cell width was measured for NIH-3T3 and NHF cells on wrinkled and flat substrates. NIH-3T3 cells on wrinkled substrates displayed an average cell width of 9 μm and standard deviation of 3.3 μm, while cells on flat substrates had an average cell width of 13 μm and a standard deviation of 8.7 μm (Fig. 4-15B). In addition, NHF cells on wrinkled substrates display an average cell width of 16 μm with a standard deviation of 8.0 μm, while cells on flat substrates had an average cell width of 29 μm with a standard deviation of 10.3 μm (Fig. 4-15B). Overall, both fibroblast lines displayed narrower morphologies with smaller standard deviations on wrinkled substrates compared to flat substrates, with highly significant differences ($p < 10\text{-}3$). These narrower cell widths were comparable to the wrinkle spacing of ~25 μm, suggesting that the elongation reflects some degree of cell micro-confinement in the inter-ridge valley spaces.

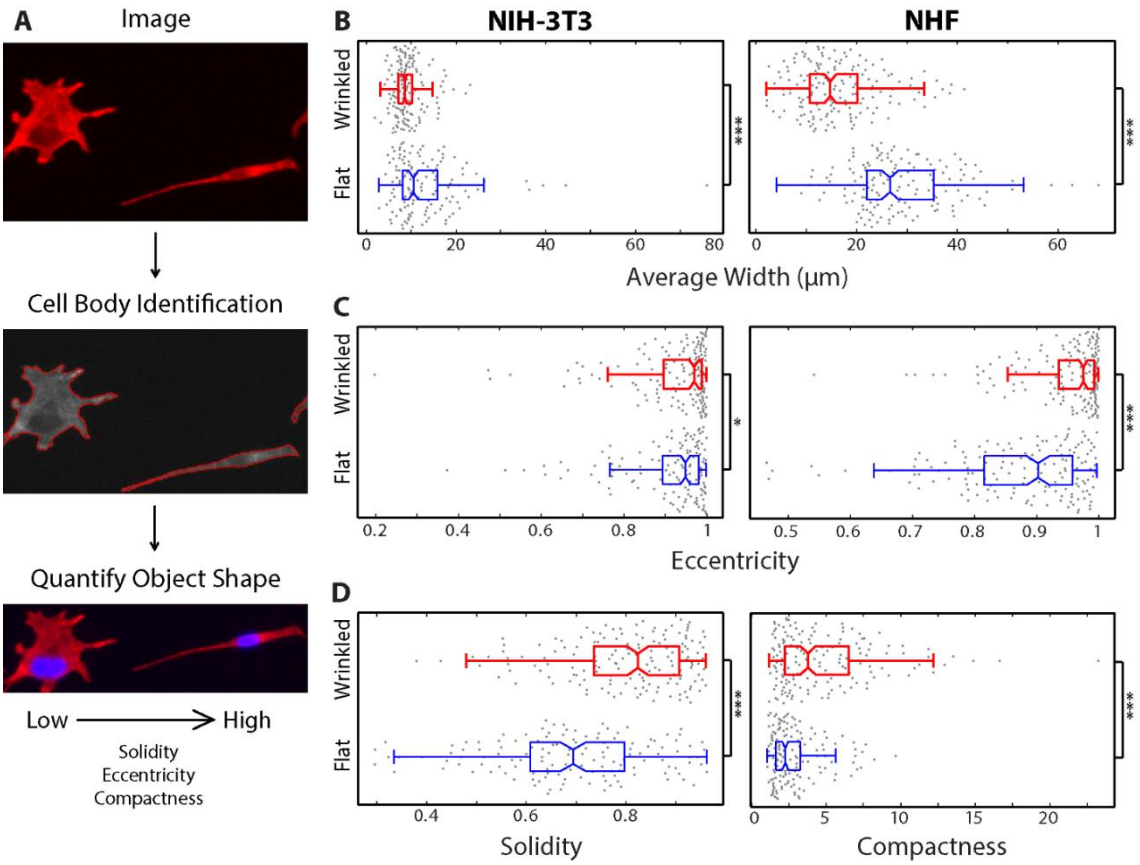

Figure 4-15. Image analysis of fibroblasts on graphene-based materials demonstrates distinct morphological features for different cell types on wrinkled vs. flat substrates. (A) Process flow for image analysis/cell segmentation: fluorescence images are split into separate channels for each color, CellProfiler outlines cells by distinguishing between pixels in the background and foreground, automated object shape features are calculated. (B-D) Boxplots of quantitative shape features for the fibroblasts were plotted with MATLAB. 25th and 75th percentiles are indicated by the box edges, the median value is displayed as the dividing line of the box, data not considered outliers are contained within the boxplot whiskers, and data points representing individual cell measurements are overlaid as plotted dots (Red boxplots= cells on wrinkled substrates, blue boxplots = cells on flat control substrates).(B) Comparison of average cell width for fibroblasts on wrinkled and flat substrates (as in Figure 4-14) for NIH-3T3 and NHF cells (left and right, respectively). (C) Comparison of eccentricity values for cells on wrinkled and flat substrates for NIH-3T3 and NHF cells (left and right, respectively). (D) Solidity values for NIH-3T3 cells on wrinkled and flat substrates (D, left) and compactness values for NHF cells on wrinkled and flat substrates (D, right). Statistical significance is indicated as follows: * $p < 0.05$; ** $p < 0.01$; *** $p < 0.001$

Next, the relative elongation of these cells was assessed in terms of the eccentricity of the best-fit ellipse to the cell morphology. An eccentricity of 0 corresponds to a circle, while an eccentricity of 1 corresponds to a line. NIH-3T3 cells on wrinkled substrates

displayed an average eccentricity of 0.921, compared to cells on flat substrates with an average eccentricity of 0.907 (Fig. 4-15C). These values, although similar, display a statistically significant difference ($p < 0.05$). NHF cells on wrinkled substrates displayed an average eccentricity of 0.947, compared to cells on flat substrates with an average eccentricity of 0.872. Interestingly, NHF cells on flat substrates display considerable variability in eccentricity, with a standard deviation of 0.112, compared to 0.069 for NHF on wrinkled substrates. Altogether, fibroblasts are intrinsically quite elongated on flat substrates, but are even more elongated on our wrinkled graphene surfaces, where they have eccentricity values close to 1, and the effect of the wrinkle texture is statistically significant. In order to further elucidate differences across these cell lines and conditions, several additional metrics were considered.

Qualitatively, NIH-3T3 fibroblasts may display multipolar, star-like morphologies, particularly on flat substrates. This shape was quantified in terms of the cell solidity metric, which describes an object shape based on the regularity of its boundaries. For example, a solid object with no holes has an area equal to the convex hull and thus has a solidity of 1, while an object with a very irregular boundary has a solidity that approaches 0. NIH-3T3 cells cultured on wrinkled substrates have an average solidity of 0.80 and a standard deviation of 0.12, while cells on flat substrates have an average solidity of 0.69 with a standard deviation of 0.16 (Fig. 4-15D). This data indicates that NIH-3T3 fibroblasts are biased towards bipolar morphologies on wrinkled substrates, compared to multipolar morphologies with more irregular boundaries on flat substrates. NHF cells (Table 4-1) display similar solidities on both wrinkled and flat substrates, which may occur due to a more dominant bipolar phenotype.

Table 4-1. Data Summary for Fibroblast Morphology Characterization. Legend: * $p < 0.05$; ** $p < 0.01$; *** $p < 0.001$; *NS* Not Significant

	NIH-3T3 Cells		**NHF Cells**	
	Control	**Wrinkled**	**Control**	**Wrinkled**
Width	***		***	
Mean	13.05	9.12	28.61	16.11
Median	10.48	8.57	26.64	14.80
SD	8.71	3.32	10.25	7.99
Eccentricity	*		***	
Mean	0.91	0.92	0.87	0.95
Median	0.95	0.97	0.90	0.97
SD	0.11	0.11	0.11	0.07
Solidity	***		*NS*	
Mean	0.69	0.80	0.58	0.61
Median	0.69	0.82	0.58	0.61
SD	0.16	0.12	0.17	0.16
Compactness	*NS*		***	
Mean	2.86	3.21	2.83	4.81
Median	2.41	2.42	2.25	3.77
SD	1.59	2.53	1.69	3.41

Finally, NHF cells displayed the greatest variability in radial distance from the object center, known as compactness. NHF cells on wrinkled substrates displayed a mean compactness of 4.8, with a standard deviation of 3.4, and cells on flat substrates have a mean compactness of 2.8, with a standard deviation of 1.7 (Fig. 4-15D, right). On the other hand, NIH-3T3 cells did not display a significant difference for cell compactness between wrinkled and flat substrates. These differences likely arise from differences in cell size between NHF and NIH-3T3 cells. Since NHF cells are larger, they are more confined and elongated on wrinkled substrates but can be more spread out on flat substrates, resulting in larger differences in compactness.

In summary, NIH-3T3 and NHF fibroblasts on wrinkled substrates display reduced cell widths and increased eccentricity relative to cells on flat substrates. Furthermore, NIH-3T3 cells on wrinkled substrates display increased solidity, while NHF cells display increased compactness. These results indicate that the topography of these wrinkled graphene substrates can strongly influence cell morphology (Table 4-1).

4.4 Conclusions

This study demonstrates the feasibility of wrinkled graphene as a surface texturing agent to direct cell alignment and morphology in tissue engineering. Wet deposition of graphene oxide multilayer tiled films on pre-stretched elastomers followed by relaxation and mild thermal treatment produces cell-culture-compatible textured substrates with long-range periodic topography in the form of parallel ridges and valleys. Both the spatial period and the wrinkle amplitude can by systematically tuned from 1 – 25 μm by selection of the substrate stiffness, by variation of pre-strain, and by alteration of the GO precursor concentration in the feed suspension. Fibroblasts are observed to attach to these textured s-GO surfaces and remain viable, while the wrinkles induce statistically significant cell alignment and elongation relative to flat s-GO substrates in a manner consistent with contact guidance on lithographically fabricated nanograting architectures. Together the results suggest that s-GO wrinkle engineering is a promising new approach for creation of functional surfaces and scaffolds in tissue engineering. In comparison with competing methods of patterning, wrinkled s-GO offers potential advantages in the ease, cost, and scale-up of fabrication. We envision a modular graphene-based platform for the application of orthogonal topographic stimuli, chemical stimuli (through functionalization or adsorption), electrical stimuli (enabled by conductive graphene), as well as dynamic mechanical actuation of topographic confinement. Furthermore, we believe these biologically inspired architectures will be widely applicable to other cell types, including neurons, skeletal, smooth muscle, cardiomyocytes and stem cells. These wrinkled s-GO architectures could potentially be integrated with soft, stretchable implantable devices such

as neural prostheses, cardiac assist devices, catheters or epidermal electronics in order to enhance biocompatibility and biointegration [56, 57].

4.5 Reference

1. Xia, Y.; Rogers, J. A.; Paul, K. E.; Whitesides, G. M. Unconventional methods for fabricating and patterning nanostructures. *Chem. Rev. (Washington, DC, U. S.)* **1999**, 99, 1823-1848.
2. Li, B.; Cao, Y.-P.; Feng, X.-Q.; Gao, H. Mechanics of morphological instabilities and surface wrinkling in soft materials: a review. *Soft Matter* **2012**, 8, 5728-5745.
3. Genzer, J.; Groenewold, J. Soft matter with hard skin: From skin wrinkles to templating and material characterization. *Soft Matter* **2006**, 2, 310-323.
4. Singamaneni, S.; Tsukruk, V. V. Buckling instabilities in periodic composite polymeric materials. *Soft Matter* **2010**, 6, 5681-5692.
5. Yang, S.; Khare, K.; Lin, P.-C. Harnessing Surface Wrinkle Patterns in Soft Matter. *Adv. Funct. Mater.* **2010**, 20, 2550-2564.
6. Bowden, N.; Brittain, S.; Evans, A. G.; Hutchinson, J. W.; Whitesides, G. M. Spontaneous formation of ordered structures in thin films of metals supported on an elastomeric polymer. *Nature* **1998**, 393, 146-149.
7. Diab, M.; Kim, K.-S. Ruga-formation instabilities of a graded stiffness boundary layer in a neo-Hookean solid. *Proc. R. Soc. A.* **2014**, 470.
8. Sun, J.-Y.; Xia, S.; Moon, M.-W.; Oh, K. H.; Kim, K.-S. In *Folding wrinkles of a thin stiff layer on a soft substrate*, Proceedings of the Royal Society of London A: Mathematical, Physical and Engineering Sciences, The Royal Society: 2012; pp 932-953.
9. Biot, M. Folding instability of a layered viscoelastic medium under compression. *Proceedings of the Royal Society of London. Series A. Mathematical and Physical Sciences* **1957**, 242, 444-454.
10. Kim, K. S.; Zhao, Y.; Jang, H.; Lee, S. Y.; Kim, J. M.; Kim, K. S.; Ahn, J.-H.; Kim, P.; Choi, J.-Y.; Hong, B. H. Large-scale pattern growth of graphene films for stretchable transparent electrodes. *Nature* **2009**, 457, 706-710.

11. Bao, W.; Miao, F.; Chen, Z.; Zhang, H.; Jang, W.; Dames, C.; Lau, C. N. Controlled ripple texturing of suspended graphene and ultrathin graphite membranes. *Nat Nano* **2009**, 4, 562-566.
12. He, Q.; Sudibya, H. G.; Yin, Z.; Wu, S.; Li, H.; Boey, F.; Huang, W.; Chen, P.; Zhang, H. Centimeter-Long and Large-Scale Micropatterns of Reduced Graphene Oxide Films: Fabrication and Sensing Applications. *ACS Nano* **2010**, 4, 3201-3208.
13. Scharfenberg, S.; Rocklin, D. Z.; Chialvo, C.; Weaver, R. L.; Goldbart, P. M.; Mason, N. Probing the mechanical properties of graphene using a corrugated elastic substrate. *Appl. Phys. Lett.* **2011**, 98, -.
14. Delle, L. E.; Lanche, R.; Law, J. K.-Y.; Weil, M.; Vu, X. T.; Wagner, P.; Ingebrandt, S. Reduced graphene oxide micropatterns as an interface for adherent cells. *physica status solidi (a)* **2013**, 210, 975-982.
15. Kunz, D. A.; Feicht, P.; Gödrich, S.; Thurn, H.; Papastavrou, G.; Fery, A.; Breu, J. Space-Resolved In-Plane Moduli of Graphene Oxide and Chemically Derived Graphene Applying a Simple Wrinkling Procedure. *Advanced Materials (Weinheim, Germany)* **2013**, 25, 1337-1341.
16. Zang, J.; Ryu, S.; Pugno, N.; Wang, Q.; Tu, Q.; Buehler, M. J.; Zhao, X. Multifunctionality and control of the crumpling and unfolding of large-area graphene. *Nature Materials* **2013**, 12, 321-325.
17. Zang, J.; Cao, C.; Feng, Y.; Liu, J.; Zhao, X. Stretchable and High-Performance Supercapacitors with Crumpled Graphene Papers. *Sci. Rep.* **2014**, 4.
18. Xu, P.; Kang, J.; Choi, J.-B.; Suhr, J.; Yu, J.; Li, F.; Byun, J.-H.; Kim, B.-S.; Chou, T.-W. Laminated Ultrathin Chemical Vapor Deposition Graphene Films Based Stretchable and Transparent High-Rate Supercapacitor. *ACS Nano* **2014**, 8, 9437-9445.
19. Faruque Ahmed, S.; Nagashima, S.; Lee, J. Y.; Lee, K.-R.; Kim, K.-S.; Moon, M.-W. Self-assembled folding of a biaxially compressed film on a compliant substrate. *Carbon* **2014**, 76, 105-112.
20. Mao, H. Y.; Laurent, S.; Chen, W.; Akhavan, O.; Imani, M.; Ashkarran, A. A.; Mahmoudi, M. Graphene: Promises, Facts, Opportunities, and Challenges in Nanomedicine. *Chem. Rev. (Washington, DC, U. S.)* **2013**, 113, 3407-3424.

21. Goenka, S.; Sant, V.; Sant, S. Graphene-based nanomaterials for drug delivery and tissue engineering. *J. Controlled Release* **2014**, 173, 75-88.
22. Bitounis, D.; Ali-Boucetta, H.; Hong, B. H.; Min, D.-H.; Kostarelos, K. Prospects and Challenges of Graphene in Biomedical Applications. *Adv. Mater. (Weinheim, Ger.)* **2013**, 25, 2258-2268.
23. Lee, W. C.; Lim, C. H. Y. X.; Shi, H.; Tang, L. A. L.; Wang, Y.; Lim, C. T.; Loh, K. P. Origin of Enhanced Stem Cell Growth and Differentiation on Graphene and Graphene Oxide. *ACS Nano* **2011**, 5, 7334-7341.
24. Chen, G.-Y.; Pang, D.-P.; Hwang, S.-M.; Tuan, H.-Y.; Hu, Y.-C. A graphene-based platform for induced pluripotent stem cells culture and differentiation. *Biomaterials* **2012**, 33, 418-427.
25. Ku, S. H.; Park, C. B. Myoblast differentiation on graphene oxide. *Biomaterials* **2013**, 34, 2017-2023.
26. Nayak, T. R.; Andersen, H.; Makam, V. S.; Khaw, C.; Bae, S.; Xu, X.; Ee, P.-L. R.; Ahn, J.-H.; Hong, B. H.; Pastorin, G.; Özyilmaz, B. Graphene for Controlled and Accelerated Osteogenic Differentiation of Human Mesenchymal Stem Cells. *ACS Nano* **2011**, 5, 4670-4678.
27. Ryoo, S.-R.; Kim, Y.-K.; Kim, M.-H.; Min, D.-H. Behaviors of NIH-3T3 Fibroblasts on Graphene/Carbon Nanotubes: Proliferation, Focal Adhesion, and Gene Transfection Studies. *ACS Nano* **2010**, 4, 6587-6598.
28. Bettinger, C. J.; Langer, R.; Borenstein, J. T. Engineering substrate topography at the micro - and nanoscale to control cell function. *Angewandte Chemie International Edition* **2009**, 48, 5406-5415.
29. Kim, D.-H.; Provenzano, P. P.; Smith, C. L.; Levchenko, A. Matrix nanotopography as a regulator of cell function. *The Journal of Cell Biology* **2012**, 197, 351-360.
30. Curtis, A.; Wilkinson, C. Topographical control of cells. *Biomaterials* **1997**, 18, 1573-1583.
31. Gasiorowski, J. Z.; Murphy, C. J.; Nealey, P. F. Biophysical cues and cell behavior: the big impact of little things. *Annual review of biomedical engineering* **2013**, 15, 155-176.

32. Charras, G.; Sahai, E. Physical influences of the extracellular environment on cell migration. *Nat. Rev. Mol. Cell Biol.* **2014**, 15, 813-824.
33. Weiss, P. Cellular Dynamics. *Reviews of Modern Physics* **1959**, 31, 11-20.
34. Luna, J. I.; Ciriza, J.; Garcia-Ojeda, M. E.; Kong, M.; Herren, A.; Lieu, D. K.; Li, R. A.; Fowlkes, C. C.; Khine, M.; McCloskey, K. E. Multiscale biomimetic topography for the alignment of neonatal and embryonic stem cell-derived heart cells. *Tissue Engineering Part C: Methods* **2011**, 17, 579-588.
35. Wang, J.; Chen, A.; Lieu, D. K.; Karakikes, I.; Chen, G.; Keung, W.; Chan, C. W.; Hajjar, R. J.; Costa, K. D.; Khine, M. Effect of engineered anisotropy on the susceptibility of human pluripotent stem cell-derived ventricular cardiomyocytes to arrhythmias. *Biomaterials* **2013**, 34, 8878-8886.
36. Cao, C.; Chan, H. F.; Zang, J.; Leong, K. W.; Zhao, X. Harnessing Localized Ridges for High‐Aspect‐Ratio Hierarchical Patterns with Dynamic Tunability and Multifunctionality. *Adv. Mater. (Weinheim, Ger.)* **2014**, 26, 1763-1770.
37. Kolind, K.; Leong, K. W.; Besenbacher, F.; Foss, M. Guidance of stem cell fate on 2D patterned surfaces. *Biomaterials* **2012**, 33, 6626-6633.
38. Yim, E. K.; Darling, E. M.; Kulangara, K.; Guilak, F.; Leong, K. W. Nanotopography-induced changes in focal adhesions, cytoskeletal organization, and mechanical properties of human mesenchymal stem cells. *Biomaterials* **2010**, 31, 1299-1306.
39. Dalby, M. J.; Riehle, M. O.; Yarwood, S. J.; Wilkinson, C. D.; Curtis, A. S. Nucleus alignment and cell signaling in fibroblasts: response to a micro-grooved topography. *Experimental cell research* **2003**, 284, 272-280.
40. Teixeira, A. I.; Abrams, G. A.; Bertics, P. J.; Murphy, C. J.; Nealey, P. F. Epithelial contact guidance on well-defined micro-and nanostructured substrates. *J. Cell Sci.* **2003**, 116, 1881-1892.
41. Kim, D.-H.; Lipke, E. A.; Kim, P.; Cheong, R.; Thompson, S.; Delannoy, M.; Suh, K.-Y.; Tung, L.; Levchenko, A. Nanoscale cues regulate the structure and function of macroscopic cardiac tissue constructs. *Proceedings of the National Academy of Sciences* **2010**, 107, 565-570.

42. Qiu, Y.; Wang, Z.; Owens, A. C.; Kulaots, I.; Chen, Y.; Kane, A. B.; Hurt, R. H. Antioxidant chemistry of graphene-based materials and its role in oxidation protection technology. *Nanoscale* **2014**, 6, 11744-11755.
43. Kamentsky, L.; Jones, T. R.; Fraser, A.; Bray, M.-A.; Logan, D. J.; Madden, K. L.; Ljosa, V.; Rueden, C.; Eliceiri, K. W.; Carpenter, A. E. Improved structure, function and compatibility for CellProfiler: modular high-throughput image analysis software. *Bioinformatics* **2011**, 27, 1179-1180.
44. Li, G. N.; Hoffman-Kim, D. Evaluation of neurite outgrowth anisotropy using a novel application of circular analysis. *Journal of neuroscience methods* **2008**, 174, 202-214.
45. Luo, J.; Jang, H. D.; Sun, T.; Xiao, L.; He, Z.; Katsoulidis, A. P.; Kanatzidis, M. G.; Gibson, J. M.; Huang, J. Compression and Aggregation-Resistant Particles of Crumpled Soft Sheets. *ACS Nano* **2011**, 5, 8943-8949.
46. Chen, Y.; Guo, F.; Jachak, A.; Kim, S.-P.; Datta, D.; Liu, J.; Kulaots, I.; Vaslet, C.; Jang, H. D.; Huang, J.; Kane, A.; Shenoy, V. B.; Hurt, R. H. Aerosol Synthesis of Cargo-Filled Graphene Nanosacks. *Nano Letters* **2012**, 12, 1996-2002.
47. Chen, X.; Hutchinson, J. W. Herringbone Buckling Patterns of Compressed Thin Films on Compliant Substrates. *Journal of Applied Mechanics* **2004**, 71, 597-603.
48. Huang, Z. Y.; Hong, W.; Suo, Z. Nonlinear analyses of wrinkles in a film bonded to a compliant substrate. *Journal of the Mechanics and Physics of Solids* **2005**, 53, 2101-2118.
49. Volynskii, A. L.; Bazhenov, S.; Lebedeva, O. V.; Bakeev, N. F. Mechanical buckling instability of thin coatings deposited on soft polymer substrates. *Journal of Materials Science* **2000**, 35, 547-554.
50. Song, J.; Jiang, H.; Liu, Z. J.; Khang, D. Y.; Huang, Y.; Rogers, J. A.; Lu, C.; Koh, C. G. Buckling of a stiff thin film on a compliant substrate in large deformation. *International Journal of Solids and Structures* **2008**, 45, 3107-3121.
51. Peng, Q.; De, S. Mechanical properties and instabilities of ordered graphene oxide C6O monolayers. *RSC Advances* **2013**, 3, 24337-24344.

52. Park, S.; Lee, K.-S.; Bozoklu, G.; Cai, W.; Nguyen, S. T.; Ruoff, R. S. Graphene Oxide Papers Modified by Divalent Ions—Enhancing Mechanical Properties via Chemical Cross-Linking. *ACS Nano* **2008**, 2, 572-578.

53. Chen, C.; Yang, Q.-H.; Yang, Y.; Lv, W.; Wen, Y.; Hou, P.-X.; Wang, M.; Cheng, H.-M. Self-Assembled Free-Standing Graphite Oxide Membrane. *Advanced Materials (Weinheim, Germany)* **2009**, 21, 3007-3011.

54. Acik, M.; Lee, G.; Mattevi, C.; Pirkle, A.; Wallace, R. M.; Chhowalla, M.; Cho, K.; Chabal, Y. The Role of Oxygen during Thermal Reduction of Graphene Oxide Studied by Infrared Absorption Spectroscopy. *The Journal of Physical Chemistry C* **2011**, 115, 19761-19781.

55. Akagi, J.; Kordon, M.; Zhao, H.; Matuszek, A.; Dobrucki, J.; Errington, R.; Smith, P. J.; Takeda, K.; Darzynkiewicz, Z.; Wlodkowic, D. Real‐time cell viability assays using a new anthracycline derivative DRAQ7®. *Cytometry Part A* **2013**, 83, 227-234.

56. Kim, D.-H.; Ghaffari, R.; Lu, N.; Rogers, J. A. Flexible and stretchable electronics for biointegrated devices. *Annual review of biomedical engineering* **2012**, 14, 113-128.

57. Minev, I. R.; Musienko, P.; Hirsch, A.; Barraud, Q.; Wenger, N.; Moraud, E. M.; Gandar, J.; Capogrosso, M.; Milekovic, T.; Asboth, L. Electronic dura mater for long-term multimodal neural interfaces. *Science* **2015**, 347, 159-163.

Chapter 5 Biological and Environmental Interactions of Emerging Two-Dimensional Nanomaterials

5.1 Introduction

We are witnessing a revolution in materials science centered on the creation and use of two-dimensional (2D) sheet-like materials of atomic-scale thickness. In addition to the discovery of graphene in 2004, the 2D material family now consists of a wide range of inorganic materials that include metal oxides, sulfides, selenides, and layered double hydroxides.[1] For instance, transition metal dichalcogenides (TMD) consist of hexagonal layers of transition metal atoms sandwiched between two layers of chalcogen atoms. The chemical bond between transition metal and chalcogen atom is strong covalent bond, but the interaction between adjacent chalcogen layers is weak van der Waals force, which makes it possible for the production of 2D nanomaterials by simple mechanical exfoliations. 2D nanomaterials, particularly TMD as the ideal two dimensional prototype, have received extensive attention and been explicitly reviewed in terms of preparation, [2] phase engineering, [3] hybrid composites,[4] and biomedical applications.[5]

However, very little is known about the potential implications of these emerging 2D nanomaterials on human health or the natural environment although some aspects are readily informed by the current literature on graphene-based 2D nanomaterials. The interactions of graphene nanomaterials with biological systems have been studied and discussed in a few review articles. [6, 7] Similar to the counterpart graphene, other 2D nanomaterials have unique dimensional properties (surface area, layer number, lateral dimension and surface chemistry), which can lead to a variety of interactions with biological molecules including physical absorption and catalytic reactions, and even toxicity to cells. Novel 2D nanomaterials also feature in the great chemical diversity and possibly undergo redox reactions, dissolution, photo-induced reactions in both

environmental and biological systems in a similar way to the conventional metal based nanoparticles discussed in Chapter 2. These transformations and their interactions with environmental or biological systems would be more complex than the case of graphene.

The environmental transformation, particularly dissolution behaviors, of various conventional transition metal based nanomaterials have been explicitly studied including the case of Cu-based nanoparticles discussed in Chapter 2. Informed by these behaviors, dissolution has been acknowledged as a critical process affecting nanomaterial properties, fate, toxicity and persistence in the relevant media. Meanwhile, dissolution of nanomaterials is also a complex chemical transformation which can be influenced by pH, presence of ligands, aggregation states, oxide/sulfide layer or shell, surfactant coatings. Even the effect of a specific factor on different nanomaterials is not necessarily identical. Oxide layer, for instance, protects the inner core from further oxidation and significantly reduces the reactivity in the case of zero valent iron nanoparticles for environmental remediation purposes.[8] In other cases, pre-oxidation of Ag NP surface can increase its antibacterial properties since oxidation of Ag(0) to Ag(I) is the prerequisite step to release the antibacterial active component silver ions.[9] Similarly, sulfidation can significantly reduce the antibacterial ability of Ag NPs even at low sulfidation extent because initially-formed silver sulfide layer work as a coherent and insoluble shell isolating the pristine silver core from oxidative release.[10] However, in the cases of Cu or Zn oxide, sulfidation doesn’t contribute to the inhibition of ion release until relatively complete sulfidation occurs because sulfidation of copper or zinc oxide produces distinct secondary particles rather than protective coatings.[11, 12]

Therefore, to answer the question of how a specific 2D nanomaterial will transform (e.g. dissolves or not), people need a well-organized matrix involving representative 2D nanomaterials and key features of the media, instead of case by case studies. The latter is impossible in practice considering the large number of 2D nanomaterials and complexity in the media. Here, we first calculate the thermodynamic oxidation and reduction potentials of 2D nanomaterials and compare the results to the redox potentials of relevant reactions in the environment to predict the stability of 2D nanomaterials in biological and environmental aqueous solutions. Then we use MoS_2 and MnO_2 nanosheets as example 2D nanomaterials to illustrate the various types of dissolution the 2D nanomaterials can possibly undergo in biological and environmental relevant media.

In addition to the impacts of environmental conditions on materials' dissolution behaviors, research and public community are particularly interested in the potential toxicities of 2D nanomaterials can bring to the environment and human health. Again due to large number of permutations in materials and media, traditional toxicity testing methods will not be suitable for risk management or safe design across the entire material family on a time scale that keeps pace with material development. Thus investigation is compromised to identify the most relevant physicochemical properties of the nanomaterials to possible toxicological effects. Recently, people have used quantitative structure-activity relationship (QSAR) method to predict the toxicity of various nanomaterials.[13-16] QSAR paradigm is basically based on calculated molecular parameter for a whole group of materials and experimental data for part of the group, to interpolate the activity of the unknown section of the group using a suitable mathematical model. Considering the limited number of reports regarding toxicity of 2D toxicity, it's too early to construct a structure-

activity paradigm. Because of the semiconductor nature for most 2D nanomaterials, the activity we investigate is the ability of nanomaterials to induce oxidative stress potential, which is one of the most well developed paradigms of unveiling the origin of nanomaterials' cytotoxicity. We use a recently developed band-structure based framework to identify 2D materials that are likely to have pro-oxidant activity in biological systems.[17, 18]

Finally, we use MoS_2 as an example 2D nanomaterial to illustrate the transformation manners these materials will behave in the ambient environment, and the impacts of those transformations on the reactivity of material studied. Particularly, the dissolution and biological catalysis of MoS_2 is investigated and used to validate the hypothesis raised above. Finally, the potential environmental application of MoS_2 is explored on the catalytic removal of 4-nitrophenol.

5.2 Materials and Methods

5.2.1 Preparation of 2D nanosheets

2D MoS_2 monolayer nanosheets were prepared by chemical exfoliation using lithium intercalation.[19] In a typical preparation procedure, 3 ml of 1.6 M n-butyllithium in hexane solution were added into 300 mg of MoS_2 powder, and the mixture was left under static conditions at room temperature for 2 days in the nitrogen-filled glovebox. The resulting lithium-intercalated product was rinsed with hexane twice to remove the excess reactant and organic by-products. The purified intercalated product was immediately exfoliated and dispersed in DI water with assistance by sonication bath for one hour. Stable and well-dispersed aqueous suspension of MoS_2 can be obtained by centrifugation at 500 rpm for 10 min to remove un-exfoliated MoS_2. The byproduct LiOH was removed from

the suspension by dialysis against DI water until neutral pH. The total Mo concentration was estimated by digestion with HNO_3/H_2O_2 solution followed by measurements in ICP-AES instrument. Morphologies of monolayer MoS_2 were characterized using atomic force microscopy (Asylum MFP-3D Origin AFM) in pulse mode, and field emission SEM (LEO 1530 VP). Preparation of h-BN was by mechanical exfoliation.[20] MnO_2-nanosheets were synthesized by conventional solid-state reaction preparing layered $K_{0.45}MnO_2$, followed by protonation and exfoliation according to previous publication.[21]

5.2.2 Dissolution of 2D nanomaterials in relevant aqueous solutions

To investigate the long-time stability of monolayer MoS_2, sets of high concentration (40 ppm of Mo) and low concentration (8 ppm of Mo) suspension were left under ambient conditions. After pre-determined time, the dissolved species were separated by ultrafiltration and its concentration is determined by ICP-OES. During the dissolution reactions, the pH change is monitored. To evaluate the stability of MoS_2 in environmentally or biologically relevant media, MoS_2 suspension was added to fresh water mimic solution (50 mM humic acid in acetate buffer, pH 5.7), RPMI 1640 cell culture medium (Sigma 51536C, pH 7.4) and seawater (Sigma S9148, pH 8.2). The dissolved Mo species were separated and measured similarly.

The reaction of MnO_2 nanosheets with reduced glutathione is too fast to allow detection with ICP-AES measurement. Here the characteristic uv-visible absorption peak of MnO_2 nanosheets at 400 nm was used to monitor the reaction with reduced glutathione. 20 ppm of MnO_2 was added to 5 mM GSH in 5mM of HEPES buffer (pH 7.1), and then

the absorbance of the mixture at 400 nm was measured by V-630 spectrophotometer (Jasco, MD) to monitor the reaction process.

5.2.3 The GSH assay of 2D nanomaterials

MoS_2 (Mo concentration is 20 ppm) or 50 ppm of h-BN was added to 5 mM reduced glutathione in PBS buffer, and the mixture was agitated on a rotator at 30 rpm for the desired reaction time. And then the suspension was subjected to ultrafiltration to remove the intact reduced glutathione from 2D nanomaterial solids. The GSH concentrations in filtrate were determined with ThioGlo-4 (Calbiochem) fluorescent reagent. A calibration curve of GSH was first established by adding 1.0-5.0 um GSH to 20 um ThioGlo-4 in PBS buffer, which was diluted from ThioGlo-4 DMSO stock solution. Filtrate solutions were added to ThioGlo-4 in PBS buffer solution similarly, followed by 30 min incubation in dark and assay for fluorescence on SpectraMax M2 using excitation at 400 nm and emission at 465 nm.[22] To study the role of oxygen, dissolved oxygen (DO) probe was used to detect the DO level during the reactions of GSH (5mM) in the presence of MoS_2 (Mo concentration is 500ppm). Higher MoS_2 concentration relative to the above GSH assay was added to accelerate the overall reaction to observe considerable oxygen decrease in a relative short period of time. After each oxygen depletion, the solution was exposed to air to recover the oxygen level in the solution. 5mM of fresh GSH was added again to initiate the reaction to evaluate the functional stability of MoS_2 as catalyst.

5.2.4 Catalytic behavior of chemically-exfoliated MoS_2 towards 4-nitrophenol reduction

In a typical reduction experiment, chemically-exfoliated MoS_2 (2 ppm of Mo) was mixed with 4-NP (0.12 mM) solution and then $NaBH_4$ (36 mM) was added to trigger catalytic reduction. The molar ratio of 4-NP: $NaBH_4$ is 300, therefore the concentration of $NaBH_4$ can be considered as constant throughout the entire process. The reaction progress was monitored by the characteristic absorbance peak of 4-NP at 400 nm using uv-vis spectroscopy. To investigate the underlying mechanism, initial $NaBH_4$ (or MoS_2) and 4-NP concentration were kept constant while varying the concentration of the other component. Control experiment under deoxygenated condition was conducted by bubbling nitrogen into all solutions to remove dissolved oxygen before the catalytic reactions.

5.3 Results and discussion

5.3.1 Chemical behavior - dissolution and transformation

Ion release of nanomaterials is a critical transformation in biological or environmental relevant media, which has significant influence on the fate, transport and toxicity of nanomaterials. Due to various composition and phase of 2D nanomaterials, the transformation in terms of dissolution behaviors can be complicated. Based on the published reports on conventional nanomaterials, it is inferred that 2D metal oxide, metal hydroxide and layered double hydroxides (LDHs) can undergo a simple dissolution in biological or environmental relevant medium, in a similar way that metal-oxide nanoparticle decomposes.[11] Figure 5-1 shows the equilibrium solubilities of selected 2D nanomaterials covering metal oxide, metal sulfide, metal hydroxide and LDHs, and the

ionic concentration range reported to be toxic (shaded area) in the literature. Although based on bulk thermodynamic properties, insights about simple-dissolution of 2D nanomaterials are obtained. First, most covered metal oxide, hydroxide and LDHs can readily release ionic species through protonation in a simple-dissolution manner. Second, although faster dissolution of nanomaterials usually occurs at lower pH, the concentration of ion that is reported to induce cytotoxicity can be reached even at neutral conditions (Figure 5-1 is based on pH 7). Furthermore, this process can be promoted by the presence of ligands (*e.g.* amino acids in cell culture medium[11]), which complex with the released free ion to drive the equilibrium towards ionic species production.

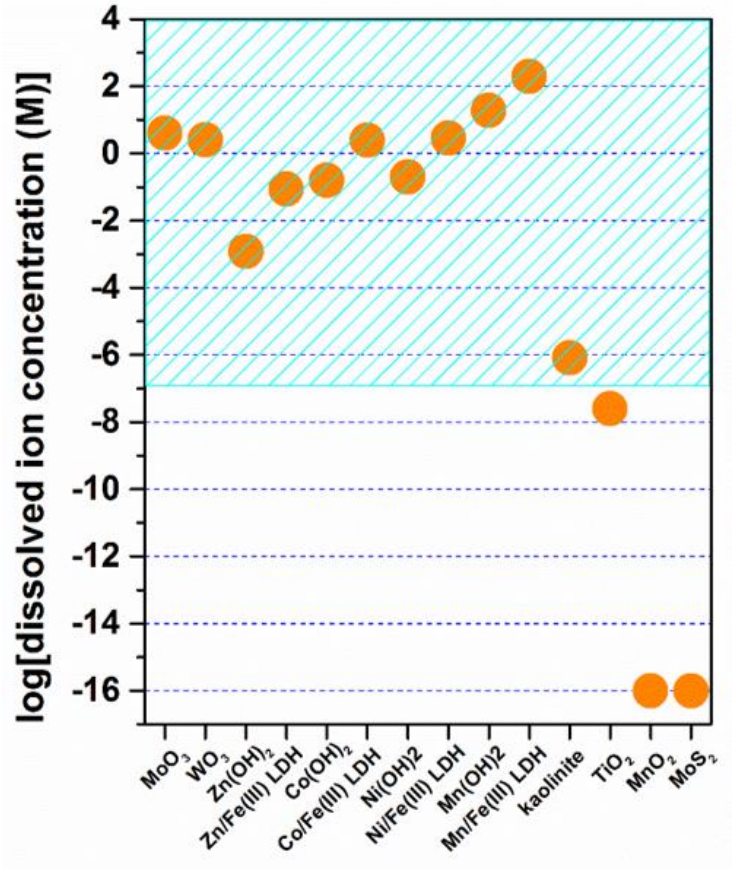

Figure 5-1. Equilibrium solubility of the metal sulfides, oxides, metal hydroxides and LDH at pH 7. The equilibrium dissolved metal ion concentration of metal hydroxide and LAHs was calculated by the solubility constants. Visual MINTEQ 3.1 was used to estimate the dissolved ion concentration for the rest metal oxide and sulfide.[23]

Among the covered 2D nanomaterials, MoO_3 and WO_3 are known to be thermodynamically unstable and readily hydrolyzed into molybdate and tungstate, respectively (e.g. $MoO_3(s) + 2OH^{-1} \rightarrow MoO_4^{2-}(aq) + H_2O$) in relatively high pH solution.[24, 25] Thus the equilibrium concentration of MoO_3 and WO_3 at pH 7 are estimated based on the solubility of sodium molybdate and sodium tungstate, respectively. Acidic condition has been reported to slow down the hydrolysis process of MoO_3 since the increased concentrations of proton can shift the above reaction to the left.[26] When pH is less than 2, MoO_3 is reported to be very stable against hydrolysis.[27] The equilibrium concentration of metal hydroxide (Zn(II), Co(II), Ni(II), Mn(II)), and their corresponding Fe(III)-based LDHs in the form of $M(II)_2Fe(III)(OH^-)_6Cl^-$ are calculated based on published solubility product constants, which indicate the 2D LDHs are even less stable than the corresponding metal(II) hydroxide raising the concerns about their potential higher toxicity.[28] The low concentration of ion release in the case of kaolinite and TiO_2 agrees with the fact that their biological response have not typically related to dissolution. The equilibrium solubility of MoS_2 and MnO_2 is predicted to be very low, however, they can decompose via different transformation pathways in biological or environmental relevant medium. (*vide infra*)

Using solubility constants to calculate the solubilities of 2D nanomaterials is simple and straightforward, but the availability of such data for most emerging 2D nanomaterials is rare. Besides, some of those 2D nanomaterials may undergo redox reactions that lead to dissolution in a similar way to oxidative degradation of silver NPs, which has been explicitly studied.[29-31] Recently, an approach has been established to calculate thermodynamic oxidation and reduction potentials of semiconductors in aqueous solution,

to predict the stability of those semiconductor against oxidative and reductive photocorrosion.[32] Here we utilize this approach to estimate the stability of 2D nanomaterials against oxidation (oxygen) and reduction (biological redox couple) in ambient conditions. Similarly, a compound semiconductor MX (e.g. M=Mo, X=S_2 in MoS_2) can decompose by gaining or losing electrons through following half reactions:

$$MX \rightleftharpoons M^{z+} + X + ze^{-}, \quad \varphi^{ox} = \frac{G(M^{z+}) + G(X) - G(MX)}{zeF} \qquad \text{(Oxidation)}$$

$$\text{Or} \qquad MX + ze^{-} \rightleftharpoons M + X^{z-}, \quad \varphi^{re} = -\frac{G(M) + G(X^{z-}) - G(MX)}{zeF} \qquad \text{(Reduction)}$$

The above reactions define the thermodynamic oxidation potential φ^{ox} and reduction potential φ^{re} of 2D nanomaterials. By comparing with the redox potential of O_2/H_2O and biological couples, one can predict if the 2D nanomaterials can undergo oxidative or reductive reactions in relevant media. Generally speaking, a 2D nanomaterial can oxidatively decompose with respect to oxygen oxidation if φ^{ox} is lower (more negative) than $\varphi(O_2/H_2O)$, and reductively decompose with respect to reduction by biological molecules if φ^{re} is higher (more positive) than the redox potential of biological couples (e.g. GSSG/GSH). In this chapter, the scope is limited to binary 2D nanomaterials for the calculation of redox potential based on the Gibbs free energy, which is restrained by absence of thermodynamic data for the reactants or products (especially for multinary ones). A more extended study covering more 2D materials needs the inputs on thermodynamic data from theoretical or experimental works. We here calculated the φ^{ox} and φ^{re} of TMD and transition metal oxide relative to $\varphi(O_2/H_2O)$ and cellular redox potential in Figure 5-2 A and B.

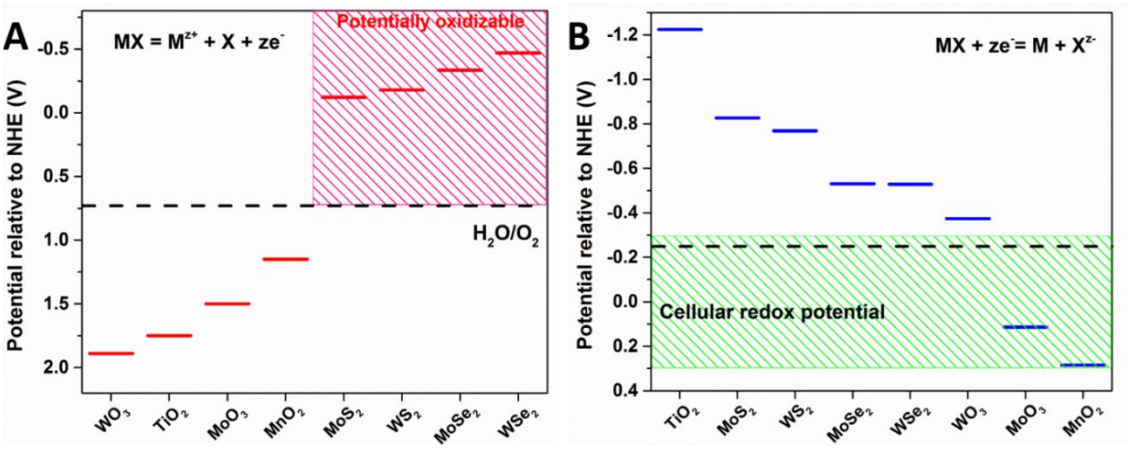

Figure 5-2. The theoretical platform of predicting the stability by comparing relevant redox potential. (A) The comparison of oxidation potential of 2D nanomaterials with *φ(O₂/H₂O)* at pH 7, indicating MoS_2, $MoSe_2$, WS_2 and WSe_2 are potentially oxidizable since their oxidation potential is more negative than *φ(O₂/H₂O)*. (B) The comparison of reduction potential of 2D nanomaterials with cellular redox potential at pH 7, indicating MoO_3 and MnO_2 are potentially reducible (*e.g.* by GSH) since their reduction potential is within the cellular redox potential range and more positive than *φ(GSH/GSSG)*.

TMD (*e.g.* MoS_2) has very low solubility indicated in Figure 5-1. Bulk TMD is also relatively stable against oxidation with thin oxide layer preventing further oxidation at room temperature.[33] Even TMD thin film, oxidative etching has to be done with strong oxidizer and high heating temperature in a self-limited manner on core protection.[34, 35] No reports are available yet on the transformation of TMD in aqueous solution at ambient conditions, such oxidative transformation, however, is predicted to occur in Figure 5-2A. The comparison of oxidation potential of 2D nanomaterials with φ(O_2/H_2O) at pH 7, indicating MoS_2, $MoSe_2$, WS_2 and WSe_2 are potentially oxidizable since their oxidation potential is more negative than φ(O2/H2O). Figure 5-2B shows the comparison of reduction potential of 2D nanomaterials with cellular redox range (e.g. GSH/GSSG couple), and predicts the nanomaterials within the cellular redox range (*e.g.* MoO_3 and MnO_2) can potentially undergo a reduction reactions.

5.3.2 Electronic and Photochemical – redox activity and band structure theory

The semiconducting properties of two dimensional materials have been demonstrated in various applications such as photoelectron-splitting of water, hydrogen evolution and solar cells. Such widespread use of 2D nanomaterials raises the question how to determine whether a specific 2D nanomaterials represent a real threat to biological and environmental systems. Considering the large family of 2D nanomaterials, it will be a very time-consuming task to determine the toxicity for every 2D nanomaterials, which is further complicated by (1) different characterization and measurement methods for understanding the transformation and potential impact in biological or environmental media, and (2) various preparation and testing process of nanomaterials for evaluating their bioavailability and cytotoxicity. Thus, establishing the relationship between physicochemical properties and the possible toxicological effects is the necessary and critical step to generate the priority list. Various theoretical frameworks have been constructed to categorize the most toxic materials out of the material pool.[14-16] One such model is to predict the oxidative stress potential of metal oxide NPs, based on comparison of nanoparticle band structure with relevant redox potentials of biological couples.[17, 18] Under physiological conditions, a reductive intracellular state is maintained by the balance between levels of oxidized (e.g. GSSG) and reduced (e.g. GSH) species present in the cell. The balance will be broken as a result of decrease of antioxidants and/or an increase of reactive oxygen species, leading to oxidative stress which may evolve into cell death eventually. If the energetic states of 2D nanomaterials are comparable within the cellular redox potential range (-4.12 to -4.84 eV relative to Vacuum),[36] 2D nanomaterials may act as catalysts and promote the electron transfer. In the band gap structures, conduction band minimum

(CBM) and valence band maximum (VBM) are the energy levels that should be paid attention to since these bands can actively transfer electrons accepting or donating from or to the donors/acceptors in biological systems. The band edge structure can be obtained by experimental or theoretical calculations. All of energy levels, cellular redox potential, particularly redox potential of O_2/ H_2O and GSH/GSSG at pH 7 are expressed relative to absolute vacuum scale in Figure 5-3.

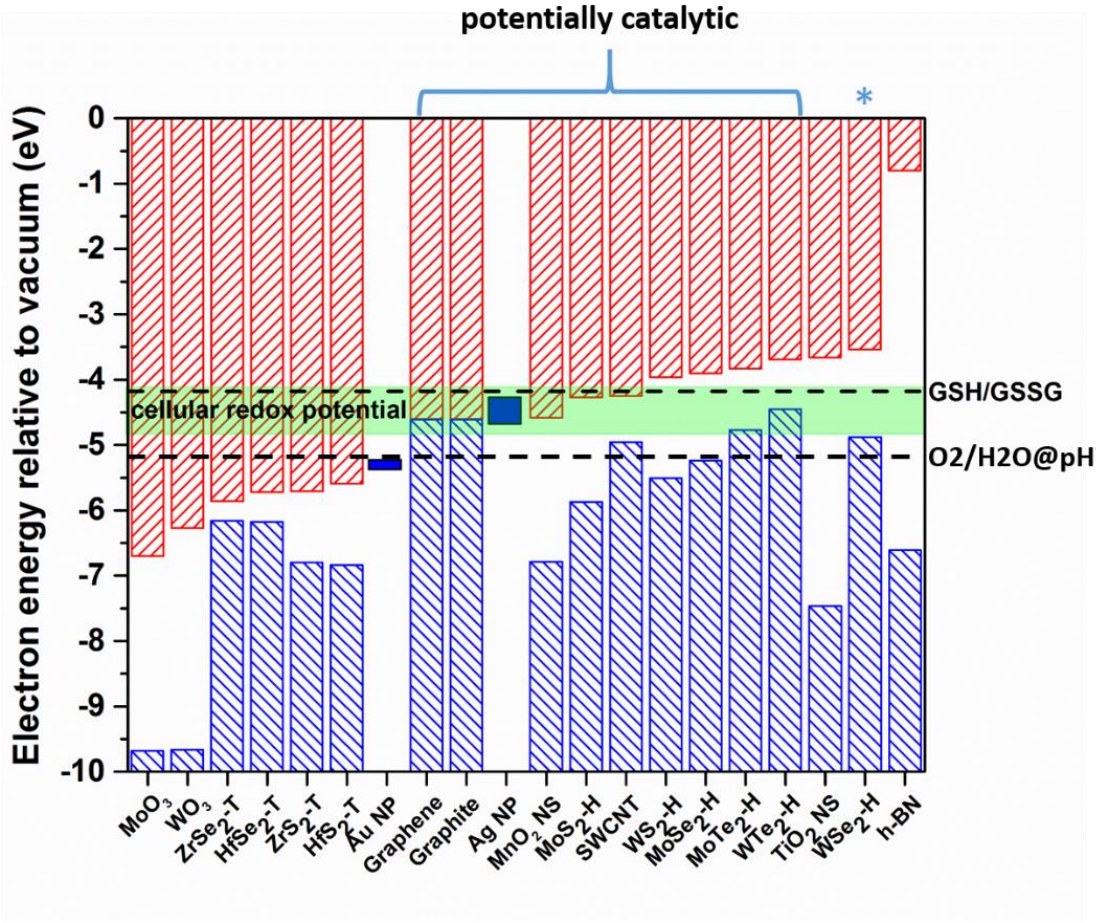

Figure 5-3. Band alignment of 2D nanomaterials (TMD,[37] MoO_3, WO_3, graphene, MnO_2 nanosheets, TiO_2 nanosheets and h-BN) and reference materials (Au NPs, Ag NPs, graphite and single wall carbon nanotube (SWCNT)) relative to cellular redox potential (e.g. GSH/GSSG) and redox potential of O_2/ H_2O.

Here, Figure 5-3 shows 2D nanomaterials band edge relationship with cellular redox potential under biological conditions. The CBM of MoS_2 for instance is within the range of cellular redox potential which means MoS_2 can potentially act as a catalyst mediating various biological redox reactions. The reduction potential of O_2/ H_2O is below the CBM of MoS_2 indicating O_2 may accept the electrons from that band level which may come from biological molecules (*e.g.* GSH). GSH plays crucial role in keeping the metabolism of redox environments in cells. The overwhelming of GSH oxidation can result in the oxidative stress and consequently cell deaths.

Since band structure in this study is based on theoretical calculation and many factors can affect the real band structure, such as doping, various thickness and surface binding.[38, 39] 2D nanomaterials are considered to be catalytically active if its CBM or VBM is within the range of cellular redox potential ± 0.3 eV. In this case, MoS_2, MnO_2, $MoSe_2$, $MoTe_2$, WS_2, WSe_2 and WTe_2 are considered as potentially catalytic-active in biological systems. The case studies of 2D nanomaterials are shown below to investigate the biological catalysis and validate the band structure-catalytic activity relationship.

Some reference materials are considered in the diagram of Figure 5-3 as well. Au NPs, Ag NPs are conductor so the band theory doesn't apply. But their Fermi level can be used to predict catalytic ability since Fermi level here works similarly in transferring electrons.[40, 41] According to the Fermi level positions relative to cellular redox potential, Ag is predicted to be able to catalyze the oxidation of GSH while gold isn't. Au and Ag NPs are known to deplete GSH by absorption which is kinetically favored.[42, 43] Graphite is semimetal with a band overlap of about 41meV, while single graphene layer is well known to be a zero-gap semiconductor .[44] Carbon nanotubes are reported to be metallic

or semiconducting, which depends on the diameter and helicity of the arrangement of graphitic rings in their walls. With diameter of 1nm, the band gap of SWCNT is predicted to be 0.7 eV. [45] Work functions of carbon nanotubes (>1nm) show little dependence on diameter or chirality, and work functions of such nanotubes can be well approximated by the graphene work function.[46] Therefore the CBM of such SWCNT is within the cellular redox potential region (Figure 5-3). With diameter increasing, the band gap is predicted to decrease leading to the CBM still falling into the cellular redox region. Therefore, all the carbon materials covered in the diagram are predicted to be catalytically active in biological systems.

5.3.3 MoS_2 synthesis and characterization

MoS_2 is a natural occurring mineral as molybdenite. (Figure 5-4A) Because of its layered structure similar to graphite (Figure 5-4B), MoS_2 has been studied since decades ago in the fields of dry lubrication.[47] It's only very recently that monolayer or few-layer MoS_2 has regained a lot of attention for its semiconducting properties and potential applications in electronics, catalysis biomedical and energy fields.[19, 39, 48, 49]

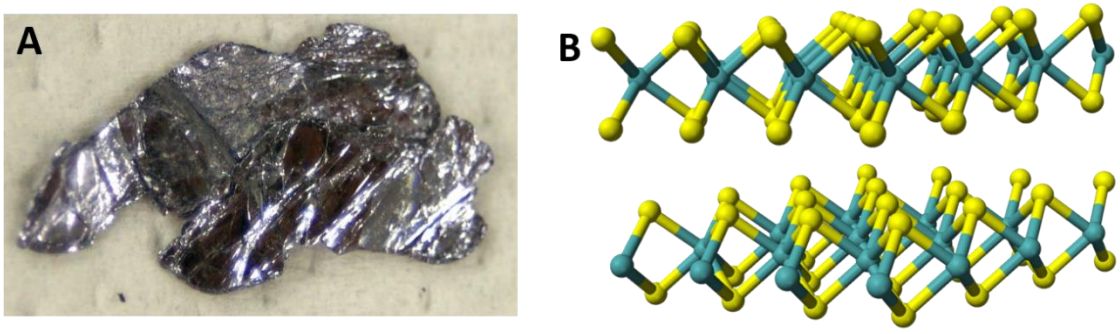

Figure 5-4. The morphology and crystal structure of molybdenite mineral (MoS_2). (A) Black molybdenite mineral (web image); (B) Crystal structure of MoS_2: a sheet of molybdenum atoms (green) sandwiched between sheets of sulfur atoms (yellow). The covalent Mo-S bond is very strong, but the interlayer interaction between sulfur atoms at the top and adjacent bottom is weak, resulting in relatively easy slippage as well as exfoliation. (web image)

Few-layer MoS_2 can be prepared by mechanical exfoliation in suitable organic solvent, or by ligand-assisted exfoliation in aqueous solution. To prepare monolayer MoS_2 in large quantities, however, chemical exfoliation using organic lithium reagent is more practical and scalable. In this method, lithium (e.g. n-butyl lithium) is inserted between MoS_2 layers, and reacts to produce hydrogen gas at the interlayer when encountering with water. Interlayer space expands in combination with ultrasonication enables the production of water dispersible monolayer MoS_2 in large quantities. Scanning electron microscopy (SEM) and atomic force microscopy (AFM) revealed sheets with average diameters of 0.35 μm, and average thicknesses between ~0.9 and 1.2 nm, consistent with reported values of monolayer MoS_2. Although the monolayer nature, a portion of semiconductor MoS_2 (2H phase) during chemical exfoliation converted to metallic 1T phase. Consequently, the monolayer chemically exfoliated MoS_2 product is a mixed 1T and 2H material.

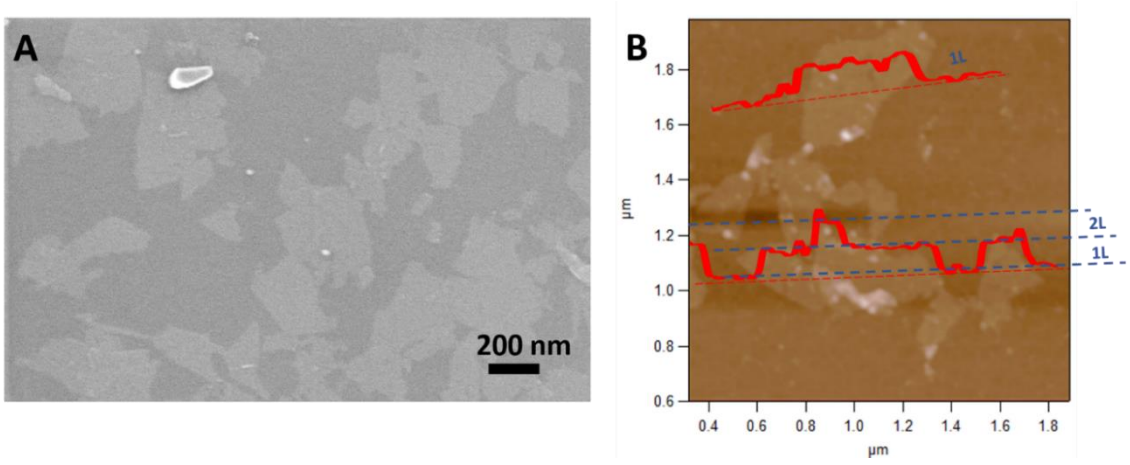

Figure 5-5. Characterization of chemically-exfoliated MoS_2 nanosheets by (A) SEM and (B) AFM.

5.3.3 Oxidative dissolution of MoS_2

Another characteristic property of chemically-exfoliated MoS_2 is the excellent dispersity and colloidal stability in aqueous solution, which is attributed to the negatively-charged nature of MoS_2. Zeta-potential of chemically exfoliated MoS_2 was determined to

be -48 mV in agreement with the reported data.[50] The origin of this negative charge though is under debate in literature. One model was proposed associated with absorbed hydroxyl ions, while the other attributed the negative charges to partially oxidized Mo atoms due to lithium intercalation. But both models agreed on the contribution of negative charge in MoS_2 to the colloidal stability. Recently, the long-time colloidal instability of chemically-exfoliated MoS_2 suspension has been observed and ascribed to restacking,[50] and thiol-containing ligands were used to maintain colloidal stability by providing steric hindrance. The cause of long-time colloidal instability is relatively unknown and needs investigation.

Here, the dissolved Mo concentrations and pH of the suspension were monitored for low- (8.4 ppm of Mo) and high-concentration (42 ppm of Mo) MoS_2 suspensions over time. Figure 5-6 (A) and (B) show that the concentration of dissolved Mo species increases over time in both samples, which is in agreement with the prediction in Figure 5-2 that MoS_2 may undergo oxidative dissolution in the presence of oxygen. Meanwhile, pH of the suspension was measured right before the ultrafiltration and found to decrease over time, which supports the oxidative dissolution by the following equation:

$$MoS_2 + 9/2\, O_2 + 3H_2O = MoO_4^{2-} + 2SO_4^{2-} + 6H^+$$

Protons are produced in the process of oxidative dissolution of MoS_2, resulting in the decrease of pH. The accumulation of protons will inevitably decrease the rate of oxidative dissolution of MoS_2, as observed in Figure 5-6 (A) and (B). Meanwhile, the dissolved Mo concentration and pH of the samples in nitrogen-filled glove box were compared and found to be relatively constant even after 100 days, which highlights the role of oxygen in oxidative dissolution. Figure 5-6 (C)-(E) show the images of various samples

w/wo oxygen after 100 days. Compared to the samples stored in glove box, the color of samples in air faded observed in Figure 5-6 (C) and (D). Severe precipitation was even observed in MoS_2 stock solution (Figure 5-6 E) and the pH of precipitated sample was found to be 2.2. The precipitated sample can be readily redispersed with adjusting pH to neutral, which implies that the accumulation of protons during MoS_2 oxidative dissolution is the primary cause for the long-term instability of MoS_2 suspensions. Relatively high pH however can significantly accelerate the oxidation of MoS_2 (vida infra), and storage in inert gas therefore is a more reasonable way to maintain the long-term colloidal stability of these potentially oxidizable 2D nanomaterials (MoS_2, $MoSe_2$, WS_2 and WSe_2 in Figure 5-2).

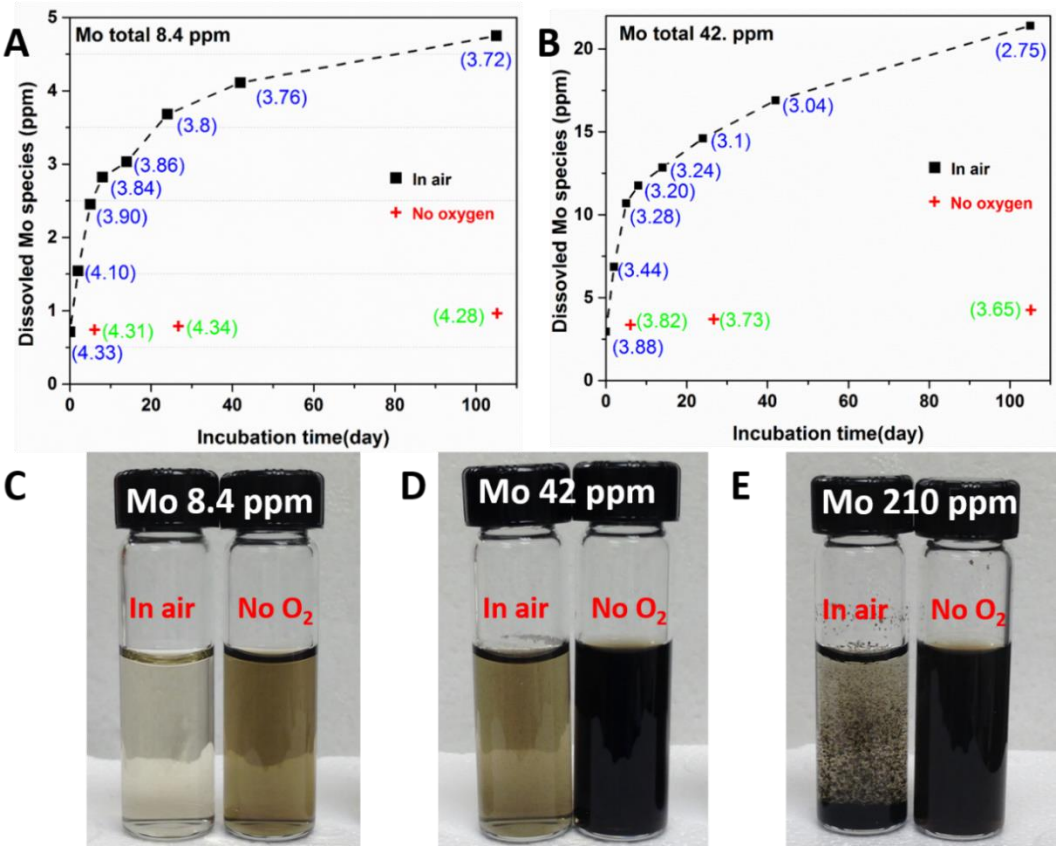

Figure 5-6. Investigation on the long-time colloidal instability of MoS_2 suspensions. The time-dependent release of dissolved Mo species in the presence of air or without oxygen and the corresponding suspension pH for low (A) and high (B) concentration MoS_2 samples. The blue or green number indicates the pH of suspension when the sample is ready for ultrafiltration. Images of low (C), high (D) concentration and MoS_2 stock solutions w/wo air after exposure for 100 days.

Oxidative dissolution of MoS_2 was further tested in a variety of biological and environmental relevant medium. (Figure 5-7) This oxidative process is affected by pH of the buffer in simple solution. In seawater mimics with relatively high pH, MoS_2 nearly completely decomposes in 10 days and gives fastest dissolution, followed by oxidative decomposition in cell culture medium and fresh water mimics. The effect of components (e.g. chloride ions, amino acids, humic acids) were not explored in this study, but cannot be neglected. Thiol-containing molecules have been reported to bind to the defects of MoS_2 and increase the stability in high ionic strength solution,[50] which may reduce the oxidative dissolution since the defects sits as potential oxidation targets are blocked. The cytotoxicity of resulting transformed species (e.g. molybdate) is insignificant, and it shows toxicity only at high dose, which implies the low toxicity observed in the current literature.[51-53]

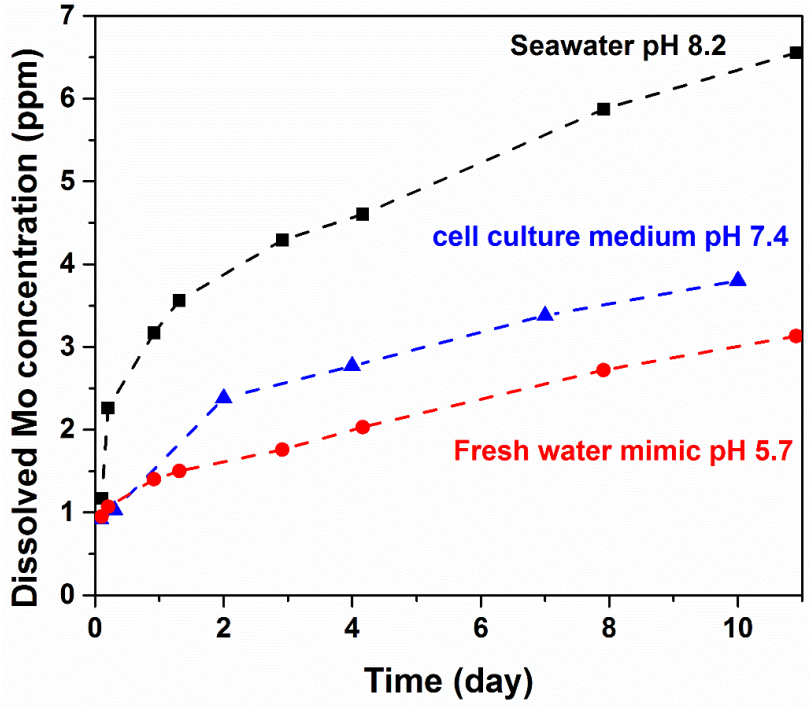

Figure 5-7. The case study shows MoS_2 can undergo oxidative dissolution in a variety of biological and environmental relevant media.

On the contrary, the metal oxide 2D nanomaterials are thermodynamically stable against oxygen further oxidation predicted in Figure 5-2, however, some of the metal oxide can be reduced by biomolecules and release ionic species in relevant biological media. Figure 5-8 shows the MnO_2 decomposes in the presence of reduced glutathione by monitoring the intensity of absorption peak of MnO_2 nanosheets at 406 nm. This reductive dissolution property has been utilized in the intracellular glutathione detection.[54] The kinetics of reduction of polymeric MnO_2 by cysteine and glutathione has been studied, and the reactions products were identified as Mn (II) and corresponding disulfide.[55]

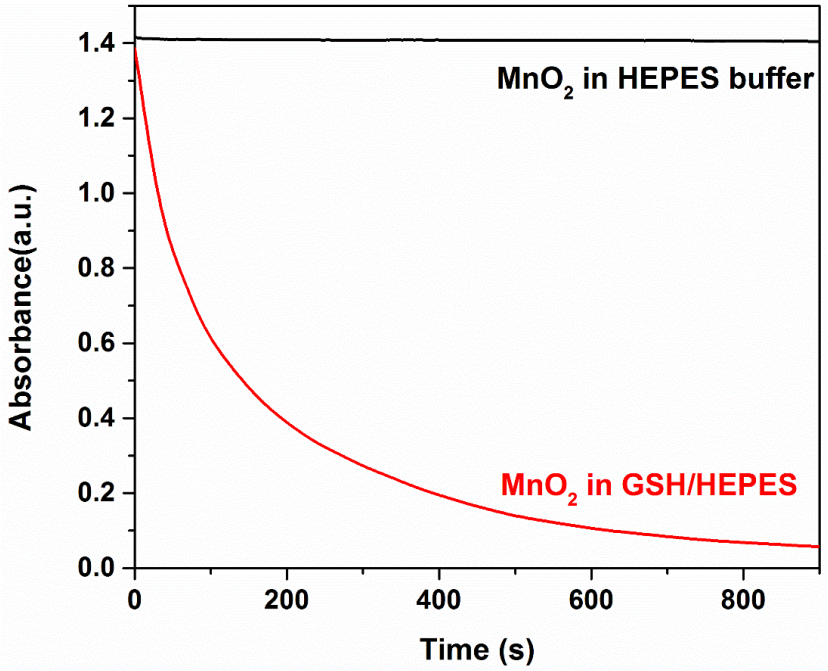

Figure 5-8. The case study of MnO_2, showing it can undergo reductive dissolution in presence of GSH otherwise can be stable in HEPES-only buffer or other solutions.

MoO_3 may undergo hydrolysis in biological relevant solutions. There's no reports yet regarding if MoO_3 or the transformed product (molybdate) is able to undergo further redox reactions in biological conditions, but it can be inferred by the reduction under relevant conditions. The reductive transformation of MoO_3 (or molybdate) in

environmental relevant solutions is available showing organic extraction from soil can reduce Mo(VI) to Mo(V), and even Mo(III) in the presence of humic acid.[56] These experimental data, along with the theoretical predictions in Figure 5-2, demonstrates that the reductive dissolution is a plausible transformation pathway for 2D nanomaterials in the biological and environmental relevant media.

5.3.4 GSH assay of 2D nanomaterials

MoS_2 is predicted to be catalytically active in biological systems in Figure 5-3. Particularly, The conduction band minimum of MoS_2 is within the redox potentials of O_2/ H_2O and GSSG/GSH couples, which according to the theory[18] indicates CBM of MoS_2 can transfer electrons from GSH and donate them to O_2 completing the catalytic GSH oxidation process. On the contrary, h-BN as an example 2D nanomaterials that CBM [57] is far above cellular redox potential is predicted to be catalytically inactive. To validate this hypothesis, the concentration of GSH was determined using ThioGlo fluorescent reagent, after incubation with 2D nanomaterials and separation using ultrafiltration. Figure 5-9 shows the time-dependent decrease of GSH concentration in the presence of either 2D MoS_2 or h-BN. Consistent with theoretical predictions, MoS_2 can decrease GSH concentration over time while h-BN can't. (Figure 5-9A) To prove that GSH is oxidatively consumed rather than physical absorption on 2D MoS_2, oxygen levels in the presence of MoS_2 and GSH were monitored by DO probe. The decreased levels of oxygen in Figure 5-9B indicate the occurrence of oxidation reactions. After the depletion of oxygen, the sample was left exposed to air until depletion of all GSH and recovery of oxygen to original level. Oxygen level was observed to decrease again if fresh GSH was supplemented indicating

the good recycle ability and stability of MoS_2 as catalyst. Furthermore, graphenic nanocarbons were reported to catalyze the oxidation of GSH,[31] which provides an additional experimental support to applicability of this framework in predicting catalytic ability in biological systems.

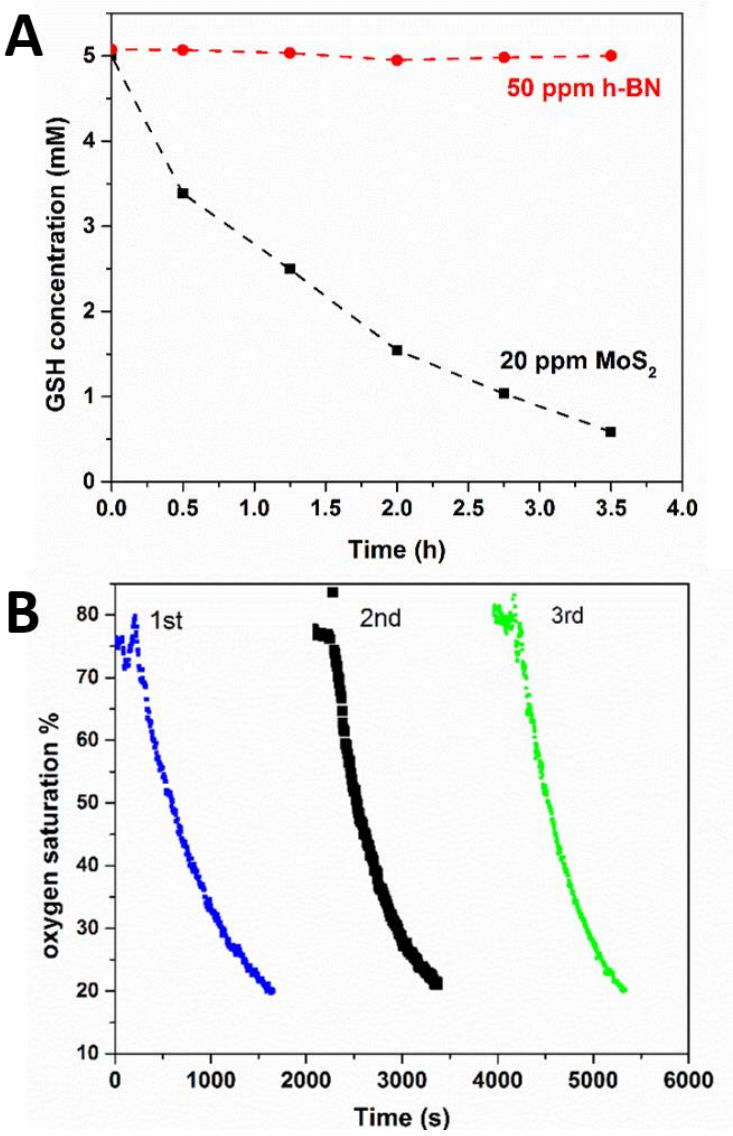

Figure 5-9. The catalytic ability of representative 2D nanomaterials towards oxidation of GSH. (A) Time-dependent catalytic oxidation of GSH in the presence 2D MoS_2 or h-BN, showing MoS_2 is catalytically active towards GSH oxidation while h-BN is catalytically inert. (B) Reduced oxygen levels in the presence of MoS_2 and GSH monitored by DO probe indicating GSH is oxidatively consumed. After the depletion of oxygen, the sample was allowed to recover oxygen level. Oxygen level was observed to decrease again if fresh GSH is supplemented showing the good recycle ability and stability of MoS_2 catalyst.

5.3.5 Environmental applications of MoS_2

Catalysts play an important role in modern science and technology. In environmental field for example, catalysts are used in conversion of car exhaust emissions into less toxic gases, and degradation of organic toxicants in aqueous systems. The most efficient and widely used catalysts are frequently noble metal based nanoparticles, but their high cost and scarcity has driven a search for alternatives which is catalytically active but more cost effective.

Chemically-exfoliated MoS_2 is intrinsically metallic 1T phase converted from the 2H phase after lithium intercalation and chemical exfoliation. This metallic nature of MoS_2 is worth exploration in potential catalytic performance in environmental-relevant applications. Here, the catalytic performance of metallic MoS_2 in environmental reactions was evaluated in the model reaction using $NaBH_4$ as reductant and 4-nitrophenol (4-NP) as target organic pollutant, which is perhaps the most often used reaction to test the catalytic activities of metal nanoparticles and provides rich data in literature for comparisons. The underlying mechanism, the origin of induction period particularly, was investigated.

The reaction can be easily monitored by UV-vis spectroscopy as shown in Figure 5-10. In the absence of catalysts, the reduction of 4-NP by $NaBH_4$ is kinetically inhibited.[58] The decrease of characteristic peak of 4-NP at 400 nm (Figure 5-10A) indicates the catalytic reduction by $NaBH_4$, which requires catalysts, metallic MoS_2 in this case. An excess amount of $NaBH_4$ (ratio of $NaBH_4$:4-NP is typically 300) was used so that its concentration can be considered as constant throughout the entire reaction. Particularly when the initial concentration of 4-NP was 0.12 mM, the concentration of $NaBH_4$ and MoS_2 employed were 36 mM and 2 ppm, respectively. Figure 5-10B shows the catalytic

reduction usually occurs under such conditions after an induction period t_0, and then can be described by a first order rate law by:

$$\frac{dc_t}{dt} = -k_{app}c_t$$

where c_t is the concentration of 4-NP at time t. The apparent rate constant k_{app} can be determined from the slope of the linear correlation of $\ln(A/A_0)$ with time t. Under the above conditions, the k_{app} value obtained for the reduction of 4-NP was $3.8*10^{-3}$ s^{-1}. To compare the catalytic efficiency of MoS_2 with those of conventional noble metal NPs, the turnover frequency (TOF) is calculated for MoS_2, which is defined as the moles of 4-NP converted per mole of catalyst per minute. Calculated TOF as well as data has been reported in the literature was listed in Table 5-1. The TOF value of chemically-exfoliated MoS_2 is determined to be 1.31 min^{-1}, which is comparable to those of noble metal based nanoparticle catalysts. Reduced GO, as 2D graphene-based nanosheets, has been recently shown to exhibit catalytic activities in the reduction of 4-NP reactions. However, the TOF values of reduced GO are three magnitude lower than that of chemically exfoliated MoS_2 nanosheets.[59]

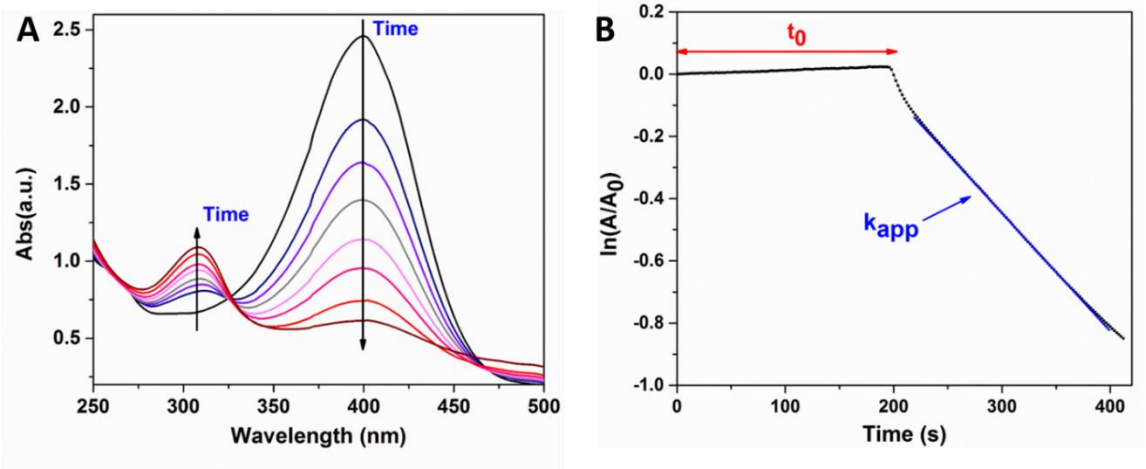

Figure 5-10. Reduction of 4-NP by $NaBH_4$ catalyzed by chemically-exfoliated MoS_2. (A) Absorption spectra as a function of time showing the decrease of characteristic 4-NP peak at 400 nm, whereas the peak of the product aminophenol slowly increasing at ~ 310 nm. (B) Typical changing curve of the absorption of 4-NP as a function of time during catalytic reduction. The catalytic reduction of 4-NP starts after an induction period t_0, and kinetic constant k_{app} can be determined from the linear section of the curve (blue portion).

Table 5-1. Comparison of TOF values for various catalysts in the 4-NP reduction reactions

Catalyst	TOF (min^{-1})	Reference
Chemically-exfoliated MoS_2	1.31	Present work
Au nanoparticles/based composites	0.19-1.5	[60-62]
Ag nanoparticles/based composites	0.1-1.9	[63-65]
Pt nanoparticles/based composites	0.03-18	[66-70]
Noble metal alloy/ based composites	0.2-1.7	[71, 72]
Pristine or N-doped reduced GO	~ $1*10^{-3}$	[19, 59, 73]

In the catalytic reduction of 4-NP, an induction period has been observed, and the origins of the induction time can be diverse: catalyst surface restruction,[74-76] diffusion-controlled adsorption of reactants on catalyst surface[77, 78] and dissolved oxygen competition with the reactants. The diffusion-determined induction period usually exists in

the systems containing shell-coated or ligands-covered metallic nanoparticles, and induction period is the diffusion time of 4-NP needed to cross the shell to reach the catalytically active surface of metallic nanoparticles. So diffusion controlled induction is not likely the cause of the activation time needed in the case of MoS_2, where the active sites are directly exposed without any barriers. The surface restruction theory in reference[74] suggests the induction time is related to a restruction of the catalyst surface induced by 4-NP. Figure 5-11 shows the impacts of reactant and catalyst concentration variations on the induction period. The length of induction period is independent on the concentration of the substrate 4-NP. This finding clearly rules out that the induction period is attributed to any reaction involving 4-NP such as diffusion of 4-NP to active surface or 4-NP-induced surface restruction.[76, 79]

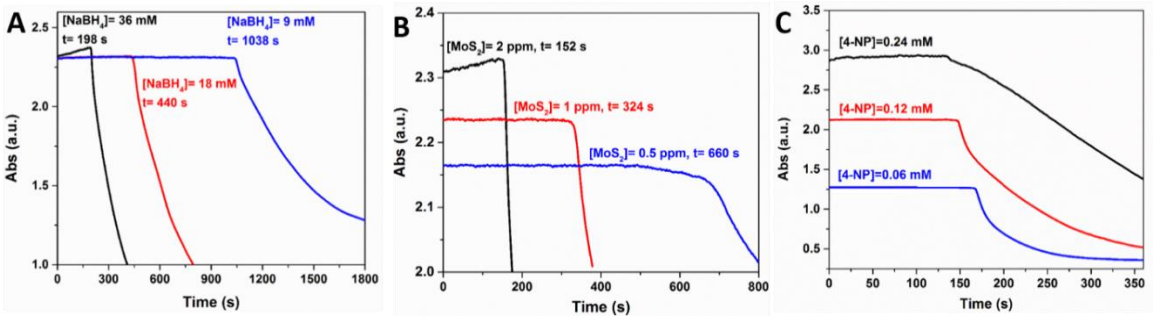

Figure 5-11. Plots of the time evolution of 4-NP absorbance at 400 nm under various conditions showing the induction time versus the concentration of (A) $NaBH_4$ varying at 9, 18, 36 mM while keeping C_{MoS2} and $C_{4\text{-}NP}$ constant at 2 ppm and 0.12 mM, respectively (B) MoS_2 varying at 0.5, 1, 2 ppm while keeping C_{NaBH4} and $C_{4\text{-}NP}$ constant at 36 mM and 0.12 mM, respectively (C) 4-NP varying at 0.24, 0.12, 0.06 mM while keep C_{MoS2} and C_{NaBH4} constant at 0.12 mM and 36 mM, respectively.

Furthermore, increasing the concentration of either reductant ($NaBH_4$) or catalyst (MoS_2) can reduce the induction time needed, which seems to follow such manner:

$$1/t \sim \{NaBH_4\}*\{MoS_2\}$$

This makes DO competition a plausible mechanism for induction period because the reaction rate of DO competition correlates with the reductant ($NaBH_4$) and the catalyst (MoS_2). DO reacts at a much faster rate with borohydride than 4-NP, therefore the reduction of 4-NP won't start until the full consumption of DO. This statement is further supported by the following experimental results in Figure 5-12. Figure 5-12 A and B show the pre-depletion of DO levels by the pre-incubation of reductant ($NaBH_4$) and catalyst (MoS_2) and nitrogen bubbling in all reagents, respectively. Both ways can significantly decrease the induction period needed to start 4-NP reduction, which supports the DO competition causes the induction period in the case of MoS2 catalysts.

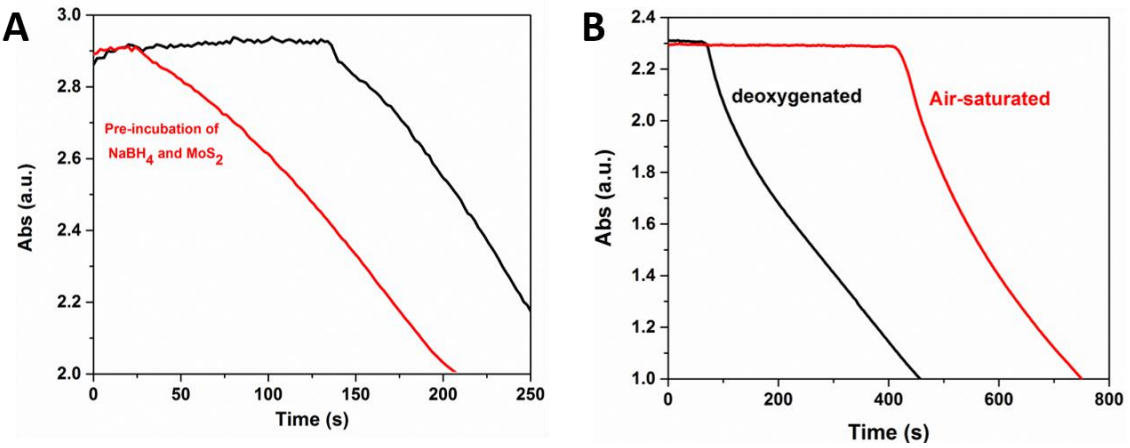

Figure 5-12. Validation of assumption that DO competition causes induction period by (A) pre-incubation of $NaBH_4$ and MoS_2 to deplete DO followed by 4-NP addition and (B) de-oxygenate all the samples before mixture by nitrogen bubbling.

5.4 Conclusions

To conclude, we use simple theoretical models to screen and predict transformation and biological reactivity of 2D nanomaterials based on their fundamental chemical attributes. The oxidation and reduction potentials of 2D nanomaterials are calculated and compared with biological redox potential range, to predict the stability of 2D nanomaterials

in environmentally and biologically relevant aqueous solution. Combined with equilibrium solubility data, 2D nanomaterials are categorized and predicted to undergo three possible dissolution pathways: simple (involving protons, ligand-assisted), oxidative (usually oxygen as oxidants) or reductive (by biomolecules, *e.g.* GSH) transformation. We also use a recently developed band-structure based framework to identify 2D materials that are likely to have pro-oxidant activity in biological systems. Accordingly, overlap of 2D materials conduction band minimum (or valence band maximum) with the cellular redox potential can lead to ROS generation, which can be assessed by simple GSH-oxidation assay. Reference materials (carbon-based materials and noble metal nanoparticles) that have been explicitly studied are also included to evaluate the applicability of this platform on predicting the 2D structure-activity relationships. Then we offer suggestions for grouping 2D materials into chemical classes for prioritization in risk management, and use MoS_2 as an example 2D material to illustrate the chemical transformation and catalytic activity in biological and environmental media. We studied the dissolution behaviors of MoS_2 in various relevant solutions and conditions involving the effects of oxygen, pH and ligands. These results provide useful information on the storage and use of MoS_2 nanomaterials, and also give the picture on the fate and possible transformation and the form the materials end up with. Finally we study the possible application of 2D metallic MoS_2 in the environmental remediation fields. Overall, this chapter provides a predictive platform to investigate the potential biological and environmental transformations and activities of novel 2D nanomaterials.

5.5 Reference

1. Xu, M.; Liang, T.; Shi, M.; Chen, H. Graphene-Like Two-Dimensional Materials. *Chem. Rev. (Washington, DC, U. S.)* **2013**, 113, 3766-3798.
2. Ji, Q.; Zhang, Y.; Zhang, Y.; Liu, Z. Chemical vapour deposition of group-VIB metal dichalcogenide monolayers: engineered substrates from amorphous to single crystalline. *Chemical Society Reviews* **2015**, 44, 2587-2602.
3. Voiry, D.; Mohite, A.; Chhowalla, M. Phase engineering of transition metal dichalcogenides. *Chemical Society Reviews* **2015**, 44, 2702-2712.
4. Tan, C.; Zhang, H. Two-dimensional transition metal dichalcogenide nanosheet-based composites. *Chemical Society Reviews* **2015**, 44, 2713-2731.
5. Chen, Y.; Tan, C.; Zhang, H.; Wang, L. Two-dimensional graphene analogues for biomedical applications. *Chemical Society Reviews* **2015**, 44, 2681-2701.
6. Jachak, A. C.; Creighton, M.; Qiu, Y.; Kane, A. B.; Hurt, R. H. Biological interactions and safety of graphene materials. *MRS Bulletin* **2012**, 37, 1307-1313.
7. Sanchez, V. C.; Jachak, A.; Hurt, R. H.; Kane, A. B. Biological Interactions of Graphene-Family Nanomaterials: An Interdisciplinary Review. *Chemical Research in Toxicology* **2012**, 25, 15-34.
8. Farrell, J.; Kason, M.; Melitas, N.; Li, T. Investigation of the Long-Term Performance of Zero-Valent Iron for Reductive Dechlorination of Trichloroethylene. *Environ. Sci. Technol.* **2000**, 34, 514-521.
9. Liu, J.; Sonshine, D. A.; Shervani, S.; Hurt, R. H. Controlled Release of Biologically Active Silver from Nanosilver Surfaces. *ACS Nano* **2010**, 4, 6903-6913.
10. Levard, C.; Reinsch, B. C.; Michel, F. M.; Oumahi, C.; Lowry, G. V.; Brown, G. E. Sulfidation Processes of PVP-Coated Silver Nanoparticles in Aqueous Solution: Impact on Dissolution Rate. *Environ. Sci. Technol.* **2011**, 45, 5260-5266.
11. Wang, Z.; von dem Bussche, A.; Kabadi, P. K.; Kane, A. B.; Hurt, R. H. Biological and Environmental Transformations of Copper-Based Nanomaterials. *ACS Nano* **2013**, 7, 8715-8727.

12. Ma, R.; Levard, C.; Michel, F. M.; Brown, G. E.; Lowry, G. V. Sulfidation Mechanism for Zinc Oxide Nanoparticles and the Effect of Sulfidation on Their Solubility. *Environ. Sci. Technol.* **2013**, 47, 2527-2534.
13. Detriche, S.; Zorzini, G.; Colomer, J.-F.; Fonseca, A.; Nagy, J. Application of the Hansen solubility parameters theory to carbon nanotubes. *J. Nanosci. Nanotechnol.* **2008**, 8, 6082-6092.
14. Zhou, H.; Mu, Q.; Gao, N.; Liu, A.; Xing, Y.; Gao, S.; Zhang, Q.; Qu, G.; Chen, Y.; Liu, G.; Zhang, B.; Yan, B. A Nano-Combinatorial Library Strategy for the Discovery of Nanotubes with Reduced Protein-Binding, Cytotoxicity, and Immune Response. *Nano Letters* **2008**, 8, 859-865.
15. Lundqvist, M.; Stigler, J.; Elia, G.; Lynch, I.; Cedervall, T.; Dawson, K. A. Nanoparticle size and surface properties determine the protein corona with possible implications for biological impacts. *Proceedings of the National Academy of Sciences* **2008**, 105, 14265-14270.
16. Puzyn, T.; Rasulev, B.; Gajewicz, A.; Hu, X.; Dasari, T. P.; Michalkova, A.; Hwang, H.-M.; Toropov, A.; Leszczynska, D.; Leszczynski, J. Using nano-QSAR to predict the cytotoxicity of metal oxide nanoparticles. *Nat Nano* **2011**, 6, 175-178.
17. Burello, E.; Worth, A. P. A theoretical framework for predicting the oxidative stress potential of oxide nanoparticles. *Nanotoxicology* **2011**, 5, 228-235.
18. Zhang, H.; Ji, Z.; Xia, T.; Meng, H.; Low-Kam, C.; Liu, R.; Pokhrel, S.; Lin, S.; Wang, X.; Liao, Y.-P.; Wang, M.; Li, L.; Rallo, R.; Damoiseaux, R.; Telesca, D.; Mädler, L.; Cohen, Y.; Zink, J. I.; Nel, A. E. Use of Metal Oxide Nanoparticle Band Gap To Develop a Predictive Paradigm for Oxidative Stress and Acute Pulmonary Inflammation. *ACS Nano* **2012**, 6, 4349-4368.
19. Guardia, L.; Paredes, J. I.; Munuera, J. M.; Villar-Rodil, S.; Ayán-Varela, M.; Martínez-Alonso, A.; Tascón, J. M. D. Chemically Exfoliated MoS2 Nanosheets as an Efficient Catalyst for Reduction Reactions in the Aqueous Phase. *ACS Appl. Mater. Interfaces* **2014**, 6, 21702-21710.
20. Lu, F.; Wang, F.; Gao, W.; Huang, X.; Zhang, X.; Li, Y. Aqueous soluble boron nitride nanosheets via anionic compound-assisted exfoliation. *Materials Express* **2013**, 3, 144-150.

21. Kadoma, Y.; Uchimoto, Y.; Wakihara, M. Synthesis and structural study on MnO2 nanosheet material by X-ray absorption spectroscopic technique. *The Journal of Physical Chemistry B* **2006**, 110, 174-177.
22. Yi, L.; Li, H.; Sun, L.; Liu, L.; Zhang, C.; Xi, Z. A Highly Sensitive Fluorescence Probe for Fast Thiol-Quantification Assay of Glutathione Reductase. *Angewandte Chemie International Edition* **2009**, 48, 4034-4037.
23. Gustafsson, J. P. Visual MINTEQ version 3.0 http://vminteq.lwr.kth.se/ Stockholm, Sweden. **2013**.
24. Wang, G.; Ling, Y.; Wang, H.; Yang, X.; Wang, C.; Zhang, J. Z.; Li, Y. Hydrogen-treated WO3 nanoflakes show enhanced photostability. *Energy & Environmental Science* **2012**, 5, 6180-6187.
25. Petrochenkov, V.; Gorichev, I.; Batrakov, V.; Izotov, A.; Kutepov, A. Catalytic effect of ammonia on the kinetics and mechanism of MoO3 dissolution in alkaline solutions. *Theoretical Foundations of Chemical Engineering* **2004**, 38, 386-393.
26. Liu, B.; Zeng, H. C. Salt-assisted deposition of SnO2 on α-MoO3 nanorods and fabrication of polycrystalline SnO2 nanotubes. *The Journal of Physical Chemistry B* **2004**, 108, 5867-5874.
27. Irmawati, R.; Shafizah, M. The production of high purity hexagonal MoO3 through the acid washing of as-prepared solids. *Int J Basic Appl Sci* **2009**, 9, 241-4.
28. Boclair, J. W.; Braterman, P. S. Layered Double Hydroxide Stability. 1. Relative Stabilities of Layered Double Hydroxides and Their Simple Counterparts. *Chemistry of Materials* **1999**, 11, 298-302.
29. Liu, J.; Hurt, R. H. Ion Release Kinetics and Particle Persistence in Aqueous Nano-Silver Colloids. *Environmental Science and Technology* **2010**, 44, 2169-2175.
30. Xiu, Z.-m.; Zhang, Q.-b.; Puppala, H. L.; Colvin, V. L.; Alvarez, P. J. Negligible particle-specific antibacterial activity of silver nanoparticles. *Nano Letters* **2012**, 12, 4271-4275.
31. Yang, X.; Gondikas, A. P.; Marinakos, S. M.; Auffan, M.; Liu, J.; Hsu-Kim, H.; Meyer, J. N. Mechanism of silver nanoparticle toxicity is dependent on dissolved silver and surface coating in Caenorhabditis elegans. *Environmental Science and Technology* **2011**, 46, 1119-1127.

32. Chen, S.; Wang, L.-W. Thermodynamic Oxidation and Reduction Potentials of Photocatalytic Semiconductors in Aqueous Solution. *Chemistry of Materials* **2012**, 24, 3659-3666.
33. Ross, S.; Sussman, A. Surface Oxidation of Molybdenum Disulfide. *The Journal of Physical Chemistry* **1955**, 59, 889-892.
34. Yamamoto, M.; Dutta, S.; Aikawa, S.; Nakaharai, S.; Wakabayashi, K.; Fuhrer, M. S.; Ueno, K.; Tsukagoshi, K. Self-Limiting Layer-by-Layer Oxidation of Atomically Thin WSe2. *Nano Letters* **2015**, 15, 2067-2073.
35. Zhou, H.; Yu, F.; Liu, Y.; Zou, X.; Cong, C.; Qiu, C.; Yu, T.; Yan, Z.; Shen, X.; Sun, L.; Yakobson, B.; Tour, J. Thickness-dependent patterning of MoS2 sheets with well-oriented triangular pits by heating in air. *Nano Res.* **2013**, 6, 703-711.
36. Plumlee, G. S.; Morman, S. A.; Ziegler, T. L. The Toxicological Geochemistry of Earth Materials: An Overview of Processes and the Interdisciplinary Methods Used to Understand Them. *Rev. Mineral. Geochem.* **2006**, 64, 5-57.
37. Gong, C.; Zhang, H.; Wang, W.; Colombo, L.; Wallace, R. M.; Cho, K. Band alignment of two-dimensional transition metal dichalcogenides: Application in tunnel field effect transistors. *Applied Physics Letters* **2013**, 103, 053513.
38. Song, S. H.; Kim, B. H.; Choe, D.-H.; Kim, J.; Kim, D. C.; Lee, D. J.; Kim, J. M.; Chang, K. J.; Jeon, S. Bandgap Widening of Phase Quilted, 2D MoS2 by Oxidative Intercalation. *Adv. Mater. (Weinheim, Ger.)* **2015**, 27, 3152-3158.
39. Hui, Y. Y.; Liu, X.; Jie, W.; Chan, N. Y.; Hao, J.; Hsu, Y.-T.; Li, L.-J.; Guo, W.; Lau, S. P. Exceptional Tunability of Band Energy in a Compressively Strained Trilayer MoS2 Sheet. *ACS Nano* **2013**, 7, 7126-7131.
40. Hirakawa, T.; Kamat, P. V. Charge Separation and Catalytic Activity of Ag@TiO2 Core−Shell Composite Clusters under UV−Irradiation. *Journal of the American Chemical Society* **2005**, 127, 3928-3934.
41. Subramanian, V.; Wolf, E. E.; Kamat, P. V. Catalysis with TiO2/Gold Nanocomposites. Effect of Metal Particle Size on the Fermi Level Equilibration. *Journal of the American Chemical Society* **2004**, 126, 4943-4950.

42. Kou, X.; Zhang, S.; Yang, Z.; Tsung, C.-K.; Stucky, G. D.; Sun, L.; Wang, J.; Yan, C. Glutathione- and Cysteine-Induced Transverse Overgrowth on Gold Nanorods. *J. Am. Chem. Soc.* **2007**, 129, 6402-6404.
43. Li, H.; Cui, Z.; Han, C. Glutathione-stabilized silver nanoparticles as colorimetric sensor for Ni2+ ion. *Sensors and Actuators B: Chemical* **2009**, 143, 87-92.
44. Partoens, B.; Peeters, F. M. From graphene to graphite: Electronic structure around the K point. *Physical Review B* **2006**, 74, 075404.
45. Odom, T. W.; Huang, J.-L.; Kim, P.; Lieber, C. M. Atomic structure and electronic properties of single-walled carbon nanotubes. *Nature* **1998**, 391, 62-64.
46. Shan, B.; Cho, K. First Principles Study of Work Functions of Single Wall Carbon Nanotubes. *Physical Review Letters* **2005**, 94, 236602.
47. Chhowalla, M.; Amaratunga, G. A. J. Thin films of fullerene-like MoS2 nanoparticles with ultra-low friction and wear. *Nature* **2000**, 407, 164-167.
48. Yin, W.; Yan, L.; Yu, J.; Tian, G.; Zhou, L.; Zheng, X.; Zhang, X.; Yong, Y.; Li, J.; Gu, Z. High-throughput synthesis of single-layer MoS2 nanosheets as a near-infrared photothermal-triggered drug delivery for effective cancer therapy. *ACS Nano* **2014**, 8, 6922-6933.
49. Mak, K. F.; Lee, C.; Hone, J.; Shan, J.; Heinz, T. F. Atomically Thin MoS2: A New Direct-Gap Semiconductor. *Phys. Rev. Lett.* **2010**, 105, 136805.
50. Chou, S. S.; De, M.; Kim, J.; Byun, S.; Dykstra, C.; Yu, J.; Huang, J.; Dravid, V. P. Ligand Conjugation of Chemically Exfoliated MoS2. *J. Am. Chem. Soc.* **2013**, 135, 4584-4587.
51. Teo, W. Z.; Chng, E. L. K.; Sofer, Z.; Pumera, M. Cytotoxicity of Exfoliated Transition‐Metal Dichalcogenides (MoS2, WS2, and WSe2) is Lower Than That of Graphene and its Analogues. *Chemistry-A European Journal* **2014**, 20, 9627-9632.
52. Chou, S. S.; Kaehr, B.; Kim, J.; Foley, B. M.; De, M.; Hopkins, P. E.; Huang, J.; Brinker, C. J.; Dravid, V. P. Chemically Exfoliated MoS2 as Near-Infrared Photothermal Agents. *Angewandte Chemie International Edition* **2013**, 52, 4160-4164.

53. Shah, P.; Narayanan, T. N.; Li, C.-Z.; Alwarappan, S. Probing the biocompatibility of MoS2 nanosheets by cytotoxicity assay and electrical impedance spectroscopy. *Nanotechnology* **2015**, 26, 315102.

54. Deng, R.; Xie, X.; Vendrell, M.; Chang, Y.-T.; Liu, X. Intracellular Glutathione Detection Using MnO2-Nanosheet-Modified Upconversion Nanoparticles. *Journal of the American Chemical Society* **2011**, 133, 20168-20171.

55. Herszage, J.; dos Santos Afonso, M.; Luther, G. W. Oxidation of Cysteine and Glutathione by Soluble Polymeric MnO2. *Environ. Sci. Technol.* **2003**, 37, 3332-3338.

56. Goodman, B. A.; Cheshire, M. V. Reduction of molybdate by soil organic matter: EPR evidence for formation of both Mo(V) and Mo(III). *Nature* **1982**, 299, 618-620.

57. Shirodkar, S. N.; Waghmare, U. V.; Fisher, T. S.; Grau-Crespo, R. Engineering the electronic bandgaps and band edge positions in carbon-substituted 2D boron nitride: a first-principles investigation. *Physical Chemistry Chemical Physics* **2015**, 17, 13547-13552.

58. Baruah, B.; Gabriel, G. J.; Akbashev, M. J.; Booher, M. E. Facile Synthesis of Silver Nanoparticles Stabilized by Cationic Polynorbornenes and Their Catalytic Activity in 4-Nitrophenol Reduction. *Langmuir* **2013**, 29, 4225-4234.

59. Kong, X.-k.; Chen, Q.-w.; Lun, Z.-y. Probing the influence of different oxygenated groups on graphene oxide's catalytic performance. *Journal of Materials Chemistry A* **2014**, 2, 610-613.

60. He, R.; Wang, Y.-C.; Wang, X.; Wang, Z.; Liu, G.; Zhou, W.; Wen, L.; Li, Q.; Wang, X.; Chen, X.; Zeng, J.; Hou, J. G. Facile synthesis of pentacle gold–copper alloy nanocrystals and their plasmonic and catalytic properties. *Nat Commun* **2014**, 5.

61. Kuroda, K.; Ishida, T.; Haruta, M. Reduction of 4-nitrophenol to 4-aminophenol over Au nanoparticles deposited on PMMA. *J. Mol. Catal. A: Chem.* **2009**, 298, 7-11.

62. Li, J.; Liu, C.-y.; Liu, Y. Au/graphene hydrogel: synthesis, characterization and its use for catalytic reduction of 4-nitrophenol. *J. Mater. Chem.* **2012**, 22, 8426-8430.

63. Zhang, P.; Shao, C.; Zhang, Z.; Zhang, M.; Mu, J.; Guo, Z.; Liu, Y. In situ assembly of well-dispersed Ag nanoparticles (AgNPs) on electrospun carbon nanofibers (CNFs) for catalytic reduction of 4-nitrophenol. *Nanoscale* **2011**, 3, 3357-3363.
64. Vadakkekara, R.; Chakraborty, M.; Parikh, P. A. Reduction of aromatic nitro compounds on colloidal hollow silver nanospheres. *Colloids and Surfaces A: Physicochemical and Engineering Aspects* **2012**, 399, 11-17.
65. You, J.; Zhao, C.; Cao, J.; Zhou, J.; Zhang, L. Fabrication of high-density silver nanoparticles on the surface of alginate microspheres for application in catalytic reaction. *Journal of Materials Chemistry A* **2014**, 2, 8491-8499.
66. Lin, X.; Wu, M.; Wu, D.; Kuga, S.; Endo, T.; Huang, Y. Platinum nanoparticles using wood nanomaterials: eco-friendly synthesis, shape control and catalytic activity for p-nitrophenol reduction. *Green Chem.* **2011**, 13, 283-287.
67. Gu, X.; Qi, W.; Xu, X.; Sun, Z.; Zhang, L.; Liu, W.; Pan, X.; Su, D. Covalently functionalized carbon nanotube supported Pd nanoparticles for catalytic reduction of 4-nitrophenol. *Nanoscale* **2014**, 6, 6609-6616.
68. Kim, C.; Lee, H. Change in the catalytic reactivity of Pt nanocubes in the presence of different surface-capping agents. *Catal. Commun.* **2009**, 10, 1305-1309.
69. Zhang, Z.; Xiao, F.; Xi, J.; Sun, T.; Xiao, S.; Wang, H.; Wang, S.; Liu, Y. Encapsulating Pd Nanoparticles in Double-Shelled Graphene@Carbon Hollow Spheres for Excellent Chemical Catalytic Property. *Sci. Rep.* **2014**, 4.
70. Li, H.; Han, L.; Cooper-White, J.; Kim, I. Palladium nanoparticles decorated carbon nanotubes: facile synthesis and their applications as highly efficient catalysts for the reduction of 4-nitrophenol. *Green Chem.* **2012**, 14, 586-591.
71. Shi, L.; Wang, A.; Zhang, T.; Zhang, B.; Su, D.; Li, H.; Song, Y. One-Step Synthesis of Au–Pd Alloy Nanodendrites and Their Catalytic Activity. *The Journal of Physical Chemistry C* **2013**, 117, 12526-12536.
72. Peng, Y.; Wu, X.; Qiu, L.; Liu, C.; Wang, S.; Yan, F. Synthesis of carbon-PtAu nanoparticle hybrids originating from triethoxysilane-derivatized ionic liquids for methanol electrooxidation and the catalytic reduction of 4-nitrophenol. *Journal of Materials Chemistry A* **2013**, 1, 9257-9263.

73. Kong, X.-k.; Sun, Z.-y.; Chen, M.; Chen, C.-l.; Chen, Q.-w. Metal-free catalytic reduction of 4-nitrophenol to 4-aminophenol by N-doped graphene. *Energy & Environmental Science* **2013**, 6, 3260-3266.
74. Wunder, S.; Lu, Y.; Albrecht, M.; Ballauff, M. Catalytic Activity of Faceted Gold Nanoparticles Studied by a Model Reaction: Evidence for Substrate-Induced Surface Restructuring. *ACS Catalysis* **2011**, 1, 908-916.
75. Johnson, J. A.; Makis, J. J.; Marvin, K. A.; Rodenbusch, S. E.; Stevenson, K. J. Size-Dependent Hydrogenation of p-Nitrophenol with Pd Nanoparticles Synthesized with Poly(amido)amine Dendrimer Templates. *The Journal of Physical Chemistry C* **2013**, 117, 22644-22651.
76. Wunder, S.; Polzer, F.; Lu, Y.; Mei, Y.; Ballauff, M. Kinetic Analysis of Catalytic Reduction of 4-Nitrophenol by Metallic Nanoparticles Immobilized in Spherical Polyelectrolyte Brushes. *The Journal of Physical Chemistry C* **2010**, 114, 8814-8820.
77. Gao, Y.; Ding, X.; Zheng, Z.; Cheng, X.; Peng, Y. Template-free method to prepare polymer nanocapsules embedded with noble metal nanoparticles. *Chem. Commun. (Cambridge, U. K.)* **2007**, 3720-3722.
78. Mahmoud, M. A.; El-Sayed, M. A. Time Dependence and Signs of the Shift of the Surface Plasmon Resonance Frequency in Nanocages Elucidate the Nanocatalysis Mechanism in Hollow Nanoparticles. *Nano Lett.* **2011**, 11, 946-953.
79. Li, M.; Chen, G. Revisiting catalytic model reaction p-nitrophenol/NaBH4 using metallic nanoparticles coated on polymeric spheres. *Nanoscale* **2013**, 5, 11919-11927.

Chapter 6 Conclusions and Recommendations

This dissertation provides a systematic study on the biological and environmental transformations and applications of two dimensional nanomaterials and hybrids. We used CuO nanoparticles as an example, and investigated the chemical transformation pathways, including particle dissolution, ion complexation, particle sulfidation and secondary particle formation. Meanwhile, the catalytic production of reactive oxygen species was measured in the presence of either CuO suspension or filtrate only, and it was found that the released copper ions were the primary source of ROS generation. Furthermore, the sulfidation reaction can reduce the amount of released ions when sulfidation is sufficient. However, sulfidation can not permanently suppress copper bioavailability and toxicity, which is contradict to what has been observed in Ag sulfidation process. This is attributed the different sulfidation pathway involving the generation of secondary CuS nanoparticles and copper ion release by oxidation of CuS, highlighting the role of transformation on the fate and toxicity of nanomaterials. The follow-up work is recommended to be the long-time exposure and toxicity assessment of metal sulfide nanoparticles.

We were inspired by the conformable and impermeable nature of graphene, and encapsulated potentially toxic nanoparticles inside crumpled graphene nanosacks in order to inhibit ion release and thus reduce toxicity. However, it turned out that the nanosack structure can't significantly isolate the encapsulated nanoparticles from surrounding environment because of its porosity. In the cases of metallic copper and silver, graphene can even enhance oxidation and dissolution rate of loaded nanoparticles in aqueous media. In addition to porosity, other fundamental behaviors of this novel 3D architecture have been explored. The particle–particle electron transfer was shown to be mediated by conductive graphene, and inner graphene walls were responsible for the observed anti-

sintering property. Consequently the nanosacks can be engineered into novel nanoreactors with these unique behaviors by filling the graphene shells with one or multiple types of chemically reactive or catalytic particles, making it attractive in catalysts, controlled release, and environmental remediation. It's recommended to explore the fundamental behaviors in electrochemistry, premised on the open structure and conductive graphene shells of nanosacks. Moreover, the anti-sintering property can be further explored in the areas where high temperature condition is required, such as catalytic methane reforming.

We have fabricated the textured graphene surface with periodic topographical features and long-range order for directing cell-material interactions. The wrinkled surfaces were prepared by graphene oxide wet deposition on pre-stretched elastomers, followed by relaxation. The wavelengths and amplitudes of the formed wrinkles can be systematically tuned by variation in the wet deposition process. The fibroblasts were shown to develop pronounced alignment and elongation relative to those on planar graphene controls. Compared with other methods of patterning (e.g. lithography), wrinkled graphene surface offers potential advantages in the ease, cost, and scale-up of fabrication. The wet deposition method can be further explored in the three dimensional matrix creating local nanoscale or microscale complexity, which could not be achieved by other patterning methods such as lithography.

Considering the complex of novel 2D nanomaterials, we have used simple theoretical models to screen and predict transformation and biological reactivity of 2D nanomaterials based on their fundamental chemical attributes. 2D nanomaterials were categorized and predicted to possibly undergo simple, oxidative or reductive dissolutions, based on the thermodynamic redox potentials and equilibrium solubilities. We also used a

band-structure based framework to identify 2D nanomaterials that were likely to have pro-oxidant activity in biological systems. The results provided suggestions for grouping 2D materials into chemical classes for prioritization in risk management. MoS_2 was used as an example 2D material to illustrate the chemical transformation and catalytic activity in biological and environmental media, which provides useful information on the storage and use of MoS_2 nanomaterials, and the picture on the fate and possible transformation. It is suggested to investigate the photo-induced reactions and transformations of these 2D semiconductor nanomaterials with various band gap in the future work.